University of Tennessee, Knoxville
TRACE: Tennessee Research and Creative Exchange

Doctoral Dissertations | Graduate School

8-2000

A Characteristics Finite Element Algorithm for Computational Open Channel Flow Analysis

Zachariah Chambers
University of Tennessee, Knoxville

Follow this and additional works at: https://trace.tennessee.edu/utk_graddiss

Part of the Engineering Science and Materials Commons

Recommended Citation

Chambers, Zachariah, "A Characteristics Finite Element Algorithm for Computational Open Channel Flow Analysis. " PhD diss., University of Tennessee, 2000.
https://trace.tennessee.edu/utk_graddiss/4181

This Dissertation is brought to you for free and open access by the Graduate School at TRACE: Tennessee Research and Creative Exchange. It has been accepted for inclusion in Doctoral Dissertations by an authorized administrator of TRACE: Tennessee Research and Creative Exchange. For more information, please contact trace@utk.edu.

To the Graduate Council:

I am submitting herewith a dissertation written by Zachariah Chambers entitled "A Characteristics Finite Element Algorithm for Computational Open Channel Flow Analysis." I have examined the final electronic copy of this dissertation for form and content and recommend that it be accepted in partial fulfillment of the requirements for the degree of Doctor of Philosophy, with a major in Engineering Science.

J. Iannelli, Major Professor

We have read this dissertation and recommend its acceptance:

A.J. Baker, Jay Frankel, Chris Pionke, Debra Polignone

Accepted for the Council:

Carolyn R. Hodges

Vice Provost and Dean of the Graduate School

(Original signatures are on file with official student records.)

To the Graduate Council:

I am submitting herewith a dissertation written by Zachariah Chambers entitled "A Characteristics Finite Element Algorithm for Computational Open Channel Flow Analysis." I have examined the final copy of this dissertation for form and content and recommend that it be accepted in partial fulfillment of the requirements for the degree of Doctor of Philosophy, with a major in Engineering Science.

Dr. J. Iannelli, Major Professor

We have read this dissertation
and recommend its acceptance:

Dr. A.J. Baker

Dr. Jay Frankel

Dr. Chris Pionke

Dr. Debra Polignone

Accepted for the Council:

Dr. Anne Mayhew
Interim Vice Provost
and Dean of the Graduate School

(Original signatures are on file in the Graduate Admissions and Records Office.)

A Characteristics Finite Element Algorithm for Computational Open Channel Flow Analysis

A Dissertation

Presented for the

Doctor of Philosophy Degree

The University of Tennessee, Knoxville

Zachariah Chambers

August 2000

Copyright © Zachariah Chambers, 2000

All rights reserved

DEDICATION

This dissertation is dedicated to my brother

Rory Chambers

who had the courage to follow his dream

and to my wife

Merry Chambers

for helping me follow mine.

ACKNOWLEDGMENTS

My four years in the Engineering Science Program of the College of Engineering at the University of Tennessee, Knoxville have been filled with people to whom I am deeply indebted. It has been a pleasure knowing the faculty in my department and my colleagues in the graduate program and I hope these friendships last beyond graduation. I am grateful to my dissertation committee, Dr. Joe Iannelli, Dr. A.J. Baker, Dr. Jay Frankel, Dr. Chris Pionke, and Dr. Debbie Polignone for their support and dedication to this work.

Winston Holmes and Nina Hathaway have been daily figures in my life and their friendship and support should not go unrecognized. I'd like to thank the Engineering Fundamentals Division, Tennessee Space Consortium, Tennessee Governor's School for Manufacturing, and CFD Laboratory for their generous financial support and especially Linda Chatham for making sure it all came through.

Finally, my wife Merry has steadfastly supported my lack of gainful employment for the last six years. Without her encouragement, support, comforting shoulder, and empathetic ear I would have never "travelled" this far.

ABSTRACT

For the reliable determination of open channel flows, a minimally dissipative flux jacobian decomposition finite element algorithm is developed for the one- and two-dimensional inviscid open channel flow equation systems. The modifed form of the parent kinetic flux divergence is biased by the characteristic speeds, i.e. eigenvalues of the kinetic flux divergence jacobian, to induce along all wavelike propogation directions a dissipation level proportional to the propogation speeds of the solution to the hyperbolic problem statement.

The analysis rigorously investigates the inviscid open channel equation system via non-linear, wave-like solutions and reveals linear dependency issues for the momentum equations in steady state flow for all values of the Froude number, which is subsequently eliminated by the modified equation. The modified equation is developed on the continuum level via decomposition of the kinetic flux divergence into components which physically correspond to convection and celerity propagation. These decomposition components are then combined to satisfy the demanding conditions that the eigenvalues of the resulting matrix within the dissipative flux divergence, hence dissipation level, correlate with the eigenvalues of the hyperbolic problem statement, for algorithm accuracy, while remaining positive and real, for algorithm stability.

In both one and two dimensions, for sub- and supercritical flows induced by various dam-break verifications and benchmarks, the algorithm is verified to yield reliable determination of the depth-averaged momentum and height fields by generating accurate and essentially non-oscillatory numerical solutions in the presence of hydraulic jumps while remaining second-order accurate in both space and time.

Contents

1 Introduction **1**

1.1 Applications 3

1.1.1 Flood Routing 3

1.1.2 Free Surface Unsteady Flow 3

1.2 Previous Research 4

1.3 Original Contributions 7

1.4 Scope 8

2 Theoretical Development,

One Dimension **9**

2.1 Governing Equations and Eigenvalue Analysis 10

2.2 Continuum Upstream-Bias Construction 11

2.3 Kinetic Flux Jacobian Decomposition 12

2.3.1 Flux Difference Splitting 14

2.3.2 Flux Vector Splitting 15

2.4 Supercritical Convection Decomposition 17

2.5 Celerity-Convection Decomposition 20

2.6 Composite Jacobian Construction 23

2.7 Evaluation of the Characteristics-Biased Flux 25

2.8 Determination of Free Parameters 28

2.9 Spatial Discretization 33

2.10 Temporal Discretization and Newton Construction 37

2.11 Determination of ψ 42

2.12 Summary 45

3 Discussion and Results,

One Dimension **46**

3.1 Problem Statement, 1D Dam Break 46

3.2 Dissipation Controller Verification 49

3.3 Quasi-Newton Algorithm Convergence Study 57

3.4 Grid Refinement Study 65

4 Theoretical Development,

Two Dimensions **70**

4.1 Non-Linear, Wave-Like Solutions 71

4.2 Governing Equations and Eigenvalue Analysis 72

4.2.1 Celerity Limit 74

4.2.2 Convection Limit 76

4.2.3 Inviscid Open Channel Flow Equations 81

4.2.4 Linear Dependency / Eigenvalue Summary 86

4.3 Polar Variation of Characteristic Speeds 87

4.4 Continuum Upstream-Bias Approximation 100

4.5 Streamline Convection Decomposition 103

4.6 Celerity-Convection Decomposition 109

4.6.1 Streamline and Crossflow Components 111

4.6.2 Absolute Celerity Matrices 114

4.7 Composite Jacobian Construction 117

4.8 Evaluation of the Characteristics-Biased Flux 120

4.9 Determination of Free Parameters 123

4.9.1 Upstream Matrix Eigenvalues 123

4.9.2 Conditions on Upstream-Bias Eigenvalues 125

4.9.3 Upstream Bias Parameters $\mathbf{a}$ and $\mathbf{a}^N$ 126

4.9.4 Streamline Eigenvalue λ_3^{Acs} 127

4.9.5 Streamline Eigenvalue λ_1^{Acs} 128

4.9.6 Upstream Bias Parameters α and δ and Streamline Eigenvalue λ_2 128

4.9.7 Upstream Bias Parameter α^N 129

4.9.8 Upstream Eigenvalue and Bias Parameter Summary 131

4.10 Upstream Bias Magnitude 135

4.11 Spatial Discretization 144

4.12 Temporal Discretization and Newton Construction 148

4.13 Determination of ψ 155

4.14 Summary 157

5 Discussion and Results,

Two Dimensions **158**

5.1 Partial Dam Break 158

5.1.1 Problem Statement 160

5.1.2 Boundary and Initial Conditions 161
5.1.3 Results 162
5.1.3.1 Dissipation Controller Verification 163
5.1.3.2 Quasi-Newton Algorithm Convergence Study 171
5.1.3.3 Grid Refinement Study 179
5.1.4 Discussion 182
5.2 Circular Dam Break 184
5.2.1 Problem Statement 185
5.2.2 Boundary and Initial Conditions 185
5.2.3 Results 186
5.2.4 Discussion 191
5.3 River Harbor 191
5.3.1 Problem Statement 192
5.3.2 Boundary and Initial Conditions 193
5.3.3 Results 193
5.3.4 Discussion 200

6 Conclusions and Recommendations **201**

Bibliography **206**

A Grid Refinement Data,
1D Dam Break **213**

B Additional Plots, 2D Dam Break **235**

B.1 Time = 1.0 s 235
B.2 Time = 3.0 s 238

B.3 Time = 5.0 s 241

B.4 Time = 7.2 s 244

C Grid Refinement Data,

2D Partial Dam Break **247**

Vita **264**

List of Figures

2.1 Correlation of One-Dimensional Open Channel and Imposed Upstream Eigenvalues . 31

2.2 One-Dimensional Spline Modified, Imposed Upstream Eigenvalue Spectra 32

2.3 One-Dimensional Upstream Bias Parameter Spectra 32

3.1 1D Dam Break : Initial Condition 48

3.2 1D Dam Break : Verification Solution ($t = 1.0\ s$) 48

3.3 1D Dissipation Controller Verification : $\psi = 0.25$ 54

3.4 1D Dissipation Controller Verification : $\psi = 0.50$ 54

3.5 1D Dissipation Controller Verification : $\psi = 0.75$ 55

3.6 1D Dissipation Controller Verification : $\psi = 1.00$ 55

3.7 1D Dissipation Controller Verification : $\psi = \psi(u)$ 56

3.8 1D Dissipation Controller Verification : h Error Evolution 56

3.9 1D Dissipation Controller Verification : m Error Evolution 57

3.10 1D Quasi-Newton Convergence Verification : $max(\delta Q_h)$ ($t = 0.1,\ 0.2,\ 0.5,\ 0.8\ s$) . . 60

3.11 1D Quasi-Newton Convergence Verification : $max(\delta Q_m)$ ($t = 0.1,\ 0.2,\ 0.5,\ 0.8\ s$) . . 60

3.12 1D Quasi-Newton Convergence Verification : h Profile, 1-3 Iterations, $t = 0.5\ s$ . . . 63

3.13 1D Quasi-Newton Convergence Verification : h Profile Zoom-In 1, 1-3 Iterations, $t = 0.5\ s$ 63

3.14 1D Quasi-Newton Convergence Verification : h Profile Zoom-In 2, 1-3 Iterations, $t = 0.5\ s$ 64

3.15 1D Quasi-Newton Convergence Verification : h Profile Zoom-In 3, 1-3 Iterations, $t = 0.5\ s$ 64

4.1 Polar Variation of Propagation Speeds : $Fr = 0.00$ 89

4.2 Polar Variation of Propagation Speeds : $Fr = 0.05$ 89

4.3 Polar Variation of Propagation Speeds : $Fr = 0.50$ 90

4.4 Polar Variation of Propagation Speeds : $Fr = 1.00$ 90

4.5 Polar Variation of Propagation Speeds : $Fr = 1.50$ 91

4.6 Polar Variation of Propagation Speeds : $Fr = 2.00$ 91

4.7 Subcritical Polar Variation of λ_1^{OC} 94

4.8 Supercritical Polar Variation of λ_1^{OC} 94

4.9 Subcritical Polar Variation of λ_2^{OC} 95

4.10 Supercritical Polar Variation of λ_2^{OC} 95

4.11 Subcritical Polar Variation of λ_3^{OC} 96

4.12 Supercritical Polar Variation of λ_3^{OC} 96

4.13 Subcritical Polar Variation of $\lambda_{1,2,3}^{OC}$: Summary 99

4.14 Supercritical Polar Variation of $\lambda_{1,2,3}^{OC}$: Summary 99

4.15 Two-Dimensional Spline Modified, Imposed Upstream Eigenvalue Spectra 133

4.16 Two-Dimensional Upstream Bias Parameter Spectra 133

4.17 Polar Variation of Upstream Eigenvalues : $Fr = 0.00$ 137

4.18 Polar Variation of Upstream Eigenvalues : $Fr = 0.05$ 137

4.19 Polar Variation of Upstream Eigenvalues : $Fr = 0.50$ 138

4.20 Polar Variation of Upstream Eigenvalues : $Fr = 1.00$ 138

4.21 Polar Variation of Upstream Eigenvalues : $Fr = 1.50$ 139

4.22 Polar Variation of Upstream Eigenvalues : $Fr = 2.00$ 139

4.23 Subcritical Polar Correlation of λ_1^{OC} and λ_1^{A} 141

4.24 Supercritical Polar Correlation of λ_1^{OC} and λ_1^{A} 141

4.25 Subcritical Polar Correlation of λ_2^{OC} and λ_2^{A} 142

4.26 Supercritical Polar Correlation of λ_2^{OC} and λ_2^{A} 142

4.27 Subcritical Polar Correlation of λ_3^{OC} and λ_3^{A} 143

4.28 Supercritical Polar Correlation of λ_3^{OC} and λ_3^{A} 143

5.1 Partial Dam Break : Computational Domain 160

5.2 2D Dissipation Controller Verification : $\psi = 0.25$ 169

5.3 2D Dissipation Controller Verification : $\psi = 0.50$ 169

5.4 2D Dissipation Controller Verification : $\psi = 0.75$ 170

5.5 2D Dissipation Controller Verification : $\psi = 1.00$ 170

5.6 2D Dissipation Controller Verification : $\psi = \psi(ke)$ 171

5.7 2D Quasi-Newton Convergence Verification : $max(\delta Q_h)$ $(t = 1.0,\ 3.0,\ 5.0,\ 7.2\ s)$ . . 174

5.8 2D Quasi-Newton Convergence Verification : $max(\delta Q_{m1})$ $(t = 1.0,\ 3.0,\ 5.0,\ 7.2\ s)$. 175

5.9 2D Quasi-Newton Convergence Verification : $max(\delta Q_{m2})$ $(t = 1.0,\ 3.0,\ 5.0,\ 7.2\ s)$. 175

5.10 2D Quasi-Newton Convergence Verification : h profile $(t = 7.2\ s, y = 130\ m)$ 178

5.11 2D Quasi-Newton Convergence Verification : h profile $(t = 7.2\ s, x = 80, 100, 120\ m)$ 178

5.12 Partial Dam Benchmark : h Carpet $(t = 7.2\ s)$ 183

5.13 Partial Dam Benchmark : h Contour $(t = 7.2\ s)$ 183

5.14 Circular Dam Break : Computational Domain 187

5.15 Circular Dam Break : Interpolated Initial Condition 187

5.16 Circular Dam Break : h Carpet Plot $(t = 0.69\ s)$ 190

5.17 Circular Dam Break : h Contour Plot ($t = 0.69\ s$) 190

5.18 River Harbor : Computational Domain 192

5.19 River Harbor : Initial Convergence in $\|q\|_{H^0}$ 196

5.20 River Harbor : Initial Convergence in $\|q\|_E$ 196

5.21 River Harbor : Final Convergence in $\|q\|_{H^0}$ 197

5.22 River Harbor : Final Convergence in $\|q\|_E$ 197

5.23 River Harbor : Carpet Plot of h 198

5.24 River Harbor : Contour Plot of h 198

5.25 River Harbor : Contour Plot of m 199

5.26 River Harbor : Quiver Plot of $m_{1,2}$ 199

B.1 Partial Dam Break : Contour Plot of ψ ($t = 1.0\ s$) 235

B.2 Partial Dam Break : Contour Plot of Fr ($t = 1.0\ s$) 236

B.3 Partial Dam Break : Contour Plot of α ($t = 1.0\ s$) 236

B.4 Partial Dam Break : Contour Plot of α^N ($t = 1.0\ s$) 237

B.5 Partial Dam Break : Contour Plot of δ ($t = 1.0\ s$) 237

B.6 Partial Dam Break : Contour Plot of ψ ($t = 3.0\ s$) 238

B.7 Partial Dam Break : Contour Plot of Fr ($t = 3.0\ s$) 239

B.8 Partial Dam Break : Contour Plot of α ($t = 3.0\ s$) 239

B.9 Partial Dam Break : Contour Plot of α^N ($t = 3.0\ s$) 240

B.10 Partial Dam Break : Contour Plot of δ ($t = 3.0\ s$) 240

B.11 Partial Dam Break : Contour Plot of ψ ($t = 5.0\ s$) 241

B.12 Partial Dam Break : Contour Plot of Fr ($t = 5.0\ s$) 242

B.13 Partial Dam Break : Contour Plot of α ($t = 5.0\ s$) 242

B.14 Partial Dam Break : Contour Plot of α^N ($t = 5.0\ s$) 243

B.15 Partial Dam Break : Contour Plot of δ $(t = 5.0\ s)$ 243

B.16 Partial Dam Break : Contour Plot of ψ $(t = 7.2\ s)$ 244

B.17 Partial Dam Break : Contour Plot of Fr $(t = 7.2\ s)$ 245

B.18 Partial Dam Break : Contour Plot of α $(t = 7.2\ s)$ 245

B.19 Partial Dam Break : Contour Plot of α^N $(t = 7.2\ s)$ 246

B.20 Partial Dam Break : Contour Plot of δ $(t = 7.2\ s)$ 246

List of Tables

2.1 Qualitative Dissipation Levels for Stability and Accuracy 42

3.1 1D Dissipation Controller Verification : Constant Parameters 50

3.2 1D Dissipation Controller Verification : Error Norms and Extrema ($t = 0.1\ s$) 51

3.3 1D Dissipation Controller Verification : Error Norms and Extrema ($t = 0.2\ s$) 52

3.4 1D Dissipation Controller Verification : Error Norms and Extrema ($t = 0.5\ s$) 52

3.5 1D Dissipation Controller Verification : Error Norms and Extrema ($t = 0.8\ s$) 52

3.6 1D Quasi-Newton Convergence Verification : $max(\delta Q)$ Convergence Rates 58

3.7 1D Quasi-Newton Convergence Verification : Iterate $max(\delta Q)$ ($t = 0.1, 0.2\ s$) 59

3.8 1D Quasi-Newton Convergence Verification : Iterate $max(\delta Q)$ ($t = 0.5, 0.8\ s$) 59

3.9 1D Quasi-Newton Convergence Verification : Solution Error Norms ($t = 0.1, 0.2\ s$) . 62

3.10 1D Quasi-Newton Convergence Verification : Solution Error Norms ($t = 0.5, 0.8\ s$) . 62

3.11 1D Grid Refinement Verification : Δt Summary 67

3.12 1D Grid Refinement Verification : Error Convergence Rate in Energy Norm 69

3.13 1D Grid Refinement Verification : Error Convergence Rate in H^0 Norm 69

3.14 1D Grid Refinement Verification : Error Convergence Rate in H^1 Norm 69

4.1 Eigenvalue / Linear Dependence Summary 86

5.1 Partial Dam Break : Boundary Conditions 161

5.2 Partial Dam Break : Initial Conditions 162

5.3 2D Dissipation Controller Verification : Constant Parameters 163

5.4 2D Dissipation Controller Verification : Extrema ($t = 1.0\ s$) 166

5.5 2D Dissipation Controller Verification : Extrema ($t = 3.0\ s$) 166

5.6 2D Dissipation Controller Verification : Extrema ($t = 5.0\ s$) 167

5.7 2D Dissipation Controller Verification : Extrema ($t = 7.2\ s$) 167

5.8 2D Dissipation Controller Verification : Norms ($t = 1.0\ s$) 167

5.9 2D Dissipation Controller Verification : Norms ($t = 3.0\ s$) 168

5.10 2D Dissipation Controller Verification : Norms ($t = 5.0\ s$) 168

5.11 2D Dissipation Controller Verification : Norms ($t = 7.2\ s$) 168

5.12 2D Quasi-Newton Convergence Verification : $max(\delta Q)$ Convergence Rates 173

5.13 2D Quasi-Newton Convergence Verification : Iterates and $max(\delta Q)$ ($t = 1.0,\ 3.0\ s$) . 173

5.14 2D Quasi-Newton Convergence Verification : Iterates and $max(\delta Q)$ ($t = 5.0,\ 7.2\ s$) . 174

5.15 2D Quasi-Newton Convergence Verification : Iterate Norms ($t = 1.0\ s$) 176

5.16 2D Quasi-Newton Convergence Verification : Iterate Norms ($t = 3.0\ s$) 176

5.17 2D Quasi-Newton Convergence Verification : Iterate Norms ($t = 5.0\ s$) 177

5.18 2D Quasi-Newton Convergence Verification : Iterate Norms ($t = 7.2\ s$) 177

5.19 2D Grid Refinement Verification : Δt Summary 180

5.20 2D Grid Refinement Verification : Error Convergence Rate in Energy Norm 181

5.21 2D Grid Refinement Verification : Error Convergence Rate in H^0 Norm 181

5.22 Circular Dam Break : Boundary Conditions 186

5.23 Circular Dam Break : Constant Parameters 188

5.24 Circular Dam Break : Extrema 189

5.25 Circular Dam Break : Norms 191

5.26 River Harbor : Boundary Conditions 193

5.27 River Harbor : Constant Parameters 194

5.28 River Harbor : Steady-State Norms 194

5.29 River Harbor : Steady State Extrema 195

A.1 1D Grid Refinement Verification : Solution Energy Norm (25 Elements) 214

A.2 1D Grid Refinement Verification : Solution Energy Norm (50 Elements) 215

A.3 1D Grid Refinement Verification : Solution Energy Norm (100 Elements) 216

A.4 1D Grid Refinement Verification : Solution Energy Norm (200 Elements) 217

A.5 1D Grid Refinement Verification : Solution Energy Norm (400 Elements) 218

A.6 1D Grid Refinement Verification : Solution H^0 Norm (25 Elements) 219

A.7 1D Grid Refinement Verification : Solution H^0 Norm (50 Elements) 220

A.8 1D Grid Refinement Verification : Solution H^0 Norm (100 Elements) 221

A.9 1D Grid Refinement Verification : Solution H^0 Norm (200 Elements) 222

A.10 1D Grid Refinement Verification : Solution H^0 Norm (400 Elements) 223

A.11 1D Grid Refinement Verification : Solution H^1 Norm (25 Elements) 224

A.12 1D Grid Refinement Verification : Solution H^1 Norm (50 Elements) 225

A.13 1D Grid Refinement Verification : Solution H^1 Norm (100 Elements) 226

A.14 1D Grid Refinement Verification : Solution H^1 Norm (200 Elements) 227

A.15 1D Grid Refinement Verification : Solution H^1 Norm (400 Elements) 228

A.16 1D Grid Refinement Verification : Solution Energy Norm ($t = 0.1\ s$) 229

A.17 1D Grid Refinement Verification : Solution Energy Norm ($t = 0.2\ s$) 229

A.18 1D Grid Refinement Verification : Solution Energy Norm ($t = 0.5\ s$) 230

A.19 1D Grid Refinement Verification : Solution Energy Norm ($t = 0.8\ s$) 230

A.20 1D Grid Refinement Verification : Solution H^0 Norm ($t = 0.1\ s$) 231

A.21 1D Grid Refinement Verification : Solution H^0 Norm ($t = 0.2\ s$) 231

A.22 1D Grid Refinement Verification : Solution H^0 Norm ($t = 0.5\ s$) 232

A.23 1D Grid Refinement Verification : Solution H^0 Norm ($t = 0.8\ s$) 232

A.24 1D Grid Refinement Verification : Solution H^1 Norm ($t = 0.1\ s$) 233

A.25 1D Grid Refinement Verification : Solution H^1 Norm ($t = 0.2\ s$) 233

A.26 1D Grid Refinement Verification : Solution H^1 Norm ($t = 0.5\ s$) 234

A.27 1D Grid Refinement Verification : Solution H^1 Norm ($t = 0.8\ s$) 234

C.1 2D Grid Refinement Verification : Solution Energy Norm (20 Elements) 248

C.2 2D Grid Refinement Verification : Solution Energy Norm (40 Elements) 249

C.3 2D Grid Refinement Verification : Solution Energy Norm (80 Elements) 250

C.4 2D Grid Refinement Verification : Solution Energy Norm (160 Elements) 251

C.5 2D Grid Refinement Verification : Solution H^0 Norm (20 Elements) 252

C.6 2D Grid Refinement Verification : Solution H^0 Norm (40 Elements) 253

C.7 2D Grid Refinement Verification : Solution H^0 Norm (80 Elements) 254

C.8 2D Grid Refinement Verification : Solution H^0 Norm (160 Elements) 255

C.9 2D Grid Refinement Verification : Solution Energy Norm ($t = 1.0\ s$) 256

C.10 2D Grid Refinement Verification : Solution Energy Norm ($t = 3.0\ s$) 257

C.11 2D Grid Refinement Verification : Solution Energy Norm ($t = 5.0\ s$) 258

C.12 2D Grid Refinement Verification : Solution Energy Norm ($t = 7.2\ s$) 259

C.13 2D Grid Refinement Verification : Solution H^0 Norm ($t = 1.0\ s$) 260

C.14 2D Grid Refinement Verification : Solution H^0 Norm ($t = 3.0\ s$) 261

C.15 2D Grid Refinement Verification : Solution H^0 Norm ($t = 5.0\ s$) 262

C.16 2D Grid Refinement Verification : Solution H^0 Norm ($t = 7.2\ s$) 263

LIST OF SYMBOLS

$\mathbf{a}$, $\mathbf{a}^N$	arbitrary, mutually perpendicular directions
a_l	principal propogation-direction unit vector
a_{il}	direction cosine of a_l along principal wave propagation direction of wave "l"
c	celerity
$f_j(\mathbf{q})$	kinetic flux
$f_j^c(\mathbf{q})$	characteristics-biased flux
$f_j^{cel}(\mathbf{q})$	celerity flux
$f_j^{conv}(\mathbf{q})$	convection flux
Fr	Froude Number
g	gravity
h	flow depth-averaged height (state variable)
m_j, $\mathbf{m}$	flow depth-averaged momentum (state variable)
n_j, $\mathbf{n}$	solution propagation-direction unit vector
P	arbitrary flowfield point
$q(\mathbf{x}, t)$	state variable
$\mathbf{q}(\mathbf{x}, t)$	vector of state variables
$\mathbf{q}^N(\mathbf{x}, t)$	continuum approximation to vector of state variables
$\mathbf{q}^h(\mathbf{x}, t)$	discrete approximation to vector of state variables
t	time
x_j, $\mathbf{x}$	cartesian coordinates
u_j, $\mathbf{u}$	flow depth-averaged velocity
v_j, $\mathbf{v}$	velocity/streamline-direction unit vector
v_j^N, $\mathbf{v}^N$	crossflow-direction unit vector
$\hat{w}$	compact support test function

$\mathbf{A}_j$	flux divergence jacobian
$\mathbf{A}_{lj}$	flux jacobian decomposition component
$\mathbf{A}_j^{cel_o}$	steady-state celerity jacobian
$\mathbf{A}_j^{conv_o}$	steady-state convection jacobian
$\mathbf{A}_j^{cel}$	celerity jacobian
$\mathbf{A}_j^{conv}$	convection jacobian
$\mathbf{A}_j^{jcel}$	decomposed celerity jacobian
$\mathbf{A}_j^{jaux}$	decomposed auxiliary jacobian
$\mathbf{A}_j^{scc}$	streamline celerity-convection jacobian
$\mathbf{A}_j^{sc}$	streamline celerity jacobian
$\mathcal{A}$	upstream matrix
$L(\mathbf{q})$	conservation law system
$L^N(\mathbf{q})$	continuum approximation to conservation law system
$L^h(\mathbf{q})$	discrete approximation to conservation law system
$N_k(\mathbf{x})$	Lagrangian interpolating polynomial of degree k
$\mathbf{X}$	right eigenvector matrix

α_l	jacobian decomposition linear combination functions
$\bar{\alpha}$	crossflow celerity differential bias
$\tilde{\alpha}$	flux divergence linear combination function
$\alpha,\ \alpha^N$	upstream parameters
β	partition function
δ	upstream parameter
δ_j^i	Kronecker delta function
$\delta_l \hat{w}$	directional test function variation
ϵ	local length scale
ϵ_{Fr}	critical transition layer parameter

λ	eigenvalue
$\lambda^{d_{\mathcal{A}}}$	dimensional upstream eigenvalue
$\lambda^{\mathcal{A}}$	non-dimensional upstream eigenvalue
$\lambda^{\mathcal{A}_{sl}}$	non-dimensional streamline upstream eigenvalue
$\lambda^{\mathcal{A}cs}$	correlated and stable non-dimensional upstream eigenvalue
$\lambda^{\mathcal{A}cs_{sl}}$	correlated and stable non-dimensional streamline upstream eigenvalue
$\lambda^{d_{OC}}$	dimensional eigenvalue of open channel kinetic flux jacobian
λ^{OC}	non-dimensional eigenvalue of open channel kinetic flux jacobian
$\lambda^{OC_{sl}}$	non-dimensional streamline eigenvalue of open channel kinetic flux jacobian
λ^{ND}	non-dimensional eigenvalue
η_j	transformed coordinate directions for non-linear, wavelike-solutions
$\hat{\eta}_j$	steady-state transformed coordinate direction
$\hat{\Omega}$	continuum domain
φ	solution continuity gauge
ψ	non-linear dissipation controller
Θ	time integration implicitness parameter
θ_v	angle between the velocity unit vector $\mathbf{v}$ and the x_1 axis
θ_{Fr}	angle between the streamline and Froude line
$\bar{\theta}$	angle between $\mathbf{n}$ and $\mathbf{v}$
Λ^{jcel}	diagonal eigenvalue matrix
Λ^{jcel^+}	positive diagonal eigenvalue matrix
Λ^{jcel^-}	negative diagonal eigenvalue matrix
Φ_α	test function
Ψ_β	trial space

Chapter 1

Introduction

Open channel flow has been investigated for over 150 years beginning with the works of Laplace and Lagrange. Advanced theoretical work began with the introduction of the heralded Saint-Venant equations. These classic coupled partial differential equations were presented by Barré de Saint-Venant in 1871 to the French Academy of Sciences. These two equations, in their original form, are [1]

$$\frac{\partial w}{\partial t} + \frac{\partial (wU)}{\partial s} = 0 \tag{1.1}$$

$$\frac{\partial \epsilon}{\partial s} = \frac{1}{g}\frac{\partial U}{\partial t} + \frac{U}{g}\frac{\partial U}{\partial s} + \frac{\chi}{\omega}\frac{F}{\rho g} \tag{1.2}$$

where: w = cross-sectional area, U = mean velocity, ϵ = height of the water surface above the reference level, $\chi F/\omega\rho g$ = friction slope, χ = wetted perimeter, ρ = water density, g = gravitational acceleration, ρg = specific weight, $\rho g F$ = boundary friction per unit area, s = length along the prismatic canal, and t = time.

These equations have remained virtually unchanged over 130 years of analysis and application. While modifications yield equation systems which are more complete and sophisticated, they invariably simplify to the original Saint-Venant equations when put to practical use.

The contributions by Saint-Venant, however, should not shadow his contemporaries and predecessors. H.L Patriot studied tidal behavior in estuaries and initiated generalizations for this branch of hydraulics. Russell and Bazin experimented with wave movement in canals and amassed the experimental data key to the verification of ensuing theories on wave celerity. Boussinesq produced several works on hydraulics, including a paper on the solitary wave and wave theory.

Saint-Venant, an accomplished engineer, mathematician, and physicist, recognized that the utility and robustness of any governing equation system rests on the chosen assumptions. The observed behavior of open channel flow provided the physical foundation of his assumptions. A century and a half of research in hydraulics have validated his approach [1], [2].

The fundamental underlying assumptions for the Saint-Venant equations are:

1. The wave surface gradually varies. Thus the pressure distribution along the height is hydrostatic and the vertical velocities are small with respect to the horizontal velocities;

2. Friction losses in unsteady flow are equivalent to those in steady flow;

3. Wave propagation is not substantially affected by the velocity distribution on the channel surface;

4. Wave movement can be considered two-dimensional;

5. The slope of the channel bed is so gradual that α, the angle made by the bed with the horizontal, is small enough such that $\cos\alpha \approx 1$ and $\sin\alpha \approx \tan\alpha$.

To date, investigators have introduced modifications to the original equations to account for: (1) vertical velocities, (2) frictional differences between steady and unsteady flow, (3) Coriolis accelera-

tions, (4) property variations in the third dimension, (5) curvilinear bed profiles, and (6) improved frictional loss models (Manning and Chezy).

While these modifications do extend the capability of the original Saint-Venant equations, a study sponsored by the US Federal Highway Administration, "Unsteady free-surface flow in a circular long drain," powerfully demonstrated the fortitude of (1.1) and (1.2). It showed that the results from an experiment designed according to Saint-Venant's assumptions are identical to numerical solutions of the equations to within experimental error. These results compared for even the large-scale models with well-measured initial and boundary conditions. The published conclusion was that, excluding extreme cases, the unmodified Saint-Venant equations yield satisfactory results.

1.1 Applications

The algorithm developed in the dissertation project to solve the Saint-Venant equations will be validated with several application problems, taken from the following collection of physical flow phenomena [1], [2].

1.1.1 Flood Routing

Flood routing procedures have been developed to model the behavior of floods through reservoirs, lakes, and rivers. The need to model flood behavior adequately arises from: (a) predicting floods in rivers due to heavy storms (b) assessing the impact of man-made reservoirs along rivers (c) designing flood prevention systems. A special type of flood, the dam break, is of substantial importance and a focus of this research project.

1.1.2 Free Surface Unsteady Flow

Aside from flood modeling, flow features within rivers, canals, and estuaries are also of interest.

Canals and partially filled tunnels in hydroelectric and pumping plants pose a number of unsteady flow situations. Flows are often affected by unsteady pressures caused by plant operations, surge tanks, and basins. These flow patterns, under operating conditions, are some of the most challenging to solve.

Navigation channels and canals are also subject to unsteady flows caused by the operation of locks, pools, and pumps and control gates. Levee and embankment breaches are other sources of unsteady flow. Municipal water supplies as well as irrigation canals are unsteady as flows are initiated and terminated.

Lake, harbor, and estuary flows are frequently unsteady due to wind shear, incoming or outgoing flood waves, induced density currents, and tidal action. An excellent example is a harbor which adjoins a river and has unsteady boundary conditions at the harbor/river interface.

The Saint-Venant equations for open-channel flow are well-established, verified, and applicable to numerous physical situations. This dissertation will present a new characteristics-biased finite element computational algorithm for the analysis of open-channel flows.

1.2 Previous Research

Numerous methods [3] - [6], be they finite difference, finite volume, or finite element, exist for the solution of one-dimensional hyperbolic equation systems of the form

$$\frac{\partial q}{\partial t} + \frac{\partial f(q)}{\partial x} = 0 \tag{1.3}$$

The beauty, and Achille's heel, of hyperbolic conservation laws is that they admit discontinuities in both solution and solution slope. This is ideal for modeling physical systems in which discontinuies occur, i.e. gas dynamic shocks within the Euler equations or bores within the open channel equations.

However, numerical simulations of problems admitting such discontinuities can induce dispersive error modes which, if left unchecked, will destabilize the solution.

In the 1970's the concepts of artificial dissipation and the modified equation were introduced and the numerical algorithms of Lax-Wendroff and MacCormack became popular. By the end of the 1970's the original ideas of Godunov, which incorporated the physics of the problem into the dissipation operator, were reconsidered. At the same time, Van Leer analysed the properties of conservation and monotonicity for convection problems. The concept of *upwinding* and *approximate Riemann solvers* appeared in the 1980's which made possible the now-common classes of *flux vector splitting* [7] and *flux difference splitting* [8].

In the late 1980's, modifications of the test space to yield dissipative Petrov-Galerkin formulations have been introduced with the famous SUPG [9] algorithm which, while monotone and accurate, remained disconnected from characteristics theory. In the open-channel community, solution characteristics were incorporated into the test function by Hicks [10] but the implementation remained ad hoc. Taylor series dissipation terms, TWS, have also been developed [11] to introduce dissipation and applied to the open channel equations [12] but, as with the Petrov-Galerkin formulations, remain independent of characteristics theory.

Thanks to these advances, the classical algorithms of Lax-Wendroff and MacCormack have become less widely used due to the increased accuracy and stability of the flux vector/flix difference splitting techniques. In addition, adaptive TVD algorithms, such as those of Osher, Roe, and van Leer, employ *flux limiters* and yield sharp solutions near discontinuities while remaining accurate in regions of smooth solution.

The extension to two- and three-dimensions is non-trivial and the associated complexity makes theoretical analyses difficult or impossible. All the theory concerning conservation laws and flux limiters has been developed in one space dimension. Morevoer, the simple concepts which drive

finite differences and subsequently finite volumes are not readily applicable to two dimensions and remain mostly heueristic. There are only a few truly two-dimensional finite difference/finite volume approaches to solving such problems and are based on operator splitting [13]. Heed that the finite element method is readily extensible to multi-dimensions with no ad-hoc implementation of boundary conditions [14].

Whereas flux vector techniques have been more frequently employed than Lax-Wendroff and MacCormack for nearly ten years, it is interesting to point out that current research and publications within the civil engineering/hydraulics community still use exactly these techniques [15] - [18]. The use of "black box" CFD codes is also evident [19] - [22] in recent civil engineering literature. No mention is made of the numerical process by which solutions were obtained - the publications instead focus on "calibration" of the software to match experimental data. While there is clearly merit in using pre-packaged software to obtain results, the need for model calibration always begs the question of accuracy when a new problem is solved without experimental data for validation.

As the finite element method is readily extensible to multi-dimensions and requires no heueristic "schemes," it is surprising that little research within the civil engineering open channel community has been performed. One possible reason is that outdated algorithms still yield answers accurate enough for most hydraulic applications [23]. Another issue, reported by Katopodes [24] was that early research into finite element solutions of the invsicid open channel equations [25] - [32] lead to the interesting conclusion that, due to dispersion evident in finite element solutions, existing finite difference techniques were superior to finite element methodolgy.

Despite excellent results obtained via operator splitting, no analysis was performed with respect to the characteristics of two-dimensional non-linear systems of equations and the propogation behavior of the dissipative mechanism. Most finite difference, volume and element algorithms remain largely independent from the physics of celerity and convection [37],[33]. The dissipation mechanisms

within these algorithms, moreover, is developed on the discrete level in connection with a specific spatial discretization. This research, utilizing the non-linear, multi-dimensional characteristics-bias algorithm developed by Iannelli [38], is the first to rigorously analyze the two-dimensional open channel equations and introduce a dissipative mechanism that is not only developed on the continuum, i.e. before discretization, level but also propogates in harmony with the solution characteristic velocities in all directions for all values of the Froude number.

1.3 Original Contributions

This PhD dissertation applies the characteristics-bias flux jacobian decomposition theory developed by Iannelli [34] - [38] to the homogenous form of the inviscid open channel equation system in one and two dimensions. Specific original contributions include

- A new stable and accurate finite element algorithm for the open channel equations.
- A robust theoretical framework which encompasses both flux-difference and flux-vector splitting methodologies.
- Presentation of solution extrema and norms for standard validation problems , previously lacking.
- A fine grid benchmark solution to the partial dam break problem which contains flow features as yet unreported.
- A critical assessment of current solutions to the circular dam break problem and hence a new benchmark solution
- A new benchmark problem, the river harbor, for the open channel equations.

1.4 Scope

This dissertation will focus upon the application of the characteristics-bias flux jacobian decomposition for the gas dynamic Euler equations to the open-channel equation system. The following items are contained in this research:

- Develop a characteristics-biased flux divergence for the one-dimensional, non-linear hyperbolic open channel flow equation system in homogemous form.
- Perform verifications for linear and non-linear dissipation controllers, assess quasi-Newton iteration performance, and verify solution convergence under grid refinement.
- Report results, along with critical comparisons, with available data.
- Develop a characteristics-biased flux divergence for the two-dimensional, non-linear hyperbolic open channel flow equation system in homogemous form.
- Perform verifications for linear and non-linear dissipation controllers, assess quasi-Newton iteration performance, and verify solution convergence under grid refinement.
- Report results, along with critical comparisons, with available data.

Chapter 2

Theoretical Development, One Dimension

This chapter develops the characteristics-biased flux divergence for the one-dimensional, inviscid open channel flow equations. Recognizing the required dissipation level to be proportional to the characteristic speeds, the eigenvalues of the kinetic flux divergence jacobian are investigated. Two decompositions of the kinetec flux divergence are taken next: one which is valid for supercritical flow, the other which is valid in the celerity limit. A linear combination is then established as a function of the local Froude number to yield a composite decomposition which is valid for all Froude numbers. The free parameters are then determined based on stability requirements and physical consistency with the original hyperbolic conservation law. Next, the semi-discrete spatial approximation to the biased equation system is generated followed by the implementation of a Theta Taylor series for time integration coupled with a Newton iteration algorithm to handle the non-linearities. The chapter concludes with the development of the non-linear dissipation controller as an element averaged parameter.

2.1 Governing Equations and Eigenvalue Analysis

The one-dimensional, inviscid open channel equations take the divergence form of

$$\frac{\partial \mathbf{q}}{\partial t} + \frac{\partial f(\mathbf{q})}{\partial x} = 0 \tag{2.1}$$

where

$$\mathbf{q} = \left\{ \begin{array}{c} h \\ m \end{array} \right\} \quad \text{and} \quad f(\mathbf{q}) = \left\{ \begin{array}{c} m \\ \frac{m}{h} m + g \frac{h^2}{2} \end{array} \right\} \tag{2.2}$$

Casting (2.1) in non-divergence form yields the flux divergence jacobian $\mathbf{A}$:

$$\frac{\partial \mathbf{q}}{\partial t} + \mathbf{A} \frac{\partial \mathbf{q}}{\partial x} = 0 \tag{2.3}$$

where

$$\mathbf{A} = \frac{\partial f(\mathbf{q})}{\partial \mathbf{q}} = \left[\begin{array}{cc} 0 & 1 \\ -\frac{m^2}{h^2} + gh & 2\frac{m}{h} \end{array} \right] \tag{2.4}$$

Substituting the definition of the fluid velocity $u = m/h$ and solving for the eigenvalues of $\mathbf{A}$ yields the characteristics to be

$$\lambda_{1,2}^{d_{OC}} = u \pm \sqrt{gh} \tag{2.5}$$

where $\sqrt{gh}$ is the gravity wave celerity, the propagation speed of surface perturbation. Introducing the non-dimensional Froude number as $Fr = u/\sqrt{gh}$ allows the classification of flow regimes as

$$
\begin{aligned}
Fr < 1 \quad & \text{subcritical} \\
Fr = 1 \quad & \text{critical} \\
Fr > 1 \quad & \text{supercritical}
\end{aligned}
$$

and the definition of the non-dimensional eigenvalues as

$$\lambda_{1,2}^{OC} = Fr \pm 1 \tag{2.6}$$

A key observation is that the eigenvalues are of similar sign for supercritical flow.

2.2 Continuum Upstream-Bias Construction

For arbitrary domains $\hat{\Omega}$ and arbitrary test functions $\hat{w}$ with compact support in $\hat{\Omega}$, the weak form statement is

$$\int_{\hat{\Omega}} \hat{w} \left(\frac{\partial \mathbf{q}}{\partial t} + \frac{\partial f(\mathbf{q})}{\partial x} \right) d\Omega = 0 \tag{2.7}$$

which, due to the theory of weak forms, is equivalent to the original hyperbolic conservation law (2.1). The characteristics-biased weak form, introduced in [37], is defined as

$$\int_{\hat{\Omega}} \hat{w} \left(\frac{\partial \mathbf{q}}{\partial t} + \frac{\partial f^c(\mathbf{q})}{\partial x} \right) d\Omega = 0 \tag{2.8}$$

where $f^c(\mathbf{q})$ is the characteristics-bias flux within (2.7). This yet-to-be-determined flux automatically introduces the upstream-biased dissipative flux vector for the original open channel kinetic flux divergence $\partial f(\mathbf{q})/\partial x$.

2.3 Kinetic Flux Jacobian Decomposition

The first step in establishing $f^c(\mathbf{q})$ is to decompose the kinetic flux jacobian into a linear combination of L contributions

$$\frac{\partial f(\mathbf{q})}{\partial \mathbf{q}} = \sum_{l=1}^{L} \alpha_l \mathbf{A}_l \;\Rightarrow\; \frac{\partial f(\mathbf{q})}{\partial x} = \sum_{l=1}^{L} \alpha_l \mathbf{A}_l \frac{\partial \mathbf{q}}{\partial x} \tag{2.9}$$

where $\mathbf{A}_l$ denotes a matrix component of the flux jacobian decomposition and α_l denotes a linear combination function which could depend on $\mathbf{q}$. Three specifications, which will become evident in ensuing analyses, shall be imposed on each of the $\mathbf{A}_l$

1. Each $\mathbf{A}_l$ must have physical significance
2. It is not required that all $\mathbf{A}_l$ are involved in the characteristics-bias
3. All eigenvalues of a matrix component $\mathbf{A}_l$ that enter the characteristics-biased flux divergence must have uniform sign

The weak form of the kinetic flux divergence $\partial f(\mathbf{q})/\partial x$ incorporating the flux jacobian decomposition of (2.9) yields

$$\int_{\hat{\Omega}} \hat{w} \frac{\partial f(\mathbf{q})}{\partial x} d\Omega = \int_{\hat{\Omega}} \sum_{l=1}^{L} \hat{w} \alpha_l \mathbf{A}_l \frac{\partial \mathbf{q}}{\partial x} d\Omega \tag{2.10}$$

The characteristics-bias flux $f^c(\mathbf{q})$ is hence defined via (2.8) as

$$\int_{\hat{\Omega}} \hat{w} \frac{\partial f^c(\mathbf{q})}{\partial x} d\Omega = \int_{\hat{\Omega}} \sum_{l=1}^{L} \left(\hat{w} + \psi \delta_l \hat{w}\right) \alpha_l \mathbf{A}_l \frac{\partial \mathbf{q}}{\partial x} d\Omega \tag{2.11}$$

where an appropriate characteristics-bias, yielding the required level of dissipation, is applied to each flux jacobian decomposition matrix component $\mathbf{A}_l$ through the perturbation $\psi \delta_l \hat{w}$.

The positive parameter ψ represents the non-linear dissipation controller which adjusts the amount of dissipation based on local solution gradient. The variation $\delta_l \hat{w}$ induces the appropriate upstream-bias to the test function $\hat{w}$ for each component of (2.11). This variation will be made to vanish or become algebraically positive or negative depending on physical consistency, magnitude, and sign of the eigenvalues of $\mathbf{A}_l$.

The variation $\delta_l \hat{w}$ is defined as

$$\delta_l \hat{w} = \frac{\partial \hat{w}}{\partial x} \delta_l x = \frac{\partial \hat{w}}{\partial x} a_l \epsilon \tag{2.12}$$

where ϵ is chosen as a local length scale and the direction cosine a_l equals 0 or ± 1 depending on the sign of a selected component of $\mathbf{q}$.

Substituting, the upstream-biased construction for the integral (2.11) becomes

$$\int_{\hat{\Omega}} \hat{w} \frac{\partial f^c(\mathbf{q})}{\partial x} d\Omega = \int_{\hat{\Omega}} \hat{w} \frac{\partial f(\mathbf{q})}{\partial x} d\Omega + \int_{\hat{\Omega}} \epsilon \psi \frac{\partial \hat{w}}{\partial x} \sum_{l=1}^{L} a_l \alpha_l \mathbf{A}_l \frac{\partial \mathbf{q}}{\partial x} d\Omega \tag{2.13}$$

Integrating the last term by parts and capitalizing upon the compact support lent by $\hat{w}$ to eliminate the boundary evaluation yields

$$\int_{\hat{\Omega}} \hat{w} \left[\frac{\partial f^c(\mathbf{q})}{\partial x} - \frac{\partial f(\mathbf{q})}{\partial x} + \frac{\partial}{\partial x} \left(\epsilon \psi \sum_{l=1}^{L} a_l \alpha_l \mathbf{A}_l \frac{\partial \mathbf{q}}{\partial x} \right) \right] d\Omega = 0 \tag{2.14}$$

Due to the arbitrariness of both the test function $\hat{w}$ and domain $\hat{\Omega}$, the integrand must be identically zero. The characteristics-bias flux is thus revealed as

$$\frac{\partial f^c(\mathbf{q})}{\partial x} = \frac{\partial f(\mathbf{q})}{\partial x} - \frac{\partial}{\partial x} \left(\epsilon \psi \sum_{l=1}^{L} a_l \alpha_l \mathbf{A}_l \frac{\partial \mathbf{q}}{\partial x} \right) \tag{2.15}$$

This expression contains both the parent kinetic flux divergence and the upstream-biased, second-order differential term containing the upstream matrix $\mathcal{A}$

$$\mathcal{A} \equiv \sum_{l=1}^{L} a_l \alpha_l \mathbf{A}_l \tag{2.16}$$

For mathematical stability of the matrix differential expression, as derived in [37], the eigenvalues of the upstream matrix $\mathcal{A}$ must be positive.

2.3.1 Flux Difference Splitting

The characteristics-biased flux divergence, coupled with the flux jacobian decomposition, is a broad theoretical umbrella which recovers the core constructions of current dissipative methodologies. The developments in sections (2.3.1) and (2.3.2) are reproduced from [37] to introduce the derivations in following sections of this dissertation.

Consider flux difference splitting as typified by Roe's algorithm, c.f. Chapter (1.2). In this formulation, the kinetic flux jacobian is split via

$$\frac{\partial f(\mathbf{q})}{\partial \mathbf{q}} = \mathbf{X}\mathbf{\Lambda}^{+}\mathbf{X}^{-1} + \mathbf{X}\mathbf{\Lambda}^{-}\mathbf{X}^{-1} \tag{2.17}$$

where $\mathbf{X}$ and $\mathbf{\Lambda} = \mathbf{\Lambda}^{+} + \mathbf{\Lambda}^{-}$ are the right eigenvector matrix and the (diagonal) eigenvalue jacobian matrix where $\mathbf{\Lambda}^{+}$ and $\mathbf{\Lambda}^{-}$ contain the non-negative and non-positive eigenvalues respectively.

The flux jacobian decomposition (2.9) clearly encompasses (2.17) for $L = 2$ and

$$\sum_{l=1}^{L} \alpha_l \mathbf{A}_l = \mathbf{X}\mathbf{\Lambda}^{+}\mathbf{X}^{-1} + \mathbf{X}\mathbf{\Lambda}^{-}\mathbf{X}^{-1} \quad \text{where} \quad \begin{cases} \alpha_1 & = & 1 \\ \alpha_2 & = & 1 \\ \mathbf{A}_1 & = & \mathbf{X}\mathbf{\Lambda}^{+}\mathbf{X}^{-1} \\ \mathbf{A}_2 & = & \mathbf{X}\mathbf{\Lambda}^{-}\mathbf{X}^{-1} \end{cases} \tag{2.18}$$

The associated characteristics-biased flux divergence form for Roe's construction is generated from (2.15) by setting $\psi = 1$, $a_1 = 1$, $a_2 = -1$, and the coefficients of (2.18) defined as

$$\begin{aligned}
\frac{\partial f^c(\mathbf{q})}{\partial x} &= \frac{\partial f(\mathbf{q})}{\partial x} - \frac{\partial}{\partial x}\left(\epsilon\psi \sum_{l=1}^{L} a_1 \alpha_l \mathbf{A}_l \frac{\partial \mathbf{q}}{\partial x}\right) && (2.19)\\
&= \frac{\partial f(\mathbf{q})}{\partial x} - \frac{\partial}{\partial x}\left(\epsilon\left(\mathbf{X}\mathbf{\Lambda}^+\mathbf{X}^{-1} - \mathbf{X}\mathbf{\Lambda}^-\mathbf{X}^{-1}\right)\frac{\partial \mathbf{q}}{\partial x}\right) && (2.20)\\
&= \frac{\partial f(\mathbf{q})}{\partial x} - \frac{\partial}{\partial x}\left(\epsilon\mathbf{X}\left(\mathbf{\Lambda}^+ - \mathbf{\Lambda}^-\right)\mathbf{X}^{-1}\frac{\partial \mathbf{q}}{\partial x}\right) && (2.21)
\end{aligned}$$

which exposes the flux difference splitting flux divergence construction in the continuum.

The upstream matrix $\mathcal{A}$ is thus

$$\mathcal{A} = \mathbf{X}\left(\mathbf{\Lambda}^+ - \mathbf{\Lambda}^-\right)\mathbf{X}^{-1} \tag{2.22}$$

which has the excellent property of non-negative eigenvalues. It therefore automatically satisifies the upstream-bias stability condition for any flow regime for which no eigenvalue vanishes. An unfortunate consequence is the operation count required with implementation on a discretization due to the matrix multiplications. Additionally, the components of the flux jacobian decomposition of (2.17) both contain convection and celerity effects as opposed to each component have unique physical significance. However, numerous computational experiments demonstrate the accuracy of the Roe construction.

2.3.2 Flux Vector Splitting

Next, consider van Leer's formulation as a representative flux vector splitting as identified in Chapter (1.2). In this formulation, the kinetic flux vector is split as

$$f(\mathbf{q}) = f^{VL+}(\mathbf{q}) + f^{VL-}(\mathbf{q}) \tag{2.23}$$

such that the jacobian matrices of $f^{VL^+}(\mathbf{q})$ and $f^{VL^-}(\mathbf{q})$ have non-negative and non-positive eigenvalues respectively. The flux jacobian decomposition expression (2.9) encompasses (2.23) for $L = 2$ via the definitions

$$\sum_{l=1}^{L} \alpha_l \mathbf{A}_l = \frac{\partial f^{VL^+}(\mathbf{q})}{\partial \mathbf{q}} + \frac{\partial f^{VL^-}(\mathbf{q})}{\partial \mathbf{q}} \quad \text{where} \quad \begin{cases} \alpha_1 & = & 1 \\ \alpha_2 & = & 1 \\ \mathbf{A}_1 & = & \frac{\partial}{\partial q}(f^{VL^+}(\mathbf{q})) \\ \mathbf{A}_2 & = & \frac{\partial}{\partial q}(f^{VL^-}(\mathbf{q})) \end{cases} \tag{2.24}$$

The associated characteristics-bias divergence for van Leer's algorithm is generated from (2.15) via $\psi = 1$, $a_1 = 1$, $a_2 = -1$, and the coefficients of (2.24) constructed as

$$\frac{\partial f^c(\mathbf{q})}{\partial x} = \frac{\partial f(\mathbf{q})}{\partial x} - \frac{\partial}{\partial x}\left(\epsilon\psi \sum_{l=1}^{L} a_1 \alpha_l \mathbf{A}_l \frac{\partial \mathbf{q}}{\partial x}\right) \tag{2.25}$$

$$= \frac{\partial f(\mathbf{q})}{\partial x} - \frac{\partial}{\partial x}\left(\epsilon\left(\frac{\partial f^{VL^+}(\mathbf{q})}{\partial \mathbf{q}} + \frac{\partial f^{VL^-}(\mathbf{q})}{\partial \mathbf{q}}\right)\frac{\partial \mathbf{q}}{\partial x}\right) \tag{2.26}$$

$$= \frac{\partial f(\mathbf{q})}{\partial x} - \frac{\partial}{\partial x}\left(\epsilon\left(\frac{\partial f^{VL^+}(\mathbf{q})}{\partial x} + \frac{\partial f^{VL^-}(\mathbf{q})}{\partial x}\right)\right) \tag{2.27}$$

which contains the flux vector splitting kinetic flux divergence construction in the continuum.

The upstream matrix $\mathcal{A}$ is thus

$$\mathcal{A} = \frac{\partial f^{VL^+}(\mathbf{q})}{\partial x} + \frac{\partial f^{VL^-}(\mathbf{q})}{\partial x} \tag{2.28}$$

which is a computationally efficient decompostion upon discretization but does not have the flux difference splitting property of uniformly non-negative eigenvalues. For supercritical flows, however the eigenvalues are both non-negative per (2.6).

2.4 Supercritical Convection Decomposition

For supercritical flow ($Fr > 1$) the (non-dimensional) kinetic flux jacobian eigenvalues have uniform, non-negative sign. Decomposing the kinetic flux vector into two physically significant components

$$\frac{\partial f(\mathbf{q})}{\partial x} = \frac{\partial f^{conv}(\mathbf{q})}{\partial x} + \frac{\partial f^{cel}(\mathbf{q})}{\partial x} \tag{2.29}$$

where $f^{conv}(\mathbf{q})$ and $f^{cel}(\mathbf{q})$ denote the convection flux and the depth-averaged hydrostatic pressure gradient flux, henceforth termed the celerity flux, components respectively.

Recalling the kinetic flux vector to be

$$f(q) = \left\{ \begin{array}{c} m \\ \frac{m}{h}m + g\frac{h^2}{2} \end{array} \right\} \tag{2.30}$$

the convection and celerity flux components are defined as

$$f^{conv} = \left\{ \begin{array}{c} m \\ \frac{m}{h}m \end{array} \right\} = \frac{m}{h} \left\{ \begin{array}{c} h \\ m \end{array} \right\} \quad , \quad f^{cel} = \left\{ \begin{array}{c} 0 \\ g\frac{h^2}{2} \end{array} \right\} \tag{2.31}$$

Solving for the convection and celerity jacobians and associated and comparing with the open channel jacobian and eigenvalues

$$\begin{array}{ccccc} \partial f(\mathbf{q})/\partial \mathbf{q} & = & \mathbf{A}^{conv} & + & \mathbf{A}^{cel} \\ \begin{bmatrix} 0 & 1 \\ -u^2 + gh & 2u \end{bmatrix} & = & \begin{bmatrix} 0 & 1 \\ -u^2 & 2u \end{bmatrix} & + & \begin{bmatrix} 0 & 0 \\ gh & 0 \end{bmatrix} \\ \lambda_{1,2}^{d_{OC}} = u \pm \sqrt{gh} & & \lambda_{1,2}^{d_{conv}} = u, u & & \lambda_{1,2}^{d_{cel}} = 0 \\ \lambda_{1,2}^{OC} = Fr \pm 1 & & \lambda_{1,2}^{conv} = Fr, Fr & & \lambda_{1,2}^{cel} = 0 \end{array} \tag{2.32}$$

where $\mathbf{A}^{conv}$ denotes the convection component and $\mathbf{A}^{cel}$ denotes the celerity component. Segregating the celerity component from the convection component yields two sets of eigenvalues: the

first set representing pure convective propagation, the second representing no propagation. While inaccurate for all values of Froude, this decomposition does feature non-negative eigenvalues. Heed that only in the limit of $Fr = \infty$ is this decomposition physically consistent with the original open channel eigenvalues.

Inserting a parameter β into the flux jacobian, following [37], yields

$$\begin{array}{ccccc} \partial f(\mathbf{q})/\partial \mathbf{q} & = & \mathbf{A}^{conv} & + & \beta\,\mathbf{A}^{cel} \\ \begin{bmatrix} 0 & 1 \\ -u^2+\beta gh & 2u \end{bmatrix} & = & \begin{bmatrix} 0 & 1 \\ -u^2 & 2u \end{bmatrix} & + & \beta \begin{bmatrix} 0 & 0 \\ gh & 0 \end{bmatrix} \\ \lambda_{1,2}^{d_\beta} = u \pm \sqrt{\beta}\sqrt{gh} & & \lambda_{1,2}^{d_{conv}} = u, u & & \lambda_{1,2}^{d_{cel}} = 0 \\ \lambda_{1,2}^{\beta} = Fr \pm \sqrt{\beta} & & \lambda_{1,2}^{conv} = Fr, Fr & & \lambda_{1,2}^{cel} = 0 \end{array} \tag{2.33}$$

For various values of β, the non-dimensional flux jacobian eigenvalues are

$$\beta = 1 \qquad \lambda_{1,2}^{\beta} = Fr \pm 1 \tag{2.34}$$

$$\beta = 0 \qquad \lambda_{1,2}^{\beta} = Fr, Fr \tag{2.35}$$

$$\beta = \beta \qquad \lambda_{1,2}^{\beta} = Fr \pm \sqrt{\beta} \tag{2.36}$$

Thus, the β parameter shifts the eigenvalues from representing a celerity/convection matrix to a pure convection matrix. For mathematical stability, constraints must be imposed on the β parameter to insure non-negative real eigenvalues. Since $Fr \geq 0$, the β eigenvalues (2.36) indicate

$$Fr + \sqrt{\beta} \geq 0 \qquad \text{automatically satisfied} \tag{2.37}$$

$$Fr - \sqrt{\beta} \geq 0 \qquad \text{not automatically satisfied} \tag{2.38}$$

The constraint of

$$\beta \leq Fr^2 \tag{2.39}$$

must therefore be imposed. Thus, in the celerity limit for $Fr = 0$, β must equal zero. Additionally, for all supercritical flows, β must equal one to remain consistent with the open channel eigenvalues. Finally, β will be selected such that all eigenvalues will be non-negative per the stability constraint.

Employing the β parameter on the flux divergence level yields a kinetic flux divergence decomposition with isolated jacobian eigenvalues of the parameterized convection/celerity and zero

$$\frac{\partial f(\mathbf{q})}{\partial x} = \left[\frac{\partial f^{conv}(\mathbf{q})}{\partial x} + \beta \frac{f^{cel}(\mathbf{q})}{\partial x}\right] + \left[(1-\beta)\,\frac{\partial f^{cel}(\mathbf{q})}{\partial x}\right] \tag{2.40}$$

hence

$$\begin{array}{ccccc} \partial f(\mathbf{q})/\partial \mathbf{q} & = & [\ \mathbf{A}^{conv} + \beta \mathbf{A}^{cel}\ ] & + & (1-\beta)\mathbf{A}^{cel} \\ & = & \mathbf{A}^{scc} & + & \mathbf{A}^{sc} \\ \lambda_{1,2}^{d_{OC}} = u \pm \sqrt{gh} & & \lambda_{1,2}^{d_{scc}} = u \pm \sqrt{\beta}\sqrt{gh} & & \lambda_{1,2}^{d_{sc}} = 0,0 \\ \lambda_{1,2}^{OC} = Fr \pm 1 & & \lambda_{1,2}^{scc} = Fr \pm \sqrt{\beta} & & \lambda_{1,2}^{sc} = 0,0 \end{array} \tag{2.41}$$

where $\mathbf{A}^{scc}$ denotes the *supercritical celerity-convection* jacobian and $\mathbf{A}^{sc}$ denotes the supercritical celerity jacobian, redefined to emphasize their fundamental difference, non-negative eigenvalues for all Froude and physically consistent eigenvalues for supercritical Froude, from the convection and celerity flux divergence jacobians $\mathbf{A}^{conv}$ and $\mathbf{A}^{cel}$ respectively.

The flux jacobian decomposition expression (2.9) is contained in (2.41) for $L = 3$ via

$$\sum_{l=1}^{L} \alpha_l \mathbf{A}_l = [\ \mathbf{A}^{conv} + \beta \mathbf{A}^{cel}\ ] + (1-\beta)\mathbf{A}^{cel}$$

$$\text{where} \begin{cases} \alpha_1 = 1 & \mathbf{A}_1 = \mathbf{A}^{conv} \\ \alpha_2 = \beta & \mathbf{A}_2 = \mathbf{A}^{cel} \\ \alpha_3 = (1-\beta) & \mathbf{A}_3 = \mathbf{A}^{cel} \end{cases} \tag{2.42}$$

2.5 Celerity-Convection Decomposition

Having obtained a physically significant decomposition which yields non-negative eigenvalues but is valid only for supercritical flow, the next step is to develop a flux divergence decomposition which is valid for subcritical flows where the eigenvalues have differing signs. Consider a non-intuitive decomposition of the open channel kinetic flux divergence as

$$\begin{aligned} \frac{\partial f(\mathbf{q})}{\partial x} &= \frac{\partial f^{conv}(\mathbf{q})}{\partial x} + \frac{\partial f^{cel}(\mathbf{q})}{\partial x} \\ &= \left(\mathbf{A}^{conv} + \mathbf{A}^{cel}\right) \frac{\partial \mathbf{q}}{\partial x} \qquad (2.43) \\ &= \left(\mathbf{A}^{conv} + \mathbf{A}^{jcel} + \mathbf{A}^{jaux}\right) \frac{\partial \mathbf{q}}{\partial x} \qquad (2.44) \end{aligned}$$

where the jacobian of the celerity flux divergence is decomposed into two components $\mathbf{A}^{jcel}$ and $\mathbf{A}^{jaux}$ while $\mathbf{A}^{conv}$ remains as defined in the previous section. This new celerity jacobian decomposition will introduce celerity eigenvalues for the $\mathbf{A}^{jcel}$ component while A^{jaux} introduces no eigenvalues an acts only to preserve matrix similtude between the decomposition and the jacobian of the original open channel kinetic flux divergence.

$$\frac{\partial f(\mathbf{q})}{\partial \mathbf{q}} = \begin{bmatrix} 0 & 1 \\ -u^2 + gh & 2u \end{bmatrix} = \mathbf{A}^{conv} + \mathbf{A}^{jcel} + \mathbf{A}^{jaux} \tag{2.45}$$

The convection component, $\mathbf{A}^{conv}$, is revealed as the convection limit of the jacobian by taking $g \to 0$ while the celerity component, $\mathbf{A}^{jcel}$, is evident as the celerity limit of the jacobian by taking $u \to 0$. Therfore

$$\mathbf{A}^{conv} = \begin{bmatrix} 0 & 1 \\ -u^2 & 2u \end{bmatrix} \tag{2.46}$$

$$\mathbf{A}^{jcel} \equiv \begin{bmatrix} 0 & 1 \\ gh & 0 \end{bmatrix} \tag{2.47}$$

$$\mathbf{A}^{jaux} \equiv \begin{bmatrix} 0 & -1 \\ 0 & 0 \end{bmatrix} \tag{2.48}$$

Substituting (2.47), (2.46) and (2.48) into (2.45) verifies that the flux jacobian decomposition replicates the original jacobian while satisfying the isolation of the physically significant eigenvalues. This new decomposition is henceforth denoted the *celerity-convection decomposition*.

$$\begin{array}{ccccccc} \partial f(\mathbf{q})/\partial \mathbf{q} & = & \mathbf{A}^{conv} & + & \mathbf{A}^{jcel} & + & \mathbf{A}^{jaux} \\ \begin{bmatrix} 0 & 1 \\ -u^2+gh & 2u \end{bmatrix} & = & \begin{bmatrix} 0 & 1 \\ -u^2 & 2u \end{bmatrix} & + & \begin{bmatrix} 0 & 1 \\ gh & 0 \end{bmatrix} & + & \begin{bmatrix} 0 & -1 \\ 0 & 0 \end{bmatrix} \\ \lambda_{1,2}^{d_{OC}} = u \pm \sqrt{gh} & & \lambda_{1,2}^{d_{conv}} = u, u & & \lambda_{1,2}^{d_{jcel}} = \pm\sqrt{gh} & & \lambda_{1,2}^{d_{jaux}} = 0, 0 \\ \lambda_{1,2}^{OC} = Fr \pm 1 & & \lambda_{1,2}^{conv} = Fr, Fr & & \lambda_{1,2}^{jcel} = \pm 1 & & \lambda_{1,2}^{jaux} = 0, 0 \end{array} \tag{2.49}$$

In the celerity limit for $Fr = 0$, the eigenvalues of $\mathbf{A}^{jcel}$ correlate exactly with those of the open channel flux jacobian. For subcritical flows, these eigenvalues maintain a differing sign but the absence of Froude number renders them inconsistent with the open channel eigenvalues. Thus, this physically signigicant decomposition is valid strictly in the celerity limit.

Further decomposing $\mathbf{A}^{jcel}$ reveals two matrices with additional physical content. Because $\mathbf{A}^{jcel}$ has a complete set of eigenvectors, it can be diagonalized by the similarity transform

$$\mathbf{A}^{jcel} = \mathbf{X}\mathbf{\Lambda}^{jcel}\mathbf{X}^{-1} \tag{2.50}$$

where $\mathbf{X}$ and $\mathbf{\Lambda}^{jcel} = \mathbf{\Lambda}^{jcel^+} + \mathbf{\Lambda}^{jcel^-}$ are the right eigenvector matrix and the (diagonal) eigenvalue matrix of the jacobian, hence $\mathbf{\Lambda}^{jcel^+}$ and $\mathbf{\Lambda}^{jcel^-}$ contain the non-negative and non-positive

eigenvalues respectively.

For $\mathbf{A}^{jcel}$ as defined by (2.47), the diagonaliziation matrices have been solved in closed form as

$$\mathbf{X} = \begin{bmatrix} 1 & 1 \\ \sqrt{gh} & -\sqrt{gh} \end{bmatrix} \quad , \quad \mathbf{\Lambda}^{jcel} = \begin{bmatrix} \sqrt{gh} & 0 \\ 0 & -\sqrt{gh} \end{bmatrix} \quad , \quad \mathbf{X}^{-1} = \frac{1}{2} \begin{bmatrix} 1 & 1/\sqrt{gh} \\ 1 & -1/\sqrt{gh} \end{bmatrix} \tag{2.51}$$

Decomposing $\mathbf{\Lambda}^{jcel}$ into $\mathbf{\Lambda}^{jcel^+} + \mathbf{\Lambda}^{jcel^-}$ yields

$$\mathbf{\Lambda}^{jcel} = \mathbf{\Lambda}^{jcel^+} + \mathbf{\Lambda}^{jcel^-} = \begin{bmatrix} \sqrt{gh} & 0 \\ 0 & 0 \end{bmatrix} + \begin{bmatrix} 0 & 0 \\ 0 & -\sqrt{gh} \end{bmatrix} \tag{2.52}$$

Substituting (2.52) into (2.50) allows further physical insight into the celerity matrix. From

$$\mathbf{A}^{cel} = \mathbf{X}\mathbf{\Lambda}^{jcel^+}\mathbf{X}^{-1} + \mathbf{X}\mathbf{\Lambda}^{jcel^-}\mathbf{X}^{-1} \tag{2.53}$$

$\mathbf{X}\mathbf{\Lambda}^{jcel^+}\mathbf{X}^{-1}$ accounts for the propogation of celerity in the $+x$ direction and $\mathbf{X}\mathbf{\Lambda}^{jcel^-}\mathbf{X}^{-1}$ accounts for propogation of celerity in the $-x$ direction.

The kinetic flux divergence has thus been decomposed into physically significant components as

$$\frac{\partial f(\mathbf{q})}{\partial x} = \left(\mathbf{X}\mathbf{\Lambda}^{jcel^+}\mathbf{X}^{-1} + \mathbf{X}\mathbf{\Lambda}^{jcel^-}\mathbf{X}^{-1}\right)\frac{\partial \mathbf{q}}{\partial x} + \frac{\partial f^{conv}(\mathbf{q})}{\partial x} + \mathbf{A}^{jaux}\frac{\partial \mathbf{q}}{\partial x} \tag{2.54}$$

with its associated flux divergence jacobian

$$\frac{\partial f(\mathbf{q})}{\partial \mathbf{q}} = \mathbf{X}\mathbf{\Lambda}^{jcel^+}\mathbf{X}^{-1} + \mathbf{X}\mathbf{\Lambda}^{jcel^-}\mathbf{X}^{-1} + \mathbf{A}^{conv} + \mathbf{A}^{jaux} \tag{2.55}$$

The flux jacobian decomposition expression (2.9) encompasses (2.55) for $L = 4$ as

$$\sum_{l=1}^{L} \alpha_l \mathbf{A}_l = \mathbf{X}\mathbf{\Lambda}^{jcel^+}\mathbf{X}^{-1} + \mathbf{X}\mathbf{\Lambda}^{jcel^-}\mathbf{X}^{-1} + \mathbf{A}^{conv} + \mathbf{A}^{jaux}$$

$$\text{where} \quad \begin{cases} \alpha_1 = 1 & \mathbf{A}_1 = \mathbf{X}\mathbf{\Lambda}^{jcel^+}\mathbf{X}^{-1} \\ \alpha_2 = 1 & \mathbf{A}_2 = \mathbf{X}\mathbf{\Lambda}^{jcel^-}\mathbf{X}^{-1} \\ \alpha_3 = 1 & \mathbf{A}_3 = \mathbf{A}^{conv} \\ \alpha_4 = 1 & \mathbf{A}_4 = \mathbf{A}^{jaux} \end{cases} \tag{2.56}$$

While this flux jacobian decomposition is diagonalized like Roe's scheme, (2.18), the matrix components have physical character. As with Roe's scheme, the high operation count associated with the diagonalization upon discretization is a detriment.

2.6 Composite Jacobian Construction

Sections (2.5) and (2.4) introduced the supercritical convection decomposition and the celerity-convection decomposition as kinetic flux jacobian decompositions for the inviscid, one-dimensional open channel flow equations. These decompositions reflect respectively

1. A parameterized form which features non-negative eigenvalues but is valid only for supercritical flows

2. A diagonalized form that features eigenvalues of differing sign but is valid only in the celerity limit

which are given as

$$\frac{\partial f(\mathbf{q})}{\partial x} = \left[\frac{\partial f^{conv}(\mathbf{q})}{\partial x} + \beta\frac{f^{cel}(\mathbf{q})}{\partial x}\right] + \left[(1-\beta)\frac{\partial f^{cel}(\mathbf{q})}{\partial x}\right] \tag{2.57}$$

$$\frac{\partial f(\mathbf{q})}{\partial x} = \left(\mathbf{X}\mathbf{\Lambda}^{jcel^+}\mathbf{X}^{-1} + \mathbf{X}\mathbf{\Lambda}^{jcel^-}\mathbf{X}^{-1}\right)\frac{\partial \mathbf{q}}{\partial x} + \frac{\partial f^{conv}(\mathbf{q})}{\partial x} + \mathbf{A}^{jaux}\frac{\partial \mathbf{q}}{\partial x} \tag{2.58}$$

A linear combination of the two shall be taken to yield an algorithm which is valid for all flow regimes. Taking a linear combination of kinetic flux vector decompositions where $0 \leq \alpha \leq 1$:

$$\frac{\partial f(\mathbf{q})}{\partial x} = \alpha \frac{\partial f(\mathbf{q})}{\partial x} + (1-\alpha)\frac{\partial f(\mathbf{q})}{\partial x} \tag{2.59}$$

Substituting the supercritical convection decomposition (2.57) and the celerity-convection decomposition (2.58) into the kinetic flux divergence linear combination (2.59)

$$\begin{aligned} \frac{\partial f(\mathbf{q})}{\partial x} &= \alpha \left\{ \left(\mathbf{X}\mathbf{\Lambda}^{jcel^+}\mathbf{X}^{-1} + \mathbf{X}\mathbf{\Lambda}^{jcel^-}\mathbf{X}^{-1} \right) \frac{\partial \mathbf{q}}{\partial x} + \frac{\partial f^{conv}(\mathbf{q})}{\partial x} + \mathbf{A}^{jaux}\frac{\partial \mathbf{q}}{\partial x} \right\} \\ &\quad + (1-\alpha) \left\{ \left[\frac{\partial f^{conv}(\mathbf{q})}{\partial x} + \beta \frac{f^{cel}(\mathbf{q})}{\partial x} \right] + \left[(1-\beta)\, \frac{\partial f^{cel}(\mathbf{q})}{\partial x} \right] \right\} \end{aligned} \tag{2.60}$$

with $0 \leq \alpha, \beta \leq 1$. Expanding terms

$$\begin{aligned} \frac{\partial f(\mathbf{q})}{\partial x} &= \alpha \left(\mathbf{X}\mathbf{\Lambda}^{jcel^+}\mathbf{X}^{-1} + \mathbf{X}\mathbf{\Lambda}^{jcel^-}\mathbf{X}^{-1} \right) \frac{\partial \mathbf{q}}{\partial x} \\ &\quad + \frac{\partial f^{conv}(\mathbf{q})}{\partial x} + \beta(1-\alpha)\frac{\partial f^{cel}(\mathbf{q})}{\partial x} \\ &\quad + (1-\alpha)(1-\beta)\frac{\partial f^{cel}(\mathbf{q})}{\partial x} + \alpha \mathbf{A}^{jaux}\frac{\partial \mathbf{q}}{\partial x} \end{aligned} \tag{2.61}$$

Extracting the composite flux divergence decomposition jacobians

$$\begin{aligned} \frac{\partial f(\mathbf{q})}{\partial \mathbf{q}} &= \alpha \mathbf{X}\mathbf{\Lambda}^{jcel^+}\mathbf{X}^{-1} + \alpha \mathbf{X}\mathbf{\Lambda}^{jcel^-}\mathbf{X}^{-1} \\ &\quad + \left[\mathbf{A}^{conv} + \beta(1-\alpha)\mathbf{A}^{cel} \right] \\ &\quad + (1-\alpha)(1-\beta)\mathbf{A}^{cel} + \alpha \mathbf{A}^{aux} \end{aligned} \tag{2.62}$$

Renaming the linear combination parameter α_l as γ_l to prevent ambiguity, the flux jacobian decomposition expression (2.9) encompasses (2.62) for $L = 6$ as

$$
\begin{aligned}
\sum_{l=1}^{L} \gamma_l \mathbf{A}_l &= \alpha \mathbf{X} \mathbf{\Lambda}^{jcel^+} \mathbf{X}^{-1} + \alpha \mathbf{X} \mathbf{\Lambda}^{jcel^-} \mathbf{X}^{-1} \\
&\quad + \left[\mathbf{A}^{conv} + \beta(1-\alpha) \mathbf{A}^{cel} \right] \\
&\quad + (1-\alpha)(1-\beta) \mathbf{A}^{cel} + \alpha \mathbf{A}^{aux}
\end{aligned} \tag{2.63}
$$

$$
\text{where} \begin{cases}
\gamma_1 = \alpha & \mathbf{A}_1 = \mathbf{X} \mathbf{\Lambda}^{jcel^+} \mathbf{X}^{-1} \\
\gamma_2 = \alpha & \mathbf{A}_2 = \mathbf{X} \mathbf{\Lambda}^{jcel^-} \mathbf{X}^{-1} \\
\gamma_3 = 1 & \mathbf{A}_3 = \mathbf{A}^{conv} \\
\gamma_4 = \beta(1-\alpha) & \mathbf{A}_4 = \mathbf{A}^{cel} \\
\gamma_5 = (1-\alpha)(1-\beta) & \mathbf{A}_5 = \mathbf{A}^{cel} \\
\gamma_6 = \alpha & \mathbf{A}_6 = \mathbf{A}^{aux}
\end{cases} \tag{2.64}
$$

2.7 Evaluation of the Characteristics-Biased Flux

Having established the composite decomposition of the kinetic flux divergence, the next step is to develop the weak form of the kinetic flux divergence from the weak form statement statement (2.7).

$$
\begin{aligned}
\int_{\hat{\Omega}} \hat{w} \frac{\partial f(\mathbf{q})}{\partial x} d\hat{\Omega} &= \int_{\hat{\Omega}} \hat{w} \left[\alpha \mathbf{X} \mathbf{\Lambda}^{jcel^+} \mathbf{X}^{-1} \right] \frac{\partial \mathbf{q}}{\partial x} d\hat{\Omega} \\
&\quad + \int_{\hat{\Omega}} \hat{w} \left[\alpha \mathbf{X} \mathbf{\Lambda}^{jcel^-} \mathbf{X}^{-1} \right] \frac{\partial \mathbf{q}}{\partial x} d\hat{\Omega} \\
&\quad + \int_{\hat{\Omega}} \hat{w} \left[\frac{\partial f^{conv}(\mathbf{q})}{\partial x} + \beta(1-\alpha) \frac{\partial f^{cel}(\mathbf{q})}{\partial x} \right] d\hat{\Omega} \\
&\quad + \int_{\hat{\Omega}} \hat{w} \left[(1-\alpha)(1-\beta) \frac{\partial f^{cel}(\mathbf{q})}{\partial x} + \alpha \mathbf{A}^{aux} \frac{\partial \mathbf{q}}{\partial x} \right] d\hat{\Omega}
\end{aligned} \tag{2.65}
$$

Forming the characteristics-biased weak form via (2.8) with perturbation parameters (2.11)

$$
\begin{aligned}
\int_{\hat{\Omega}} \hat{w} \frac{\partial f^c(\mathbf{q})}{\partial x} d\hat{\Omega} \quad = \quad & \int_{\hat{\Omega}} (\hat{w} + \psi \delta \hat{w}) \left[\alpha \mathbf{X} \mathbf{\Lambda}^{jcel^+} \mathbf{X}^{-1} \right] \frac{\partial \mathbf{q}}{\partial x} d\hat{\Omega} \\
& + \int_{\hat{\Omega}} (\hat{w} - \psi \delta \hat{w}) \left[\alpha \mathbf{X} \mathbf{\Lambda}^{jcel^-} \mathbf{X}^{-1} \right] \frac{\partial \mathbf{q}}{\partial x} d\hat{\Omega} \\
& + \int_{\hat{\Omega}} (\hat{w} + s \psi \delta \hat{w}) \left[\frac{f^{conv}(\mathbf{q})}{\partial x} + \beta (1 - \alpha) \frac{f^{cel}(\mathbf{q})}{\partial x} \right] d\hat{\Omega} \\
& + \int_{\hat{\Omega}} \hat{w} \left[(1 - \alpha)(1 - \beta) \frac{f^{cel}(\mathbf{q})}{\partial x} + \alpha \mathbf{A}^{aux} \frac{\partial \mathbf{q}}{\partial x} \right] d\hat{\Omega} \qquad (2.66)
\end{aligned}
$$

A discussion of the form of the perturbation parameters in (2.66) is warranted. The first two terms represent the propagation of celerity information in the positive and negative x directions respectively. The variation $\delta \hat{w}$ thus points in the $+x$ direction for the first term and in the $-x$ direction for the second term. The third term models convection for supercritical flows. The eigenvalues of this term are similar signed and are positive signed along the x axis in the direction of the velocity, hence $\delta \hat{w}$ will point in the velocity direction. Its sign is therefore the sign of the velocity, s. The final terms have vanishing eigenvalues and hence no propagation direction. Their directional variation is therefore zero.

Subtracting (2.65) from (2.66)

$$
\begin{aligned}
\int_{\hat{\Omega}} \hat{w} \left[\frac{\partial f^c(\mathbf{q})}{\partial x} - \frac{\partial f(\mathbf{q})}{\partial x} \right] d\hat{\Omega} \quad = \quad & \int_{\hat{\Omega}} \psi \delta \hat{w} \left[\alpha \left(\mathbf{X} \mathbf{\Lambda}^{jcel^+} \mathbf{X}^{-1} - \mathbf{X} \mathbf{\Lambda}^{jcel^-} \mathbf{X}^{-1} \right) \frac{\partial \mathbf{q}}{\partial x} \right. \\
& \left. + s \left[\frac{\partial f^{conv}(\mathbf{q})}{\partial x} + \beta (1 - \alpha) \frac{\partial f^{cel}(\mathbf{q})}{\partial x} \right] \right] d\hat{\Omega} \qquad (2.67)
\end{aligned}
$$

Recall $\delta \hat{w}$ is a variation of the test function $\hat{w}$, (2.12), which has been previously identified as $\epsilon \partial \hat{w} / \partial x$. The linear combination parameter α_l is recovered from the directional variation of the test function and the upstream parameter of each decomposition term. Recognizing the absolute value matrix within the diagonalized term, equation (2.67) can be simplified to

$$\int_{\hat{\Omega}} \hat{w} \left[\frac{\partial f^c(\mathbf{q})}{\partial x} - \frac{\partial f(\mathbf{q})}{\partial x} \right] d\hat{\Omega} = \int_{\hat{\Omega}} \epsilon\psi \frac{\partial \hat{w}}{\partial x} \left[\alpha \mathbf{X} |\mathbf{\Lambda}^{jcel}| \mathbf{X}^{-1} \frac{\partial \mathbf{q}}{\partial x} + s \left[\frac{\partial f^{conv}(\mathbf{q})}{\partial x} + \beta(1-\alpha) \frac{\partial f^{cel}(\mathbf{q})}{\partial x} \right] \right] d\hat{\Omega} \tag{2.68}$$

Integrating the left-hand term by parts transfers the derivative onto the decomposition terms which generates an endpoint evaluation on the domain boundary $\partial\hat{\Omega}$

$$\begin{aligned} & - \int_{\hat{\Omega}} \hat{w} \frac{\partial}{\partial x} \left(\epsilon\psi \left[\alpha \mathbf{X} |\mathbf{\Lambda}^{jcel}| \mathbf{X}^{-1} \frac{\partial \mathbf{q}}{\partial x} + s \left[\frac{\partial f^{conv}(\mathbf{q})}{\partial x} + \beta(1-\alpha) \frac{\partial f^{cel}(\mathbf{q})}{\partial x} \right] \right] \right) d\hat{\Omega} \\ + & \left[\hat{w} \left(\alpha \mathbf{X} |\mathbf{\Lambda}^{jcel}| \mathbf{X}^{-1} \frac{\partial \mathbf{q}}{\partial x} + s \left[\frac{\partial f^{conv}(\mathbf{q})}{\partial x} + \beta(1-\alpha) \frac{\partial f^{cel}(\mathbf{q})}{\partial x} \right] \right) \right]_{\partial\hat{\Omega}} \end{aligned} \tag{2.69}$$

Again the compact support of $\hat{w}$ eliminates the boundary evaluation. Combining terms yields the integral statement

$$\int_{\hat{\Omega}} \hat{w} \left[\frac{\partial f^c(\mathbf{q})}{\partial x} - \frac{\partial f(\mathbf{q})}{\partial x} + \frac{\partial}{\partial x} \left(\psi\epsilon \left(\alpha \mathbf{X} |\mathbf{\Lambda}^{jcel}| \mathbf{X}^{-1} \frac{\partial \mathbf{q}}{\partial x} + s \left[\frac{\partial f^{conv}(\mathbf{q})}{\partial x} + \beta(1-\alpha) \frac{\partial f^{cel}(\mathbf{q})}{\partial x} \right] \right) \right) \right] d\hat{\Omega} = 0 \tag{2.70}$$

Owing to the arbitrariness of the test function $\hat{w}$ and the subdomain $\hat{\Omega}$ the integrand must be identically zero. The characteristics-biased kinetic flux vector derivative is thus

$$\frac{\partial f^c(\mathbf{q})}{\partial x} = \frac{\partial f(\mathbf{q})}{\partial x} - \frac{\partial}{\partial x} \left(\epsilon\psi \left(\alpha \mathbf{X} |\mathbf{\Lambda}^{jcel}| \mathbf{X}^{-1} \frac{\partial \mathbf{q}}{\partial x} + s \left[\frac{\partial f^{conv}(\mathbf{q})}{\partial x} + \beta(1-\alpha) \frac{\partial f^{cel}(\mathbf{q})}{\partial x} \right] \right) \right) \tag{2.71}$$

Matching matrix components and linear combination parameters with the decomposition components and decompostion combination parameters of (2.15), renaming α_l to γ_l to prevent ambiguity

$$
\begin{aligned}
\frac{\partial f^c(\mathbf{q})}{\partial x} &= \frac{\partial f(\mathbf{q})}{\partial x} - \frac{\partial}{\partial x}\left(\epsilon\psi\left(\alpha\mathbf{X}|\mathbf{\Lambda}^{jcel}|\mathbf{X}^{-1}\,\frac{\partial \mathbf{q}}{\partial x} + s\left[\frac{\partial f^{conv}(\mathbf{q})}{\partial x} + \beta(1-\alpha)\frac{\partial f^{cel}(\mathbf{q})}{\partial x}\right]\right)\right) \\
&= \frac{\partial f(\mathbf{q})}{\partial x} - \frac{\partial}{\partial x}\left(\epsilon\psi\sum_{l=1}^{L} a_1\gamma_l\mathbf{A}_l\frac{\partial \mathbf{q}}{\partial x}\right) \qquad (2.72)
\end{aligned}
$$

$$
\text{where}\quad \begin{cases}
a_1 = 1 & \gamma_1 = \alpha & \mathbf{A}_1 = \mathbf{X}|\mathbf{\Lambda}^{jcel}|\mathbf{X}^{-1} \\
a_2 = s & \gamma_2 = 1 & \mathbf{A}_2 = \mathbf{A}^{conv} \\
a_3 = s & \gamma_3 = \beta(1-\alpha) & \mathbf{A}_3 = \mathbf{A}^{cel}
\end{cases} \qquad (2.73)
$$

The upstream matrix $\mathcal{A}$ is thus

$$
\mathcal{A} = \alpha\mathbf{X}|\mathbf{\Lambda}^{jcel}|\mathbf{X}^{-1} + s\left[\mathbf{A}^{conv} + \beta(1-\alpha)\mathbf{A}^{cel}\right] \qquad (2.74)
$$

Thus the upstream matrix is represented by two physically significant components which smoothly transition from celerity/convection to pure convection. The final step is to determine the free parameters.

2.8 Determination of Free Parameters

As developed in [37], the eigenvalues of the matrix within the second-order differential term must be real and positive to ensure solution boundedness with dispersion control. Thus the eigenvalues of the upstream matrix

$$
\mathcal{A} = \alpha\mathbf{X}|\mathbf{\Lambda}^{jcel}|\mathbf{X}^{-1} + s\left[\mathbf{A}^{conv} + \beta(1-\alpha)\mathbf{A}^{cel}\right] \qquad (2.75)
$$

are sought. From (2.51), (2.52), and some matrix algebra,

$$\mathbf{X}|\mathbf{\Lambda}^{jcel}|\mathbf{X}^{-1} = \sqrt{gh}\,\mathbf{I} \tag{2.76}$$

Redefining $\beta(1-\alpha) = \delta$, the upstream matrix becomes

$$\mathcal{A} = \alpha\sqrt{gh}\,\mathbf{I} + s\mathbf{A}^{conv} + s\delta\mathbf{A}^{cel} \tag{2.77}$$

Substituting the definitions of $\mathbf{A}^{conv}$ and $\mathbf{A}^{cel}$, (2.33), the upstream matrix becomes

$$\mathcal{A} = \begin{bmatrix} \alpha\sqrt{gh} & s \\ s(\delta gh - u^2) & s2u + \alpha\sqrt{gh} \end{bmatrix} \tag{2.78}$$

with dimensional upstream eigenvalues

$$\lambda_{1,2}^{d_{\mathcal{A}}} = \alpha\sqrt{gh} + u \pm \sqrt{\delta}\sqrt{gh} \tag{2.79}$$

Non-dimensionalizing the upstream eigenvalues reveals the dependence upon the Froude number and the upstream-bias parameters

$$\lambda_{1,2}^{\mathcal{A}} = Fr + \alpha \pm \sqrt{\delta} \tag{2.80}$$

Recalling that the level of dissipation is to be proportional to the characteristic speeds, the upstream parameters α and δ can be obtained as functions of the upstream eigenvalues and the Froude number by adding and subtracting (2.80)

$$\alpha = \frac{\lambda_1^{\mathcal{A}} + \lambda_2^{\mathcal{A}}}{2} - Fr \tag{2.81}$$

$$\delta = \frac{(\lambda_1^{\mathcal{A}} - \lambda_2^{\mathcal{A}})^2}{4} \tag{2.82}$$

Comparing with the non-dimensional open channel eigenvalues

$$\lambda_{1,2}^{OC} = Fr \pm 1 \tag{2.83}$$

To insure that the upstream eigenvalues are positive for all values of Froude while correlating with the open channel eigenvalues by maintaining a similar magnitude, imposed variations of the upstream eigenvalues are employed via

$$\lambda_1^{Acs} = \lambda_1^{OC} = Fr + 1 \tag{2.84}$$

$$\lambda_2^{Acs} = |\lambda_2^{OC}| = |Fr - 1| \tag{2.85}$$

where $\lambda_{1,2}^{Acs}$ denotes the correlated and stable imposed forms of the upstream matrix eigenvalues. Plotting the imposed upstream eigenvalues (2.84)-(2.85) along with the open channel eigenvalues (2.83) in Figure (2.1) for $0 \leq Fr \leq 2$ indicates that $\lambda_{1,2}^{Acs}$ is positive and has the same magnitude as $\lambda_{1,2}^{OC}$ for all Froude.

At the crictical point, $Fr = 1$, λ_2^{Acs} exhibits a discontinuity in slope. Heed that λ_2^{Acs}, along with λ_1^{Acs}, determines α and δ. The upstream parameters α and δ are within a second-order differential. As such, α and δ must be smooth and continuous, hence λ_2^{Acs} must be smooth and continuous. A composite spline shall be employed to patch the sub- and supercritical regimes together, thereby admitting a smooth variation in λ_2^{Acs}. The terminal imposed variations of $\lambda_{1,2}^{Acs}$ with respect to Fr are thus

$$\lambda_1^{Acs} = Fr + 1 \tag{2.86}$$

$$\lambda_2^{Acs} = \begin{cases} 1 - Fr & Fr \leq 1 - \epsilon_{Fr} \\ \frac{(Fr-1)^2}{2\epsilon_{Fr}} + \frac{\epsilon_{Fr}}{2} & 1 - \epsilon_{Fr} < Fr < 1 + \epsilon_{Fr} \\ Fr - 1 & 1 + \epsilon_{Fr} \leq Fr \end{cases} \tag{2.87}$$

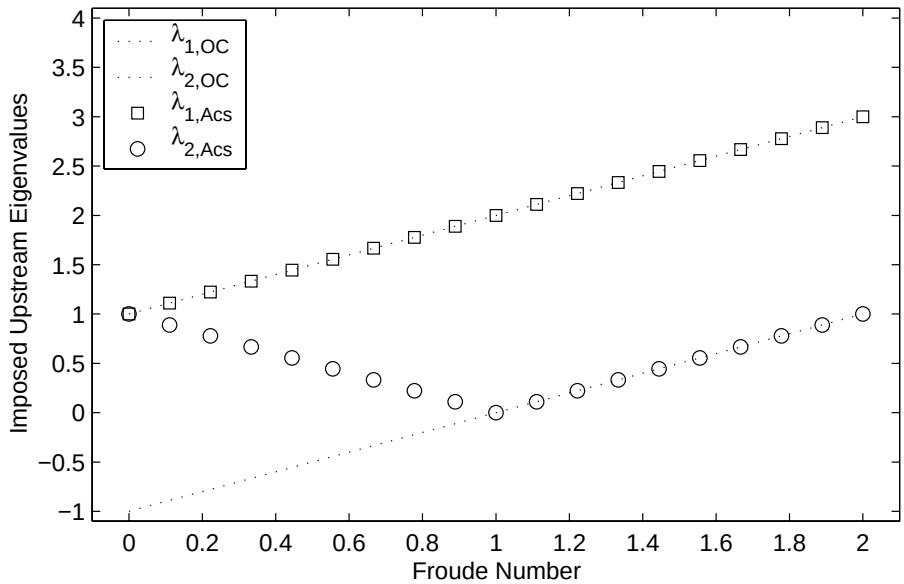

Figure 2.1: Correlation of One-Dimensional Open Channel and Imposed Upstream Eigenvalues

where ϵ_{Fr} has been found through numeric experiments to equal one-fifth [37]. The terminal imposed upstream eigenvalues are plotted in Figure (2.2), showing a smooth and continuous variation in λ_2^{Acs}

Having established the desired terminal form of the spline modified, imposed upstream eigenvalues of the characteristics-flux jacobian, the introduced upstream parameters can now be determined as functions of the Froude number. The resultant variation for (2.84) - (2.85) is graphed in Figure (2.3), verifying that the formulation smoothly transitions from a celerity/convection formulation to a pure convection formulation as a function of Froude number.

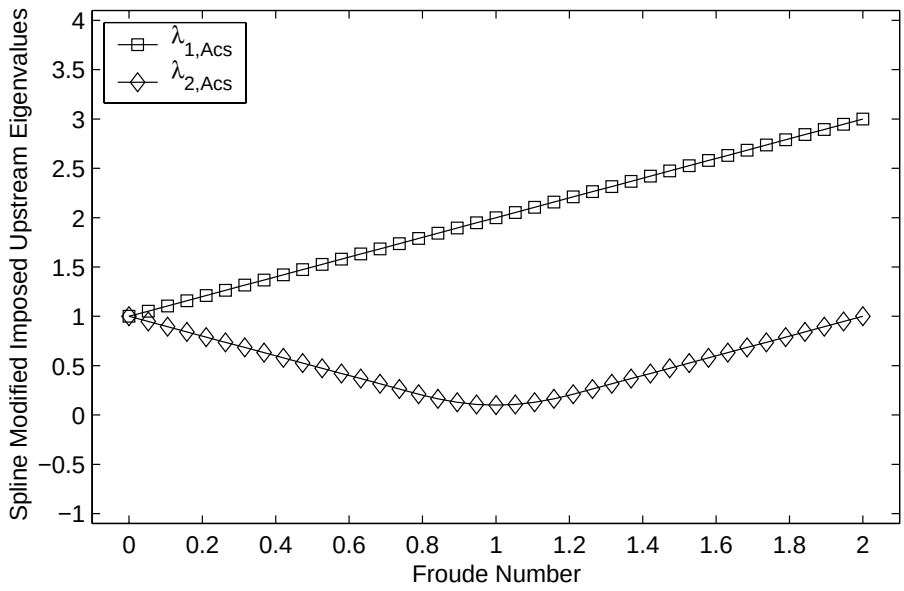

Figure 2.2: One-Dimensional Spline Modified, Imposed Upstream Eigenvalue Spectra

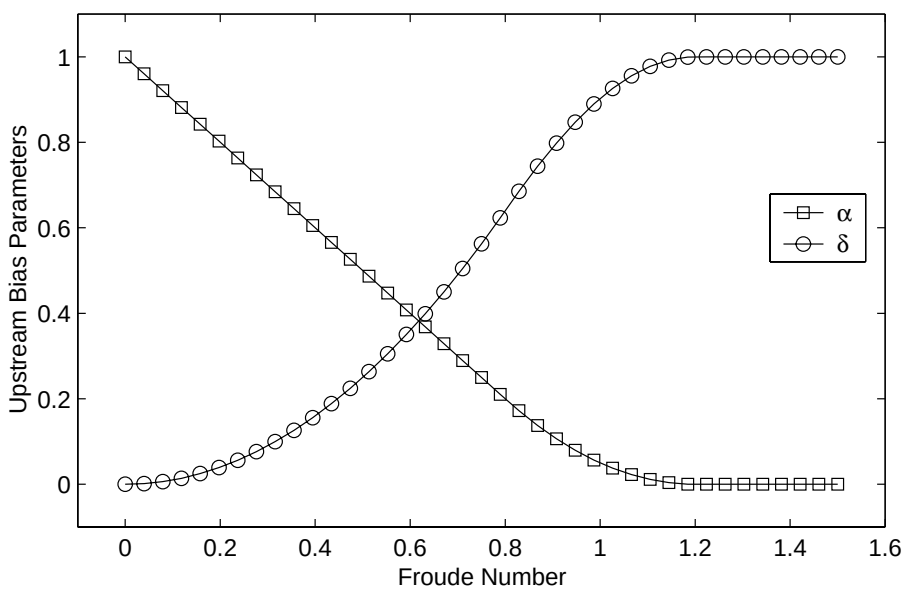

Figure 2.3: One-Dimensional Upstream Bias Parameter Spectra

2.9 Spatial Discretization

The final step is to generate the semi-discrete spatial approximation to the characteristics-biased open channel flow conservation law system weak form. The standard procedure [14], [40] is to

1. Define a conservation law system $L(\mathbf{q}) = 0$

2. Constrain the weak form test function arbitrariness

3. Implement the resultant weak statement formulation $\int_\Omega \Phi_\alpha L(\mathbf{q}) d\Omega = 0$

4. Define a continuum approximation to the state and group variables $\mathbf{q}(x,t) \approx \mathbf{q}^N(x,t) \equiv \Psi_\beta(x)\mathbf{Q}_\beta(t)$, hence the approximate weak statement $\int_{\hat{\Omega}} \Phi_\alpha L^N(\mathbf{q}) d\hat{\Omega} \approx 0$

5. Extremize the approximation error via the Galerkin definition $\Phi_\alpha = \Psi_\beta$

6. Select the discrete form of the approximation to be the inner product of a set of compact support Lagrangian interpolating polynomials of degree k and their associated expansion coefficients, hence $q^N(x,t) \equiv \mathbf{q}^h(x,t) \equiv \{N_k(x)\}^T\{\mathbf{Q}(t)\}$ and $\Psi_\alpha(x) \equiv \{N_k(x)\}$, hence form

$$\bigcup_{\Omega^h} \int_{\Omega^h} \{N_k(x)\} L(\mathbf{q}^h) d\Omega \equiv 0 \tag{2.88}$$

By the identified steps:

1. The conservation law system from (2.71)

$$\begin{aligned} L(\mathbf{q}) &= \frac{\partial \mathbf{q}}{\partial t} + \frac{\partial f^c(\mathbf{q})}{\partial x} = 0 && (2.89) \\ &= \frac{\partial \mathbf{q}}{\partial t} + \frac{\partial f(\mathbf{q})}{\partial x} \\ &\quad - \frac{\partial}{\partial x}\left(\epsilon\psi\left(\alpha \mathbf{X}|\mathbf{\Lambda}^{cel}|\mathbf{X}^{-1}\frac{\partial \mathbf{q}}{\partial x} + s\left[\delta\frac{\partial f^{cel}(\mathbf{q})}{\partial x} + \frac{\partial f^{conv}(\mathbf{q})}{\partial x}\right]\right)\right) = 0 && (2.90) \end{aligned}$$

Expanding and dropping the notation ($\mathbf{q}$) from the parent kinetic flux divergence and the associated kinetic flux divergence components for simplicity,

$$L(\mathbf{q}) = \frac{\partial \mathbf{q}}{\partial t} + \frac{\partial f}{\partial x} - \frac{\partial}{\partial x}\left(\epsilon\psi\left(\alpha\sqrt{gh}\,\frac{\partial \mathbf{q}}{\partial x} + s\delta\frac{\partial f^{cel}}{\partial x} + s\frac{\partial f^{conv}}{\partial x}\right)\right) = 0 \tag{2.91}$$

2,3. Forming the weak form for (2.91) with extremization leading to the set of test functions Φ_α, dropping the variable dependency notation for simplicity,

$$\begin{aligned}\int_\Omega \Phi_\alpha L(\mathbf{q}) d\Omega \quad &= \quad \int_\Omega \Phi_\alpha \left[\frac{\partial \mathbf{q}}{\partial t} + \frac{\partial f}{\partial x}\right. \\ &\qquad \left. - \frac{\partial}{\partial x}\left(\epsilon\psi\left(\alpha\sqrt{gh}\,\frac{\partial \mathbf{q}}{\partial x} + s\delta\frac{\partial f^{cel}}{\partial x} + s\frac{\partial f^{conv}}{\partial x}\right)\right)\right] d\Omega = 0\end{aligned} \tag{2.92}$$

Distributing the test function Φ_α and expanding the integral isolates the second-order differential term

$$\int_\Omega \Phi_\alpha \left[\frac{\partial \mathbf{q}}{\partial t} + \frac{\partial f}{\partial x}\right] d\Omega - \int_\Omega \Phi_\alpha \left[\frac{\partial}{\partial x}\left(\epsilon\psi\left(\alpha\sqrt{gh}\,\frac{\partial \mathbf{q}}{\partial x} + s\delta\frac{\partial f^{cel}}{\partial x} + s\frac{\partial f^{conv}}{\partial x}\right)\right)\right] d\Omega = 0 \tag{2.93}$$

Integrating the second-order differential term by parts

$$\begin{aligned}&-\int_\Omega \frac{\partial \Phi_\alpha}{\partial x}\left(\epsilon\psi\left(\alpha\sqrt{gh}\,\frac{\partial \mathbf{q}}{\partial x} + s\delta\frac{\partial f^{cel}}{\partial x} + s\frac{\partial f^{conv}}{\partial x}\right)\right) d\Omega = 0 \\ &+\Phi_\alpha\left(\frac{\partial}{\partial x}\left(\epsilon\psi\left(\alpha\sqrt{gh}\,\frac{\partial \mathbf{q}}{\partial x} + s\delta\frac{\partial f^{cel}}{\partial x} + s\frac{\partial f^{conv}}{\partial x}\right)\right)\right)\Bigg|_{\partial\Omega}\end{aligned} \tag{2.94}$$

The characteristics-bias should be of no influence on the domain boundary conditions, hence $\Phi(\partial\Omega) = 0$. Having eliminated the boundary integral, the terminal continuum weak statement is

$$\begin{aligned}\int_\Omega \Phi_\alpha L(\mathbf{q}) d\Omega \quad &= \quad \int_\Omega \left[\Phi_\alpha\left(\frac{\partial \mathbf{q}}{\partial t} + \frac{\partial f}{\partial x}\right)\right. \\ &\qquad \left. + \epsilon\psi\frac{\partial \Phi_\alpha}{\partial x}\left(\alpha\sqrt{gh}\,\frac{\partial \mathbf{q}}{\partial x} + s\delta\frac{\partial f^{cel}}{\partial x} + s\frac{\partial f^{conv}}{\partial x}\right)\right] d\Omega = 0\end{aligned} \tag{2.95}$$

4. Continuum approximations to the state variable q and characteristics-biased flux divergence terms are formed via a linear combination of spatially dependent weight functions and temporally dependent expansion coefficients. For a generic scalar variable p

$$p(x,t) \approx p^N(x,t) \equiv \sum_{j=1}^{N} \Psi_\beta(x) P_j(t) \tag{2.96}$$

Approximating the state and group variables as

$$\mathbf{q}(x,t) \approx \mathbf{q}^N(x,t) \equiv \sum_{j=1}^{N} \Psi_\beta(x) \mathbf{Q}_\beta(t) \tag{2.97}$$

$$f(x,t) \approx f^N(x,t) \approx f^N(\mathbf{q}^N(x,t)) \equiv \sum_{j=1}^{N} \Psi_\beta(x) F_\beta(\mathbf{q}^N,t) \tag{2.98}$$

$$f^{cel}(x,t)) \approx f^{cel^N}(x,t) \approx f^{cel^N}(\mathbf{q}^N(x,t)) \equiv \sum_{j=1}^{N} \Psi_\beta(x) F_\beta^{cel}(\mathbf{q}^N,t) \tag{2.99}$$

$$f^{conv}(x,t) \approx f^{conv^N}(x,t) \approx f^{conv^N}(\mathbf{q}^N(x,t)) \equiv \sum_{j=1}^{N} \Psi_\beta(x) F_\beta^{conv}(\mathbf{q}^N,t) \tag{2.100}$$

where

$$\mathbf{q} = \left\{ \begin{array}{c} h \\ m \end{array} \right\} \quad \text{and} \quad f = \left\{ \begin{array}{c} m \\ \frac{m}{h} m + g\frac{h^2}{2} \end{array} \right\} \tag{2.101}$$

$$f^{cel} = \left\{ \begin{array}{c} 0 \\ g\frac{h^2}{2} \end{array} \right\} \quad \text{and} \quad f^{conv} = \left\{ \begin{array}{c} m \\ \frac{m}{h} \end{array} \right\} \tag{2.102}$$

While the continuum approximation (2.96) can accomodate the upstream parameters, for computational efficiency this dissertation project employs piecewise constant, locally averaged values for ϵ, ψ, s, α, and δ. The final issue is the handling of $\sqrt{gh}$ in the dissipation term. The square root of gh will be approximated via (2.96) as a grouped variable

$$\sqrt{gh(x,t)} \approx \sqrt{(gh)^N(x,t)} \quad \equiv \quad \sum_{\beta=1}^{N} \Psi_\beta(x) SQRGH_\beta(\mathbf{q}^N, t) \tag{2.103}$$

Generating the continuum approximation to the continum statement (2.95)

$$\begin{aligned}\int_\Omega \Phi_\alpha L^N(\mathbf{q}) d\Omega \quad &= \quad \int_\Omega \left[\Phi_\alpha \left(\Psi_\beta \frac{d\mathbf{Q}_\beta}{dt} + \frac{\partial \Psi_\beta}{\partial x} F_\beta \right) \right. \\ &\quad \left. + \epsilon\psi \frac{\partial \Phi_\alpha}{\partial x} \left(\alpha\sqrt{gh}\, \frac{\partial \Psi_\beta}{\partial x} \mathbf{Q}_\beta + s\delta \frac{\partial \Psi_\beta}{\partial x} F_\beta^{cel} + s \frac{\partial \Psi_\beta}{\partial x} F_\beta^{conv} \right) \right] d\Omega \approx 0 \end{aligned} \tag{2.104}$$

5. Forming the Galerkin weak statement of (2.104), by defining $\Phi_\alpha = \Psi_\alpha$, to extremize the approximation error

$$\begin{aligned}\int_\Omega \Psi_\alpha L^N(\mathbf{q}) d\Omega \quad &= \quad \int_\Omega \Psi_\alpha \Psi_\beta \; d\Omega \; \frac{d\mathbf{Q}_\beta}{dt} \\ &\quad + \int_\Omega \Psi_\alpha \frac{\partial \Psi_\beta}{\partial x} \; d\Omega \; F_\beta \\ &\quad + \epsilon\psi\alpha SQRGH_\beta \int_\Omega \Psi_\beta \frac{\partial \Psi_\alpha}{\partial x} \frac{\partial \Psi_\beta}{\partial x} \; d\Omega \; \mathbf{Q}_\beta \\ &\quad + \epsilon\psi s\delta \int_\Omega \frac{\partial \Psi_\alpha}{\partial x} \frac{\partial \Psi_\beta}{\partial x} \; d\Omega \; F_\beta^{cel} \\ &\quad + \epsilon\psi s \int_\Omega \frac{\partial \Psi_\alpha}{\partial x} \frac{\partial \Psi_\beta}{\partial x} \; d\Omega \; F_\beta^{conv} \\ &\approx \quad 0 \end{aligned} \tag{2.105}$$

Performing the integrals, the essential form of (2.105) is

$$[\mathbf{M}] \frac{d\{\mathbf{Q}\}}{dt} + \{\mathbf{RES}\} = \{\mathbf{0}\} \tag{2.106}$$

where $[\mathbf{M}]$ is the matrix of coefficients pre-multiplying the time derivative and $\{\mathbf{RES}\}$ contains the remainder of the continuum weak statement (2.105).

6. For this research, the linear finite element will used as the interpolating function $\{N_k(\mathbf{x})\}$.

2.10 Temporal Discretization and Newton Construction

Having formed the semi-discrete spatial approximation to the characteristics-biased conservation law system, a time step and iteration process must be selected and implemented. Numerous options are available for these choices: Θ Taylor series and Runge-Kutta; Picard, SOR, and Newton, for example. This dissertation employs the Θ Taylor series, yielding second order accuracy via $\Theta = 0.5$, coupled with the Newton iteration algorithm for optimal solution convergence.

The Θ Taylor series, well-discussed in [39], generalizes the (explicit) forward Euler, backward Euler, and trapezoidal rule for time integration via

$$\{\mathbf{Q}\}^{n+1} = \{\mathbf{Q}\}^{n} + \Delta t \left(\Theta \frac{d\{\mathbf{Q}\}^{n+1}}{dt} + (1-\Theta) \frac{d\{\mathbf{Q}\}^{n}}{dt} \right) + O(\Delta t^2, \Delta t^3) \tag{2.107}$$

where $n+1$ is the current time station, n is the previous time station, and $O(\cdot)$ is the associated time truncation error. Setting $\Theta = 0$ or $\Theta = 1$ yields the first order backward and forward Euler algorithms. The second order trapezoid rule is obtained via $\Theta = 0.5$.

The weak statement form readily permits evaulating any time derivative required as the time derivatives $d\{\mathbf{Q}\}/dt$ can be isolated algebraically in (2.106) as

$$\frac{d\{\mathbf{Q}\}}{dt} = \mathbf{M}^{-1}\{\mathbf{RES}\} \tag{2.108}$$

Substituting (2.108) into (2.107) and defining $\{\Delta\mathbf{Q}\}^{n+1} \equiv \{\mathbf{Q}\}^{n+1} - \{\mathbf{Q}\}^{n}$ yields

$$[\mathbf{M}]\{\Delta\mathbf{Q}\}_{n+1} = -\Delta t \left(\Theta\{\mathbf{RES}\}_{n+1} + (1-\Theta)\{\mathbf{RES}\}_{n} \right) \tag{2.109}$$

Thus, the fully discrete algebraic system is

$$[\mathbf{M}]\{\Delta\mathbf{Q}\} + \Delta t\{\mathbf{RES}\}_{n+\theta} = \{\mathbf{F}\} = \{\mathbf{0}\} \tag{2.110}$$

For linear problem statements, (2.110) converges in one step and $\mathbf{Q}_{n+1}$ is immediately realized. Non-linear problem statements require an iterative process to produce $\mathbf{Q}_{n+1}$ to within an acceptable tolerance. The Newton iteration algorithm provides quadratic convergence when fully implemented. Quasi-Newton constructs, formed for computational efficiency, yield convergence rates anywhere from nearly quadratic to divergent.

The terminal iterative form for solving (2.110) is [14]

$$\left([\mathbf{M}] + \frac{\partial\{\mathbf{RES}\}}{\partial\{\mathbf{Q}\}}\right)\delta\mathbf{Q}^{p+1} = -\{\mathbf{F}\}^p \tag{2.111}$$

and

$$\{\Delta\mathbf{Q}\} = \sum_{1}^{p+1}\{\delta\mathbf{Q}\} \quad , \quad \{\mathbf{Q}\}_{n+1} = \{\mathbf{Q}\}_n + \{\Delta\mathbf{Q}\} \tag{2.112}$$

Determination of $\partial\{\mathbf{RES}\}/\partial\{\mathbf{Q}\}$ from the Galerkin weak statement form of the characteristics biased conservation law system (2.105) starts with

$$\{\mathbf{RES}\} = \left\{ \begin{array}{c} \mathbf{RH} \\ \mathbf{RM} \end{array} \right\} \tag{2.113}$$

hence

$$\frac{\partial\{\mathbf{RES}\}}{\partial\{\mathbf{Q}\}} = \left[\begin{array}{cc} \frac{\partial RH}{\partial H} & \frac{\partial RH}{\partial M} \\ \frac{\partial RM}{\partial H} & \frac{\partial RM}{\partial M} \end{array} \right] = \left[\begin{array}{cc} \mathbf{JHH} & \mathbf{JHM} \\ \mathbf{JMH} & \mathbf{JMM} \end{array} \right] = [\mathbf{JAC}] \tag{2.114}$$

Expressing each component of $\{\mathbf{RES}\}$ courtesy (2.105) where the state variable and grouped flux approximations are expressed in the interior and rightmost brackets.

$$
\begin{aligned}
\mathbf{RH} \quad = \quad & \int_\Omega \Psi_\alpha \frac{\partial \Psi_\beta}{\partial x}\, d\Omega \;\; [m]_\beta \\
& + \epsilon\psi\alpha \left[\sqrt{gh}\right]_\beta \int_\Omega \Psi_\beta \frac{\partial \Psi_\alpha}{\partial x}\frac{\partial \Psi_\beta}{\partial x}\, d\Omega \;\; [h]_\beta \\
& + \epsilon\psi s\delta \int_\Omega \frac{\partial \Psi_\alpha}{\partial x}\frac{\partial \Psi_\beta}{\partial x}\, d\Omega \;\; [0] \\
& + \epsilon\psi s \int_\Omega \frac{\partial \Psi_\alpha}{\partial x}\frac{\partial \Psi_\beta}{\partial x}\, d\Omega \;\; [m]_\beta
\end{aligned} \tag{2.115}
$$

$$
\begin{aligned}
\mathbf{RM} \quad = \quad & \int_\Omega \Psi_\alpha \frac{\partial \Psi_\beta}{\partial x}\, d\Omega \;\; \left[\frac{m}{h}m + \frac{g}{2}h^2\right]_\beta \\
& + \epsilon\psi\alpha \left[\sqrt{gh}\right]_\beta \int_\Omega \Psi_\beta \frac{\partial \Psi_\alpha}{\partial x}\frac{\partial \Psi_\beta}{\partial x}\, d\Omega \;\; [m]_\beta \\
& + \epsilon\psi s\delta \int_\Omega \frac{\partial \Psi_\alpha}{\partial x}\frac{\partial \Psi_\beta}{\partial x}\, d\Omega \;\; \left[\frac{g}{2}h^2\right]_\beta \\
& + \epsilon\psi s \int_\Omega \frac{\partial \Psi_\alpha}{\partial x}\frac{\partial \Psi_\beta}{\partial x}\, d\Omega \;\; \left[\frac{m}{h}m\right]_\beta
\end{aligned} \tag{2.116}
$$

The jacobian is thus generated according to (2.114). Note that the terms within the bracketed state variable and flux group approximations are subject to differentiation by the state variable approximation as the β index can be considered as distributed throughout the entire term. To prevent conflicts with indicial notation convention and to emphasize that the variable group is being approximated, the β is kept outside as the bracket subscript. Hence

$$
\begin{aligned}
\mathbf{JHH} \quad = \quad & \frac{\partial}{\partial h_\beta}\left(\int_\Omega \Psi_\alpha \frac{\partial \Psi_\beta}{\partial x}\, d\Omega\ \ [m]_\beta\right) \\
& + \frac{\partial}{\partial h_\beta}\left(\epsilon\psi\alpha\left[\sqrt{gh}\right]_\beta \int_\Omega \Psi_\beta \frac{\partial \Psi_\alpha}{\partial x}\frac{\partial \Psi_\beta}{\partial x}\, d\Omega\ \ [h]_\beta\right) \\
& + \frac{\partial}{\partial h_\beta}\left(\epsilon\psi s\delta \int_\Omega \frac{\partial \Psi_\alpha}{\partial x}\frac{\partial \Psi_\beta}{\partial x}\, d\Omega\ 0\right) \\
& + \frac{\partial}{\partial h_\beta}\left(\epsilon\psi s \int_\Omega \frac{\partial \Psi_\alpha}{\partial x}\frac{\partial \Psi_\beta}{\partial x}\, d\Omega\ \ [m]_\beta\right) \\
= \quad & 0 \\
& + \epsilon\psi\alpha\left[\sqrt{gh}\right]_\beta \int_\Omega \Psi_\beta \frac{\partial \Psi_\alpha}{\partial x}\frac{\partial \Psi_\beta}{\partial x}\, d\Omega\ 1 \\
& + \epsilon\psi\alpha\,[h]_\beta \int_\Omega \frac{\partial \Psi_\beta}{\partial x}\frac{\partial \Psi_\alpha}{\partial x}\Psi_\beta\, d\Omega\ \ \left[\frac{1}{2\sqrt{gh}}\right]_\beta \\
& + 0 \\
& + 0
\end{aligned}
\tag{2.117}
$$

$$
\begin{aligned}
\mathbf{JHM} \quad = \quad & \frac{\partial}{\partial m_\beta}\left(\int_\Omega \Psi_\alpha \frac{\partial \Psi_\beta}{\partial x}\, d\Omega\ \ [m]_\beta\right) \\
& + \frac{\partial}{\partial m_\beta}\left(\epsilon\psi\alpha\left[\sqrt{gh}\right]_\beta \int_\Omega \Psi_\beta \frac{\partial \Psi_\alpha}{\partial x}\frac{\partial \Psi_\beta}{\partial x}\, d\Omega\ \ [h]_\beta\right) \\
& + \frac{\partial}{\partial m_\beta}\left(\epsilon\psi s\delta \int_\Omega \frac{\partial \Psi_\alpha}{\partial x}\frac{\partial \Psi_\beta}{\partial x}\, d\Omega\ 0\right) \\
& + \frac{\partial}{\partial m_\beta}\left(\epsilon\psi s \int_\Omega \frac{\partial \Psi_\alpha}{\partial x}\frac{\partial \Psi_\beta}{\partial x}\, d\Omega\ \ [m]_\beta\right) \\
= \quad & \int_\Omega \Psi_\alpha \frac{\partial \Psi_\beta}{\partial x}\, d\Omega\ 1 \\
& + 0 \\
& + 0 \\
& + \epsilon\psi s \int_\Omega \frac{\partial \Psi_\alpha}{\partial x}\frac{\partial \Psi_\beta}{\partial x}\, d\Omega\ 1
\end{aligned}
\tag{2.118}
$$

$$
\begin{aligned}
\mathbf{JMH} \quad = \quad & \frac{\partial}{\partial h_\beta}\left(\int_\Omega \Psi_\alpha \frac{\partial \Psi_\beta}{\partial x}\, d\Omega \ \left[\frac{m}{h}m + g\frac{h^2}{2}\right]_\beta\right) \\
& + \frac{\partial}{\partial h_\beta}\left(\epsilon\psi\alpha\left[\sqrt{gh}\right]_\beta \int_\Omega \Psi_\beta \frac{\partial \Psi_\alpha}{\partial x}\frac{\partial \Psi_\beta}{\partial x}\, d\Omega \ [m]_\beta\right) \\
& + \frac{\partial}{\partial h_\beta}\left(\epsilon\psi s\delta \int_\Omega \frac{\partial \Psi_\alpha}{\partial x}\frac{\partial \Psi_\beta}{\partial x}\, d\Omega \ \left[g\frac{h^2}{2}\right]_\beta\right) \\
& + \frac{\partial}{\partial h_\beta}\left(\epsilon\psi s \int_\Omega \frac{\partial \Psi_\alpha}{\partial x}\frac{\partial \Psi_\beta}{\partial x}\, d\Omega \ \left[\frac{m}{h}m\right]_\beta\right) \\
= \quad & \int_\Omega \Psi_\alpha \frac{\partial \Psi_\beta}{\partial x}\, d\Omega \ \left[-\frac{m^2}{h^2} + gh\right]_\beta \\
& + 0 \\
& + \epsilon\psi\alpha\,[m]_\beta \int_\Omega \frac{\partial \Psi_\beta}{\partial x}\frac{\partial \Psi_\alpha}{\partial x}\Psi_\beta\, d\Omega \ \left[\frac{1}{2\sqrt{gh}}\right]_\beta \\
& + \epsilon\psi s\delta \int_\Omega \frac{\partial \Psi_\alpha}{\partial x}\frac{\partial \Psi_\beta}{\partial x}\, d\Omega \ [gh]_\beta \\
& + \epsilon\psi s \int_\Omega \frac{\partial \Psi_\alpha}{\partial x}\frac{\partial \Psi_\beta}{\partial x}\, d\Omega \ \left[-\frac{m^2}{h^2}\right]_\beta
\end{aligned} \tag{2.119}
$$

$$
\begin{aligned}
\mathbf{JMM} \quad = \quad & \frac{\partial}{\partial m_\beta}\left(\int_\Omega \Psi_\alpha \frac{\partial \Psi_\beta}{\partial x}\, d\Omega \ \left[\frac{m^2}{h} + g\frac{h^2}{2}\right]_\beta\right) \\
& + \frac{\partial}{\partial m_\beta}\left(\epsilon\psi\alpha\left[\sqrt{gh}\right]_\beta \int_\Omega \Psi_\beta \frac{\partial \Psi_\alpha}{\partial x}\frac{\partial \Psi_\beta}{\partial x}\, d\Omega \ [m]_\beta\right) \\
& + \frac{\partial}{\partial m_\beta}\left(\epsilon\psi s\delta \int_\Omega \frac{\partial \Psi_\alpha}{\partial x}\frac{\partial \Psi_\beta}{\partial x}\, d\Omega \ \left[g\frac{h^2}{2}\right]_\beta\right) \\
& + \frac{\partial}{\partial m_\beta}\left(\epsilon\psi s \int_\Omega \frac{\partial \Psi_\alpha}{\partial x}\frac{\partial \Psi_\beta}{\partial x}\, d\Omega \ \left[\frac{m}{h}m\right]_\beta\right) \\
= \quad & \int_\Omega \Psi_\alpha \frac{\partial \Psi_\beta}{\partial x}\, d\Omega \ \left[2\frac{m}{h}\right]_\beta \\
& + \sqrt{g}\epsilon\psi\alpha\sqrt{h_\beta} \int_\Omega \Psi_\beta \frac{\partial \Psi_\alpha}{\partial x}\frac{\partial \Psi_\beta}{\partial x}\, d\Omega \ 1 \\
& + 0 \\
& + \epsilon\psi s \int_\Omega \frac{\partial \Psi_\alpha}{\partial x}\frac{\partial \Psi_\beta}{\partial x}\, d\Omega \ \left[2\frac{m}{h}\right]_\beta
\end{aligned} \tag{2.120}
$$

Substantial non-linearity is evident in the jacobian via the grouped variables. A key comment is that the contributions from the parameters ψ, α, and δ, while implicit functions of m and h, are not included for computational efficiency.

2.11 Determination of ψ

The dissipation level controller ψ should be a solution-dependent element value for increased solution accuracy and stability. To prevent spurious transitions in problem character, i.e. parabolic to hyperbolic, a low-level of background diffusion is required throughout the entire solution domain. Varying qualitative dissipation levels are therefore required according to Table (2.1).

Many current dissipative finite element algorithms use a constant value for the dissipation level controller. This simplification either over-diffuses the continuous regions to stabilize the discontinuities or under-diffuses the discontinuous regions to maintain accuracy in the continous regions. Either approach yields an inaccurate solution.

Setting $\psi = 1$ induces a full upwind/downwind bias based on s while $\psi = 0$ removes all dissipation from the characteristics-biased flux divergence. The dissipation controller thus ranges

$$0 < \psi_{min} \leq \psi \leq \psi_{max} < 1 \tag{2.121}$$

As developed in [37], the nodal solution slopes, hence solution and slope continuity, can be

Table 2.1: Qualitative Dissipation Levels for Stability and Accuracy

Solution Character	**Dissipation Level**	**Effect**
Discontinuous Solution	*Maximum*	Stability
Continuous Solution - Discontinuous Slope	*Medium*	Stability and Accuracy
Continuous Solution - Continuous Slope	*Minimum*	Accuracy

qualified by subtracting the element unit normal vectors at the common node:

$$|\hat{n}_R - \hat{n}_L| \approx 0 \qquad \text{solution and slope are continuous} \tag{2.122}$$

$$|\hat{n}_R - \hat{n}_L| \approx 1 \qquad \text{solution is continuous, slope is discontinuous} \tag{2.123}$$

$$|\hat{n}_R - \hat{n}_L| \to 2 \qquad \text{solution is discontinuous} \tag{2.124}$$

This qualitative behavior can be normalized in terms of a solution continuity gauge φ

$$\varphi = \frac{1}{2}|\hat{n}_R - \hat{n}_L| = \sqrt{\frac{1 - cos(\theta)}{2}} \tag{2.125}$$

where θ is the angle between $\hat{n}_R$ and $\hat{n}_L$.

At a normal hydraulic jump, $\theta = 90°$ and hence $\varphi = 1/\sqrt{2} \approx \psi_{max}$. Following [37], ψ can be mapped to φ with a spline:

$$\psi \quad = \quad \begin{cases} \psi_{min} & \varphi \leq \varphi_C \\ \psi_{max} + \frac{\psi_{max} - \psi_{min}}{(\varphi_D - \varphi_C)^3}[-(\varphi_D - 3\varphi_C)\varphi_D^2 & \\ \quad -6\varphi_D\varphi_C + 3(\varphi_D + \varphi_C)\varphi^2 - 2\varphi^3] & \varphi_C < \varphi < \varphi_D \\ \psi_{max} & \varphi \geq \varphi_D \end{cases} \tag{2.126}$$

where $\varphi_C = 0$, $\varphi_D = 1/\sqrt{2}$, $\psi_{max} \leq 2 - \psi_{min}$, and experimental results indicate $1/4 \leq \psi_{min} \leq 1/2$.

The final step is to solve φ from the unit normals of the element common nodes. For a function q in the (x, q) plane, the unit normal to q is defined as

$$n = \frac{\left(\frac{\partial q}{\partial x}\hat{i} \;+\; \frac{\partial q}{\partial q}\hat{j}\right)}{\sqrt{\left(\frac{\partial q}{\partial x}\right)^2 + \left(\frac{\partial q}{\partial q}\right)^2}} = \frac{\left(\frac{\partial q}{\partial x}\hat{i} \;+\; 1\hat{j}\right)}{\sqrt{\left(\frac{\partial q}{\partial x}\right)^2 + 1}} \tag{2.127}$$

where $(\hat{\imath}, \hat{\jmath})$ are unit vectors in the (x, q) directions respectively.

For a two element discretization, a first-order finite difference approximation to $\partial q/\partial x$ at node i on the left and right elements is

$$\frac{\partial q}{\partial x}_L = \frac{q_i - q_{i-1}}{\Delta x_{i-1/2}} \quad , \quad \frac{\partial q}{\partial x}_R = -\frac{q_{i+1} - q_i}{\Delta x_{i+1/2}} \tag{2.128}$$

where $\Delta x_{\pm 1/2}$ is the length of the left and right elements respectively. Substituting into the unit normal definition (2.127), again into the definition of φ, and rearranging, (2.125) yields

$$\varphi = \frac{1}{2}\left[\left(\frac{\Delta x_{i+1/2}}{\sqrt{\Delta x_{i+1/2}^2 + (q_{i+1} - q_i)^2}} - \frac{\Delta x_{i-1/2}}{\sqrt{\Delta x_{i-1/2}^2 + (q_i - q_{i-1})^2}}\right)^2 \tag{2.129}$$

$$- \left(\frac{q_{i+1} - q_i}{\sqrt{\Delta x_{i+1/2}^2 + (q_{i+1} - q_i)^2}} - \frac{q_i - q_{i-1}}{\sqrt{\Delta x_{i-1/2}^2 + (q_i - q_{i-1})^2}}\right)^2\right]^{1/2} \tag{2.130}$$

as presented in [37]. Thus, the dissipation controller ψ is formulated as an implicit function of the solution q and recovered through the calculation of the solution continuity gauge φ and the spline mapping.

The final issue is the selection of the variable used to gauge solution continuity. As will be demonstrated in the following chapter, the state variables h and m exhibit discontinuities at different points in the x domain, hence neither operating alone is an adequate continuity gauge. Examining the derived scalar variables of velocity, specific kinetic energy, specific potential energy, and specific total energy provides several combinations of h and m:

$$\text{velocity} \quad \rightarrow \quad u = \frac{m}{h} \tag{2.131}$$

$$\text{specific kinetic energy} \quad \rightarrow \quad ke = \frac{1}{2}u^2 \tag{2.132}$$

$$\text{specific potential energy} \quad \rightarrow \quad pe = gh \tag{2.133}$$

$$\text{specific total energy} \quad \rightarrow \quad e = \frac{1}{2}u^2 + gh \tag{2.134}$$

For the one-dimensional research, the scalar velocity will be used to gauge continuity.

2.12 Summary

The one-dimensional inviscid open channel equations have been parabolized for numerical solution via determination of the characteristics-biased dissipatve flux divergence. This dissipative mechanism was developed on the continuum level and the modified problem statement, coupled with the trapezoid time integration rule, remains second order accurate in both space in time. This minimally dissipative mechanism induces a variable level of dissipation based on local solution continuity. Moreover, the dissipation induced by the dissipative flux divergence (by design) propogates along the characteristics of the original hyperbolic problem statement, with a dissipation magnitude that remains proportional to the characteristic speeds of the original hyperbolic conservation law.

Chapter 3

Discussion and Results, One Dimension

This chapter presents the results of a dam break verification-type problem for the one-dimensional, inviscid open channel flow characteristics-biased flus divergence formulation. This challenging verification exhibits time dependent discontinuities in slope and solution for both state variables.

3.1 Problem Statement, 1D Dam Break

The one-dimensional, inviscid, open channel flow conservation law form, (2.1) and (2.2), repeated for convenience, is

$$L(\mathbf{q}) = \frac{\partial \mathbf{q}}{\partial t} + \frac{\partial f(\mathbf{q})}{\partial x} = 0 \tag{3.1}$$

where

$$\mathbf{q} = \left\{ \begin{array}{c} h \\ m \end{array} \right\} \quad \text{and} \quad f(\mathbf{q}) = \left\{ \begin{array}{c} m \\ \frac{m^2}{h} + g\frac{h^2}{2} \end{array} \right\} \tag{3.2}$$

The associated initial and boundary conditions along the real line, presented in Figure (3.1) for $(-1.5 \leq x \leq 1.5)$, are

$$\mathbf{q}(x,0) = \mathbf{q}_0(x) \quad = \quad \left\{ \begin{array}{ccc} h_0(x) = h_o & , & x \leq 0 \\ h_0(x) = 0.13827 h_o & , & 0 < x \\ m_0(x) = 0 & , & x \subset R \end{array} \right. \tag{3.3}$$

$$\mathbf{q}(-\infty,t) = \mathbf{q}_{-\infty}(t) \quad = \quad \left\{ \begin{array}{ccc} h_{-\infty}(t) & = & h_o \\ m_{-\infty}(t) & = & 0 \end{array} \right. \tag{3.4}$$

$$\mathbf{q}(\infty,t) = \mathbf{q}_{\infty}(t) \quad = \quad \left\{ \begin{array}{ccc} h_{\infty}(t) & = & 0.13827 h_o \\ m_{\infty}(t) & = & 0 \end{array} \right. \tag{3.5}$$

The verification closed-form solution to this well-posed initial-value problem, presented in Figure (3.2) for $t = 1.0$, is

$$h(x,t) \quad = \quad \left\{ \begin{array}{ccccccc} h_o & , & -\infty & \leq & x & \leq & -t\sqrt{h_o} \\ \left(\frac{2}{3}\sqrt{h_o} - \frac{x}{3t}\right)^2 & , & -t\sqrt{h_o} & < & x & < & 0 \\ \frac{4}{9}h_o & , & 0 & \leq & x & \leq & x_s \\ 0.13827 h_o & , & x_s & < & x & \leq & \infty \end{array} \right. \tag{3.6}$$

$$m(x,t) \quad = \quad \left\{ \begin{array}{ccccccc} 0 & , & -\infty & \leq & x & \leq & -t\sqrt{h_o} \\ \left(\frac{2}{3}\sqrt{h_o} - \frac{x}{3t}\right)^2 * & & & & & & \\ \left(\frac{2}{3}\sqrt{h_o} + \frac{2}{3}\frac{x}{t}\right) & , & -t\sqrt{h_o} & < & x & < & 0 \\ \frac{8}{27}(h_o)^{3/2} & , & 0 & \leq & x & \leq & x_s \\ 0 & , & x_s & < & x & \leq & \infty \end{array} \right. \tag{3.7}$$

where $x_s = 0.967737309\sqrt{h_o}\, t$ and, for the non-dimensional form of the equation system, $h_o = 1$.

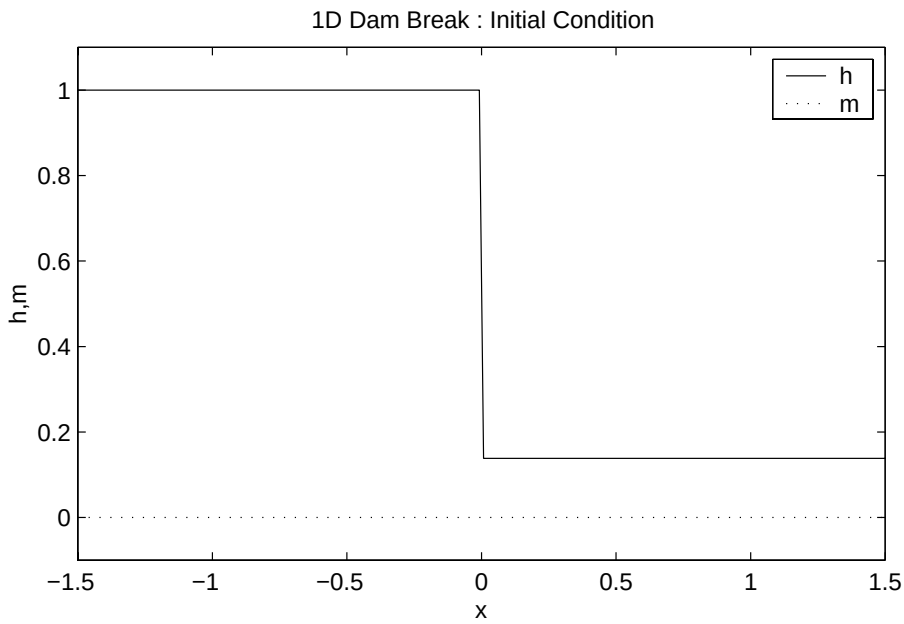

Figure 3.1: 1D Dam Break : Initial Condition

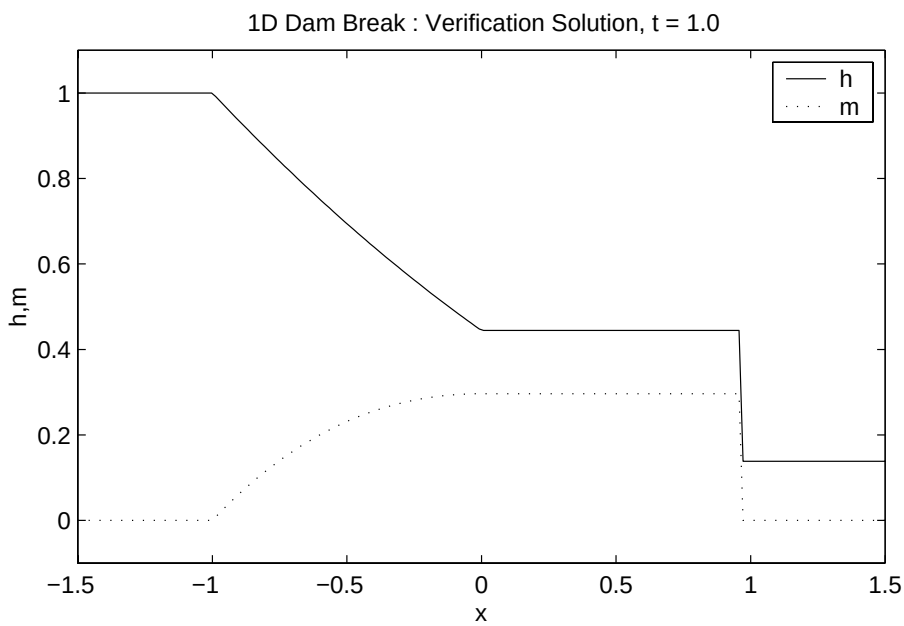

Figure 3.2: 1D Dam Break : Verification Solution ($t = 1.0\ s$)

For a suitable space-time domain

$$(-1 \leq x \leq 1) \text{ and } (0 \leq t \leq 1) \tag{3.8}$$

equations (3.6) and (3.7) indicate the domain boundary values are

$$\begin{aligned} h(-1, 0 \leq t \leq 1) &= h_o \qquad & h(1, 0 \leq t \leq 1) &= 0.13827 h_o \\ m(-1, 0 \leq t \leq 1) &= 0 \qquad & m(1, 0 \leq t \leq 1) &= 0 \end{aligned} \tag{3.9}$$

Thus, mathematically exact Dirichlet boundary conditions are available to be applied to the boundaries of computational domain.

A key feature of the exact solution (3.6, 3.7) is the non-dimensional propagation speed of the hydraulic jump, $u_{jump} = 0.967737309\sqrt{h_o}$, inherent to the x_s definition. Knowing u_{jump} and specifying the values of t, a solution-adapted spatial discretization $\Delta x = u_{jump}\Delta t$ can be constructed such that the exact and computational solutions propagate nodally in tandem. As this propagation velocity is generally not known a priori, the optimized spatial grid will be used only for the discrete L_2 error norm analyses. All other analyses will employ arbitrary spatial meshes and temporal discretizations.

3.2 Dissipation Controller Verification

The first assessment is the effectiveness of the dissipation controller ψ, operating both linearly (constant) and non-linearly (solution dependent). Operating as a constant, low levels of dissipation will not fully stabilize the solution while high levels of dissipation will diffuse the discontinuities. As stated in (2.11), the non-linear operator should deploy the minimum amount of diffusion in smooth, continuous regions, a medium amount at points of slope discontinuity, and the maximum amount at

Table 3.1: 1D Dissipation Controller Verification : Constant Parameters

Parameter	**Value**	
Number of Elements (N)	102	
Courant Number (C)	0.5	
Number Newton Iterations	2	
$2\mu_o$	0.2	
ϵ_{Fr}	0.2	
ψ_{min}	0.25	(non-linear ψ only)
ψ_{max}	1.00	

solution discontinuities. Finally, a fundamental concept in the section on spatial discretization (2.9) is that the dissipation should not affect the solution boundary conditions, hence $\psi(\partial\Omega) = 0$.

All tests were conducted on the solution-adapted grid with the problem parameters held constant as given in Table (3.1).

Five tests were conducted employing constant $\psi = 0.25,\ 0.50,\ 0.75,\ 1.0$ and $\psi = \psi(u)$ where $u = m/h$ is the nodal scalar speed. Note that the values of ψ_{min} and ψ_{max}, for the non-linear evaluation, were not adjusted in any manner. A constant value of $\psi = 0$ is not reported as the solution was completely divergent. Data were extracted at representative times of $t = 0.1,\ 0.2,\ 0.5,\ 0.8$. Solution stabilty and accuracy was qualified through solution plots and quanitified via solution extrema and discrete L_2 error norms where

$$||err_q||_{2,d} = \left(\sum_{j=1}^{N} \int_{\hat{\Omega}} (q^{exact} - q^h)_j^2 d\hat{\Omega} \right)^{1/2} \tag{3.10}$$

Tables (3.2) - (3.5) summarize the results to six decimal places with integer values representing double precision reals with all zeros to the right of the decimal. Results extremized by the non-linear dissipation controller ψ are boldfaced, while non-linear controller ψ results which are nearly

extremized are italicized. It is clear that the unadjusted non-linear controller extremized the error in h and nearly extremized the error in m for all times. Note that the m error was extremized for all times with $\psi = 0.25$. This constant value of ψ, however, resulted in substantial error in h for all times. The overall distribution of h and m from the non-linear controller therefore appears optimal.

Quantifying the values of $h_{min,max}$ and $m_{min,max}$ reveals the amount of under/overshoot inherent to the solutions, hence solution stability. The non-linear controller minimized the overshoot in h_{max} for all times except $t = 0.2$ where it was nearly minimized. Overshoot in m_{max} was minimized for all times by the non-linear controller. Undershoot in h_{min} was nearly minimized by the non-linear controller for all times while the undershoot in m_{min} was not minimized at any time. Values of $\psi = 0.25$ minimized the h_{min} undershoot while increasingly larger constant values of ψ minimized the m_{min} undershoot. Thus, the unadjusted non-linear controller clearly performs well in stabilizing the solution with respect to overshoot but needs improvement to extremize the undershoot.

Table 3.2: 1D Dissipation Controller Verification : Error Norms and Extrema ($t = 0.1\ s$)

t = 0.1		**h results**			**m results**		
Test	ψ	$\|\|err_h\|\|_{2,d}$	h_{min}	h_{max}	$\|\|err_m\|\|_{2,d}$	m_{min}	m_{max}
Theo.	0	0	0.138270	1	0	0	0.296296
1	0.25	0.042985	0.128302	1.000206	0.017826	-0.006437	0.310650
2	0.50	0.039903	0.135262	1.000066	0.022289	-0.002434	0.292748
3	0.75	0.045571	0.134296	1.000086	0.028070	-0.000442	0.289775
4	1.00	0.051421	0.137608	1.000096	0.033416	-0.000128	0.283487
5	$\psi(u)$	**0.032389**	*0.135936*	**1.000050**	*0.019096*	-0.001899	**0.294336**

Table 3.3: 1D Dissipation Controller Verification : Error Norms and Extrema ($t = 0.2\ s$)

t = 0.2		**h results**			**m results**		
Test	ψ	$\|\|err_h\|\|_{2,d}$	h_{min}	h_{max}	$\|\|err_m\|\|_{2,d}$	m_{min}	m_{max}
Theo.	0	0	0.138270	1	0	0	0.296296
1	0.25	0.039844	0.128809	1.000021	0.015880	-0.006512	0.310192
2	0.50	0.035193	0.134842	1.000006	0.022530	-0.001786	0.294426
3	0.75	0.042524	0.134786	1.000004	0.029345	-0.000454	0.293859
4	1.00	0.049791	0.137814	1.000011	0.035240	-0.000131	0.292721
5	$\psi(u)$	**0.027289**	*0.135928*	*1.000006*	*0.018218*	-0.001876	**0.295540**

Table 3.4: 1D Dissipation Controller Verification : Error Norms and Extrema ($t = 0.5\ s$)

t = 0.5		**h results**			**m results**		
Test	ψ	$\|\|err_h\|\|_{2,d}$	h_{min}	h_{max}	$\|\|err_m\|\|_{2,d}$	m_{min}	m_{max}
Theo.	0	0	0.138270	1	0	0	0.296296
1	0.25	0.033048	0.128752	1.000000	0.014218	-0.006487	0.309803
2	0.50	0.030166	0.135187	1.000000	0.022833	-0.001955	0.295626
3	0.75	0.038583	0.135124	1.000000	0.030234	-0.000412	0.295293
4	1.00	0.046440	0.137882	1.000000	0.036608	-0.000088	0.295041
5	$\psi(u)$	**0.022934**	*0.136203*	**1.000000**	*0.017796*	-0.001812	**0.295949**

Table 3.5: 1D Dissipation Controller Verification : Error Norms and Extrema ($t = 0.8\ s$)

t = 0.8		**h results**			**m results**		
Test	ψ	$\|\|err_h\|\|_{2,d}$	h_{min}	h_{max}	$\|\|err_m\|\|_{2,d}$	m_{min}	m_{max}
Theo.	0	0	0.138270	1	0	0	0.296296
1	0.25	0.029083	0.128554	1	0.013606	-0.006403	0.309382
2	0.50	0.028066	0.135571	1	0.022915	-0.002199	0.295885
3	0.75	0.036544	0.135112	1	0.030317	-0.000399	0.295666
4	1.00	0.044405	0.137915	1	0.036705	-0.000088	0.295487
5	$\psi(u)$	**0.021392**	*0.136375*	**1**	*0.017686*	-0.001752	**0.296062**

The complete nodal solutions are plotted at $t = 0.50\ s$, as a representative time station, to qualify the solution behavior. The h solution for $\psi = 0.25$ (Figure 3.3) exhibits serious undershoot in the vicinity of $x = 0$, a clear indicator of inadequate diffusion. This undershoot developed in the early stage of the solution when the discontinuities were near the origin and was propagated through time. The oscillation in h and m at the discontinuity at $x = 0.5$ also supports the lack of adequate diffusion. The "corners" in the h and m solutions are, however, resolved quite crisply. Increasing ψ from 0.25 to 0.50, 0.75 1.00 shows the solution to become more stable at the step discontinuities while overly diffused at the corners.

The non-linear $\psi = \psi(u)$ solution exhibits both solution stability in terms of over/undershoot and accuracy in terms of clear representation of the solution corners. As indicated by the L_2 error characterization, it is clearly the preferred formulation.

Examining the behavior of ψ, it is clear that ψ on the boundaries is zero as the element average value of ψ is halved. For the non-linear ψ test, it is seen to be inducing minimal dissipation in smooth continuous regions, medium dissipation at points of slope discontinuity, and maximum dissipation at points of solution discontinuity. Thus, the dissipation controller is behaving according to theory.

Plotting the time evolution of the error in h and m sheds further insight into the solution behavior. The evolution of $\|err_h\|_{2,d}$, Figure (3.8) is seen to decrease with time for all values of ψ, a prime indicator of solution stability and accuracy. The non-linear controller is clearly the preferred choice for all times. The evolution of $\|err_m\|_{2,d}$, Figure (3.9), is a bit more interesting. The error decreases with respect to time for $\psi = 0.25$ and $\psi = \psi(u)$ and *increases* for all other values of ψ. Thus, the large values of constant dissipation increasingly diffuse the m profile and lead to increasingly inaccurate results. Inappropriate implementation of artificial dissipation is once again shown to be detrimental to computational results.

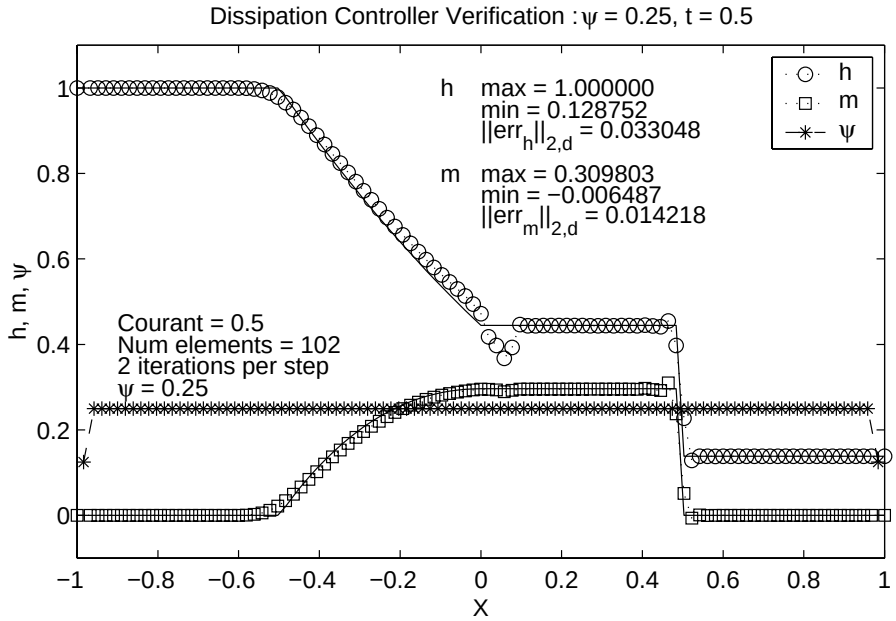

Figure 3.3: 1D Dissipation Controller Verification : $\psi = 0.25$

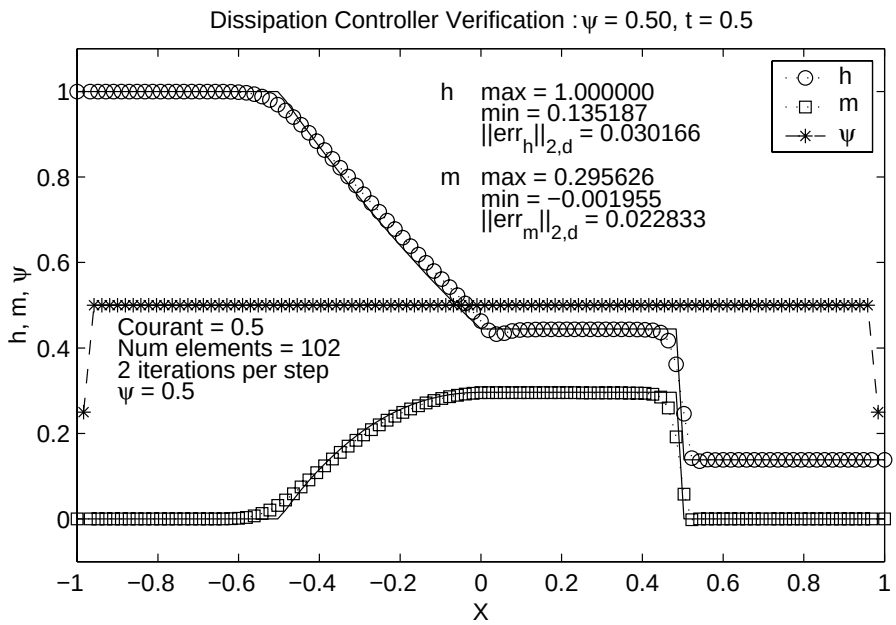

Figure 3.4: 1D Dissipation Controller Verification : $\psi = 0.50$

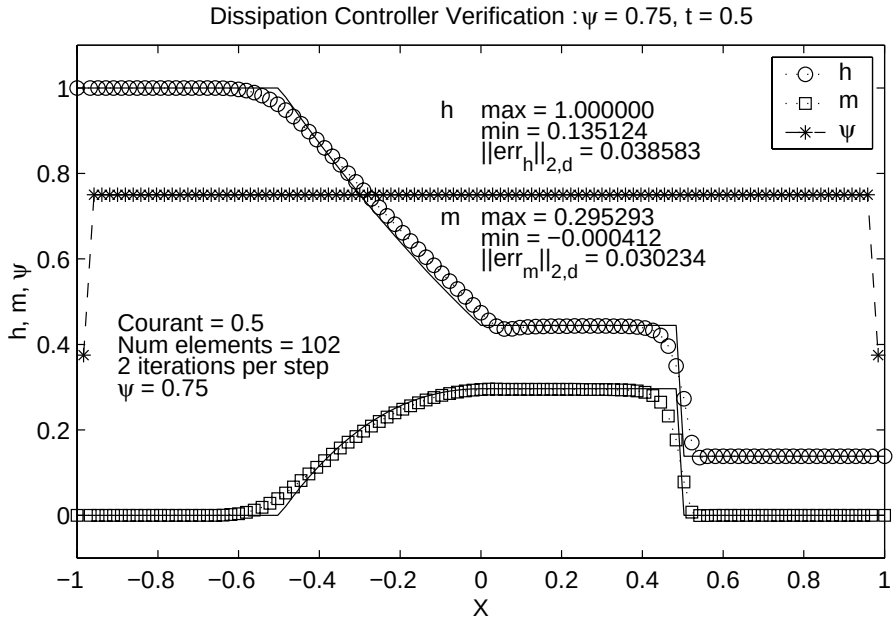

Figure 3.5: 1D Dissipation Controller Verification : $\psi = 0.75$

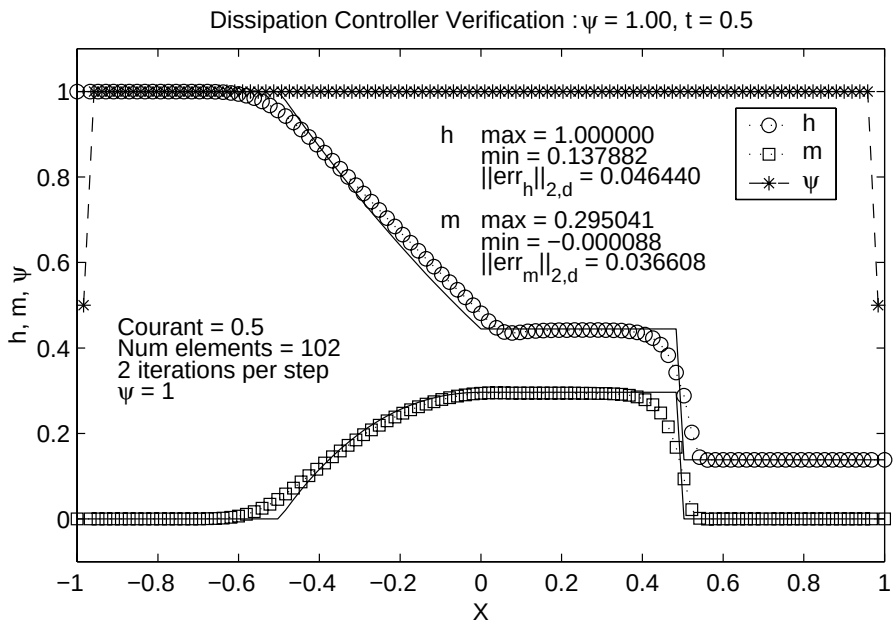

Figure 3.6: 1D Dissipation Controller Verification : $\psi = 1.00$

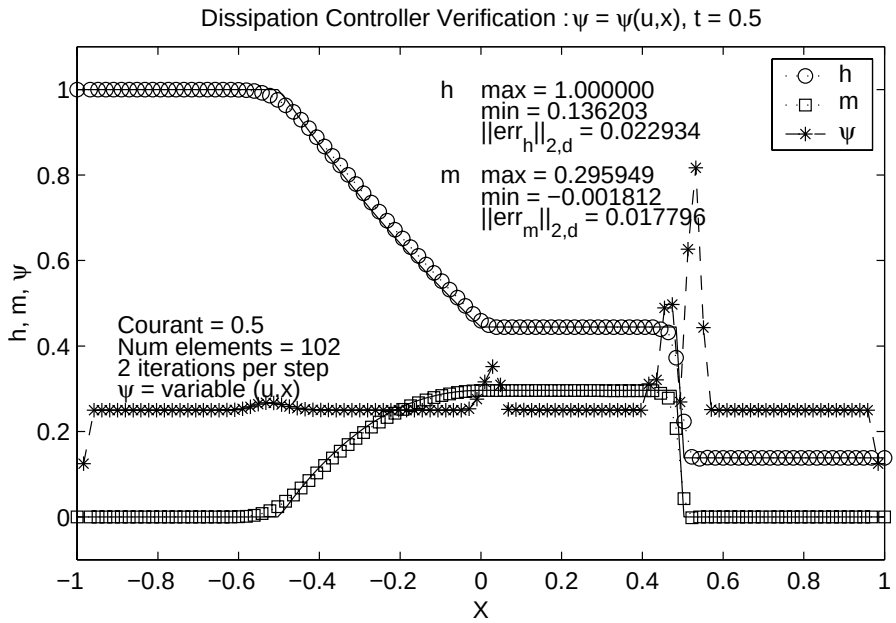

Figure 3.7: 1D Dissipation Controller Verification : $\psi = \psi(u)$

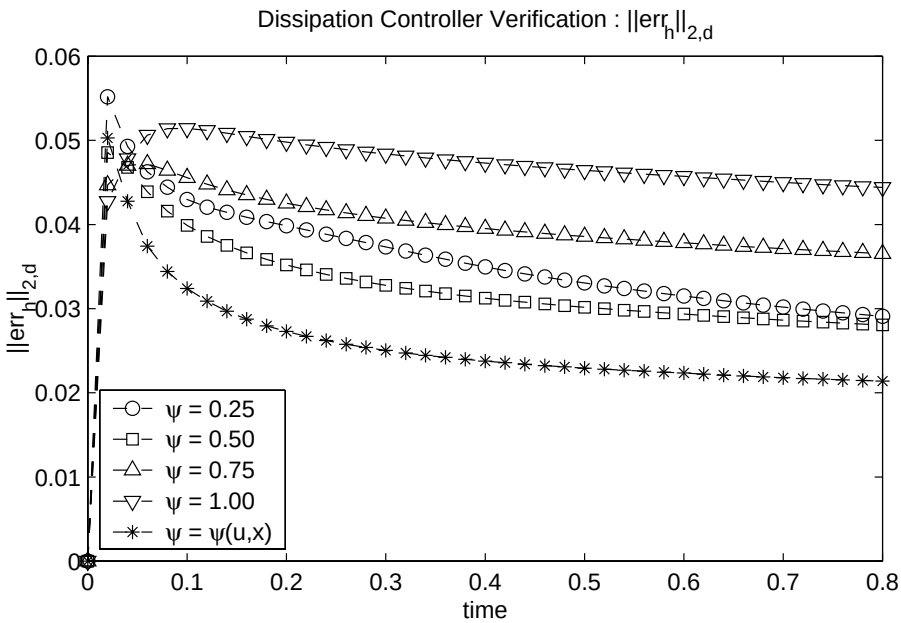

Figure 3.8: 1D Dissipation Controller Verification : h Error Evolution

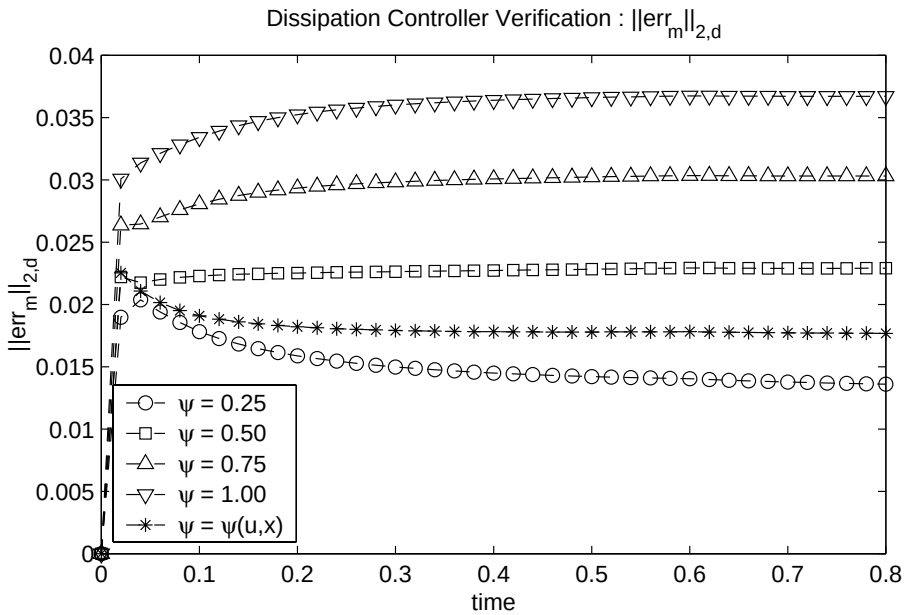

Figure 3.9: 1D Dissipation Controller Verification : m Error Evolution

3.3 Quasi-Newton Algorithm Convergence Study

The next test is to determine the convergence rate of the quasi-Newton iteration algorithm. Recalling Chapter (2.10), a fully Newton jacobian algorithm will converge quadratically. Quasi-Newton formulations will behave anywhere from nearly quadratically convergent to divergent. Having explicitly formed a quasi-Newton iteration construction in Chapter (2.10), iterate convergence and solution impact must be assessed.

For this test, eight iterate values of $max(\delta Q_h, \delta Q_m)$ for the non-linear $\psi = \psi(u)$ were studied at time stations of $t = 0.1,\ 0.2,\ 0.5,\ 0.8\ s$ with the parameters held constant as given in Table (3.1) excluding the number of iterates.

Solution convergence rates, obtained as best straight fit lines to all convergence rates at each time station, are presented in Table (3.6). The iterate solution increments are summarized in

Table 3.6: 1D Quasi-Newton Convergence Verification : $max(\delta Q)$ Convergence Rates

	Best Fit Convergence Rates			
Region	**Iterates**	$max(\delta Q_h)$	**Iterates**	$max(\delta Q_m)$
1	2-3	1.2633	2-4	0.5461
2	3-4	0.2413	4-8	0.9982
3	4-8	0.9925		

Tables (3.7) - (3.8). The convergence in $max(\delta Q_h)$, Figure (3.10), exhibits three distinct regions: an initial sup-linear convergence rate from iteration two to three, a sub-linear convergence rate from iterations three to four, and a linear convergence rate for iterations four through eight. The convergence in $max(\delta Q_m)$, Figure (3.11), exhibits two distinct regions: an intial sub-linear rate for iterations two through four and a linear convergence rate from iterations four through eight. Thus, the quasi-Newton formulation requires several iterations before exhibiting solid linear convergence. The sup-linear convergence in $max(\delta Q_h)$ has an interesting effect on the error norm, discussed next.

Table 3.7: 1D Quasi-Newton Convergence Verification : Iterate $max(\delta Q)$ $(t = 0.1, 0.2\ s)$

	$t = 0.1$		$t = 0.2$	
Iterate	δQ_h^p	δQ_m^p	δQ_h^p	δQ_m^p
1	7.277520e-02	9.085785-02	7.197001e-02	9.030415e-02
2	5.709164e-03	3.489493-03	5.732156e-03	3.361277e-03
3	2.783005e-04	4.468616-04	2.798119e-04	2.750231e-04
4	1.558891e-04	1.812360-04	1.125828e-04	1.296485e-04
5	4.449043e-05	5.297909-05	3.113908e-05	3.712126e-05
6	1.341308e-05	1.592413-05	9.346119e-06	1.109133e-05
7	4.011924e-06	4.765165-06	2.772676e-06	3.292729e-06
8	1.201019e-06	1.426385-06	8.238363e-07	9.782242e-07

Table 3.8: 1D Quasi-Newton Convergence Verification : Iterate $max(\delta Q)$ $(t = 0.5, 0.8\ s)$

	$t = 0.5$		$t = 0.8$	
Iterate	δQ_h^p	δQ_m^p	δQ_h^p	δQ_m^p
1	7.113957e-02	9.044410e-02	7.048387e-02	9.039090e-02
2	7.215832e-03	3.009215e-03	8.158528e-03	3.349686e-03
3	3.255982e-04	5.100549e-04	4.493967e-04	6.602635e-04
4	1.812673e-04	2.102128e-04	2.276852e-04	2.642750e-04
5	5.356483e-05	6.355197e-05	6.938159e-05	8.206960e-05
6	1.669195e-05	1.974841e-05	2.208486e-05	2.606449e-05
7	5.165186e-06	6.113576e-06	6.991534e-06	8.254099e-06
8	1.599727e-06	1.893303e-06	2.214727e-06	2.614518e-06

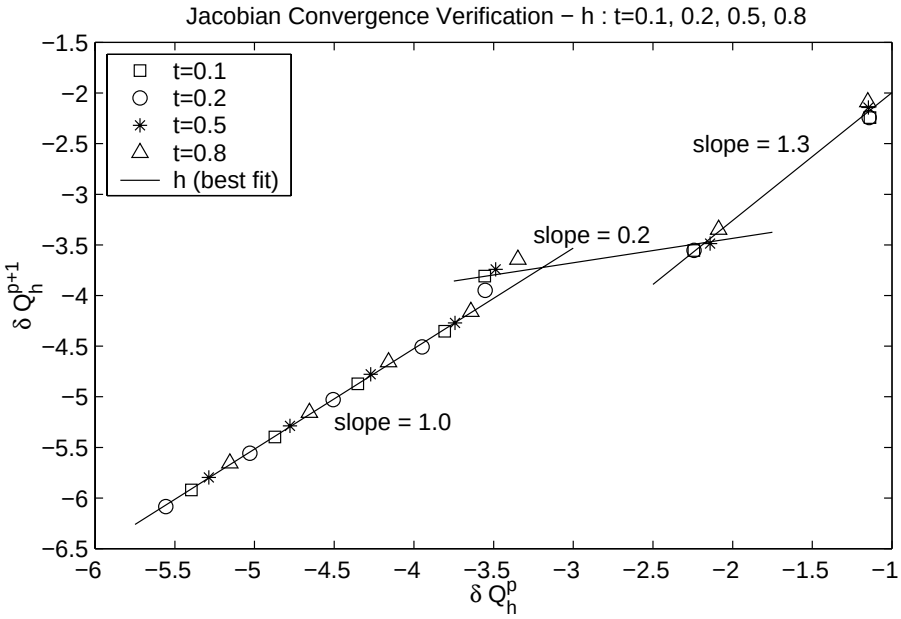

Figure 3.10: 1D Quasi-Newton Convergence Verification : $max(\delta Q_h)$ $(t = 0.1,\ 0.2,\ 0.5,\ 0.8\ s)$

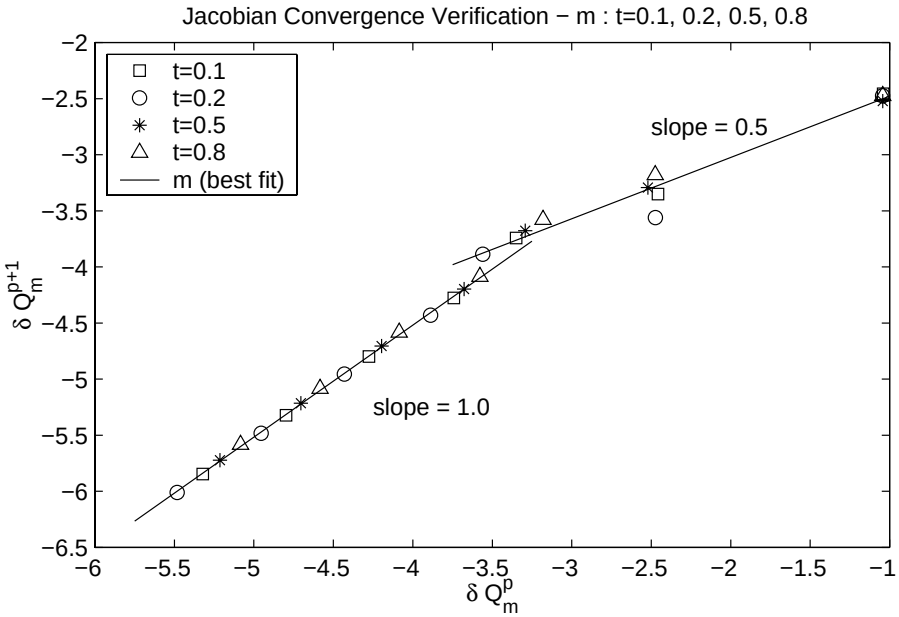

Figure 3.11: 1D Quasi-Newton Convergence Verification : $max(\delta Q_m)$ $(t = 0.1,\ 0.2,\ 0.5,\ 0.8\ s)$

Having quantified the quasi-Newton iteration convergence, solution impact must be assessed. Solution error norms are presented in Tables (3.9) - (3.10) for time stations of $t = 0.1,\ 0.2,\ 0.5,\ 0.8\ s$ for each iterate value. For each time station, the error norm has converged to six significant digits with seven iterations. Three iterations, however, yields a lower error norm than the converged value. Examining the data, the error norm oscillates as it converges with respect to the iterate number: odd iterates have lower error, even iterates have higher. This behavior indicates that three iterations, while not exhibiting convergence in $||err_q||_{2,d}$, yields the lowest solution error for this verification. This is substantiated by the sup-linear convergence rate in $max(\delta Q_h)$ going from iteration two to three. While the convergence rate in $max(\delta Q_m)$ is sub-linear in this region, the highly accurate values of h nonlinearly optimize the values of m as well.

Examining the solution profiles at $t = 0.5\ s$, Figure (3.12), to assess the regions most affected by the iterations reveals no discernable changes. As the qualitative behavior of the m solution is identical to the h solution, only h results are presented. Zooming in on the solution discontinuities, Figures (3.13 - 3.15), shows the change in the solutions with respect to iteration to be insignificant. Hence, not only is two iterations adequate for the mesh and Courant number studied, error norm convergence to four significant digits indicates nearly identical solution profiles.

Table 3.9: 1D Quasi-Newton Convergence Verification : Solution Error Norms ($t = 0.1, 0.2\ s$)

	$t = 0.1$		$t = 0.2$	
Iterations	$\|\|err_h\|\|_{2,d}$	$\|\|err_m\|\|_{2,d}$	$\|\|err_h\|\|_{2,d}$	$\|\|err_m\|\|_{2,d}$
2	0.032389	0.019096	0.027289	0.018218
3	0.032088	0.018847	0.026945	0.017901
4	0.032139	0.018905	0.027019	0.017994
5	0.032122	0.018889	0.026999	0.017969
6	0.032126	0.018893	0.027004	0.017976
7	0.032125	0.018892	0.027003	0.017974
8	0.032125	0.018892	0.027003	0.017974

Table 3.10: 1D Quasi-Newton Convergence Verification : Solution Error Norms ($t = 0.5, 0.8\ s$)

	$t = 0.5$		$t = 0.8$	
Iterations	$\|\|err_h\|\|_{2,d}$	$\|\|err_m\|\|_{2,d}$	$\|\|err_h\|\|_{2,d}$	$\|\|err_m\|\|_{2,d}$
2	0.022934	0.017796	0.021392	0.017686
3	0.022564	0.017493	0.021018	0.017401
4	0.022658	0.017590	0.021117	0.017496
5	0.022632	0.017565	0.021088	0.017471
6	0.022639	0.017572	0.021096	0.017479
7	0.022638	0.017570	0.021094	0.017477
8	0.022638	0.017570	0.021094	0.017477

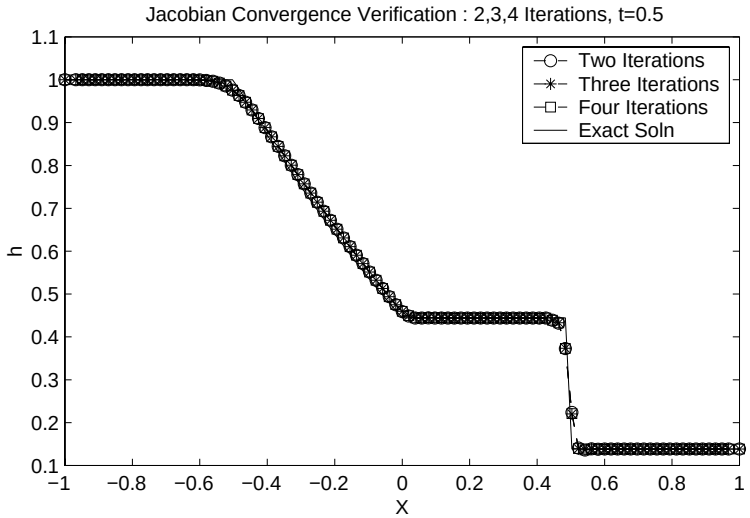

Figure 3.12: 1D Quasi-Newton Convergence Verification : h Profile, 1-3 Iterations, $t = 0.5\ s$

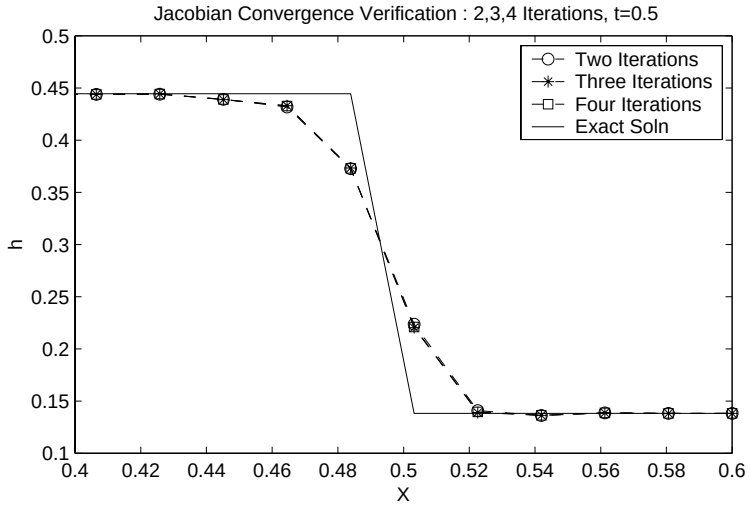

Figure 3.13: 1D Quasi-Newton Convergence Verification : h Profile Zoom-In 1, 1-3 Iterations, $t = 0.5\ s$

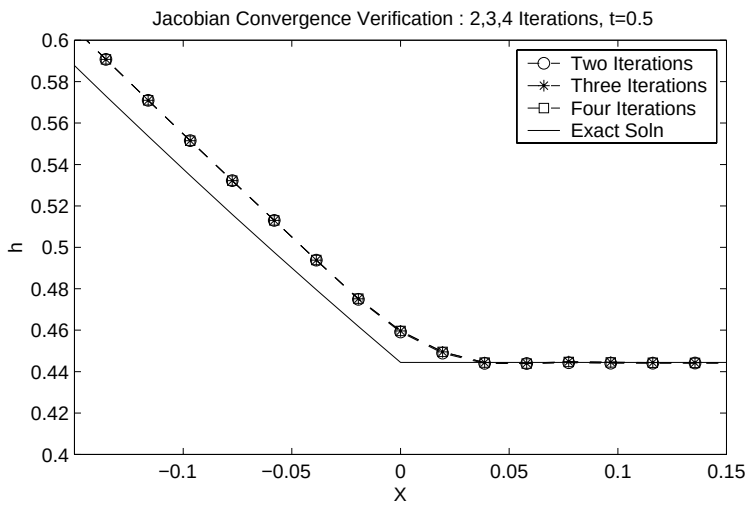

Figure 3.14: 1D Quasi-Newton Convergence Verification : h Profile Zoom-In 2, 1-3 Iterations, $t = 0.5\ s$

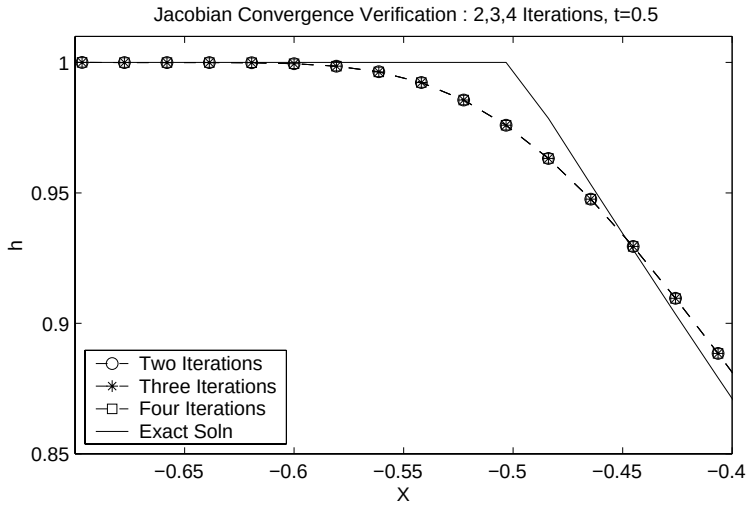

Figure 3.15: 1D Quasi-Newton Convergence Verification : h Profile Zoom-In 3, 1-3 Iterations, $t = 0.5\ s$

3.4 Grid Refinement Study

The final test is to verify solution convergence under spatial and temporal refinement. Oden and Reddy (41) developed the theoretical convergence for the linear initial value problem statement. Application of the linear theory to non-linear problem statements has been repeatedly verified by Baker (14). Error in the finite element approximate solution derives, in Oden's analysis, from

Semidiscrete approximation error	$e^h(x, n\Delta t) = q(x, n\Delta t) - q^h(x, n\Delta t)$
Discrete approximation error	$\sigma(x, n\Delta t) = q(x, n\Delta t) - Q(x, n\Delta t)$
Temporal Truncation error	$\tau(x, n\Delta t) = Q(x, n\Delta t) - q^h(x, n\Delta t)$

For any norm, the triangle inequality yields

$$\|e^h\| = \|\sigma + \tau\| \leq \|\sigma\| + \|\tau\| \tag{3.11}$$

Having extremized the semidiscrete approximation errror via the Galerkin weak statement, the discrete approximation and temporal truncation error are assessed according to

$$\|e^h\|_E \leq C_1 \Delta_e^{2(k+1-m)} \|F(n\Delta t)\|^2_{H^0(\Omega)} + C_2 \Delta t^{f(\theta)} \|Q_0\|_{H^m(\Omega)} \tag{3.12}$$

where the C_α are constants independent of the mesh measure Δ_e, k is the degree of the basis function, $m = 1$ for the parabolic problem statement, and $\|Q_0\|_{H^m}$ is the H^m norm of the initial data interpolation. Recognizing $\|\cdot\|_{H^0}$ to be the L_2 norm of the problem, hence solution energy, it is evident that under refinement the solution error will converge at a rate of $2(k+1-m)$ assuming the temporal truncation error is adequately small. Thus, a refinement convergence study requires that

1. An initial spatial discretization is selected and the transient solution is solved repeatedly with uniform temporal refinements. Upon solution convergence at all time stations, the temporal truncation error has been rendered negligible.

2. The spatial discretization is uniformly refined and (1) is repeated.

3. (2) is repeated until the temporally converged solutions exhibit convergence in spatial discretization.

Three norms are appropriate to assess convergence: the H^0 norm, the Sobolev H^1 norm, and the energy norm.

The H^n norms are defined as

$$\|q\|_{H^n} = H^n(q,q) = \left[\int_\Omega q(x)q(x)\ d\Omega + \sum_{\alpha,\beta=1}^{n} \int_\Omega \frac{\partial^\alpha}{\partial x^\alpha}\frac{\partial^\beta}{\partial x^\beta}\ d\Omega\right]^{1/2} \tag{3.13}$$

where Ω is the entire solution domain, including the boundaries. Heed that the H^n norm is valid for equations where n is less than the degree of the equation. Hence, the H^0 norm is a valid norm for the hyperbolic conservation law while the H^1 norm is not. However, the addition of the characteristics-biased flux divergence parabolizes the equation system and increases the order to two. The impact of this term on the H^1 norm will therefore be assesed.

The energy norm, or energy inner product, is defined via extremization of the linear energy functional for the heat conduction problem as

$$\|Q\|_E = E(Q,Q) = \int_{R^n} \frac{1}{2}\nabla Q \cdot k\nabla Q d\tau + \int_{R^n} \frac{1}{2} hQ^2 d\sigma \tag{3.14}$$

Unlike the H^n norms, it includes the diffusion coefficient, hence problem data, in the norm. Note that the diffusion coefficient is typically a parameter inherent to the physics of the problem, not

Table 3.11: 1D Grid Refinement Verification : Δt Summary

		Δt for Each Grid				
Test	C	25	50	100	200	400
1	0.12500000	1.0000e-02	5.0000e-03	2.5000e-03	1.2500e-03	6.2500e-04
2	0.06250000	5.0000e-03	2.5000e-03	1.2500e-03	6.2500e-04	3.1250e-04
3	0.03125000	2.5000e-03	1.2500e-03	6.2500e-04	3.1250e-04	1.5625e-04
4	0.01562500	1.2500e-03	6.2500e-04	3.1250e-04	1.5625e-04	7.8125e-05
5	0.00781250	6.2500e-04	3.1250e-04	1.5625e-04	7.8125e-05	3.9063e-05
6	0.00390625	3.1250e-04	1.5625e-04	7.8125e-05	3.9063e-05	1.9531e-05

an artificial mechanism. However, it is of interest to measure convergence in this norm, hence the modified equation system, and compare it with convergence in the H^n norms.

For the dam break model, no Robin boundary conditions are applied, thus the convective transfer coefficient $h = 0$. Applying (3.14) to the characteristics-biased parabolic open channel equation system yields

$$\|h\|_E = E(h,h) = \int_{R^n} \frac{1}{2}\nabla h \cdot (\epsilon\psi\alpha\sqrt{gh})\nabla h d\tau \tag{3.15}$$

$$\|m\|_E = E(m,m) = \int_{R^n} \frac{1}{2}\nabla m \cdot (\epsilon\psi\alpha\sqrt{gh})\nabla m d\tau \tag{3.16}$$

Grid discretizations of 25, 50, 100, 200, and 400 elements were considered with initial Courant numbers (C) of 0.125. Temporal convergence was assessed at time stations of $t = 0.1, 0.2, 0.5, 0.8\,s$. Table (3.11) gives the test, discretization, Courant number, and corresponding Δt for each test. All other solution parameters are held constant as given in Table (3.1).

Tables (A.1) - (A.5) present the energy norm temporal convergence data for each spatial discretization respectively. Each table contains the four time stations at which the energy norms were extracted and the respective six temporal refinement tests. Tables (A.6 - A.10) and (A.11 - A.15)

follow an identical format for the H^0 and H^1 norms respectively.

For each discretization and related time station, the sixth temporal discretization, Table (3.11), was selected as the discretization which sufficiently minimizes the temporal truncation error in (3.12). Thus, the error convergence rate becomes effectively a function of the grid refinement. Tables (A.16 - A.19) list the temporally converged energy norms and convergence rates for each mesh at each time station. The Sobolev norms are given in Tables (A.20 - A.23) and (A.24 - A.27).

The final error convergence rates measured in each norm are compiled in Tables (3.12 - 3.14). Studying the convergence in energy norm shows that the grid is insufficient to support an adequate solution for discretizations of 25 and 50 elements. Round-off error is evident in the 400 element solution. The middle slope ranges from 1.0286 to 3.7994 with three of the rates in $e^h(\|m\|_E)$ exceeding quadratic, hence outperforming the theoretical convergence rate. Convergence in the H^0 norm is essentially quadratic for all grids and time stations and is thus less sensitive to the coarse grid solutions and round-off errors. The coarse grid error, $e^h(\|h\|_{H^0})$, clearly outperforms the theoretical prediction of a quadratic convergence rate. The H^1 error is seen to *diverge* at a nearly quadratic rate, hence is an inappropriate norm for measuring error convergence in this minimally dissipative algorithm. More important is the role of the modified statement data in conditioning the energy norm.

Table 3.12: 1D Grid Refinement Verification : Error Convergence Rate in Energy Norm

	$e^h(\|\|h\|\|_E)$				$e^h(\|\|m\|\|_E)$			
Mesh	$t = 0.1$	$t = 0.2$	$t = 0.5$	$t = 0.8$	$t = 0.1$	$t = 0.2$	$t = 0.5$	$t = 0.8$
100	1.6649	1.2161	0.8383	-0.4066	-0.1473	1.3222	0.8367	-2.3910
200	1.1950	1.6950	1.0286	3.7994	1.3813	2.5113	2.3262	2.0948
400	1.8354	-0.7855	-0.8557	-3.1217	2.5020	-2.1221	-2.6374	-1.5024

Table 3.13: 1D Grid Refinement Verification : Error Convergence Rate in H^0 Norm

	$e^h(\|\|h\|\|_{H^0})$				$e^h(\|\|m\|\|_{H^0})$			
Mesh	$t = 0.1$	$t = 0.2$	$t = 0.5$	$t = 0.8$	$t = 0.1$	$t = 0.2$	$t = 0.5$	$t = 0.8$
100	3.4982	3.5705	3.6727	3.7041	1.3905	1.7286	1.8890	1.8518
200	2.0177	1.9931	1.9879	2.0053	1.8046	2.0075	1.9495	1.8918
400	1.9804	1.9732	-9.4605	2.0024	2.0753	2.0344	-10.1355	1.9261

Table 3.14: 1D Grid Refinement Verification : Error Convergence Rate in H^1 Norm

	$e^h(\|\|h\|\|_{H^1})$				$e^h(\|\|m\|\|_{H^1})$			
Mesh	$t = 0.1$	$t = 0.2$	$t = 0.5$	$t = 0.8$	$t = 0.1$	$t = 0.2$	$t = 0.5$	$t = 0.8$
100	-2.7287	-1.6827	-1.8170	-1.7528	-1.3774	-1.8307	-2.1294	-2.0778
200	-1.7827	-2.1226	-2.0230	-2.3197	-1.7914	-2.2352	-2.0319	-2.2703
400	-2.0264	-1.7216	-1.8719	-1.7843	-2.1258	-1.8323	-1.9517	-1.8819

Chapter 4

Theoretical Development, Two Dimensions

This chapter details the development of the characteristics-bias flux for the two-dimensional open channel equations. The non-linear, wave-like solution, developed in [38], is highlighted and followed by the presentation of the open channel flow equations. The celerity and convection limits of the equations system is next investigated with key observations on solution instabilities and eigenvalue limits. The entire open channel flow equation system is then analyzed to extract the inviscid-solution eigenvalues as a function of local Froude number. Additionally, a previously unreported linear dependence issue is documented. The variation of the eigenvalues, via polar plots developed in [38], are presented to identify fundamental propagation modes, denoted mono-axial and bi-modal, of the open channel equations. After having studied the inviscid form of the equation system, the continuum upstream bias approximation is introduced. Under this encompassing theoretical umbrella, two flux jacobian decompositions are presented: one which models mono-axial supercritical flow within the streamline wedge, the other which models bi-modal flow in the celerity limit. A

convex sum of the jacobian decompositions is taken next to form a composite approximation which is valid for all flow regimes. The free parameters introduced in the formulation are solved to enforce both physical consistency of the approximation while simultaneously inducing a stable and accurate dissipative operator. The development of the Galerkin weak statement of the modified equation system and its associated residual and jacobian terms are detailed next. The chapter concludes with the development of the non-linear dissipation controller ψ.

4.1 Non-Linear, Wave-Like Solutions

The two-dimensional open channel flow analysis begins with the consideration of the non-linear wave-like solutions to the generic multi-dimensional hyperbolic conservation law (4.9). As presented in [38], non-linear wave-like solutions take the form of

$$\mathbf{q} = \mathbf{q}(\eta_1) \quad , \quad \eta_1 = \mathbf{x} \cdot \hat{\mathbf{n}} - \lambda(\mathbf{q})t \tag{4.1}$$

where $\hat{\mathbf{n}}$ is a propagation-direction unit vector, independent of $(\mathbf{x}, t)$ and $\lambda = \lambda(\mathbf{q})$ represents a wave-propagation velocity component along the $\hat{\mathbf{n}}$ direction. Several key results, fundamental to the ensuing analyses, are

1. The transformed coordinate system, (η_1, η_2, η_3), is orthogonal like (x_1, x_2, t). Moreover, the η_1 axis direction vector $(\frac{\partial \eta_1}{\partial x_1}, \frac{\partial \eta_1}{\partial x_2}, \frac{\partial \eta_1}{\partial t})$ is parallel to $(n_1, n_2, -\lambda(q))$.

2. The non-linear, wave-like solution is only a function of η_1 upon transformation, hence independent of η_2 and η_3.

3. Upon substituting the transformed coordinate system into the hyperbolic conservation law, the following eigenvalue statement for hyperbolic conservation laws is realized

$$\left(-\lambda(\mathbf{q})\mathbf{I} + \frac{\partial f(\mathbf{q})_j}{\partial \mathbf{q}} n_j\right) \frac{\partial \mathbf{q}}{\partial \eta_1} = 0 \tag{4.2}$$

4. For non-trivial solutions, the eigenvalues of the untransformed hyperbolic equation system become the eigenvalues of the original jacobian contracted along the n_j propagation direction, i.e.

$$-\lambda(\mathbf{q})I + \mathbf{A}_j n_j = 0 \tag{4.3}$$

5. For system stability, the eigenvalues of the dissipative flux vector divergence jacobian must be real and positive.

4.2 Governing Equations and Eigenvalue Analysis

The two-dimensional free surface equations for inviscid flow take the form of

$$\frac{\partial h}{\partial t} + \frac{\partial m_j}{\partial x_j} = 0 \tag{4.4}$$

$$\frac{\partial m_1}{\partial t} + \frac{\partial}{\partial x_j}\left(\frac{m_j}{h} m_1\right) + \frac{\partial}{\partial x_1}\left(g\frac{h^2}{2}\right) = 0 \tag{4.5}$$

$$\frac{\partial m_2}{\partial t} + \frac{\partial}{\partial x_j}\left(\frac{m_j}{h} m_2\right) + \frac{\partial}{\partial x_2}\left(g\frac{h^2}{2}\right) = 0 \tag{4.6}$$

where h denotes the free surface height and, for two-dimensional flows, $1 \leq j \leq 2$ m_j are the momentum state variables aligned with the (x_1, x_2) coordinate directions with summation implied on the j subscripts, and $\mathbf{m} = h\mathbf{u}$ where $\mathbf{u}$ is the local Eularian flow velocity.

Rewriting compactly:

$$\frac{\partial h}{\partial t} + \frac{\partial m_j}{\partial x_j} = 0 \tag{4.7}$$

$$\frac{\partial m_i}{\partial t} + \frac{\partial}{\partial x_j}\left(\frac{m_j}{h} m_i + g\frac{h^2}{2}\delta_i^j\right) = 0 \tag{4.8}$$

where $1 \leq i \leq 2$ are the governing equations for m_1 and m_2 aligned with the (x_1, x_2) coordinate directions.

Casting (4.7, 4.8) in flux vector form, hence recovering the hyperbolic conservation law statement,

$$\frac{\partial \mathbf{q}}{\partial t} + \frac{\partial f_j(\mathbf{q})}{\partial x_j} = 0 \tag{4.9}$$

where

$$\mathbf{q} = \left\{ \begin{array}{c} h \\ m_1 \\ m_2 \end{array} \right\} \quad \text{and} \quad f_j(\mathbf{q}) = \left\{ \begin{array}{c} m_j \\ \frac{m_j}{h} m_1 + g\frac{h^2}{2}\delta_1^j \\ \frac{m_j}{h} m_2 + g\frac{h^2}{2}\delta_2^j \end{array} \right\} \tag{4.10}$$

Casting (4.9) in non-divergence form yields the flux divergence jacobian $\mathbf{A}_j$:

$$\frac{\partial \mathbf{q}}{\partial t} + \mathbf{A}_j \frac{\partial \mathbf{q}}{\partial x_j} = 0 \tag{4.11}$$

where

$$\mathbf{A}_j = \frac{\partial f_j(\mathbf{q})}{\partial \mathbf{q}} = \left[\begin{array}{ccc} 0 & \delta_j^1 & \delta_j^2 \\ -m_1\frac{m_j}{h^2} + gh\delta_j^1 & \frac{1}{h}(m_j + m_1\delta_j^1) & \frac{1}{h}(m_1\delta_j^2) \\ -m_2\frac{m_j}{h^2} + gh\delta_j^2 & \frac{1}{h}(m_2\delta_j^1) & \frac{1}{h}(m_j + m_2\delta_j^2) \end{array} \right] \tag{4.12}$$

with δ_j^i denoting the Kronecker delta function.

Substituting the definition of the fluid velocity $u_j = m_j/h$ yields a simplified form for $\mathbf{A}_j$ as:

$$\mathbf{A}_j = \begin{bmatrix} 0 & \delta_j^1 & \delta_j^2 \\ -u_1 u_j + gh\delta_j^1 & u_j + u_1\delta_j^1 & u_1\delta_j^2 \\ -u_2 u_j + gh\delta_j^2 & u_2\delta_j^1 & u_j + u_2\delta_j^2 \end{bmatrix} \tag{4.13}$$

4.2.1 Celerity Limit

The first part of the two-dimensional analysis is to investigate the behavior of the governing equations in the celerity limit as the norm of the velocity approaches zero. The multi-dimensional Froude number, defined as $Fr = |u|/\sqrt{gh}$ where $|u| = \sqrt{u_j u_j}$ is the velocity magnitude, is key to this analysis. For notational convenience, the celerity term will be expressed, for the limit analyses, as $c = \sqrt{gh}$, hence $Fr = |u|/c$. Establishing the flow direction unit vector v_j, parallel to the the local flow velocity $\mathbf{u}$, allows the reformulation of the velocity $\mathbf{u}$ as a function of the local Froude number via

$$\mathbf{u} = c\, Fr\, \mathbf{v} \tag{4.14}$$

Subsitituting into (4.13) and again into the non-divergence hyperbolic conservation law (4.11) and collecting terms yields

$$\frac{\partial}{\partial t}\begin{Bmatrix} h \\ m_1 \\ m_2 \end{Bmatrix} + \left(\begin{bmatrix} 0 & \delta_j^1 & \delta_j^2 \\ gh\delta_j^1 & 0 & 0 \\ gh\delta_j^2 & 0 & 0 \end{bmatrix} + cFr\mathbf{C}_j \right) \frac{\partial}{\partial x_j}\begin{Bmatrix} h \\ m_1 \\ m_2 \end{Bmatrix} = 0 \tag{4.15}$$

where $\mathbf{C}_j$ denotes the matrix

$$\mathbf{C}_j \equiv \begin{bmatrix} 0 & 0 & 0 \\ -u_1 v_j & v_j + v_1\delta_j^1 & v_1\delta_j^2 \\ -u_2 v_j & v_2\delta_j^1 & v_j + v_2\delta_j^2 \end{bmatrix} \tag{4.16}$$

For vanishing Froude numbers these equations reduce to the celerity equations

$$\frac{\partial}{\partial t}\left\{\begin{array}{c} h \\ m_1 \\ m_2 \end{array}\right\} + \left[\begin{array}{ccc} 0 & \delta_j^1 & \delta_j^2 \\ gh\delta_j^1 & 0 & 0 \\ gh\delta_j^2 & 0 & 0 \end{array}\right] \frac{\partial}{\partial x_j}\left\{\begin{array}{c} h \\ m_1 \\ m_2 \end{array}\right\} = 0 \tag{4.17}$$

for which $\mathbf{A}_j^{cel_o}$ will indicate the celerity jacobian premultiplying the gradient of $\mathbf{q}$ in (4.17).

Per the non-linear, wave-like solution, the solution propagation velocities of the celerity limit of the open-channel equations are dimensional eigenvalues of the matrix $\mathbf{A}_j^{cel_o} n_j$ which are

$$\lambda_1^{d,cel_o} = 0 \quad , \quad \lambda_{2,3}^{d,cel_o} = \pm c \tag{4.18}$$

where the superscript d denotes dimensional.

Recognize these propagation velocities to be independent of the wave-propagation unit vector n_j, thereby correctly reflecting isotropic celerity. Also note eigenvalues $\lambda_{2,3}$ to be exactly the celerity term.

Non-dimensionalizing these eigenvalues by dividing through by the celerity c yields a final key result:

$$\lambda_1^{cel_o} = 0 \quad , \quad \lambda_{2,3}^{cel_o} = \pm 1 \tag{4.19}$$

Thus, in the celerity limit, the non-dimensional eigenvalues are $0, \pm 1$. These results will be employed in the development of the upstream-bias formulation.

Examining the celerity equations in the steady state limit reveals

$$\frac{\partial m_1}{\partial x_1} + \frac{\partial m_2}{\partial x_2} = 0 \tag{4.20}$$

$$gh\frac{\partial h}{\partial x_1} = 0 \tag{4.21}$$

$$gh\frac{\partial h}{\partial x_2} = 0 \tag{4.22}$$

Heed that, per the momentum equations, h must equal a constant and the equations become linearly dependent. Numeric algorithms for the open channel equations in the celerity limit, therefore, will experience numeric difficulties.

This result can also be obtained through the non-linear wave-like solutions. For steady-state, wave-like solutions $q = q(\mathbf{x} \cdot \mathbf{n}) = q(\tilde{\eta}_1)$, equation (4.20) transforms to

$$\frac{\partial m_1}{\partial x_1} + \frac{\partial m_2}{\partial x_2} \Rightarrow \frac{\partial m_1}{\partial \tilde{\eta}_1}\frac{\partial \tilde{\eta}_1}{\partial x_1} + \frac{\partial m_2}{\partial m_2}\frac{\partial \tilde{\eta}_1}{\partial x_2} = \frac{\partial m_1}{\partial \tilde{\eta}_1}n_1 + \frac{\partial m_2}{\partial \tilde{\eta}_1}n_2 = 0 \tag{4.23}$$

revealing the relationship between the momentum divergence components. For the same steady state condition, equations (4.21 - 4.22) become

$$gh\frac{\partial h}{\partial x_1} \Rightarrow gh\frac{\partial h}{\partial \tilde{\eta}_1}\frac{\partial \tilde{\eta}_1}{\partial x_1} = gh\frac{\partial h}{\partial \tilde{\eta}_1}n_1 = 0 \tag{4.24}$$

$$gh\frac{\partial h}{\partial x_2} \Rightarrow gh\frac{\partial h}{\partial \tilde{\eta}_1}\frac{\partial \tilde{\eta}_1}{\partial x_2} = gh\frac{\partial h}{\partial \tilde{\eta}_1}n_2 = 0 \tag{4.25}$$

Note that the celerity momentum equations become linearly dependent upon each other in the steady state, hence posing algorithm convergence problems for this flow state. The two-dimensional characteristics-bias flux must therefore operate to eliminate this linear dependence issue.

4.2.2 Convection Limit

Having investigated the celerity limit of the two-dimensional, inviscid, open channel flow equations, the next extremum, the convection limit, is to be investigated. For convection dominated flows,

hence $Fr \to \infty$, equation (4.15) simplifies to

$$\frac{\partial}{\partial t}\left\{\begin{array}{c} h \\ m_1 \\ m_2 \end{array}\right\} + cFr \left[\begin{array}{ccc} 0 & 0 & 0 \\ -u_1 v_j & v_j + v_1 \delta_j^1 & v_1 \delta_j^2 \\ -u_2 v_j & v_2 \delta_j^1 & v_j + v_2 \delta_j^2 \end{array}\right] \frac{\partial}{\partial x_j}\left\{\begin{array}{c} h \\ m_1 \\ m_2 \end{array}\right\} = 0 \tag{4.26}$$

for which $\mathbf{A}_j^{conv_o}$ will indicate the convection jacobian premultiplying the gradient of $\mathbf{q}$ in (4.26).

Per the non-linear, wave-like solution, the propagation velocities of the convection limit of the open-channel equations are dimensional eigenvalues of the matrix $\mathbf{A}_j^{conv_o} n_j$ which are

$$\lambda_1^{d,conv_o} = 0 \quad , \quad \lambda_2^{d,conv_o} = v_j n_j cFr \quad , \quad \lambda_3^{d,conv_o} = 2 v_j n_j cFr \tag{4.27}$$

Non-dimensionalizing the eigenvalues via division by c

$$\lambda_1^{conv_o} = 0 \quad , \quad \lambda_2^{conv_o} = v_j n_j \; Fr \quad , \quad \lambda_3^{conv_o} = 2 v_j n_j \; Fr \tag{4.28}$$

These eigenvalues are physically inconsistent since, for the convection limit, all solution information propogates at the Froude number. Consider instead the following decomposition of the convection limit jacobian

$$\mathbf{A}_j^{conv_o} = cFr \left(\left[\begin{array}{ccc} 0 & \delta_j^1 & \delta_j^2 \\ -u_1 v_j & v_j + v_1 \delta_j^1 & v_1 \delta_j^2 \\ -u_2 v_j & v_2 \delta_j^1 & v_j + v_2 \delta_j^2 \end{array}\right] + \left[\begin{array}{ccc} 0 & -\delta_j^1 & -\delta_j^2 \\ 0 & 0 & 0 \\ 0 & 0 & 0 \end{array}\right] \right) \tag{4.29}$$

Solving for the eigenvalues for the first term in the composition reveals

$$\lambda_1^{d,conv_o} = v_j n_j cFr \quad , \quad \lambda_2^{d,conv_o} = v_j n_j cFr \quad , \quad \lambda_3^{d,conv_o} = v_j n_j cFr \tag{4.30}$$

while the eigenvalues of the second term are

$$\lambda_1^{d,conv_o} = 0 \quad , \quad \lambda_2^{d,conv_o} = 0 \quad , \quad \lambda_3^{d,conv_o} = 0 \tag{4.31}$$

Non-dimensionalizing the eigenvalues via division by c:

$$\lambda_{1,2,3}^{conv_o} = v_j n_j Fr \quad , \quad \lambda_{1,2,3}^{conv_o} = 0 \tag{4.32}$$

Thus, an additional decomposition of the convection jacobian was required to obtain physically consistent eigenvalues. This procedure will be employed again in later developments.

Examining the convection equations in the steady state limit reveals

$$0 = 0 \tag{4.33}$$

$$-u_1\left(v_1\frac{\partial h}{\partial x_1} + v_2\frac{\partial h}{\partial x_2}\right) + \left(2v_1\frac{\partial m_1}{\partial x_1} + v_2\frac{\partial m_1}{\partial x_2}\right) + v_1\frac{\partial m_2}{\partial x_2} = 0 \tag{4.34}$$

$$-u_2\left(v_1\frac{\partial h}{\partial x_1} + v_2\frac{\partial h}{\partial x_2}\right) + \left(v_1\frac{\partial m_2}{\partial x_1} + 2v_2\frac{\partial m_2}{\partial x_2}\right) + v_2\frac{\partial m_1}{\partial x_1} = 0 \tag{4.35}$$

To investigate linear dependency issues in the convection limit requires that the derivatives of the state variables with respect to η_1 remain bounded for $Fr = \infty$. Unfortunately, no guarantee of this condition currently exists [43]. Under the assumption that the derivatives remain bounded, however, the non-linear wave-like solutions may be employed to assess any linear dependency issues. Thus, for steady-state, wave-like solutions $q = q(\mathbf{x} \cdot \mathbf{n}) = q(\tilde{\eta_1})$, equation (4.33) remains $0 = 0$. Equations (4.34 - 4.35), however, become

$$-u_1\left(v_1\frac{\partial h}{\partial \tilde{\eta_1}}n_1 + v_2\frac{\partial h}{\partial \tilde{\eta_1}}n_2\right) + \left(2v_1\frac{\partial m_1}{\partial \tilde{\eta_1}}n_1 + v_2\frac{\partial m_1}{\partial \tilde{\eta_1}}n_2\right) + v_1\frac{\partial m_2}{\partial \tilde{\eta_1}}n_2 = 0 \tag{4.36}$$

$$-u_2\left(v_1\frac{\partial h}{\partial \tilde{\eta_1}}n_1 + v_2\frac{\partial h}{\partial \tilde{\eta_1}}n_2\right) + \left(v_1\frac{\partial m_2}{\partial \tilde{\eta_1}}n_1 + 2v_2\frac{\partial m_2}{\partial \tilde{\eta_1}}n_2\right) + v_2\frac{\partial m_1}{\partial \tilde{\eta_1}}n_1 = 0 \tag{4.37}$$

Collecting terms reveals

$$-u_1\left(v_1n_1+v_2n_2\right)\frac{\partial h}{\partial\tilde{\eta}_1}+\left(2v_1n_1+v_2n_2\right)\frac{\partial m_1}{\partial\tilde{\eta}_1}+v_1n_2\frac{\partial m_2}{\partial\tilde{\eta}_1} = 0 \tag{4.38}$$

$$-u_2\left(v_1n_1+v_2n_2\right)\frac{\partial h}{\partial\tilde{\eta}_1}+\left(v_1n_1+2v_2n_2\right)\frac{\partial m_2}{\partial\tilde{\eta}_1}+v_2n_1\frac{\partial m_1}{\partial\tilde{\eta}_1} = 0 \tag{4.39}$$

Substituting $v_1n_1+v_2n_2=v_jn_j$ for simplification and rearranging

$$\frac{\partial h}{\partial\tilde{\eta}_1}+\left(\frac{2v_1n_1+v_2n_2}{-u_1v_jn_j}\right)\frac{\partial m_1}{\partial\tilde{\eta}_1}+\left(\frac{v_1n_2}{-u_1v_jn_j}\right)\frac{\partial m_2}{\partial\tilde{\eta}_1} = 0 \tag{4.40}$$

$$\frac{\partial h}{\partial\tilde{\eta}_1}+\left(\frac{v_2n_1}{-u_2v_jn_j}\right)\frac{\partial m_1}{\partial\tilde{\eta}_1}+\left(\frac{v_1n_1+2v_2n_2}{-u_2v_jn_j}\right)\frac{\partial m_2}{\partial\tilde{\eta}_1} = 0 \tag{4.41}$$

Employing the velocity transformation (4.14) to get u_j in terms of v_j yields

$$\frac{\partial h}{\partial\tilde{\eta}_1}+\left(\frac{2v_1n_1+v_2n_2}{-cFr\ v_1v_jn_j}\right)\frac{\partial m_1}{\partial\tilde{\eta}_1}+\left(\frac{v_1n_2}{-cFr\ v_1v_jn_j}\right)\frac{\partial m_2}{\partial\tilde{\eta}_1} = 0 \tag{4.42}$$

$$\frac{\partial h}{\partial\tilde{\eta}_1}+\left(\frac{v_2n_1}{-cFr\ v_2v_jn_j}\right)\frac{\partial m_1}{\partial\tilde{\eta}_1}+\left(\frac{v_1n_1+2v_2n_2}{-cFr\ v_2v_jn_j}\right)\frac{\partial m_2}{\partial\tilde{\eta}_1} = 0 \tag{4.43}$$

Since, for the convection limit, $Fr\rightarrow\infty$ the momentum gradient terms vanish leaving

$$\frac{\partial h}{\partial\tilde{\eta}_1} = 0 \tag{4.44}$$

$$\frac{\partial h}{\partial\tilde{\eta}_1} = 0 \tag{4.45}$$

As with the celerity limit, the momentum equations become linearly dependent in the steady state. More fundamental is that the state variable h does not vary in the η_1 direction.

Recognize that $v_1n_1+v_2n_2=v_jn_j$ and that the inner product of the unit vectors v_jn_j allows the introduction of the cosine of the angle between them, $\cos(\theta-\theta_v)$, where θ and θ_v are the angles measured from the positive x_1 axis to the vectors $\mathbf{n}$ and $\mathbf{v}$ respectively. This implies that when the

propagation velocity is perpendicular to the flow velocity, the convection limit momentum equations (4.36 - 4.37) simplify to

$$(2v_1n_1 + v_2n_2)\frac{\partial m_1}{\partial \tilde{\eta}_1} + v_1n_2\frac{\partial m_2}{\partial \tilde{\eta}_1} = 0 \tag{4.46}$$

$$(v_1n_1 + 2v_2n_2)\frac{\partial m_2}{\partial \tilde{\eta}_1} + v_2n_1\frac{\partial m_1}{\partial \tilde{\eta}_1} = 0 \tag{4.47}$$

Rearranging

$$\frac{\partial m_1}{\partial \tilde{\eta}_1} + \left(\frac{v_1n_2}{2v_1n_1 + v_2n_2}\right)\frac{\partial m_2}{\partial \tilde{\eta}_1} = 0 \tag{4.48}$$

$$\frac{\partial m_1}{\partial \tilde{\eta}_1} + \left(\frac{v_1n_1 + 2v_2n_2}{v_2n_1}\right)\frac{\partial m_2}{\partial \tilde{\eta}_1} = 0 \tag{4.49}$$

For these equations to be linearly independent, the (v_j, n_j) combinations which premultiply the $\partial m_2/\partial \tilde{\eta}_1$ terms can not be equal, hence their ratio can not be unity. The earlier simplification that $\mathbf{n}$ and $\mathbf{v}$ are perpendicular implies that $v_1 = n_2$ and $v_2 = -n_1$. Forming the ratio and substituting:

$$\frac{(v_1n_2)/(2v_1n_1 + v_2n_2)}{(v_1n_1 + 2v_2n_2)/(v_2n_1)} \Rightarrow \frac{(n_2n_2)/(2n_2n_1 - n_1n_2)}{(n_2n_1 - 2n_1n_2)/(-n_1n_1)} \tag{4.50}$$

$$\Rightarrow \frac{n_1^2n_2^2}{n_1^2n_2^2} = 1 \tag{4.51}$$

The momentum equations are therefore linearly dependent and do not admit a unique solution for this special case of the steady-state convection equations. In conclusion, the steady state convection limit momentum equations are linearly dependent for all directions of $\mathbf{v}$ and $\mathbf{n}$ under the assumption that the state variable derivatives with respect ot η_1 remain bounded for $Fr = \infty$. As with the celerity limit, the two-dimensional characteristics-bias flux must operate to eliminate this potential linear dependence issue.

4.2.3 Inviscid Open Channel Flow Equations

Having examined both the celerity and convection limits of the open channel equations, the next step is to obtain the solution-dependent flux jacobian eigenvalues, hence solution propagation velocities, and compare with the celerity/convection extremum values of $Fr = 0, \infty$. The steady state case for the entire inviscid, open channel conservation law system for Froude numbers between the extremum values will then be investigated.

The non-linear wavelike solution yields the eigenvalue statement

$$\left(-\lambda(\mathbf{q})I + \frac{\partial f_j(\mathbf{q})}{\partial \mathbf{q}} n_j\right) \frac{\partial \mathbf{q}}{\partial \eta_1} = 0 \tag{4.52}$$

Seeking non-trivial solutions, i.e $\mathbf{q} = \mathbf{q}(\eta_1)$, the propagation velocities are the eigenvalues of the flux jacobian (4.13) contracted along the propagation directions via $\mathbf{A}_j n_j$:

$$\mathbf{A}_j n_j = \begin{bmatrix} 0 & n_1 & n_2 \\ -u_1(u_1 n_1 + u_2 n_2) + ghn_1 & 2u_1 n_1 + u_2 n_2 & u_1 n_2 \\ -u_2(u_1 n_1 + u_2 n_2) + ghn_2 & u_2 n_1 & u_1 n_1 + 2u_2 n_2 \end{bmatrix} \tag{4.53}$$

Solving for the dimensional eigenvalues, denoted λ_j^{doc} to signify dimensional open-channel, gives

$$\begin{aligned} \lambda_1^{doc} &= u_1 n_1 + u_2 n_2 &&= u_j n_j \\ \lambda_{2,3}^{doc} &= u_1 n_1 + u_2 n_2 \pm \sqrt{gh} &&= u_j n_j \pm \sqrt{gh} \end{aligned} \tag{4.54}$$

As with the celerity limit analysis, casting the flow velocity $\mathbf{u}$ as a funtion of the local Froude number Fr, celerity c, and the flow direction unit vector $\mathbf{v}$, courtesy (4.14), simplifies the eigenvalues to

$$\lambda_1^{doc} = v_j n_j c Fr \quad \Rightarrow \quad \lambda_1^{OC} = v_j n_j Fr \tag{4.55}$$

$$\lambda_{2,3}^{doc} = v_j n_j c Fr \pm c \quad \Rightarrow \quad \lambda_{2,3}^{OC} = v_j n_j Fr \pm 1 \tag{4.56}$$

where λ_j^{OC} denotes the non-dimensional propagation velocities, obtained by dividing the dimensional eigenvalues by the celerity term. For clarification, the eigenvalue λ_1^{OC} shall be henceforth referred to as the *open channel convection eigenvalue* while eigenvalues $\lambda_{2,3}^{OC}$ shall be called the *open channel celerity-convection eigenvalues.* Furthermore, the curve generated by $\lambda_1^{OC} = v_j n_j Fr$ shall be called *open channel convection curve* while the curves generated by $\lambda_{2,3}^{OC} = v_j n_j Fr \pm 1$ shall be called *open channel celerity-convection curves.* These curves will be investigated in Section (4.3).

Substituting $v_j n_j = \cos(\theta - \theta_v)$

$$\lambda_1^{OC} = \cos(\theta - \theta_v) Fr \quad , \quad \lambda_{2,3}^{OC} = \cos(\theta - \theta_v) Fr \pm 1 \tag{4.57}$$

This form of the eigenvalues implies that the propagation velocities are extremized for $\theta = \pm\theta_v$, i.e. when $\mathbf{n}$ is aligned with the *streamwise* direction, and that the propagation velocities are independent of Fr when $\theta \perp \theta_v$, i.e. when $\mathbf{n}$ is aligned with the *crossflow* direction. The streamline open channel eigenvalues, fundamental to the development of the upstream characteristices flux, are thus

$$\lambda_1^{OC_{sl}} = Fr \quad , \quad \lambda_{2,3}^{OC_{sl}} = Fr \pm 1 \tag{4.58}$$

Note that $\lambda_{2,3}^{OC_{sl}}$ are identical to the one-dimensional eigenvalues. Following [38], the variation in the characteristic velocities with respect to $\theta - \theta_v$ and Fr are investigated with polar plots in the following section (4.3).

Determining the values of θ for which the eigenvalues vanish reveals additional mathematical and physical character of the solution. Mathematically, the values of θ for which the eigenvalues vanish represent a direction which marks the boundary between two regions where the eigenvalues have differing sign. These regions are key to the ensuing determination of flowfield propagation modes,

Section (4.3). From a physical perspective, for the convection eigenvalue λ_1^{OC}, the value is zero for $\cos(\theta - \theta_v) = 0$. This occurs when $\theta \perp \theta_v$ or, equivalently, when $\mathbf{n}$ is aligned with the crossflow direction. For the celerity-convection eigenvalues $\lambda_{2,3}^{OC}$, $|\cos(\theta - \theta_v)| \leq 1$, hence these eigenvalues can only vanish for $(Fr \geq 1)$. For these supercritical flows,

$$\lambda_{2,3}^{OC} = 0 \quad \rightarrow \quad \mp \cos(\theta - \theta_v) = \frac{1}{Fr} \tag{4.59}$$

From the definition of the Froude line [2], analagous to the Mach line in compressible flow theory,

$$\pm \sin(\theta_{Fr}) = \frac{1}{Fr} \tag{4.60}$$

where θ_{Fr} is the angle between the streamline and a Froude line. Using a trigonometric substitution

$$\mp \cos(\theta - \theta_v) = \pm \sin((\theta - 90^{\cdot}) - \theta_v) = \frac{1}{Fr} \tag{4.61}$$

Thus, the celerity-convection eigenvalues are zero for $\mathbf{n}$ perpendicular to the Froude lines. These lines are henceforth denoted the *conjugate* lines. These lines segregate the supercritical flow fields in which the eigenvalues have differing signs. In conclusion, the lines perpendicular to $\mathbf{n}$, for vanishing values of λ_1^{OC} and $\lambda_{2,3}^{OC}$, are the streamline and Froude lines respectively. For all subcritical flows, the Froude and conjugate lines do not exist, while for supercritical flows, the conjugate lines are perpendicular to the Froude lines as described. As the Froude number increases, the Froude lines approach the streamline direction and the conjugate lines approach the crossflow direction.

For steady state, equation (4.11) becomes

$$\begin{bmatrix} 0 & \delta_j^1 & \delta_j^2 \\ -u_1 u_j + gh\delta_j^1 & u_j + u_1\delta_j^1 & u_1\delta_j^2 \\ -u_2 u_j + gh\delta_j^2 & u_2\delta_j^1 & u_j + u_2\delta_j^2 \end{bmatrix} \frac{\partial}{\partial x_j} \begin{Bmatrix} h \\ m_1 \\ m_2 \end{Bmatrix} = 0 \tag{4.62}$$

Expanding

$$\frac{\partial m_1}{\partial x_1} + \frac{\partial m_2}{\partial x_2} = 0 \tag{4.63}$$

$$\left(-u_1\left(u_1\frac{\partial h}{\partial x_1} + u_2\frac{\partial h}{\partial x_2}\right) + gh\frac{\partial h}{\partial x_1}\right) + \left(2u_1\frac{\partial m_1}{\partial x_1} + u_2\frac{\partial m_1}{\partial x_2}\right) + \left(u_1\frac{\partial m_2}{\partial x_2}\right) = 0 \tag{4.64}$$

$$\left(-u_2\left(u_1\frac{\partial h}{\partial x_1} + u_2\frac{\partial h}{\partial x_2}\right) + gh\frac{\partial h}{\partial x_2}\right) + \left(u_1\frac{\partial m_2}{\partial x_1} + 2u_2\frac{\partial m_2}{\partial x_2}\right) + \left(u_2\frac{\partial m_1}{\partial x_1}\right) = 0 \tag{4.65}$$

For steady-state, wave-like solutions $q = q(\mathbf{x}\cdot\mathbf{n}) = q(\tilde{\eta_1})$, equations (4.63 - 4.65) transform to

$$\frac{\partial m_1}{\partial \tilde{\eta_1}}n_1 + \frac{\partial m_2}{\partial \tilde{\eta_1}}n_2 = 0 \tag{4.66}$$

$$-u_1\left(u_1\frac{\partial h}{\partial \tilde{\eta_1}}n_1 + u_2\frac{\partial h}{\partial \tilde{\eta_1}}n_2\right) + gh\frac{\partial h}{\partial \tilde{\eta_1}}n_1 + 2u_1\frac{\partial m_1}{\partial \tilde{\eta_1}}n_1 + u_2\frac{\partial m_1}{\partial \tilde{\eta_1}}n_2 + u_1\frac{\partial m_2}{\partial \tilde{\eta_1}}n_2 = 0 \tag{4.67}$$

$$-u_2\left(u_1\frac{\partial h}{\partial \tilde{\eta_1}}n_1 + u_2\frac{\partial h}{\partial \tilde{\eta_1}}n_2\right) + gh\frac{\partial h}{\partial \tilde{\eta_1}}n_2 + u_1\frac{\partial m_2}{\partial \tilde{\eta_1}}n_1 + 2u_2\frac{\partial m_2}{\partial \tilde{\eta_1}}n_2 + u_2\frac{\partial m_1}{\partial \tilde{\eta_1}}n_1 = 0 \tag{4.68}$$

Collecting terms

$$n_1\frac{\partial m_1}{\partial \tilde{\eta_1}} + n_2\frac{\partial m_2}{\partial \tilde{\eta_1}} = 0 \tag{4.69}$$

$$\left(-u_1(u_1n_1 + u_2n_2) + ghn_1\right)\frac{\partial h}{\partial \tilde{\eta_1}} + \left(2u_1n_1 + u_2n_2\right)\frac{\partial m_1}{\partial \tilde{\eta_1}} + u_1n_2\frac{\partial m_2}{\partial \tilde{\eta_1}} = 0 \tag{4.70}$$

$$\left(-u_2(u_1n_1 + u_2n_2) + ghn_2\right)\frac{\partial h}{\partial \tilde{\eta_1}} + u_2n_1\frac{\partial m_1}{\partial \tilde{\eta_1}} + \left(u_1n_1 + 2u_2n_2\right)\frac{\partial m_2}{\partial \tilde{\eta_1}} = 0 \tag{4.71}$$

Substituting $u_1n_1 + u_2n_2 = u_jn_j$ and the velocity transform (4.14)

$$
\begin{aligned}
n_1 \frac{\partial m_1}{\partial \tilde{\eta}_1} + n_2 \frac{\partial m_2}{\partial \tilde{\eta}_1} &= 0 \quad (4.72) \\
\left(-(cFr)^2 n_1 v_j n_j + ghn_1\right) \frac{\partial h}{\partial \tilde{\eta}_1} + \left(2cFrv_1 n_1 + cFrv_2 n_2\right) \frac{\partial m_1}{\partial \tilde{\eta}_1} + cFrv_1 n_2 \frac{\partial m_2}{\partial \tilde{\eta}_1} &= 0 \quad (4.73) \\
\left(-(cFr)^2 n_2 v_j n_j + ghn_2\right) \frac{\partial h}{\partial \tilde{\eta}_1} + cFrv_2 n_1 \frac{\partial m_1}{\partial \tilde{\eta}_1} + \left(cFrv_1 n_1 + 2cFrv_2 n_2\right) \frac{\partial m_2}{\partial \tilde{\eta}_1} &= 0 \quad (4.74)
\end{aligned}
$$

Rearranging

$$
\begin{aligned}
n_1 \frac{\partial m_1}{\partial \tilde{\eta}_1} + n_2 \frac{\partial m_2}{\partial \tilde{\eta}_1} &= 0 \quad (4.75) \\
\frac{\partial h}{\partial \tilde{\eta}_1} + \left(\frac{2cFrv_1 n_1 + cFrv_2 n_2}{-(cFr)^2 n_1 v_j n_j + ghn_1}\right) \frac{\partial m_1}{\partial \tilde{\eta}_1} + \left(\frac{cFrv_1 n_2}{-(cFr)^2 n_1 v_j n_j + ghn_1}\right) \frac{\partial m_2}{\partial \tilde{\eta}_1} &= 0 \quad (4.76) \\
\frac{\partial h}{\partial \tilde{\eta}_1} + \left(\frac{cFrv_2 n_1}{-(cFr)^2 n_2 v_j n_j + ghn_2}\right) \frac{\partial m_1}{\partial \tilde{\eta}_1} + \left(\frac{cFrv_1 n_1 + 2cFrv_2 n_2}{-(cFr)^2 n_2 v_j n_j + ghn_2}\right) \frac{\partial m_2}{\partial \tilde{\eta}_1} &= 0 \quad (4.77)
\end{aligned}
$$

It is clear that the continuity equation (4.75) is linearly independent from the momentum equations (4.76 - 4.77). To insure that momentum equations are linearly independent, the ratio of the coefficients preceeding the momentum derivatives must not equal unity. Hence

$$
\frac{(2cFrv_1 n_1 + cFrv_2 n_2)/(-(cFr)^2 n_1 v_j n_j + ghn_1)}{(cFrv_2 n_1)/(-(cFr)^2 n_2 v_j n_j + ghn_2)} \neq 1 \quad (4.78)
$$

$$
\frac{(cFrv_1 n_2)/(-(cFr)^2 n_1 v_j n_j + ghn_1)}{(cFrv_1 n_1 + 2cFrv_2 n_2)/(-(cFr)^2 n_2 v_j n_j + ghn_2)} \neq 1 \quad (4.79)
$$

Simplifying

$$
Fr^2 v_j n_j \neq 1 \quad (4.80)
$$

$$
Fr^2 v_j n_j \neq 1 \quad (4.81)
$$

Since $v_j n_j = \cos(\theta - \theta_n)$ and $0 \leq \|\cos(\theta)\| \leq 1$, the equations remain linearly independent for all

values $Fr < 1$. For critical and supercritical flows, the equations become linearly dependent along the lines defined by

$$\cos(\theta - \theta_v) = \frac{1}{Fr^2} \tag{4.82}$$

These lines, denoted *dependency* lines, give considerable insight to why numeric instabilities arise in purely inviscid open channel flows experiencing critical and supercritical flows. As with the celerity and convection limit, the two-dimensional characteristics-bias flux must operate to eliminate this linear dependence issue.

4.2.4 Linear Dependency / Eigenvalue Summary

The results of the three previous analyses are summarized in Table (4.1) for convenience. Heed that the linear dependence issue for the convection limit rests upon the assumption that the state variable derivatives with respect to η_1 remain bounded for $Fr = \infty$.

Table 4.1: Eigenvalue / Linear Dependence Summary

		Celerity Limit	**Convection Limit**	**Open Channel**
Froude Number		$Fr = 0$	$Fr = \infty$	$0 < Fr < \infty$
Eigenvalues	λ_1	0	$v_j n_j Fr$	$v_j n_j Fr$
	λ_2	$+1$	$v_j n_j Fr$	$v_j n_j Fr + 1$
	λ_3	-1	$v_j n_j Fr$	$v_j n_j Fr - 1$
Steady State Linear Dependency		unconditionally dependent $\forall\ v_j n_j$	unconditionally dependent $\forall\ v_j n_j$	conditionally dependent $\forall\ v_j n_j = 1/Fr^2$

4.3 Polar Variation of Characteristic Speeds

Section (4.2.3) concluded with the identification of the solution propagation velocity unit vector $\mathbf{n}$ to be perpendicular to the streamline and Froude lines for select values of θ such that the eigenvalues vanish. Considerable insight is gained through plots of the polar variation of the eigenvalues for all values of θ, as introduced in [38]. Figures (4.1) - (4.6) present these variations for subcritical, critical, and supercritical Froude numbers for an arbitray flow field point P in the (x_1, x_2) plane. The variations presented are for a variable characteristic direction unit vector $(n_1, n_2) = (\cos\theta, \sin\theta)$ and a fixed local flow velocity unit vector (v_1, v_2) inclined at $+30^{\cdot}$ with respect to the x_1 axis.

Figures (4.1) - (4.6) present the absolute values of the eigenvalues for the subsequent identification of the primary propagation axes for Froude numbers of $Fr = 0, 0.05, 0.5, 1, 1.5, 2$. Figures (4.7) - (4.12) present individual plots of absolute values of the eigenvalues and their associated sign for the identification of propagation modes. Figure (4.13) - (4.14) conclude the section with a summary of eigenvalue signs for subcritical and supercritical flow and the identification of the wedge regions key to the development of the characteristics bias flux. All figures include the streamline direction $\mathbf{v}$ and the crossflow direction $\mathbf{v}^N$. In addition, all supercritical figures include the conjugate lines denoted by $\mathbf{C}$.

Studying figures (4.1) - (4.6) reveals four features for all Froude numbers:

1. The maximum characteristic speed occurs in the flow velocity direction, hence along a streamline.

2. Along the cross-flow direction, $|\lambda_1^{OC}| = 0$ and $|\lambda_{2,3}^{OC}| = 1$, hence only $\lambda_{2,3}^{OC}$ propogate information in this direction. Moreover, this propagation mode is pure celerity.

3. All characteristic speeds are distributed symmetrically about the flow velocity direction.

4. Mirror-skew symmetry about the cross-flow direction is displayed by $|\lambda_1^{OC}|$ and by $(|\lambda_2^{OC}|, |\lambda_3^{OC}|)$.

This means that, with respect to the cross-flow axis, $|\lambda_1^{OC}|$ is a mirror image of itself and $|\lambda_3^{OC}|$ is a mirror image of $|\lambda_2^{OC}|$.

The streamline and crossflow directions are therefore the two principal wave propagation axes.

For vanishing Froude numbers, the convection curve degenerates to a point centered at P while celerity-convection curves approach circles with radius of one centered at point P. As such, the celerity-convection curves become isotropic and thus correctly represent the direction-invariant propagation of celerity waves. As the Froude number increases, the convection curves become two identical circles tangent at P and aligned with the streamline direction. Heed that the eigenvalues have opposite signs and thus correctly represent pure convection. The celerity-convection curves become increasingly anisotropic, hence correctly reflecting the addition of convection effects in the solution propagation velocities.

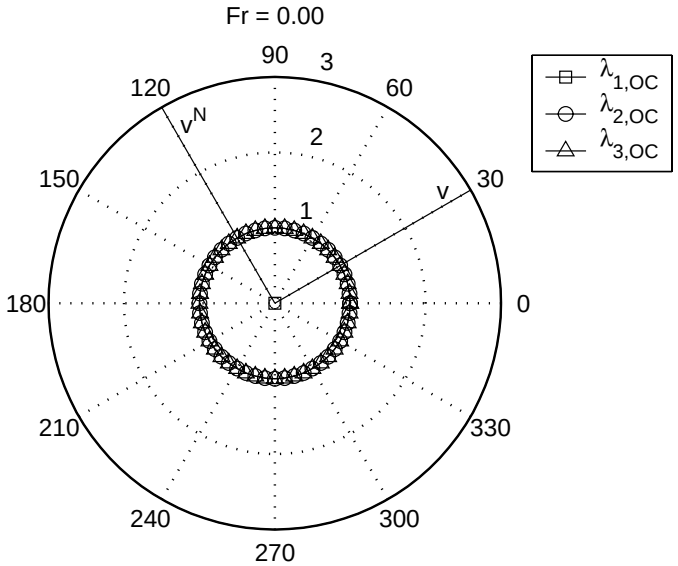

Figure 4.1: Polar Variation of Propagation Speeds : $Fr = 0.00$

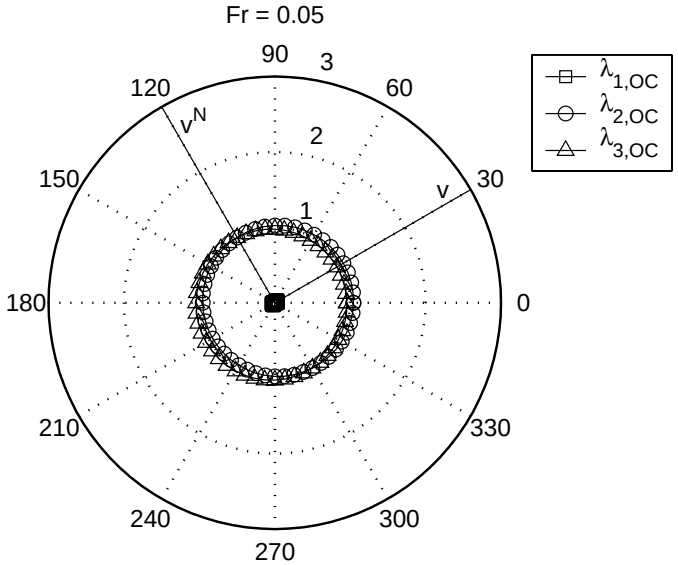

Figure 4.2: Polar Variation of Propagation Speeds : $Fr = 0.05$

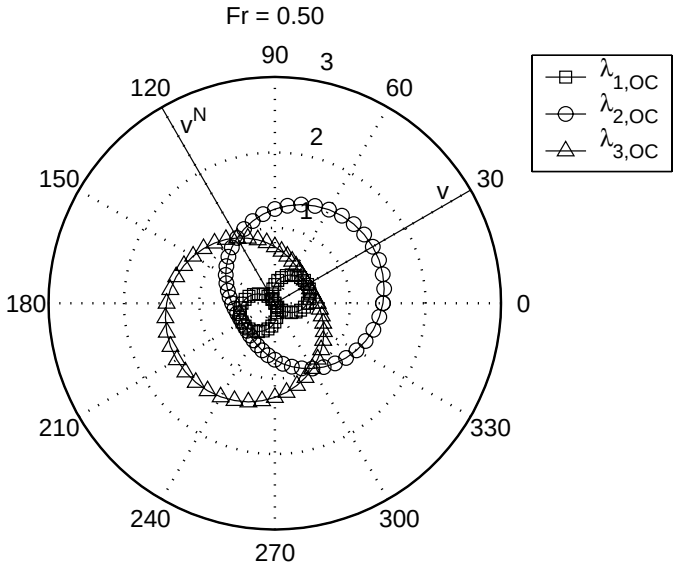

Figure 4.3: Polar Variation of Propagation Speeds : $Fr = 0.50$

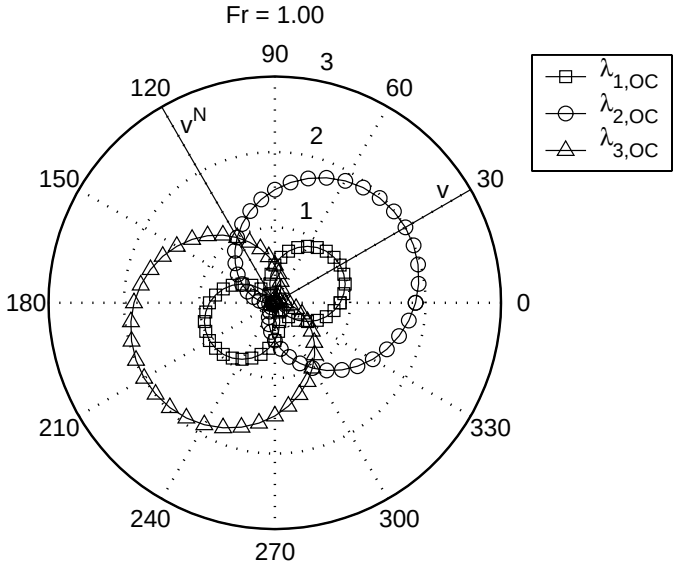

Figure 4.4: Polar Variation of Propagation Speeds : $Fr = 1.00$

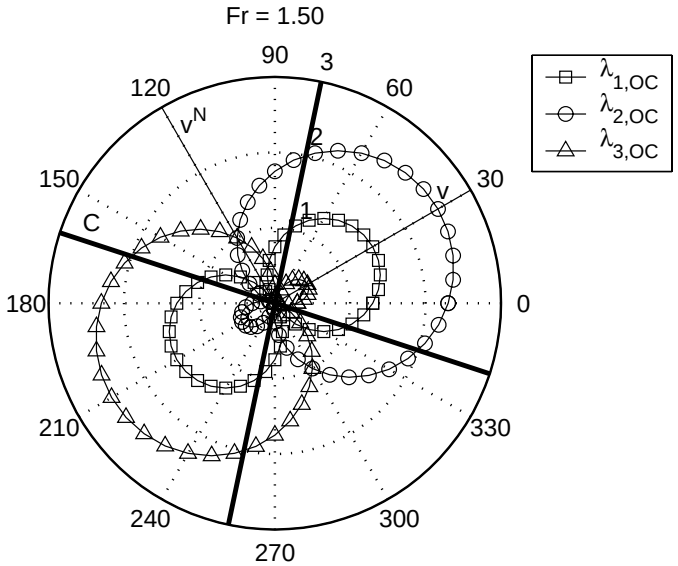

Figure 4.5: Polar Variation of Propagation Speeds : $Fr = 1.50$

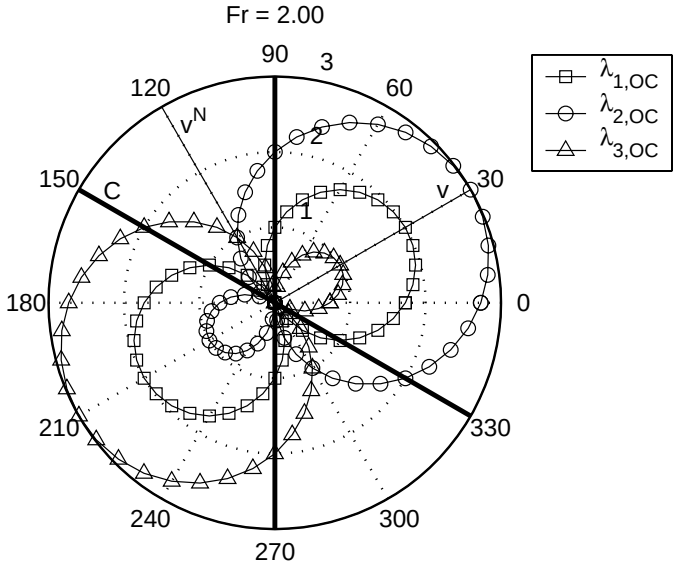

Figure 4.6: Polar Variation of Propagation Speeds : $Fr = 2.00$

Studying the sign of the eigenvalues and their associated directions reveals further information about the field behavior of the propagation modes. Note that, for an arbitrary flowfield point P, positive eigenvalues correspond to propagation that radiates from the point P outwards whereas negative eigenvalues correspond to propatation that radiates inwards towards P. For demonstrative purposes, each eigenvalue is plotted individually for $Fr = 0.5, 2.0$ to represent subcritical and supercritical behavior respectively. Two propagation modes are recognized from the polar plots: *mono-axial* and *bi-modal*. These modes give considerable insight into the propagation mechanisms of the two-dimensional flow field as a function of both eigenvalue and Froude number. Moreover, for supercritical flows, the conjugate lines define two key flow subfields, based on the sign of the eigenvalues within these fields, denoted the *streamline wedge* and the *crossflow wedge*. The primary axes of these wedge regions are the streamline and crossflow directions respectively.

The mono-axial mode is indicative of convection dominated propagation. For all values of Fr, the convection eigenvalue λ_1^{OC} experiences a change in sign when the $\mathbf{n}$ direction crosses the crosflow axis, i.e. shifts from pointing upstream to pointing downstream with respect to the flow direction $\mathbf{v}$. The convection curve therefore crosses the polar origin as the magnitude of λ_1^{OC} is zero as stated in the previous section. The (negative) eigenvalues within the upstream circle all point towards P while the (positive) eigenvalues within the downstream circle all point away from P. Decomposing the eigenvalues into streamline and crossflow components, the streamline components for all $\mathbf{n}$ point in the downstream direction, hence exhibit a mono-axial propagation along the streamline axis.

Beginning with the critical point and extending through super-critical flow, the celerity-convection curves also exhibit mono-axial character. Unlike the convection eigenvalues, the celerity-convection eigenvalues change signs when $\mathbf{n}$ cross the conjugate lines. The curves, nevertheless, cross the polar origin and the propagation axis is the streamline.

The bi-modal mode reflects celerity driven propagation. For sub-critical flow, the celerity-

convection eigenvalues $\lambda_{2,3}^{OC}$ do not experience a change in sign going from downstream to upstream. Rather, λ_2^{OC} remains positive and λ_3^{OC} negative for all directions $\mathbf{n}$. As such, both curves contain the polar origin. Decomposing the eigenvalues into streamline and crossflow components, the streamline components are positive and negative for both eigenvalues. Therefore, for sub-critical flow, the celerity-convection information propogates bi-modally along the streamline axis, from upstream and downstream toward and away from P for all values of $\mathbf{n}$.

With regard to the ideas of *domains of dependence* and *regions of influence* from classical gas dynamics [46], the signs of the eigenvalues, and hence their propagation directions, indicate identical regions for the open channel equations. Studying the subcritical and supercritical distributions and signs of λ_1^{OC}, Figures (4.7), (4.8) shows the domain of dependence to be the entire upstream flowfield, as all eigenvalue directions point toward P, and the entire downstream flowfield to be the range of influence, as all eigenvalue directions point away from P. The propagation directions of the celerity eigenvalues, Figures (4.9) - (4.11), show the entire flowfield, for subcritical flows, to be simultaneously the region of influence and the domain of dependence as λ_2^{OC} points away from P and λ_3^{OC} points towards P. For supercritical flow, however, each eigenvalue has its own regions of influence and domains of dependence within "wedges" bounded by the conjugate lines, Figures (4.10) - (4.12). Note that λ_2^{OC} has a larger region of influence than λ_3^{OC} while λ_3^{OC} has the greater domain of dependence.

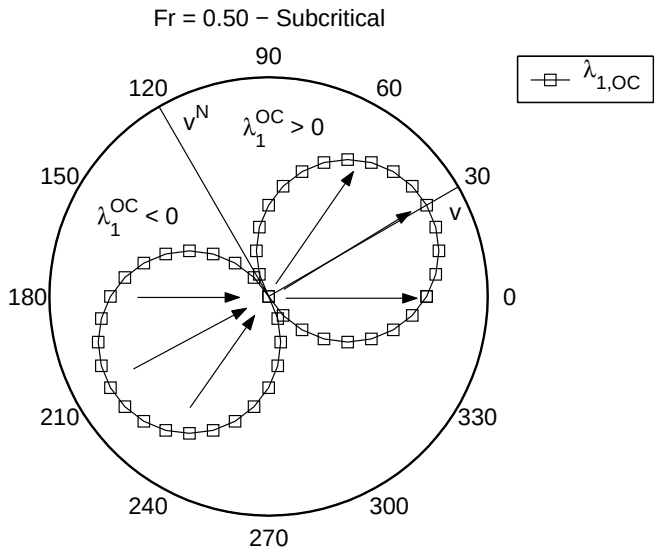

Figure 4.7: Subcritical Polar Variation of λ_1^{OC}

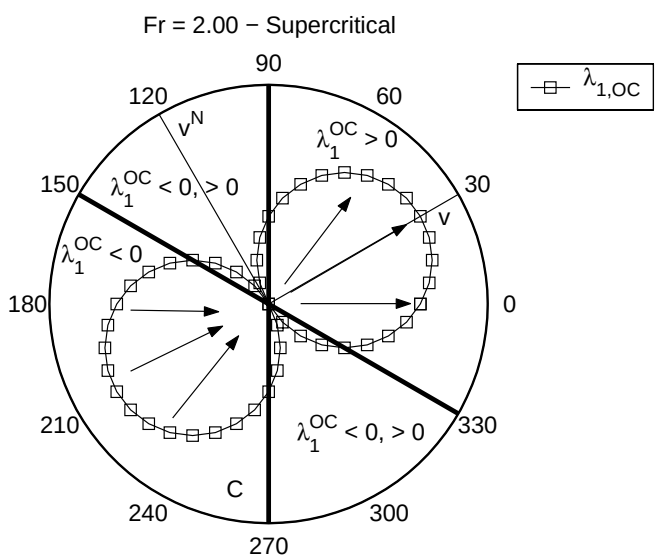

Figure 4.8: Supercritical Polar Variation of λ_1^{OC}

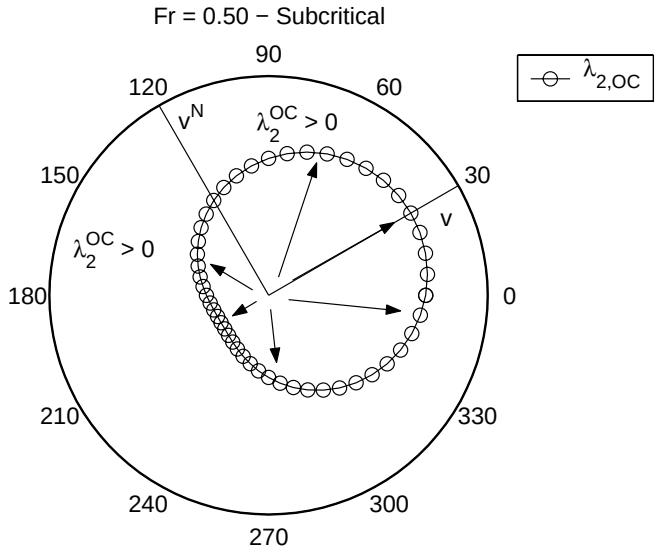

Figure 4.9: Subcritical Polar Variation of λ_2^{OC}

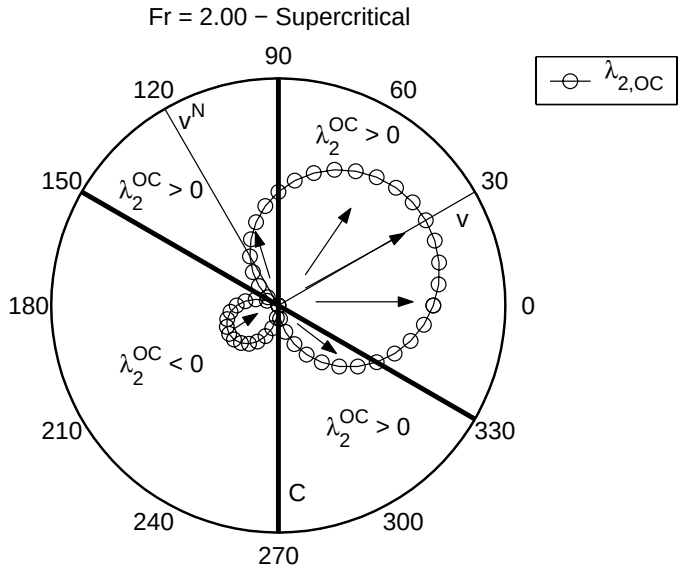

Figure 4.10: Supercritical Polar Variation of λ_2^{OC}

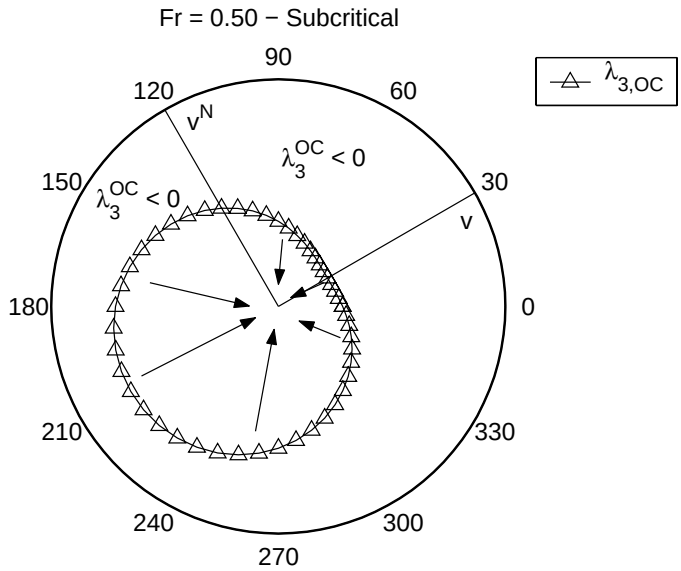

Figure 4.11: Subcritical Polar Variation of λ_3^{OC}

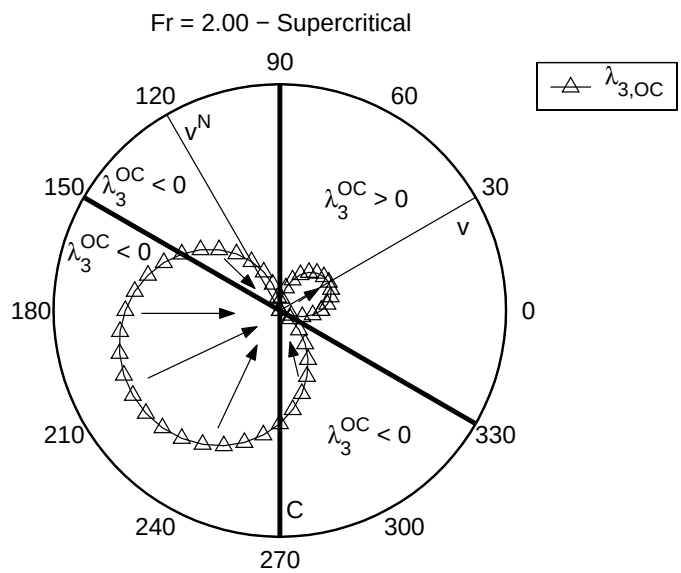

Figure 4.12: Supercritical Polar Variation of λ_3^{OC}

The distributions for the eigenvalue signs for subcritical and super critical flow, Figures (4.7) - (4.12) suggest that distinct regions of bi-modal and mono-axial propagation exist within the flow field for each flow regime. Compiling the eigenvalue signs for subcritical flow, Figure (4.13), shows the entire flow field to be bi-modal. Although the convection eigenvalue is mono-axial, the celerity-convection eigenvalues are bi-modal, thus yielding an overall bi-modal propagation mode. Hence, the entire flow field is simultaneously the domain of dependence and the region of influence.

For supercritical flow, two distinct propagation mode subfields are evident. The subfield "wedge" bisected by the streamline direction and bounded by the conjugate lines is mono-axial as all three eigenvalues are positive within the downstream wedge and negative within the upstream wedge. This region of mono-axial behavior is denoted the *streamline wedge* and represents distinct domains of dependence and regions of influence. The subfield wedge bisected by the crossflow direction and bounded by the conjugate lines is bi-modal as the eigenvalues have differing signs. This region of bi-modal behavior is denoted the *crossflow wedge* and reflects regions which are simultaneously the domains of dependence and regions of influence. Note that the eigenvalue signs are identical in both wedges.

The conjugate lines, as the bi-modal/mono-axial demarcation lines for supercritical flow, admit further analysis of the field propagation behavior. Because the conjugate lines are perpendicular to the Froude lines and the Froude lines exist only for critical/supercritical flow, no mono-axial propagation modes can exist within the subcritical flow regime. For critical flow, the Froude lines point in the crossflow direction and the conjugate lines are aligned with the streamline direction. As the Froude number increases, the Froude lines approach the streamline direction and the conjugate lines approach the crossflow direction, hence "widening" the mono-axial wedge and "closing" the bi-modal wedge. For infinite Froude number, the Froude line is the streamline and the mono-axial wedge becomes the entire flow field, correctly eliminating all bi-modal celerity effects.

A key observation is the existence of a bi-modal, hence simulataneous domain of dependence/region of influence, region within a supercritical flowfield. This perhaps suprising result is readily reconciled as the flowfield itself is comprised of an infinite number of arbitrary points P_f, each with its own domain of dependence and range of influence. Thus, the bi-modal region for P is simply the space within the domain of dependence and range of influence for other flow field points P_f.

Heed that the eigenvalues of the characterisitics-biased flux divergence jacobian should exhibit character similar to that presented to insure physical consistency. The flux vector decompositions introduced in Sections (4.5) - (4.6) will rely heavily on these developments, generating one decomposition which accurately induces mono-axial flow and a second which accurately induces bi-modal flow.

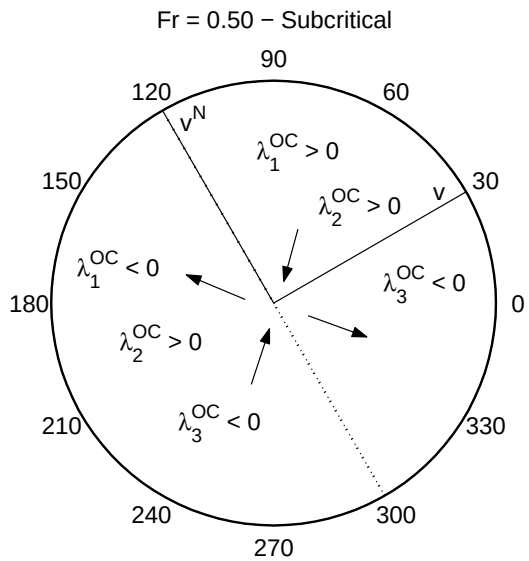

Figure 4.13: Subcritical Polar Variation of $\lambda^{OC}_{1,2,3}$: Summary

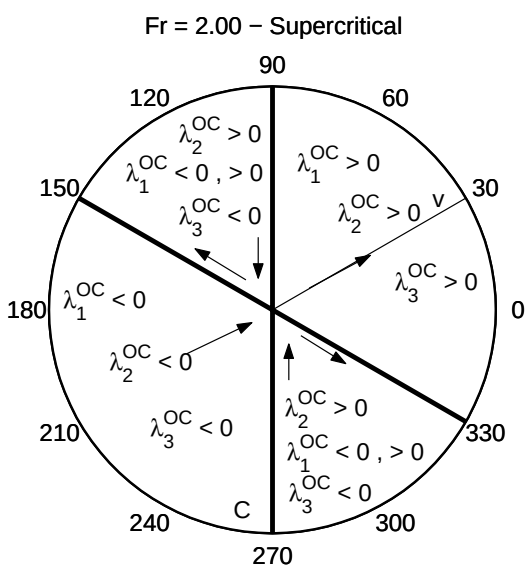

Figure 4.14: Supercritical Polar Variation of $\lambda^{OC}_{1,2,3}$: Summary

4.4 Continuum Upstream-Bias Approximation

For arbitrary domains $\hat{\Omega} \subset \Omega$ and arbitrary test functions $\hat{w}$ with compact support in $\hat{\Omega}$, the weak form statement is

$$\int_{\hat{\Omega}} \hat{w} \left(\frac{\partial \mathbf{q}}{\partial t} + \frac{\partial f_j(\mathbf{q})}{\partial x_j} \right) d\Omega = 0 \tag{4.83}$$

Due to the theory of weak forms, (4.83) is equivalent to the original hyperbolic conservation law system (4.9). As introduced in [38], the characteristics-biased weak form is next defined as

$$\int_{\hat{\Omega}} \hat{w} \left(\frac{\partial \mathbf{q}}{\partial t} + \frac{\partial f_j^c}{\partial x_j} \right) d\Omega = 0 \tag{4.84}$$

where $f_j^c(\mathbf{q})$ is the characteristics-bias flux within (4.83). This yet-to-be-determined flux automatically introduces the upstream-bias approximation for the original open channel kinetic flux divergence $\partial f_j(\mathbf{q})/\partial x_j$.

The first step in establishing $f_j^c(\mathbf{q})$, as in the one dimensional analysis, is to consider the flux jacobian decomposition into a linear combination of L contributions

$$\frac{\partial f_j(\mathbf{q})}{\partial \mathbf{q}} = \sum_{l=1}^{L} \alpha_l \mathbf{A}_{lj} \;\Rightarrow\; \frac{\partial f_j(\mathbf{q})}{\partial x_j} = \sum_{l=1}^{L} \alpha_l \mathbf{A}_{lj} \frac{\partial \mathbf{q}}{\partial x_j} \tag{4.85}$$

where $\mathbf{A}_{lj}$ denotes a matrix component of the flux jacobian decomposition and α_l denotes a linear combination function which could depend on $\mathbf{q}$. As in the one dimensional analysis, three specifications shall be imposed on each of the $\mathbf{A}_{lj}$

1. Each $\mathbf{A}_{lj}$ must have physical significance

2. It is not required that all $\mathbf{A}_{lj}$ are involved in the characteristics-bias

3. All eigenvalues of a matrix component $\mathbf{A}_{lj}n_j$ that enter the characteristics bias must have uniform-sign eigenvalues for the wedge region spanned by n_j

The weak form, (4.83), of the kinetic flux divergence $\partial f_j(\mathbf{q})/\partial x_j$ incorporating the flux jacobian decomposition of (4.85) yields

$$\int_{\hat{\Omega}} \hat{w} \frac{\partial f_j(\mathbf{q})}{\partial x_j} d\hat{\Omega} = \int_{\hat{\Omega}} \sum_{l=1}^{L} \hat{w} \alpha_l \mathbf{A}_{lj} \frac{\partial \mathbf{q}}{\partial x_j} d\hat{\Omega} \tag{4.86}$$

The characteristics-bias flux $f_j^c(\mathbf{q})$ is hence defined via (4.84) as

$$\int_{\hat{\Omega}} \hat{w} \frac{\partial f_j^c(\mathbf{q})}{\partial x_j} d\hat{\Omega} = \int_{\hat{\Omega}} \sum_{l=1}^{L} \left(\hat{w} + \psi \delta_l \hat{w}\right) \alpha_l \mathbf{A}_{lj} \frac{\partial \mathbf{q}}{\partial x_j} d\hat{\Omega} \tag{4.87}$$

where an appropriate characteristics-bias is applied to each flux jacobian decomposition matrix component $\mathbf{A}_{lj}$. As in the one-dimensional analysis, the parameter ψ is an "upstream-bias" controller which varies from zero to one. This controller effects variable levels of diffusion as a function of local solution continuity. The term $\delta_l \hat{w}$ represents a directional variation of the test function $\hat{w}$ along the axis of a wedge region within the flow plane. For each l component within (4.87), an appropriate upstream-bias is induced for $\hat{w}$ by this variation. The variation $\delta_l \hat{w}$ will become algebraically positive, negative, or zero depending on the algebraic sign of the eigenvalues of $\mathbf{A}_{lj}n_j$. These signs correspond to an upstream bias in the negative sense of the wedge axis for positive sign and a positive sense of the wedge axis for negative sign.

The directional test function variation, introduced in [38], $\delta_l \hat{w}$ in (4.87) becomes

$$\delta_l \hat{w} = \frac{\partial \hat{w}}{\partial x_i} \delta_l x_i = \frac{\partial \hat{w}}{\partial x_i} a_{il} \epsilon \quad , \quad \delta_l x_i = a_{il} \epsilon \tag{4.88}$$

where ϵ denotes a local positive differential length and a_{il} is the ith direction cosine of a unit vector a_l along the principal wave propagation direction of wave "l".

Substituting (4.88) and (4.86) into the upstream-bias weak form (4.87)

$$\int_{\hat{\Omega}} \hat{w} \frac{\partial f_j^c(\mathbf{q})}{\partial x_j} d\hat{\Omega} = \int_{\hat{\Omega}} \hat{w} \frac{\partial f_j(\mathbf{q})}{\partial x_j} d\hat{\Omega} + \int_{\hat{\Omega}} \epsilon\psi \frac{\partial \hat{w}}{\partial x_i} \sum_{l=1}^{L} a_{il}\alpha_l \mathbf{A}_{lj} \frac{\partial \mathbf{q}}{\partial x_j} d\hat{\Omega} \tag{4.89}$$

Capitalizing upon the compact support lent by $\hat{w}$, integrating (4.89) by parts will not introduce a boundary evaluation. Hence

$$\int_{\hat{\Omega}} \hat{w} \left(\frac{\partial f_j^c(\mathbf{q})}{\partial x_j} - \frac{\partial f_j(\mathbf{q})}{\partial x_j} + \frac{\partial}{\partial x_i} \left(\epsilon\psi \sum_{l=1}^{L} a_{il}\alpha_l \mathbf{A}_{lj} \frac{\partial \mathbf{q}}{\partial x_j} \right) \right) d\hat{\Omega} = 0 \tag{4.90}$$

Again, owing to the arbitrariness of $\hat{w}$ and $\hat{\Omega}$, the integrand must be identically zero which reveals the divergence of the characteristics-biased flux to be

$$\frac{\partial f_j^c(\mathbf{q})}{\partial x_j} = \frac{\partial f_j(\mathbf{q})}{\partial x_j} - \frac{\partial}{\partial x_i} \left(\epsilon\psi \sum_{l=1}^{L} a_{il}\alpha_l \mathbf{A}_{lj} \frac{\partial \mathbf{q}}{\partial x_j} \right) \tag{4.91}$$

This expressions contains both the parent kinetic flux divergence and an upstream-biased, second-order differential term

$$\frac{\partial}{\partial x_i} \left(\epsilon\psi \sum_{l=1}^{L} a_{il}\alpha_l \mathbf{A}_{lj} \frac{\partial \mathbf{q}}{\partial x_j} \right) \tag{4.92}$$

Recalling the non-linear, wave-like solution $\mathbf{q} = \mathbf{q}(\mathbf{x} \cdot \mathbf{n} - \lambda(\mathbf{q})t)$, differentiation reveals the upstream matrix $\mathcal{A}$ to be

$$\mathcal{A} = n_i \left(\sum_{l=1}^{L} a_{il}\alpha_l \mathbf{A}_{lj} \right) n_j \tag{4.93}$$

where n_i indicates the ith directional cosine of a unit vector $\mathbf{n}$ along an arbitrary wave-propagation direction.

Integrating (4.91) to within an arbitrary divergence-free function yields the ith component of the characteristics biased flux to be

$$f_i^c(\mathbf{q}) = f_i(\mathbf{q}) - \epsilon\psi \sum_{l=1}^{L} a_{il}\alpha_l \mathbf{A}_{lj} \frac{\partial \mathbf{q}}{\partial x_j} \tag{4.94}$$

Inherent to this multi-dimensional expression is the dependence of each cartesian component $f_i^c(\mathbf{q})$ upon the derivatives of the solution $\mathbf{q}$ along all cartesian directions. As such, the continuum expression for the characteristics flux encompasses the current continuum and discrete algorithms presented in Chapter (1).

4.5 Streamline Convection Decomposition

The two-dimensional open channel kinetic flux divergence can be intuitively decomposed into convection and non-convection components as

$$\frac{\partial f_j(\mathbf{q})}{\partial x_j} = \frac{\partial f_j^{conv}(\mathbf{q})}{\partial x_j} + \frac{\partial f_j^{cel}(\mathbf{q})}{\partial x_j} \tag{4.95}$$

where $f_j^{conv}(\mathbf{q})$ and $f_j^{cel}(\mathbf{q})$ denote the convection flux and the depth-averaged hydrostatic pressure gradient flux, henceforth termed the celerity flux, components respectively. Recalling the kinetic flux (4.10) to be

$$f_j(\mathbf{q}) = \left\{ \begin{array}{c} m_j \\ \frac{m_j}{h} m_1 + g\frac{h^2}{2}\delta_1^j \\ \frac{m_j}{h} m_2 + g\frac{h^2}{2}\delta_2^j \end{array} \right\} \tag{4.96}$$

the convection and celerity flux components are defined as

$$f_j^{conv}(\mathbf{q}) \equiv \left\{ \begin{array}{c} m_j \\ \frac{m_j}{h} m_1 \\ \frac{m_j}{h} m_2 \end{array} \right\} = \frac{m_j}{h} \left\{ \begin{array}{c} h \\ m_1 \\ m_2 \end{array} \right\} \quad , \quad f_j^{cel}(\mathbf{q}) \equiv \left\{ \begin{array}{c} 0 \\ g\frac{h^2}{2}\delta_1^j \\ g\frac{h^2}{2}\delta_2^j \end{array} \right\} \tag{4.97}$$

For supercritical flow ($Fr > 1$) the non-dimensional flux jacobian eigenvalues (4.55) have uniform algebraic sign within the streamline wedge region as shown in Figure (4.14). The entire flux divergence can therefore be approximated as a mono-axial propagation mode within the streamline wedge. The crossflow wedge, however, has eigenvalues of differing sign and must therefore be approximated as bi-modal. For sub-critical flow, the eigenvalues also have mixed sign throughout the entire flowfield and a mono-axial approximation is therfore physically inconsistent with the bi-modal propagation of the celerity-convection eigenvalues. Focusing on generating a physically consistent mono-axial approximation within the streamline wedge begin by solving for the convection and celerity-gradient jacobians and comparing with the original jacobian:

$$\mathbf{A}_j^{conv} = \left[\begin{array}{ccc} 0 & \delta_j^1 & \delta_j^2 \\ -u_1 u_j & u_j + u_1\delta_j^1 & u_1\delta_j^2 \\ -u_2 u_j & u_2\delta_j^1 & u_j + u_2\delta_j^2 \end{array} \right] \tag{4.98}$$

$$\mathbf{A}_j^{cel} = \left[\begin{array}{ccc} 0 & 0 & 0 \\ gh\delta_j^1 & 0 & 0 \\ gh\delta_j^2 & 0 & 0 \end{array} \right] \tag{4.99}$$

$$\mathbf{A}_j = \left[\begin{array}{ccc} 0 & \delta_j^1 & \delta_j^2 \\ -u_1 u_j + gh\delta_j^1 & u_j + u_1\delta_j^1 & u_1\delta_j^2 \\ -u_2 u_j + gh\delta_j^2 & u_2\delta_j^1 & u_j + u_2\delta_j^2 \end{array} \right] \tag{4.100}$$

The flux jacobian decomposition components clearly sum to yield the open channel flux jacobian. Employing the non-linear, wave-like solution reveals the dimensional eigenvalues of the flux jacobian decomposition and the open channel flux jacobian to be

$$
\begin{array}{ccccccc}
 & & \lambda_1^d & & \lambda_2^d & & \lambda_3^d \\
\mathbf{A}_j^{conv}\, n_j & \rightarrow & u_j n_j & , & u_j n_j & , & u_j n_j \\
\mathbf{A}_j^{cel}\, n_j & \rightarrow & 0 & , & 0 & , & 0 \\
\mathbf{A}_j\, n_j & \rightarrow & u_j n_j & , & u_j n_j + \sqrt{gh} & , & u_j n_j - \sqrt{gh}
\end{array}
\tag{4.101}
$$

Employing the velocity transformation and non-dimensionalizing the eigenvalues via division by $\sqrt{gh}$:

$$
\begin{array}{ccccccc}
 & & \lambda_1 & & \lambda_2 & & \lambda_3 \\
\mathbf{A}_j^{conv}\, n_j & \rightarrow & v_j n_j Fr & , & v_j n_j Fr & , & v_j n_j Fr \\
\mathbf{A}_j^{cel}\, n_j & \rightarrow & 0 & , & 0 & , & 0 \\
\mathbf{A}_j\, n_j & \rightarrow & v_j n_j Fr & , & v_j n_j Fr + 1 & , & v_j n_j Fr - 1
\end{array}
\tag{4.102}
$$

Segregating the celerity component from the convection component yields two sets of eigenvalues: the first set representing pure convective propagation for all three eigenvalues, the second set representing no propagation for all three eigenvalues. For subcritical flow, this approximation has identically signed convection eigenvalues for the entire flowfield, indicating a physically inconsistent mono-axial propagation mode. The supercritical crossflow wedge, a physically bi-modal region as well, is also incorrectly approximated as mono-axial. The streamline wedge, however, is correctly approximated as mono-axial. Morevoer, the approximate convection eigenvalue λ_1 is identical to the open channel convection eigenvalue while, in the convection limit, the approximate celerity-convection eigenvalues $\lambda_{2,3}$ are identical to the open channel celerity-convection eigenvalues. This intuitive decomposition is therefore strictly physically consistent only within the streamline wedge region for $Fr = \infty$. As the Froude number decreases from infinity to the critical point, $Fr = 1$, the approximation within the streamline wedge becomes increasingly inconsistent as the approximate celerity-convection eigenvalues, while maintaining similar sign, differ by ± 1 in magnitude from the open channel celerity-convection eigenvalues.

Decomposing the flux divergence instead as the convection component and a linear combination of the celerity component as in the one-dimensional development

$$\frac{\partial f_j(\mathbf{q})}{\partial x_j} = \left[\frac{\partial f_j^{conv}(\mathbf{q})}{\partial x_j} + \beta \frac{\partial f_j^{cel}(\mathbf{q})}{\partial x_j}\right] + \left[(1-\beta)\frac{\partial f_j^{cel}(\mathbf{q})}{\partial x_j}\right] \quad , \quad 0 \leq \beta \leq 1 \tag{4.103}$$

where β is the celerity partition function and each bracketed term is unique. This positive partition function is chosen such that all three approximate eigenvalues associated with each of the bracketed components maintain similar algebraic sign and, more demandingly, remain equal to the open channel eigenvalues within the streamline wedge region for all $Fr \geq 1$, thereby admitting a consistent and accurate mono-axial upstream bias for this specific flow case. While the approximate eigenvalues within the crossflow wedge are exact, a mono-axial upstream bias is physically inconsistent with the bi-modal propagation of the open channel eigenvalues. Additionally, β will enforce similar signed eigenvalues for subcritical flows which, while convenient for applying a mono-axial upsream bias, is physically inconsistent with the exhibited bi-modal character of the subcritical open channel eigenvalues. Additionally, the approximate celerity-convection eigenvalues will not accurately correlate with the open channel eigenvalues.

Embedding this parameter within the fluxes, and hence their respective jacobians, is viable as the eigenvalues of a matrix are continuous functions of the matrix entries [44]. Therefore, the eigenvalues of the jacobians associated with the fluxes of (4.103) will be continuous functions of β. With respect to the bracketed quantitites, as β approaches 1 the left bracketed term remains, yielding the divergence of the original flux (4.96), while as β appropaches zero, the divergence of the segregated fluxes of (4.97) remain. To insure mono-axial propagation, β must therefore be zero when $Fr = 0$ and increase to one for critical and supercritical Froude numbers. Solving for the jacobians of the bracketed terms:

$$\mathbf{A}_j = [\, \mathbf{A}_j^{conv} + \beta \mathbf{A}_j^{cel} \,] + (1-\beta)\mathbf{A}_j^{cel} \tag{4.104}$$

$$= \mathbf{A}_j^{scc} + \mathbf{A}_j^{sc} \tag{4.105}$$

where $\mathbf{A}_j^{scc}$ denotes the *streamline celerity-convection* jacobian and $\mathbf{A}_j^{sc}$ denotes the *streamline celerity* jacobian, redefined to highlight their fundamental difference, physically consistent mono-axial propagation within the streamline wedge, from the convection and celerity gradient flux divergence jacobians $\mathbf{A}_j^{conv}$ and $\mathbf{A}_j^{cel}$respectively. Expanding the streamline wedge jacobians:

$$\mathbf{A}_j^{scc} = \begin{bmatrix} 0 & \delta_j^1 & \delta_j^2 \\ -u_1 u_j + \beta g h \delta_j^1 & u_j + u_1 \delta_j^1 & u_1 \delta_j^2 \\ -u_2 u_j + \beta g h \delta_j^2 & u_2 \delta_j^1 & u_j + u_2 \delta_j^2 \end{bmatrix} \tag{4.106}$$

$$\mathbf{A}_j^{sc} = \begin{bmatrix} 0 & 0 & 0 \\ (1-\beta) g h \delta_j^1 & 0 & 0 \\ (1-\beta) g h \delta_j^2 & 0 & 0 \end{bmatrix} \tag{4.107}$$

$$\mathbf{A}_j = \begin{bmatrix} 0 & \delta_j^1 & \delta_j^2 \\ -u_1 u_j + g h \delta_j^1 & u_j + u_1 \delta_j^1 & u_1 \delta_j^2 \\ -u_2 u_j + g h \delta_j^2 & u_2 \delta_j^1 & u_j + u_2 \delta_j^2 \end{bmatrix} \tag{4.108}$$

Employing the non-linear, wave-like solution reveals the dimensional eigenvalues to be

$$\begin{array}{ccccccc} & & \lambda_1^d & & \lambda_2^d & & \lambda_3^d \\ \mathbf{A}_j^{scc}\, n_j & \rightarrow & u_j n_j & , & u_j n_j + \beta\sqrt{gh} & , & u_j n_j - \beta\sqrt{gh} \\ \mathbf{A}_j^{sc}\, n_j & \rightarrow & 0 & , & 0 & , & 0 \\ \mathbf{A}_j\, n_j & \rightarrow & u_j n_j & , & u_j n_j + \sqrt{gh} & , & u_j n_j - \sqrt{gh} \end{array} \tag{4.109}$$

Employing the velocity transformation and non-dimensionalizing the eigenvalues via division by $\sqrt{gh}$:

$$
\begin{array}{ccccccc}
 & & \lambda_1 & & \lambda_2 & & \lambda_3 \\
\mathbf{A}_j^{scc}\, n_j & \rightarrow & v_j n_j Fr & , & v_j n_j Fr + \beta & , & v_j n_j Fr - \beta \\
\mathbf{A}_j^{sc}\, n_j & \rightarrow & 0 & , & 0 & , & 0 \\
\mathbf{A}_j\, n_j & \rightarrow & v_j n_j Fr & , & v_j n_j Fr + 1 & , & v_j n_j Fr - 1
\end{array}
\tag{4.110}
$$

As stated previously, setting $\beta = 1$ for $Fr \geq 1$ recovers exactly the original flux divergence jacobian and its associated eigenvalues and, as such, is an exact approximation to the flux divergence jacobian for critical and supercritical flow regimes in both the streamline and crossflow wedge regions. However, the approximate celerity-convection eigenvalues become increasingly inaccurate as the Froude number decreases from one to zero since β decreases from one to zero as the Froude number decreases from one to zero. In the celerity limit ($Fr = \beta = 0$), the approximate celerity-convection eigenvalues completely lose their celerity character ($\lambda_{2,3} = 0$) and do not correlate with the open channel celerity-convection eigenvalues ($\lambda_{2,3}^{OC} = 1$). Note that the approximate convection eigenvalue λ_1 remains physically consistent for all Fr.

In conclusion, decomposition (4.103), satisfies the design goal of generating a mono-axial flux divergence approximation with strictly similarly signed eigenvalues. This approximation accurately reflects the mono-axial propagation modes inherent to the open channel flow equation system within the supercritical streamline wedge. Additionally, a nearly exact flux divergence approximation for subcritical flow (nearly mono-axial) is realized which becomes increasingly inaccurate as the Froude number decreases (increasingly bi-modal). While the supercritical eigenvalues are accurate within the crossflow wedge region, this correctly signed bi-modal propagation mode is inconsistent with the design goal of a mono-axial formulation. The following decompostion will address these two issues, generating a bi-modal flux divergence approximation which handles subcritical flow and the supercritical crossflow wedge region.

4.6 Celerity-Convection Decomposition

Having generated a flux divergence approximation which models the mono-axial propagation modes of the open channel equation system within the streamline wedge region, the next step is to develop a flux divergence approximation which reflects the bi-modal propagation modes of the subcritical flow field and the supercritical crossflow wedge. Consider a non-intuitive decomposition of the open-channel flux divergences as

$$\begin{aligned}
\frac{\partial f_j(\mathbf{q})}{\partial x_j} &= \frac{\partial f_j^{conv}(\mathbf{q})}{\partial x_j} + \frac{\partial f_j^{cel}(\mathbf{q})}{\partial x_j} \\
&= \left(\mathbf{A}_j^{conv} + \mathbf{A}_j^{cel}\right) \frac{\partial \mathbf{q}}{\partial x_j} && (4.111) \\
&= \left(\mathbf{A}_j^{conv} + \mathbf{A}_j^{jcel} + \mathbf{A}_j^{jaux}\right) \frac{\partial \mathbf{q}}{\partial x_j} && (4.112)
\end{aligned}$$

where the jacobian of the celerity flux divergence is decomposed into two components $\mathbf{A}_j^{jcel}$ and $\mathbf{A}_j^{jaux}$ while $\mathbf{A}_j^{conv}$ remains as defined in the previous section. This new celerity jacobian decomposition will introduce celerity eigenvalues for the $\mathbf{A}_j^{jcel}$ component while $\mathbf{A}_j^{jaux}$ introduces no eigenvalues and acts only to preserve matrix similtude between the decompositions and the original open channel flux divergence jacobian. These three FJD take the form of

$$\mathbf{A}_j^{conv} = \begin{bmatrix} 0 & \delta_j^1 & \delta_j^2 \\ -u_1 u_j & u_j + u_1\delta_j^1 & u_1\delta_j^2 \\ -u_2 u_j & u_2\delta_j^1 & u_j + u_2\delta_j^2 \end{bmatrix} \tag{4.113}$$

$$\mathbf{A}_j^{jcel} = \begin{bmatrix} 0 & \delta_j^1 & \delta_j^2 \\ gh\delta_j^1 & 0 & 0 \\ gh\delta_j^2 & 0 & 0 \end{bmatrix} \tag{4.114}$$

$$\mathbf{A}_j^{jaux} = \begin{bmatrix} 0 & -\delta_j^1 & -\delta_j^2 \\ 0 & 0 & 0 \\ 0 & 0 & 0 \end{bmatrix} \tag{4.115}$$

$$\mathbf{A}_j = \begin{bmatrix} 0 & \delta_j^1 & \delta_j^2 \\ -u_1 u_j + gh\delta_j^1 & u_j + u_1\delta_j^1 & u_1\delta_j^2 \\ -u_2 u_j + gh\delta_j^2 & u_2\delta_j^1 & u_j + u_2\delta_j^2 \end{bmatrix} \tag{4.116}$$

It is clear that the components of the FJD sum to yield the open channel flux jacobian. Employing the non-linear, wave-like solution to obtain the dimensional eigenvalues of the FJD components

$$\begin{array}{lcccccc} & & \lambda_1^d & & \lambda_2^d & & \lambda_3^d \\ \mathbf{A}_j^{conv}\, n_j & \rightarrow & u_j n_j & , & u_j n_j & , & u_j n_j \\ \mathbf{A}_j^{jcel}\, n_j & \rightarrow & 0 & , & \sqrt{gh} & , & -\sqrt{gh} \\ \mathbf{A}_j^{jaux}\, n_j & \rightarrow & 0 & , & 0 & , & 0 \\ \mathbf{A}_j\, n_j & \rightarrow & u_j n_j & , & u_j n_j + \sqrt{gh} & , & u_j n_j - \sqrt{gh} \end{array} \tag{4.117}$$

Using the velocity transformation and non-dimensionalizing

$$\begin{array}{lcccccc} & & \lambda_1 & & \lambda_2 & & \lambda_3 \\ \mathbf{A}_j^{conv}\, n_j & \rightarrow & v_j n_j Fr & , & v_j n_j Fr & , & v_j n_j Fr \\ \mathbf{A}_j^{jcel}\, n_j & \rightarrow & 0 & , & 1 & , & -1 \\ \mathbf{A}_j^{jaux}\, n_j & \rightarrow & 0 & , & 0 & , & 0 \\ \mathbf{A}_j\, n_j & \rightarrow & v_j n_j Fr & , & v_j n_j Fr + 1 & , & v_j n_j Fr - 1 \end{array} \tag{4.118}$$

This new decomposition, *celerity-convection decomposition* (CCD), grants the satisfying isolation of the physically significant convection/celerity non-dimensional eigenvalues (4.118) from the FJD components while satisfying the design goal of developing a bi-modal flux divergence approximation. Note the eigenvalues of $\mathbf{A}_j^{jcel} n_j$ are independent of n_j, hence correctly model isotropic wave propagation. This matrix is thus denoted the *celerity matrix* for its eigenvalues correlate with the open channel eigenvalues of ± 1 for vanishing Froude number. For vanishing Froude number, the convection eigenvalues also vanish while the auxilliary eigenvalues remain zero for all Froude numbers. This three component decomposition is therefore an exact, bi-modal approximation to the open channel flux divergence in the celerity limit. As the Froude number increases towards one, this decomposition becomes minimally inaccurate for low subcritical flows (nearly bi-modal) and increasingly inaccurate for high subcritical flows (nearly mono-axial), yet retains the desired bi-modal character. For supercritical flow within the crossflow wedge region, the propagation is bi-modal, in harmony with the open channel results, but the eigenvalues do not correlate with the open channel eigenvalues, hence the approximation is inaccurate. Within the streamline wedge, the approximation is inconsistent with the required mono-axial propagation and the eigenvalues are inaccurate.

4.6.1 Streamline and Crossflow Components

Having generated a mono-axial and a bi-modal approximation to the open channel flux divergence, it is clear that each approximation is exact for certain flow conditions and inexact for other flow conditions. Taking a linear combination of the two may result in a composite approximation that is physcially consistent with the propagation modes for all Froude numbers while correlating well with the eigenvalues of the original open channel flux divergence jacobian. Before forming this combination, the effects of the multiple celerity fields must be investigated.

Heed that the streamline convection decompostion exactly yields the correct amount of celerity

within the supercritical streamline wedge and thus needs no celerity contribution from the celerity-convection decompostion. Similarly, the supercritical crossflow wedge, while having the correct amount of celerity from the streamline convection decompostion, must have a contribution from the celerity-convection decompostion as the propagation mode is bi-modal, contrary to the design of the streamline convection decomposition. For the celerity limit, the contribution from the celerity matrix is the only physically valid component, hence it must uniformly influence the entire flowfield.

As the Froude number increases from zero to one, the mono-axial streamline convection decomposition becomes increasingly accurate while the bi-modal celerity-convection decompostion becomes increasingly inaccurate. Both the streamline and crossflow contribution of the celerity matrix must decrease but at different rates: the streamline contribution must decrease faster than the crossflow contribuion. Finally, at the critical point and beyond, the contribution from the celerity matrix must smoothly transition to the required supercritical distribution of no contribution in the streamline wedge and an appropriate "balancing" amount in the crossflow wedge.

It is therefore expedient to project the effects of the celerity matrix upon two arbitrary, mutually perpendicular unit vectors. Defining these vectors as $\mathbf{a} = (a_1, a_2)$ and $\mathbf{a}^N = (a_1^N, a_2^N)$ allows the re-expression of the celerity component within the celerity-convection decomposition as

$$\mathbf{A}_j^{jcel} \frac{\partial \mathbf{q}}{\partial x_j} = \mathbf{A}_j^{jcel} a_j a_k \frac{\partial \mathbf{q}}{\partial x_k} + \mathbf{A}_j^{jcel} a_j^N a_k^N \frac{\partial \mathbf{q}}{\partial x_k} \tag{4.119}$$

following the analogous developments in [38] for the gas dynamic Euler equations.

Note that for $\mathbf{a}$ parallel to the velocity unit vector $\mathbf{v}$, (4.119) corresponds to a projection of the open channel celerity component into streamline and crossflow components. For non-linear, wave-like solutions, the dimensional eigenvalues of this special case of $\mathbf{a}$ are

$$
\begin{array}{rcccccccc}
 & & \lambda_1^d & & \lambda_2^d & & \lambda_3^d & & \\
\mathbf{A}_j^{jcel} a_j a_k n_k & \rightarrow & 0 & , & a_k n_k \sqrt{gh} & , & -a_k n_k \sqrt{gh} & \equiv & \lambda_{1,2,3}^s \\
\mathbf{A}_j^{jcel} a_j^N a_k^N n_k & \rightarrow & 0 & , & a_k^N n_k \sqrt{gh} & , & -a_k^N n_k \sqrt{gh} & \equiv & \lambda_{1,2,3}^N
\end{array}
\tag{4.120}
$$

where $\lambda_{1,2,3}^s$ and $\lambda_{1,2,3}^N$ denote the streamline and crossflow celerity eigenvalues respectively. Expressing the left hand side of (4.119) as the sum of the right hand side terms, i.e,

$$
\mathbf{A}_j^{jcel} n_j = \mathbf{A}_j^{jcel} a_j a_k n_k + \mathbf{A}_j^{jcel} a_j^N a_k^N n_k \tag{4.121}
$$

$$
= \begin{bmatrix} 0 & a_1 a_k n_k + a_1^N a_k^N n_k & a_2 a_k n_k + a_2^N a_k^N n_k \\ gh(a_1 a_k n_k + a_1^N a_k^N n_k) & 0 & 0 \\ gh(a_2 a_k n_k + a_2^N a_k^N n_k) & 0 & 0 \end{bmatrix} \tag{4.122}
$$

and solving for the eigenvalues yields

$$
\mathbf{A}_j^{jcel} n_j \rightarrow \lambda_1^d = 0 \quad , \quad \lambda_{2,3}^d = \sqrt{gh} \left((a_k n_k)^2 + (a_k^N n_k)^2 \right)^{1/2} \tag{4.123}
$$

with

$$
(a_k n_k)^2 + \left(a_k^N n_k \right)^2 = 1 \tag{4.124}
$$

hence

$$
\mathbf{A}_j^{jcel} n_j \rightarrow \lambda_1^d = 0 \quad , \quad \lambda_{2,3}^d = \sqrt{gh} \tag{4.125}
$$

which shows that the square of the celerity eigenvalues (4.117) equals the sum of the square of the streamline and crossflow celerity eigenvalues (4.120).

Thus, for $\mathbf{a}$ and $\mathbf{a}^N$ pointing in the streamline and crossflow directions respectively, the celerity-convection approximation to the open channel flux divergence can be further decomposed as

$$\frac{\partial f_j(\mathbf{q})}{\partial x_j} = \frac{\partial f_j^{conv}(\mathbf{q})}{\partial x_j} + \bar{\alpha}\mathbf{A}_j^{jcel} a_j a_k \frac{\partial \mathbf{q}}{\partial x_k} + \mathbf{A}_j^{jcel} a_j^N a_k^N \frac{\partial \mathbf{q}}{\partial x_k} + (1-\bar{\alpha})\mathbf{A}_j^{jcel} a_j a_k \frac{\partial \mathbf{q}}{\partial x_k} + \mathbf{A}_j^{jaux} \frac{\partial \mathbf{q}}{\partial x_k} \tag{4.126}$$

The weights of $\bar{\alpha}$, $0 \leq \bar{\alpha} \leq 1$, for the streamline component and 1 for the crossflow component in (4.126) conveniently introduce the differential bias required for physical consistency.

4.6.2 Absolute Celerity Matrices

Note that the eigenvalues $\lambda_{2,3}^{jcel}$ (4.117) do not have uniform sign. Taking cue from the one-dimensional analysis, an *a priori* similarity transformation of the streamwise celerity component $\mathbf{A}_j^{cel} a_j$ will be employed satisfy the impending stability constraint of non-negative eigenvalues.

$$\mathbf{A}_j^{jcel} a_j = \mathbf{X}\mathbf{\Lambda}^{jcel}\mathbf{X}^{-1} \tag{4.127}$$

where $\mathbf{X}$ and $\mathbf{\Lambda}^{jcel} = \mathbf{\Lambda}^{jcel^+} + \mathbf{\Lambda}^{cel^-}$ are the right eigenvector matrix and the diagonal eigenvalue matrix of the jacobian and $\mathbf{\Lambda}^{jcel^+}$ and $\mathbf{\Lambda}^{jcel^-}$ contain the non-negative and non-positive eigenvalues respectively. Despite its zero eigenvalue λ_1^{jcel}, $\mathbf{A}_j^{cel} a_j$ features a complete set of eigenvectors, hence the diagonalization matrices are

$$\mathbf{X} = \begin{bmatrix} 1 & 1 & 0 \\ a_1\sqrt{gh} & -a_1\sqrt{gh} & 1/a_1 \\ a_2\sqrt{gh} & -a_2\sqrt{gh} & -1/a_2 \end{bmatrix} \quad , \quad \mathbf{X}^{-1} = \frac{1}{2}\begin{bmatrix} 1 & a_1/\sqrt{gh} & a_2/\sqrt{gh} \\ 1 & -a_1/\sqrt{gh} & a_2/\sqrt{gh} \\ 0 & 2a_1a_2^2 & -2a_1^2a_2 \end{bmatrix} \tag{4.128}$$

and the diagonal eigenvalue matrix is

$$\mathbf{\Lambda}^{jcel} = \begin{bmatrix} \sqrt{gh} & 0 & 0 \\ 0 & -\sqrt{gh} & 0 \\ 0 & 0 & 0 \end{bmatrix} \tag{4.129}$$

Substituting (4.129) into (4.127), keeping $\mathbf{X}$ and $\mathbf{X}^{-1}$ in variable form, and carefully adding zero to the $(3,3)$ entry of (4.129)

$$\mathbf{X}\mathbf{\Lambda}^{jcel}\mathbf{X}^{-1} = \mathbf{X}\begin{bmatrix} \sqrt{gh} & 0 & 0 \\ 0 & -\sqrt{gh} & 0 \\ 0 & 0 & 1/2(\sqrt{gh}-\sqrt{gh}) \end{bmatrix}\mathbf{X}^{-1} \tag{4.130}$$

$$= \mathbf{X}\left(\begin{bmatrix} \sqrt{gh} & 0 & 0 \\ 0 & 0 & 0 \\ 0 & 0 & \frac{\sqrt{gh}}{2} \end{bmatrix} + \begin{bmatrix} 0 & 0 & 0 \\ 0 & -\sqrt{gh} & 0 \\ 0 & 0 & -\frac{\sqrt{gh}}{2} \end{bmatrix}\right)\mathbf{X}^{-1} \tag{4.131}$$

$$= \mathbf{X}\begin{bmatrix} \sqrt{gh} & 0 & 0 \\ 0 & 0 & 0 \\ 0 & 0 & \frac{\sqrt{gh}}{2} \end{bmatrix}\mathbf{X}^{-1} + \mathbf{X}\begin{bmatrix} 0 & 0 & 0 \\ 0 & -\sqrt{gh} & 0 \\ 0 & 0 & -\frac{\sqrt{gh}}{2} \end{bmatrix}\mathbf{X}^{-1} \tag{4.132}$$

Compactly expressing (4.132) reveals two physically significant matrices:

$$\mathbf{A}_j^{jcel}a_j = \mathbf{X}\mathbf{\Lambda}^{jcel^+}\mathbf{X}^{-1} + \mathbf{X}\mathbf{\Lambda}^{jcel^-}\mathbf{X}^{-1} \tag{4.133}$$

Note that the matrices $\mathbf{X}\mathbf{\Lambda}^{jcel^+}\mathbf{X}^{-1}$ and $\mathbf{X}\mathbf{\Lambda}^{jcel^-}\mathbf{X}^{-1}$ respectively represent downstream and upstream propagation matrix components of $\mathbf{A}_j^{jcel}a_j$. In anticipation of the soon-to-be applied bi-modal bias (4.150), the following signs of the principal propagation unit vectors will be applied:

$$\mathbf{A}_j^{jcel}a_j \rightarrow +\mathbf{X}\mathbf{\Lambda}^{jcel^+}\mathbf{X}^{-1} - \mathbf{X}\mathbf{\Lambda}^{jcel^-}\mathbf{X}^{-1} \tag{4.134}$$

where the positive sign preceeding the first right hand term indicates downstream propagation and the negative sign preceeding the second right hand term indicates upstream propagation. This bi-modal approximation directly yields the non-negative absolute value matrix

$$|\mathbf{A}_j^{jcel} a_j| = \mathbf{X} \left(\mathbf{\Lambda}^{jcel^+} - \mathbf{\Lambda}^{jcel^-} \right) \mathbf{X}^{-1} \tag{4.135}$$

Substituting the values of $\mathbf{\Lambda}^{cel^+}$ and $\mathbf{\Lambda}^{cel^-}$

$$|\mathbf{A}_j^{jcel} a_j| = \mathbf{X} \begin{bmatrix} \sqrt{gh} & 0 & 0 \\ 0 & \sqrt{gh} & 0 \\ 0 & 0 & \sqrt{gh} \end{bmatrix} \mathbf{X}^{-1} \tag{4.136}$$

which reduces to the beautifully simple result of

$$|\mathbf{A}_j^{jcel} a_j| = \sqrt{gh}\, \mathbf{I} \tag{4.137}$$

Following an idential procedure, the crossflow celerity component $\mathbf{A}_j^{jcel} a_j^N$ is found to be

$$|\mathbf{A}_j^{jcel} a_j^N| = \sqrt{gh}\, \mathbf{I} \tag{4.138}$$

both of which yield the associated celerity field results

$$|\mathbf{A}_j^{jcel} a_j| a_k \frac{\partial \mathbf{q}}{\partial x_k} = \sqrt{gh}\, \mathbf{I}\, a_k \frac{\partial \mathbf{q}}{\partial x_k} = \sqrt{gh}\, a_k \frac{\partial \mathbf{q}}{\partial x_k} \tag{4.139}$$

$$|\mathbf{A}_j^{jcel} a_j^N| a_k^N \frac{\partial \mathbf{q}}{\partial x_k} = \sqrt{gh}\, \mathbf{I}\, a_k^N \frac{\partial \mathbf{q}}{\partial x_k} = \sqrt{gh}\, a_k^N \frac{\partial \mathbf{q}}{\partial x_k} \tag{4.140}$$

This computationally advantageous form is physically consistent with flows in the celerity limit and hence becomes an exact approximation to the flux divergence jacobian while it becomes increasingly inexact as the Froude number increases. Thus, this decomposition will be used for celerity and subcritical flow regimes.

4.7 Composite Jacobian Construction

Chapters (4.5) and (4.6) introduced the streamline convection decomposition and the celerity-convection decomposition as viable flux jacobian decompositions for the inviscid, two-dimensional open channel flow equations. These decompositions reflect respectively

1. A parameterized form that induces a mono-axial propagation mode and is valid strictly in the streamline wedge

2. A diagonalized form that induces a bi-modal propagation mode and is valid strictly in the celerity limit

which are given as

$$\frac{\partial f_j(\mathbf{q})}{\partial x_j} = \left[\frac{\partial f_j^{conv}(\mathbf{q})}{\partial x_j} + \beta\frac{\partial f_j^{cel}(\mathbf{q})}{\partial x_j}\right] + \left[(1-\beta)\frac{\partial f_j^{cel}(\mathbf{q})}{\partial x_j}\right] \tag{4.141}$$

$$\begin{aligned}\frac{\partial f_j(\mathbf{q})}{\partial x_j} &= \bar{\alpha}\left(\mathbf{X}\mathbf{\Lambda}^{jcel^+}\mathbf{X}^{-1} + \mathbf{X}\mathbf{\Lambda}^{jcel^-}\mathbf{X}^{-1}\right)a_k\frac{\partial \mathbf{q}}{\partial x_k} \\ &\quad + \left(\mathbf{X}_N\mathbf{\Lambda}^{jcel^+}\mathbf{X}_N^{-1} + \mathbf{X}_N\mathbf{\Lambda}^{jcel^-}\mathbf{X}_N^{-1}\right)a_k^N\frac{\partial \mathbf{q}}{\partial x_k} \\ &\quad + \frac{\partial f_j^{conv}(\mathbf{q})}{\partial x_j} + (1-\bar{\alpha})\mathbf{A}_j^{jcel}a_j a_k\frac{\partial \mathbf{q}}{\partial x_k} + \mathbf{A}_j^{jaux}\frac{\partial \mathbf{q}}{\partial x_j}\end{aligned} \tag{4.142}$$

A linear combination of the two shall be taken to generate an approximation which remains valid in the streamline wedge and the celerity limit while becoming valid for all other flow situations. Taking a linear combination of flux divergences:

$$\frac{\partial f_j(\mathbf{q})}{\partial x_j} = (1-\tilde{\alpha})\frac{\partial f_j(\mathbf{q})}{\partial x_j} + \tilde{\alpha}\frac{\partial f_j(\mathbf{q})}{\partial x_j} \tag{4.143}$$

Substituting (4.141) and (4.142) into the flux divergence linear combination (4.143)

$$
\begin{aligned}
\frac{\partial f_j(\mathbf{q})}{\partial x_j} &= (1-\tilde{\alpha})\left\{\left[\frac{\partial f_j^{conv}(\mathbf{q})}{\partial x_j} + \beta\frac{\partial f_j^{cel}(\mathbf{q})}{\partial x_j}\right] + \left[(1-\beta)\frac{\partial f_j^{cel}(\mathbf{q})}{\partial x_j}\right]\right\} \\
&\quad + \tilde{\alpha}\left\{\bar{\alpha}\left(\mathbf{X}\mathbf{\Lambda}^{jcel^+}\mathbf{X}^{-1} + \mathbf{X}\mathbf{\Lambda}^{jcel^-}\mathbf{X}^{-1}\right)a_k\frac{\partial \mathbf{q}}{\partial x_k}\right. \\
&\quad + \left(\mathbf{X}_N\mathbf{\Lambda}^{jcel^+}\mathbf{X}_N^{-1} + \mathbf{X}_N\mathbf{\Lambda}^{jcel^-}\mathbf{X}_N^{-1}\right)a_k^N\frac{\partial \mathbf{q}}{\partial x_k} \\
&\quad + \left.\frac{\partial f_j^{conv}(\mathbf{q})}{\partial x_j} + (1-\bar{\alpha})\mathbf{A}_j^{jcel}a_j a_k\frac{\partial \mathbf{q}}{\partial x_k} + \mathbf{A}_j^{jaux}\frac{\partial \mathbf{q}}{\partial x_j}\right\}
\end{aligned} \tag{4.144}
$$

with $0 \leq \tilde{\alpha}, \bar{\alpha}, \beta \leq 1$. Expanding terms

$$
\begin{aligned}
\frac{\partial f_j(\mathbf{q})}{\partial x_j} &= \tilde{\alpha}\bar{\alpha}\left(\mathbf{X}\mathbf{\Lambda}^{jcel^+}\mathbf{X}^{-1} + \mathbf{X}\mathbf{\Lambda}^{jcel^-}\mathbf{X}^{-1}\right)a_k\frac{\partial \mathbf{q}}{\partial x_k} \\
&\quad + \tilde{\alpha}\left(\mathbf{X}_N\mathbf{\Lambda}^{jcel^+}\mathbf{X}_N^{-1} + \mathbf{X}_N\mathbf{\Lambda}^{jcel^-}\mathbf{X}_N^{-1}\right)a_k^N\frac{\partial \mathbf{q}}{\partial x_k} \\
&\quad + \left[\frac{\partial f_j^{conv}(\mathbf{q})}{\partial x_j} + (1-\tilde{\alpha})\beta\frac{\partial f_j^{cel}(\mathbf{q})}{\partial x_j}\right] + \left[(1-\tilde{\alpha})(1-\beta)\frac{\partial f_j^{cel}(\mathbf{q})}{\partial x_j}\right] \\
&\quad + \tilde{\alpha}(1-\bar{\alpha})\mathbf{A}_j^{jcel}a_j a_k\frac{\partial \mathbf{q}}{\partial x_k} + \tilde{\alpha}\mathbf{A}_j^{jaux}\frac{\partial \mathbf{q}}{\partial x_j}
\end{aligned} \tag{4.145}
$$

Eight terms are present in this decomposition. To assess the physical character of each term, hence the type of upstream bias each term should receive, the principal direction associated with each term must be determined. Heed that, to ensure physical consistency of the composite approximation, some terms may have an imposed principal direction and some terms may not be used in the approximation. The first two terms account for bi-modal celerity propagation in the streamline direction. The third and forth terms account for bi-modal celerity in the crossflow direction. They will therefore receive a bi-modal bias based on the direction of their principal axis. Recall that the $jcel^+$ term accounts for propagation in the downstream (+**v**) direction while the $jcel^-$ accounts for propagation in the upstream (-**v**) direction. The principal directions are thus

$$\mathbf{X}\mathbf{\Lambda}^{jcel^+}\mathbf{X}^{-1} \quad \Rightarrow \quad +\mathbf{v} \quad , \quad \mathbf{X}\mathbf{\Lambda}^{jcel^-}\mathbf{X}^{-1} \quad \Rightarrow \quad -\mathbf{v} \tag{4.146}$$

$$\mathbf{X}_N\mathbf{\Lambda}^{jcel^+}\mathbf{X}_N^{-1} \quad \Rightarrow \quad +\mathbf{v} \quad , \quad \mathbf{X}_N\mathbf{\Lambda}^{jcel^-}\mathbf{X}_N^{-1} \quad \Rightarrow \quad -\mathbf{v} \tag{4.147}$$

The fifth term, $[\partial f_j^{conv}(\mathbf{q})/\partial x_j + (1-\tilde{\alpha})\beta\partial f_j^{cel}(\mathbf{q})/\partial x_j]$, is considered one term as the eigenvalues will keep the same sign within the streamline wedge region since $(1-\tilde{\alpha})\beta \leq \beta$. It will receive a mono-axial bias as the eigenvalues are similarly signed in crossflow wedge and are aligned with the streamline axis, hence the principal axis is $\mathbf{v}$.

The sixth term is the streamline celerity component coupled with the fifth term, the streamline celerity-convection component. As the Froude number increases from zero, an increasing fraction of the component which induces the physically consistent celerity content in the eigenvalues, $(1-\tilde{\alpha})\beta\partial f_j^{cel}(\mathbf{q})/\partial x_j$, is mono-axially propogated in the streamline direction. For physical consistency in the subcritical flow regime, a bi-modal propagation mode is required, hence the sixth term $(1-\tilde{\alpha})(1-\beta)\partial f_j^{cel}(\mathbf{q})/\partial x_j$ must be biased in the opposite direction. The principal direction is therefore -$\mathbf{v}$.

The seventh and eighth terms were introduced with the first four terms and complement the weighted streamline component of the celerity matrix and preserve the open channel flux jacobian matrix form respectively. Since the eigenvalues of the auxilliary coupling matrix are zero, it does not contribute to the propagation of information. Thus, the principal direction is zero. The seventh term, $\tilde{\alpha}(1-\bar{\alpha})\mathbf{A}_j^{jcel}a_j a_k \partial\mathbf{q}/\partial x_k$, accounts for subcritical celerity in the streamline direction. The contribution from this term arises from an analysis of the parameters $0 \leq \tilde{\alpha}, \bar{\alpha}, \beta \leq 1$.

For supercritical flows, the flux divergence $[\partial f_j^{conv}(\mathbf{q})/\partial x_j + \partial f_j^{cel}(\mathbf{q})/\partial x_j]$ is mono-axial within the streamline wedge region, hence $(1-\tilde{\alpha})\beta$ must approach one as the Froude number increase towards $Fr > 1$ while $0 \leq \tilde{\alpha}, \bar{\alpha}, \beta \leq 1$ simultaneously. The combination $\tilde{\alpha}\bar{\alpha}$ which preceeds the subcritical celerity component along the streamline direction (terms one and two) must approach zero

for Froude approaching one. The parameter $\tilde{\alpha}$, however, controls the magnitude of the subcritical celerity in the crossflow direction which does not vanish for $Fr > 1$ which implies that $(1 - \tilde{\alpha})$ remains less than one for finite Fr. Moreover, since $\tilde{\alpha}$ controls the level of subcritical celerity in the crossflow direction, and by design terms three and four account for this propagation, hence the seventh term should not be involved in the subcritical crossflow. No principal direction therefore exists for this term.

4.8 Evaluation of the Characteristics-Biased Flux

Having assessed the physical character of each term and its associated upstream bias contribution, the principal direction unit vectors a_{il} (4.88) of the characteristics flux jacobian decomposition (4.91) must be identified, thus yielding the final form of the characteristics bias flux. Repeating (4.91) for convenience:

$$\frac{\partial f_j^c(\mathbf{q})}{\partial x_j} = \frac{\partial f_j(\mathbf{q})}{\partial x_j} - \frac{\partial}{\partial x_i}\left(\epsilon\psi \sum_{l=1}^{L} a_{il}\alpha_l \mathbf{A}_{lj}\frac{\partial \mathbf{q}}{\partial x_j}\right) \tag{4.148}$$

Expanding the inviscid open channel flux divergence decomposition of (4.145) exposes eight components, hence $1 \leq l \leq 8$. Thus

$$
\begin{aligned}
a_{i1}\alpha_1\mathbf{A}_{1j}\frac{\partial\mathbf{q}}{\partial x_j} &= a_{i1}\ \tilde{\alpha}\bar{\alpha}\left(\mathbf{X}\mathbf{\Lambda}^{jcel^+}\mathbf{X}^{-1}\right)a_k\frac{\partial\mathbf{q}}{\partial x_k} \\
a_{i2}\alpha_2\mathbf{A}_{2j}\frac{\partial\mathbf{q}}{\partial x_j} &= a_{i2}\ \tilde{\alpha}\bar{\alpha}\left(\mathbf{X}\mathbf{\Lambda}^{jcel^-}\mathbf{X}^{-1}\right)a_k\frac{\partial\mathbf{q}}{\partial x_k} \\
a_{i3}\alpha_3\mathbf{A}_{3j}\frac{\partial\mathbf{q}}{\partial x_j} &= a_{i3}\ \tilde{\alpha}\left(\mathbf{X}_N\mathbf{\Lambda}^{jcel^+}\mathbf{X}_N^{-1}\right)a_k\frac{\partial\mathbf{q}}{\partial x_k} \\
a_{i4}\alpha_4\mathbf{A}_{4j}\frac{\partial\mathbf{q}}{\partial x_j} &= a_{i4}\ \tilde{\alpha}\left(\mathbf{X}_N\mathbf{\Lambda}^{jcel^-}\mathbf{X}_N^{-1}\right)a_k\frac{\partial\mathbf{q}}{\partial x_k} \\
a_{i5}\alpha_5\mathbf{A}_{5j}\frac{\partial\mathbf{q}}{\partial x_j} &= a_{i5}\ \left[\frac{\partial f_j^{conv}(\mathbf{q})}{\partial\mathbf{q}}+(1-\tilde{\alpha})\beta\frac{\partial f_j^{cel}(\mathbf{q})}{\partial\mathbf{q}}\right]\frac{\partial\mathbf{q}}{\partial x_j} \\
a_{i6}\alpha_6\mathbf{A}_{6j}\frac{\partial\mathbf{q}}{\partial x_j} &= a_{i6}\ (1-\tilde{\alpha})(1-\beta)\frac{\partial f_j^{cel}(\mathbf{q})}{\partial\mathbf{q}}\frac{\partial\mathbf{q}}{\partial x_j} \\
a_{i7}\alpha_7\mathbf{A}_{7j}\frac{\partial\mathbf{q}}{\partial x_j} &= a_{i7}\ \tilde{\alpha}(1-\bar{\alpha})\mathbf{A}_j^{jcel}a_ja_k\frac{\partial\mathbf{q}}{\partial x_k} \\
a_{i8}\alpha_8\mathbf{A}_{8j}\frac{\partial\mathbf{q}}{\partial x_j} &= a_{i8}\ \tilde{\alpha}\mathbf{A}_j^{jaux}\frac{\partial\mathbf{q}}{\partial x_j}
\end{aligned}
\tag{4.149}
$$

Per the physical behavior of each component, the principal direction unit vectors are

$$
\mathbf{a}_1 = \text{-}\mathbf{a}_2 = \mathbf{a}_5 = \text{-}\mathbf{a}_6 = \mathbf{a} \quad , \quad \mathbf{a}_3 = \text{-}\mathbf{a}_4 = \mathbf{a}^N \quad , \quad \mathbf{a}_7 = \mathbf{a}_8 = 0 \tag{4.150}
$$

Introducing the upstream-bias parameters δ, α, and α^N, defined as

$$
\delta = (1-\tilde{\alpha}\bar{\alpha})(2\beta-1) \quad , \quad \alpha = \tilde{\alpha}\bar{\alpha} \quad , \quad \alpha^N = \tilde{\alpha} \tag{4.151}
$$

and the absolute celerity matrix results (4.137) - (4.138) the celerity-convection characteristics flux divergence is revealed as

$$
\begin{aligned}
\frac{\partial f_j^c(\mathbf{q})}{\partial x_j} &= \frac{\partial f_j(\mathbf{q})}{\partial x_j} \\
&\quad -\frac{\partial}{\partial x_i}\left[\epsilon\psi\left(\sqrt{gh}(\alpha a_ia_j+\alpha^N a_i^N a_j^N)\frac{\partial\mathbf{q}}{\partial x_j}+a_i\delta\frac{\partial f_j^{cel}(\mathbf{q})}{\partial x_j}+a_i\frac{\partial f_j^{conv}(\mathbf{q})}{\partial x_j}\right)\right]
\end{aligned}
\tag{4.152}
$$

For vanishing Froude numbers, α and α^N approach one while δ will approach zero. For this celerity limit, (4.152) reduces to

$$\frac{\partial f_j^c(\mathbf{q})}{\partial x_j} = \frac{\partial f_j(\mathbf{q})}{\partial x_j} - \frac{\partial}{\partial x_i}\left[\epsilon\psi\left(\sqrt{gh}(a_i a_j + a_i^N a_j^N)\frac{\partial \mathbf{q}}{\partial x_j} + a_i \frac{\partial f_j^{conv}(\mathbf{q})}{\partial x_j}\right)\right] \tag{4.153}$$

Recalling $a_1^N = -a_2$ and $a_2^N = a_1$, expansion of the indices indicates

$$\frac{\partial f_j^c(\mathbf{q})}{\partial x_j} = \frac{\partial f_j(\mathbf{q})}{\partial x_j} - \frac{\partial}{\partial x_i}\left[\epsilon\psi\left(\sqrt{gh}\,\frac{\partial \mathbf{q}}{\partial x_i} + a_i \frac{\partial f_j^{conv}(\mathbf{q})}{\partial x_j}\right)\right] \tag{4.154}$$

Note that this form is independent of $(a_i a_j + a_i^N a_j^N)$ and is therefore independent of the specific propagation directions. The bias is thus isotropic and correctly reflects the isotropic propagation of celerity waves. Recalling the celerity limit analysis of section (4.2.1), the strictly hyperbolic open channel momentum equations became linearly dependent in the steady state. Significantly, the momentum equations in the characteristics biased form remains linearly independent for the celerity limit, hence eliminating the linear-dependence instability issues of the purely hyperbolic form.

For supercritical flows, $\alpha = 0$ and $\delta = 1$. The characteristics biased flux (4.152) thus reduces to

$$\frac{\partial f_j^c(\mathbf{q})}{\partial x_j} = \frac{\partial f_j(\mathbf{q})}{\partial x_j} - \frac{\partial}{\partial x_i}\left[\epsilon\psi\left(\sqrt{gh}\,\alpha^N a_i^N a_j^N \frac{\partial \mathbf{q}}{\partial x_i} + a_i \frac{\partial f_j^{conv}(\mathbf{q})}{\partial x_j}\right)\right] \tag{4.155}$$

which depends on both the crossflow component of the absolute celerity matrix and the entire open channel flux divergence. As with the celerity limit, the momentum equations of the steady state, characteristics biased open channel equations remain linearly independent, unlike the convection limit analysis of the strictly hyperbolic open channel equations of section (4.2.2).

Finally, with respect to the dependency lines of section (4.2.3), the momentum equations of characteristics biased flux divergence remains linearly independent for all supercritical choices of

$v_j n_j$. In conclusion, not only does the characteristics biased flux divergence induce physically consistent dissipation, it also eliminates the linear dependence instabilities identified in the celerity limit, convection limit, and along the supercritical dependency lines.

4.9 Determination of Free Parameters

For two-dimensional flows, the open-channel characteristics bias flux depends on the five upstream-bias functions $\mathbf{a}$, $\mathbf{a}^N$, α, α^N, and δ. For stability, as stated in Section (4.1), the eigenvalues of the upstream matrix must remain positive for all Fr and all directions $\mathbf{n}$. Therefore, the upstream matrix eigenvalues must be identified in closed form. These eigenvalues are then modified to satisfy the stability requirements while remaining physically consistent. The upstream parameters are then solved as functions of the modified eigenvalues to ensure physicaly consistency of the upstream-bias dissipation.

4.9.1 Upstream Matrix Eigenvalues

Expressing (4.152) in jacobian form and eliminating the $\mathbf{q}$ from the flux divergence terms without loss of ambiguity,

$$\frac{\partial f_j^c}{\partial x_j} = \frac{\partial f_j}{\partial x_j} - \frac{\partial}{\partial x_i}\left[\epsilon\psi\left(\sqrt{gh}(\alpha a_i a_j + \alpha^N a_i^N a_j^N)\,\mathbf{I} + a_i\delta\frac{\partial f_j^{cel}}{\partial \mathbf{q}} + a_i\frac{\partial f_j^{conv}}{\partial \mathbf{q}}\right)\frac{\partial \mathbf{q}}{\partial x_j}\right] \tag{4.156}$$

The upstream matrix is thus extracted as

$$\mathcal{A} \equiv n_i\left(\sqrt{gh}(\alpha a_i a_j + \alpha^N a_i^N a_j^N)\,\mathbf{I} + a_i\delta\frac{\partial f_j^{cel}}{\partial \mathbf{q}} + a_i\frac{\partial f_j^{conv}}{\partial \mathbf{q}}\right)n_j \tag{4.157}$$

which, each of the three right hand side terms expands to

$$n_i\ \sqrt{gh}(\alpha a_i a_j + \alpha^N a_i^N a_j^N)\ \mathbf{I}\ n_j \quad = \quad \begin{bmatrix} n_i\sqrt{gh}\ d\ n_j & 0 & 0 \\ 0 & n_i\sqrt{gh}\ d\ n_j & 0 \\ 0 & 0 & n_i\sqrt{gh}\ d\ n_j \end{bmatrix} \tag{4.158}$$

$$d = (\alpha a_i a_j + \alpha^N a_i^N a_j^N)$$

$$n_i a_i \delta \frac{\partial f_j^{cel}}{\partial \mathbf{q}} n_j = \begin{bmatrix} 0 & 0 & 0 \\ n_i a_i\ \delta\ gh\ n_1 & 0 & 0 \\ n_i a_i\ \delta\ gh\ n_2 & 0 & 0 \end{bmatrix} \tag{4.159}$$

$$n_i a_i \frac{\partial f_j^{conv}}{\partial \mathbf{q}} n_j = \begin{bmatrix} 0 & n_i a_i n_1 & n_i a_i n_2 \\ -n_i a_i u_1 u_j n_j & n_i a_i u_j n_j + n_i a_i u_1 n_1 & n_i a_i u_1 n_2 \\ -n_i a_i u_2 u_j n_j & n_i a_i u_2 n_1 & n_i a_i u_j n_j + n_i a_i u_2 n_2 \end{bmatrix} \tag{4.160}$$

Hence

$$\mathcal{A} = \begin{bmatrix} n_i d\sqrt{gh}\ n_j & n_i a_i n_1 & n_i a_i n_2 \\ n_i a_i(-u_1 u_j n_j + \delta g h n_1) & n_i(a_i(u_j n_j + u_1 n_1) + d\sqrt{gh}\ n_j) & n_i a_i u_1 n_2 \\ n_i a_i(-u_2 u_j n_j + \delta g h n_2) & n_i a_i u_2 n_1 & n_i(a_i(u_j n_j + u_2 n_2) + d\sqrt{gh}\ n_j) \end{bmatrix} \tag{4.161}$$

Solving for the dimensional eigenvalues of $\mathcal{A}$

$$\lambda_1^{\mathcal{A},d} \quad = \quad n_i\ (\alpha a_i a_j + \alpha^N a_i^N a_j^N)\ n_j \sqrt{gh}\ +\ n_i a_i u_j n_j \tag{4.162}$$

$$\lambda_{2,3}^{\mathcal{A},d} \quad = \quad n_i\ (\alpha a_i a_j + \alpha^N a_i^N a_j^N)\ n_j \sqrt{gh}\ +\ n_i a_i u_j n_j \pm a_i n_i \sqrt{\delta g h} \tag{4.163}$$

Using the velocity transformation and non-dimensionalizing by division of $\sqrt{gh}$

$$\lambda_1^{\mathcal{A}} \quad = \quad n_i\ (\alpha a_i a_j + \alpha^N a_i^N a_j^N)\ n_j\ +\ n_i a_i v_j n_j Fr \tag{4.164}$$

$$\lambda_{2,3}^{\mathcal{A}} \quad = \quad n_i\ (\alpha a_i a_j + \alpha^N a_i^N a_j^N)\ n_j\ +\ n_i a_i v_j n_j Fr \pm a_i n_i \sqrt{\delta} \tag{4.165}$$

Note that for the case of $\mathbf{a} = \mathbf{n} = \mathbf{v}$, the alignment of the arbitrarily perpendicular axes component and the solution propagation direction with the local velocity, hence streamline direction, the functions α and δ prescribe the associated streamline upstream-bias eigenvalues

$$\lambda_1^{\mathcal{A}_{sl}} = \alpha + Fr \quad , \quad \lambda_{2,3}^{\mathcal{A}_{sl}} = \alpha + Fr \pm \sqrt{\delta} \tag{4.166}$$

where $\lambda_{2,3}^{\mathcal{A}_{sl}}$ are identical to $\lambda_{1,2}^{\mathcal{A}_{sl}}$ for the one-dimensional analysis. This special case of $\mathbf{a} = \mathbf{n} = \mathbf{v}$ is key the ensuing determination of the upstream parameters as the upstream eigenvalues are strictly functions of α and δ and independent of $\mathbf{n}$, $\mathbf{a}$, and $\mathbf{v}$.

4.9.2 Conditions on Upstream-Bias Eigenvalues

Rather than selecting some arbitrary expressions for α and δ and accepting the variations in the upstream-bias eigenvalues, and hence the dissipative character of the upstream matrix, physically consistent forms for the streamline eigenvalues are instead prescribed. From these forms of the eigenvalues, the upstream parameters are then solved to insure physical consistency.

Restating the upstream eigenvalues (4.163) as

$$\lambda_{1,2,3}^{\mathcal{A}} = \lambda_{1,2,3}^{\mathcal{A}}(Fr, \mathbf{n}) \tag{4.167}$$

to stress the dependence upon the Froude number and propagation direction. Five conditions exist for the constraint of the five upstream parameters $\mathbf{a}$, $\mathbf{a}^N$, α, δ, and α^N

$$a_1^2 + a_2^2 = 1 \quad , \quad \lambda_1^{\mathcal{A}}(Fr, \mathbf{n}) \geq 0 \tag{4.168}$$

$$\lambda_1^{\mathcal{A}}(Fr, \mathbf{v}) = \lambda_1^{\mathcal{A}cs} \quad , \quad \lambda_3^{\mathcal{A}}(Fr, \mathbf{v}) = \lambda_3^{\mathcal{A}cs} \tag{4.169}$$

$$\lambda_{2,3}^{\mathcal{A}}(Fr, \mathbf{n}) \geq 0 \tag{4.170}$$

where λ_1^{Acs} and λ_3^{Acs} are the imposed correlated and stable upstream-bias eigenvalues which in turn determine the upstream parameters α and δ. The first condition enforces $\mathbf{a}$ as perpendicular components of a unit vector while the second condition demands that $\mathbf{a} = \mathbf{v}$. Importantly, these two conditions verify that $\mathbf{a}$ and $\mathbf{a}^N$ point in the streamline and crossflow directions respectively. The third and fourth conditions impose specified behavior on the upstream eigenvalues to insure physical consistency. Having established $\mathbf{a}$, $\mathbf{a}^N$, α, and δ, the fifth condition determines α^N.

4.9.3 Upstream Bias Parameters a and $\mathbf{a}^N$

The upstream eigenvalue $\lambda_1^{\mathcal{A}}$, (4.164), repeated for convenience

$$\lambda_1^{\mathcal{A}} = n_i \left(\alpha a_i a_j + \alpha^N a_i^N a_j^N\right) n_j \; + \; n_i a_i v_j n_j Fr \tag{4.171}$$

can be expanded to yield

$$\lambda_1^{\mathcal{A}} = \left(n_i a_i a_j n_j\right) \alpha + \left(n_i a_i^N a_j^N n_j\right) \alpha^N + \left(n_i a_i v_j n_j\right) Fr \tag{4.172}$$

The combinations of $\mathbf{n}$, $\mathbf{a}$, and $\mathbf{a}^N$ preceeding α and α^N are clearly non-negative since

$$n_i a_i a_j n_j = (a_k n_k)^2 \quad , \quad n_i a_i^N a_j^N n_j = (a_k^N n_k)^2 \tag{4.173}$$

Combining this result with the non-negative values of $0 \leq \alpha, \alpha^N \leq 1$ reveals that the first two terms are non-negative for all choices $\mathbf{n}$, $\mathbf{a}$, and $\mathbf{a}^N$. Examining the third term of (4.172), $Fr \geq 0$, hence the upstream convection eigenvalue $\lambda_1^{\mathcal{A},d}$ will remain non-negative when $n_i a_i v_j n_j$ remains non-negative for all $\mathbf{n}$ and $\mathbf{v}$. This condition is satisfied when $\mathbf{a} = \mathbf{v}$

$$n_i a_i v_j n_j = (v_k n_k)^2 \tag{4.174}$$

Thus, for system stability, $\mathbf{a} = \mathbf{v}$ which stipulates $\mathbf{a}$ points in the streamline direction and $\mathbf{a}^N$ points in the crossflow direction. Moreover, from the two-dimensional relationship between $\mathbf{a}$ and $\mathbf{a}^N$

$$a_1 = a_2^N = v_1 \quad , \quad a_2 = -a_1^N = v_2 \tag{4.175}$$

4.9.4 Streamline Eigenvalue $\lambda_3^{\mathcal{A}cs}$

The non-dimensional streamline open-channel eigenvalue $\lambda_3^{OC,sl}$ becomes negative for $Fr < 1$. Per the stability constraint, the upstream-bias eigenvalue $\lambda_3^{\mathcal{A}cs}$ will correlate to the absolute open-channel eigenvalue, hence

$$\lambda_3^{OC,sl} = Fr - 1 \quad \Rightarrow \quad \lambda_3^{\mathcal{A}cs} = |Fr - 1| \tag{4.176}$$

As in the one-dimensional development, a smooth transition at the critical point is desired. Introducing the critical transition layer defined as $1-\epsilon_{Fr} \leq Fr \leq 1+\epsilon_{Fr}$ where ϵ_{Fr} is the transition-layer parameter admits a candidate definition for $\lambda_3^{\mathcal{A}cs}$ as the composite spline [38]

$$\lambda_3^{\mathcal{A}cs}(Fr) \equiv \begin{cases} 1 - Fr & , \quad 0 \leq Fr \leq 1 - \epsilon_{Fr} \\ \frac{(Fr-1)^2}{2\epsilon_{Fr}} + \frac{\epsilon_{Fr}}{2} & , \quad 1 - \epsilon_{Fr} < Fr < 1 + \epsilon_{Fr} \\ Fr - 1 & , \quad 1 + \epsilon_{Fr} \leq Fr \end{cases} \tag{4.177}$$

where, as in one dimension, $\epsilon_{Fr} = 1/5$. The variation of $\lambda_3^{\mathcal{A}cs}(Fr)$ with respect to Fr is presented in Figure (4.15).

4.9.5 Streamline Eigenvalue $\lambda_1^{\mathcal{A}cs}$

The open channel streamline eigenvalue $\lambda_1^{OC,sl}$ remains non-negative for all Froude numbers. As with streamline eigenvalue $\lambda_3^{\mathcal{A}cs}$, streamline eigenvalue $\lambda_1^{\mathcal{A}cs}$ must also equal one for $Fr = 0$. Furthermore, for physical consistencey with the open channel eigenvalues, $\lambda_1^{\mathcal{A}cs} > \lambda_3^{\mathcal{A}cs}$ since

$$\lambda_1^{OC,sl} = Fr \quad > \quad \lambda_3^{OC,sl} = Fr - 1 \tag{4.178}$$

These conditions imply that $\lambda_1^{\mathcal{A}cs} \geq \frac{1}{2}$. A candidate definition for $\lambda_1^{\mathcal{A}cs}$ is the smooth composite spline [38]

$$\lambda_1^{\mathcal{A}cs}(Fr) \equiv \begin{cases} 1 - Fr & , \quad 0 \leq Fr \leq \frac{1}{2} - \epsilon_{Fr} \\ \frac{(Fr - \frac{1}{2})^2}{2\epsilon_{Fr}} + \frac{1+\epsilon_{Fr}}{2} & , \quad \frac{1}{2} - \epsilon_{Fr} < Fr < \frac{1}{2} + \epsilon_{Fr} \\ Fr & , \quad \frac{1}{2} + \epsilon_{Fr} \leq Fr \end{cases} \tag{4.179}$$

where again $\epsilon_{Fr} = 1/5$. The variation of $\lambda_1^{\mathcal{A}cs}(Fr)$ with respect to Fr is presented in Figure (4.15).

4.9.6 Upstream Bias Parameters α and δ and Streamline Eigenvalue λ_2

From the streamline upstream eigenvalues (4.166), eigenvalues $\lambda_1^{\mathcal{A}_{sl}}$ and $\lambda_3^{\mathcal{A}}$ can be solved for the upstream parameters α and δ

$$\lambda_1^{\mathcal{A}_{sl}} = \alpha + Fr \quad \rightarrow \quad \alpha = \lambda_1^{\mathcal{A}cs} - Fr \tag{4.180}$$

$$\lambda_3^{\mathcal{A}_{sl}} = \alpha + Fr - \sqrt{\delta} \quad \rightarrow \quad \delta = (\lambda_1^{\mathcal{A}cs} - \lambda_3^{\mathcal{A}cs})^2 \tag{4.181}$$

where $\lambda_1^{\mathcal{A}cs}$ and $\lambda_3^{\mathcal{A}cs}$ are the imposed upstream eigenvalues of (4.179) and (4.177) respectively.

The upstream streamline eigenvalue $\lambda_2^{\mathcal{A},sl}$ remains a non-negative function of α, δ, and Fr and will therefore not have an imposed functional variation. As a function of the imposed eigenvalue variation, however, it will bear the $\mathcal{A}cs$ superscript for clarity. Substituting

$$\lambda_2^{\mathcal{A},sl} = \alpha + Fr + \sqrt{\delta} \quad \Rightarrow \quad \lambda_2^{\mathcal{A}cs}(Fr) = 2\lambda_1^{\mathcal{A}cs} - \lambda_3^{\mathcal{A}cs} \tag{4.182}$$

4.9.7 Upstream Bias Parameter α^N

The final free parameter, α^N, is constrained from the fifth condition $\lambda_{2,3}(Fr, \mathbf{n}) \geq 0$ (4.170) following the analagous development for the gas dynamic Euler equations in [38]. Recall that $\mathbf{a} = \mathbf{v}$ is perpendicular to $\mathbf{a}^N$. The vector dot products $n_i a_i = n_i v_i$ and $n_i a_i^N = n_i v_i^N$ between the solution propagation direction unit vector n_i and the velocity unit vectors v_i and v_i^N permit the expressions

$$n_i v_i = \cos(\bar{\theta}) \quad , \quad n_i v_i^N v_j^N n_j = \sin^2(\bar{\theta}) \quad , \quad \bar{\theta} \equiv \theta - \theta_v \tag{4.183}$$

where, as in the convection limit analysis, θ and θ_v denote the angles between the x_1 axis and $\mathbf{n}$ and $\mathbf{v}$ respectively.

Recalling eigenvalue $\lambda_3(Fr, \mathbf{n})$ from (4.165), the condition $\lambda_3(Fr, \mathbf{n}) \geq 0$ indicates

$$\lambda_3 = n_i \left(\alpha v_i v_j + \alpha^N v_i^N v_j^N\right) n_j \; + \; n_i v_i v_j n_j Fr - v_i n_i \sqrt{\delta} \;\; \geq 0 \tag{4.184}$$

Employing the trigonometric substitutions (4.183) and solving for α^N

$$\alpha^N \;\; \geq \;\; g(\bar{\theta}, Fr) \equiv \frac{\cos\bar{\theta}\sqrt{\delta} - \cos^2\bar{\theta}(\alpha + Fr)}{1 - \cos^2\bar{\theta}} \tag{4.185}$$

For supercritical flows where $Fr \geq 1 + \epsilon_{Fr}$, the upstream bias parameters α and δ simplify to $\alpha = 0$ and $\delta = 1$, hence

$$\alpha^N \;\geq\; g(\bar{\theta}, Fr) = \frac{\cos\bar{\theta} - Fr\cos^2\bar{\theta}}{1 - \cos^2\bar{\theta}} \tag{4.186}$$

Importantly, α^N will be greater than the maximum value of $g(\bar{\theta}, Fr)$ with respect to $\bar{\theta}$ for every value of Fr, denoted $g_{max}(Fr)$. Solving for the extremums of (4.186) with respect to $\bar{\theta}$

$$\frac{\partial g(\bar{\theta}, Fr)}{\partial \bar{\theta}} = 0 \quad \Rightarrow \quad \cos^2\bar{\theta} - 2Fr\cos\bar{\theta} + 1 = 0 \tag{4.187}$$

which yields

$$\cos\bar{\theta}\Big|_{g=g_{max}} = Fr - \sqrt{Fr^2 - 1} \quad , \quad g_{max}(Fr) = \frac{1}{2}\left(Fr - \sqrt{Fr^2 - 1}\right) \tag{4.188}$$

Heed that the same solution for $g_{max}(Fr)$ arises from the condition $\lambda_2 \geq 0$. Hence

$$\alpha^N(Fr) \geq \frac{1}{2}\left(Fr - \sqrt{Fr^2 - 1}\right) \quad , \quad Fr \geq Fr_{Fr} \equiv 1 + \epsilon_{Fr} \tag{4.189}$$

where Fr_{Fr} is the ceiling of the supercritical transition layer. Noting that $\lambda_3(1, \mathbf{v}) = \epsilon_{Fr}/2$, an analogous equality for α^N evaluated at Fr_{Fr} yields

$$\alpha^N(Fr_{Fr}) = g_{max}(Fr_{Fr}) + \frac{\epsilon_{Fr}}{2} \tag{4.190}$$

Having established the form of α^N in the supercritical flow regime, the subcritical form of α^N must be determined. Under the constraint of isotropic acoustic upstreaming for vanishing Fr, $\alpha^N(0) = 1$. A smooth approach to $\alpha^N(0) = 1$ is also required as one derivative of α^N must exist,

hence $\partial\alpha^N/\partial Fr|_{Fr=0}$. The final constraint is that α^N must smoothly transition to (4.189) for supercritical flows. A smooth variation for α^N which satisfies these constraints is the spline [38]

$$\alpha^N \equiv \begin{cases} 1 + \left(\frac{3(\alpha^N(Fr_{Fr})-1)}{Fr_{Fr}^2} - \frac{\alpha^{N'}(Fr_{Fr})}{Fr_{Fr}}\right) Fr^2 & \\ \quad + \left(\frac{\alpha^{N'}(Fr_{Fr})}{Fr_{Fr}^2} - \frac{2(\alpha^N(Fr_{Fr})-1)}{Fr_{Fr}^3}\right) Fr^3 & , \quad 0 \leq Fr < Fr_{Fr} \\ \frac{1}{2}\left(1 + \frac{\epsilon_{Fr}}{Fr_{Fr}-\sqrt{Fr_{Fr}^2-1}}\right)\left(Fr - \sqrt{Fr^2-1}\right) & , \quad Fr_{Fr} \leq Fr \end{cases} \tag{4.191}$$

where

$$\alpha^N(Fr_{Fr}) = \frac{1}{2}\left(Fr_{Fr} - \sqrt{Fr_{Fr}^2 - 1}\right) + \frac{\epsilon_{Fr}}{2} \tag{4.192}$$

and $\alpha^{N'}$ denotes differentiation with respect to Fr, hence

$$\alpha^{N'}(Fr_{Fr}) = \frac{1}{2}\left(1 - \frac{Fr_{Fr}}{\sqrt{Fr_{Fr}^2 - 1}}\right) \tag{4.193}$$

4.9.8 Upstream Eigenvalue and Bias Parameter Summary

Plotting the variation of the imposed streamline upstream eigenvalues $\lambda_{1,2,3}^{\mathcal{A}cs,sl}$ with respect to Fr in Figure (4.15) shows them to remain positive for all values of Fr while the associated streamline open channel eigenvalue $\lambda_3^{OC_{sl}}$ is negative for $Fr < 0$. Additionally, both the streamline upstream eigenvalues and their slopes remain continuous for all Froude numbers. Within the subcritical flow regime, $0 \leq Fr \leq 1 + \epsilon_{Fr}$, all three eigenvalues smoothly approach one for vanishing Froude numbers. The physically consistent isotropic upstream-bias approximation of the celerity limit is thus correctly reflected. Within the super-critical flow regime, $Fr > 1 + \epsilon_{Fr}$, these eigenvalues coincide with the streamline open channel eigenvalues $\lambda_1^{OC_{sl}} = Fr$, $\lambda_2^{OC_{sl}} = Fr + 1$, $\lambda_3^{OC_{sl}} = Fr - 1$. A physically consistent streamline upstream bias approximation of the entire dissipative flux vector is thus correctly reflected. Streamline upstream eigenvalue $\lambda_1^{\mathcal{A}cs,sl}$ clearly remains greater than $\lambda_3^{\mathcal{A}cs,sl}$

as stipulated by section (4.9.5). Finally, within the critical transition layer $1 - \epsilon_{Fr} \leq Fr \leq 1 + \epsilon_{Fr}$, the streamline open channel eigenvalue $\lambda_3^{OC_{sl}}$ vanishes while the streamline upstream eigenvalue $\lambda_3^{Acs,sl}$ smoothly transitions while remaining no less than $\epsilon_{Fr}/2$.

Plotting the variations in the upstream parameters α, δ, and α^N in Figure (4.16) shows these three functions and their slopes to be continuous and smooth for all Froude numbers. Their values correctly range as $0 \leq \alpha, \delta, \alpha^N \leq 1$ while $\alpha = 0$ for $Fr > 1/2 + \epsilon_{Fr}$, $\alpha = 1$ for $Fr = 1$, $\delta = 0$ for $Fr < 0.3$, and $\delta = 1$ for $Fr > 1 + \epsilon_{Fr}$.

The variation in the celerity gradient upstream bias parameter δ is seen to increase monotonically, yet remains less than 25% of its maximum for $0 \leq Fr \leq 0.7$. As δ increases, the celerity flow parameter α monotonically decreases to 75% of its maximum value for $Fr = 0.4$. This balance in upstream components correctly reflects the shifting of bi-modal propagation modes to mono-axial as the Froude number increases.

The decrease of the cross-flow upstream bias α^N is monotone while less rapid than that exhibited by α as it is the only contribution to the cross-flow wedge region. At the critical point, nevertheless, α^N is decreased by 50% and by 80% for $Fr = 2.0$. Heed that the enforcement of $\lambda_3 \geq 0$ to yield a functional form for α^N as opposed to the arbitrary assignment of a constant or positive function to α^N insures appropriate crossflow dissipation. In the limit as $Fr \to \infty$, the composite spline for α^N, (4.191), indicates

$$\lim_{Fr \to \infty} \alpha^N(Fr) = 0 \quad , \quad \lim_{Fr \to \infty} \frac{\partial \alpha^N}{\partial Fr} = 0 \tag{4.194}$$

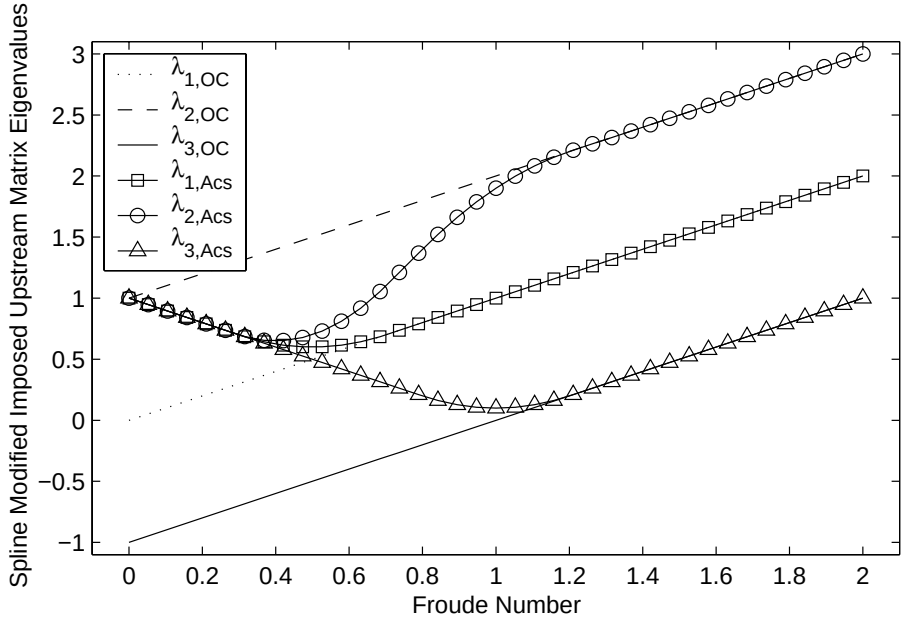

Figure 4.15: Two-Dimensional Spline Modified, Imposed Upstream Eigenvalue Spectra

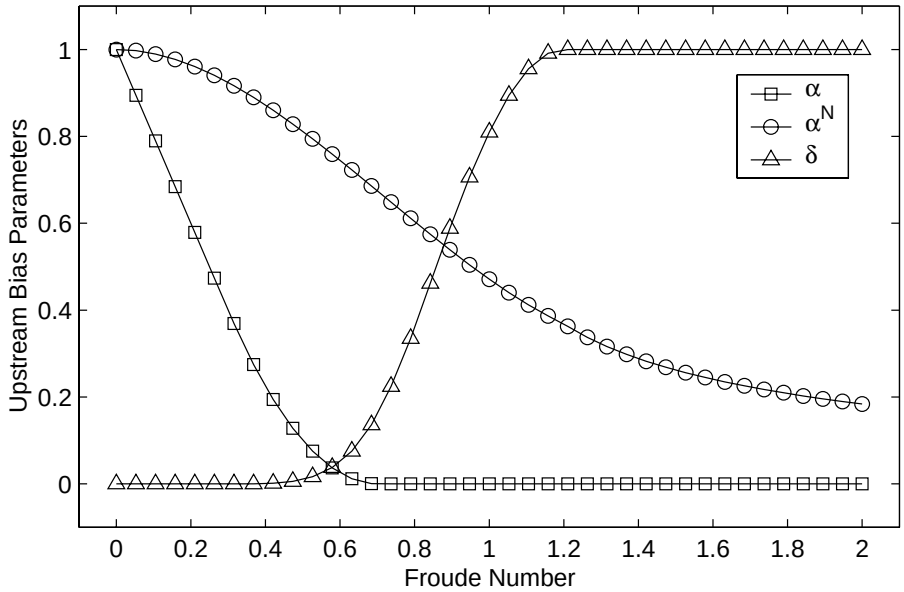

Figure 4.16: Two-Dimensional Upstream Bias Parameter Spectra

The magnitude of the crossflow dissipation contribution therefore smoothly approaches zero with increasing Froude number. Again physical consistency of the upstream parameters is witnessed as, in the high Froude discussion of (4.3), the bi-modal propagation region narrows about the crossflow direction. As such, the need for celerity crossflow dissipation is reduced and correctly reflected in α^N.

Summarizing the upstream eigenvalues and upstream bias parameters for convenience:

$$\lambda_1^{\mathcal{A}cs}(Fr) \equiv \begin{cases} 1 - Fr & , \quad 0 \leq Fr \leq \frac{1}{2} - \epsilon_{Fr} \\ \frac{(Fr-\frac{1}{2})^2}{2\epsilon_{Fr}} + \frac{1+\epsilon_{Fr}}{2} & , \quad \frac{1}{2} - \epsilon_{Fr} < Fr < \frac{1}{2} + \epsilon_{Fr} \\ Fr & , \quad \frac{1}{2} + \epsilon_{Fr} \leq Fr \end{cases} \tag{4.195}$$

$$\lambda_3^{\mathcal{A}cs}(Fr) \equiv \begin{cases} 1 - Fr & , \quad 0 \leq Fr \leq 1 - \epsilon_{Fr} \\ \frac{(Fr-1)^2}{2\epsilon_{Fr}} + \frac{\epsilon_{Fr}}{2} & , \quad 1 - \epsilon_{Fr} < Fr < 1 + \epsilon_{Fr} \\ Fr - 1 & , \quad 1 + \epsilon_{Fr} \leq Fr \end{cases} \tag{4.196}$$

where $\epsilon_{Fr} = 1/5$.

$$\lambda_2^{\mathcal{A}cs}(Fr) = \alpha + Fr + \sqrt{\delta} \tag{4.197}$$

$$a_i = v_i = \frac{u_i}{\sqrt{u_k u_k}} \quad ; \quad a_1 = a_2^N \quad , \quad a_2 = -a_1^N \tag{4.198}$$

$$\alpha = \lambda_1^{\mathcal{A}cs} - Fr \quad , \quad \delta = (\lambda_1^{\mathcal{A}cs} - \lambda_3^{\mathcal{A}cs})^2 \tag{4.199}$$

$$\alpha^N \equiv \begin{cases} 1 + \left(\frac{3(\alpha^N(Fr_{Fr})-1)}{Fr_{Fr}^2} - \frac{\alpha^{N'}(Fr_{Fr})}{Fr_{Fr}} \right) Fr^2 \\ \quad + \left(\frac{\alpha^{N'}(Fr_{Fr})}{Fr_{Fr}^2} - \frac{2(\alpha^N(Fr_{Fr})-1)}{Fr_{Fr}^3} \right) Fr^3 & , \quad 0 \leq Fr < Fr_{Fr} \\ \frac{1}{2}\left(1 + \frac{\epsilon_{Fr}}{Fr_{Fr} - \sqrt{Fr_{Fr}^2 - 1}}\right)\left(Fr - \sqrt{Fr^2 - 1}\right) & , \quad Fr_{Fr} \leq Fr \end{cases} \tag{4.200}$$

where $Fr_{Fr} = 1 + \epsilon_{Fr}$ and

$$\alpha^N(Fr_{Fr}) = \frac{1}{2}\left(Fr_{Fr} - \sqrt{Fr_{Fr}^2 - 1}\right) + \frac{\epsilon_{Fr}}{2} \tag{4.201}$$

$$\alpha^{N'}(Fr_{Fr}) = \frac{1}{2}\left(1 - \frac{Fr_{Fr}}{\sqrt{Fr_{Fr}^2 - 1}}\right) \tag{4.202}$$

4.10 Upstream Bias Magnitude

The directional variation of the upstream bias eigenvalues, hence upstream bias magnitude, is presented in Figures (4.17) - (4.22) for representative subcritical and supercritical Froude numbers of $Fr = 0.00, 0.05, 0.5, 1.5, 2.0$. As with the preliminary polar variation analysis of the open channel eigenvalues, Section (4.3), a variable propagation unit vector $\mathbf{n} \equiv (\cos\theta, \sin\theta)$ and a fixed velocity unit vector $\mathbf{a} = \mathbf{v}$, inclined at 30˙ from the x_1 axis, are employed.

Repeating the non-dimensional upstream eigenvalues (4.164)-(4.165) with $\mathbf{a} = \mathbf{v}$

$$\lambda_1^{\mathcal{A}} = n_i\left(\alpha v_i v_j + \alpha^N v_i^N v_j^N\right) n_j + n_i v_i v_j n_j Fr \tag{4.203}$$

$$\lambda_{2,3}^{\mathcal{A}} = n_i\left(\alpha v_i v_j + \alpha^N v_i^N v_j^N\right) n_j + n_i v_i v_j n_j Fr \pm v_i n_i \sqrt{\delta} \tag{4.204}$$

Employing the trigonometric substitutions (4.183) introduced in the determination of α^N, Section (4.9.7)

$$n_i v_i = \cos\bar{\theta} \quad , \quad n_i v_i^N v_j^N n_j = \sin^2\bar{\theta} \quad , \quad \bar{\theta} \equiv \theta - \theta_v \tag{4.205}$$

where θ and θ_v denote the angles between the x_1 axis and $\mathbf{n}$ and $\mathbf{v}$ respectively, admits the simplification

$$\lambda_1^{\mathcal{A}} = \alpha \cos^2 \bar{\theta} + \alpha^N \sin^2 \bar{\theta} + Fr \ \cos^2 \bar{\theta} \tag{4.206}$$

$$\lambda_{2,3}^{\mathcal{A}} = \alpha \cos^2 \bar{\theta} + \alpha^N \sin^2 \bar{\theta} + Fr \ \cos^2 \bar{\theta} \pm \sqrt{\delta} \ \cos \bar{\theta} \tag{4.207}$$

Heed that the upstream bias parameters α and δ, as given in (4.180), are functions of the imposed streamline eigenvalues and thus independent of $\mathbf{n}$. Additionally, the upstream bias parameter α^N, while initially a function of $\mathbf{n}$ and $\mathbf{v}$, is nevertheless computed strictly as a function of Fr and hence also independent of $\mathbf{n}$.

These polar plots of the upstream eigenvalues, hence magnitudes of the dissipative upstream flux divergence, demonstrate a physically consistent upstream bias because, for all Fr and propagations directions $\mathbf{n}$, the upstream eigenvalues remain positive and their directional variation mirrors the directional variation of the open channel eigenvalues shown in Figures (4.1) - (4.6). As with the open channel eigenvalues, the upstream eigenvalues are symmetric about the streamline and crossflow directions.

For $Fr = 0$, all three upstream eigenvalues are uniformly unity, thus correctly reflecting an isotropic celerity bias. As the Froude number increases to $Fr = 0.05$, the directional variation in the upstream eigenvalues becomes slightly anisotropic and hence correlates with the open channel eigenvalue distribution of Figure (4.2). The upstream eigenvalue distribution becomes increasingly anisotropic as the Froude number increases and is well evident at $Fr = 0.5$. For supercritical Froude numbers, the anisotropy is fully evolved while its distribution correlates with the anisotropic distribution of the open channel eigenvalues in Figures (4.5) - (4.6).

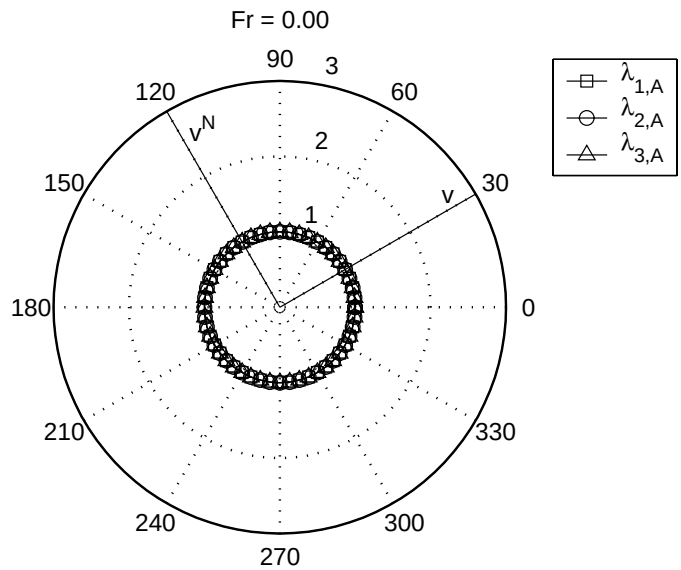

Figure 4.17: Polar Variation of Upstream Eigenvalues : $Fr = 0.00$

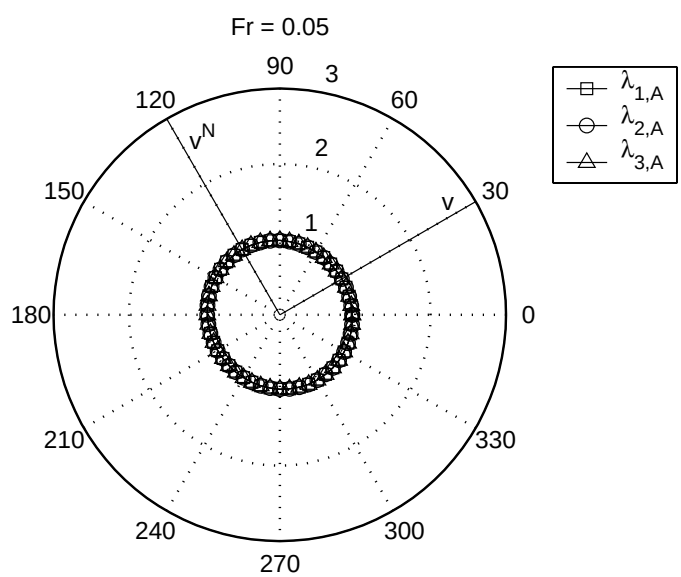

Figure 4.18: Polar Variation of Upstream Eigenvalues : $Fr = 0.05$

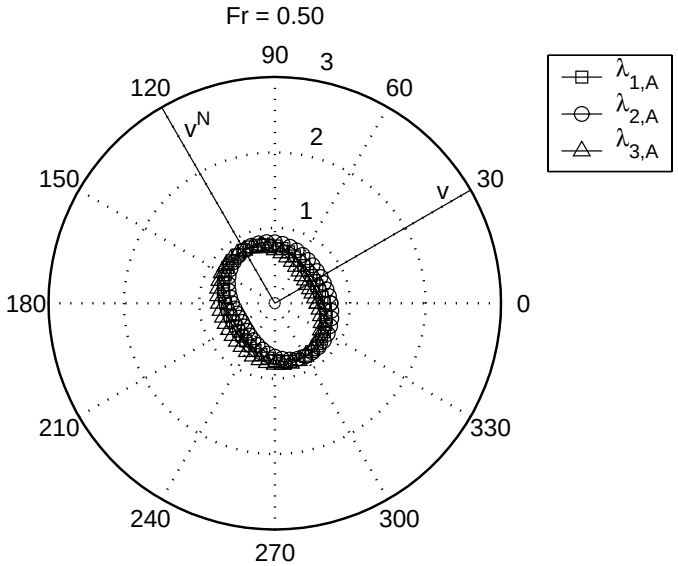

Figure 4.19: Polar Variation of Upstream Eigenvalues : $Fr = 0.50$

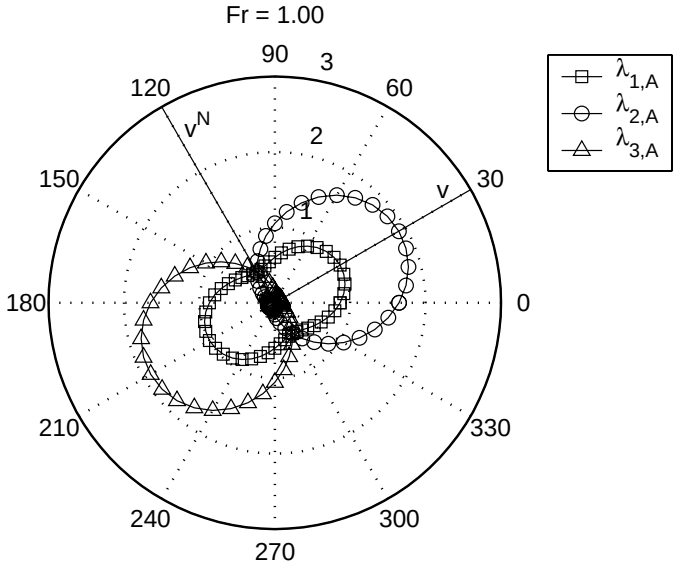

Figure 4.20: Polar Variation of Upstream Eigenvalues : $Fr = 1.00$

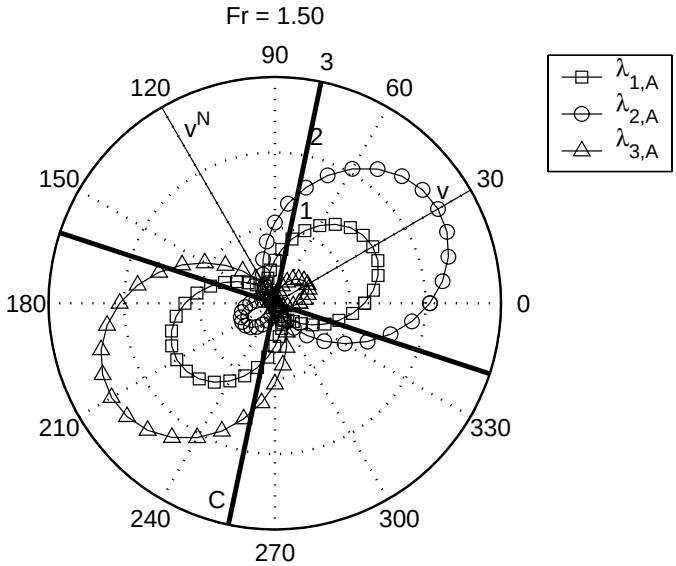

Figure 4.21: Polar Variation of Upstream Eigenvalues : $Fr = 1.50$

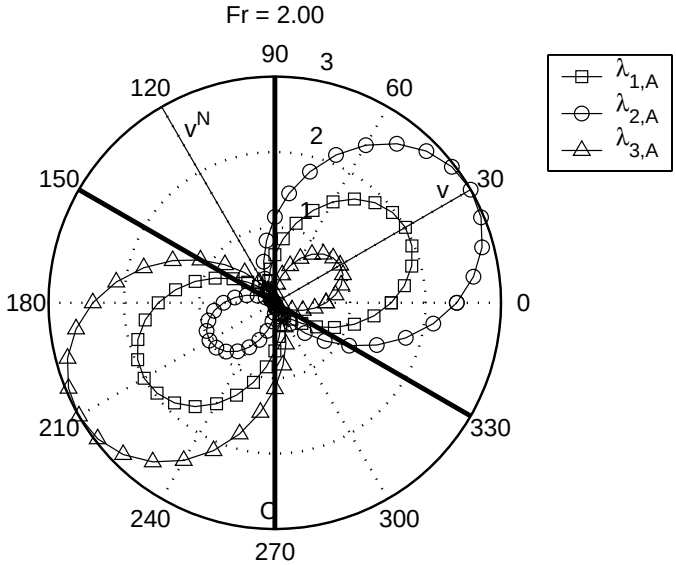

Figure 4.22: Polar Variation of Upstream Eigenvalues : $Fr = 2.00$

Directly comparing the directional variation of the open channel eigenvalues with their associated upstream eigenvalues clearly verifies their correlation. Representative sub- and supercritical Froude numbers of $Fr = 0.5, 2.0$ for each eigenvalue under the previous conditions of a fixed velocity unit vector $\mathbf{a} = \mathbf{v}$, inclined at $30^{\cdot}$ from the x_1 axis are presented in Figures (4.23) - (4.28).

As indicated in Figures (4.23) - (4.24), the upstream convection eigenvalue λ_1^A, just like the open channel convection eigenvalue λ_1^{OC}, is symmetric about the streamline direction. For subcritical Froude numbers, λ_1^A strongly exhibits the bi-modal propagation mode in the crossflow wedge region. As the Froude number increases to the critical point, the distribution of λ_1^A becomes topologically similar to λ_1^{OC}, hence correctly decreasing the amount of crossflow dissipation. For supercritical flows, the crossflow dissipation continues to decrease. Note that, in the streamline direction, $\lambda_1^A = \lambda_1^{OC}$ while $\lambda_1^A < \lambda_1^{OC}$ as $\mathbf{n}$ rotates from $\mathbf{v}$ to $\mathbf{v}^N$, again correctly decreasing the level of dissipation away from the streamline direction.

The celerity-convection upstream eigenvalues $\lambda_{2,3}^A$, being mirror-skew symmetric, will be discussed with λ_2^A, Figures (4.25) - (4.26), being representative. Unlike λ_1^A and λ_1^{OC}, λ_2^A and λ_2^{OC} are topologically similar for all Froude numbers, hence correctly exhibiting the bi-modal and mono-axial flow modes inherent to the open channel celerity-convection eigenvalue. For subcritical flows, λ_2^A and λ_2^{OC} nearly coincide, hence correctly reflecting isotropic celerity propagation. As the Froude number increase, the distributions of both eigenvalues becomes increasingly anisotropic, correctly reflecting the shifting from bi-modal to mono-axial propagation modes. Heed that, for the anisotropic subcritical modes, $\lambda_2^A < \lambda_2^{OC}$ in the streamline direction. This correctly reflects minimal streamline diffusion as depicted in Figure (4.15) where $\lambda_2^A < Fr + 1$. For supercritical flows, the streamline values of λ_2^A are identical to the streamline values of λ_2^{OC}, in accordance to streamline eigenvalue distribution of Figure (4.15). Within the crossflow wedge, the upstream celerity-convection eigenvalues become vanishingly small, correctly corresponding to minimal crossflow dissipation.

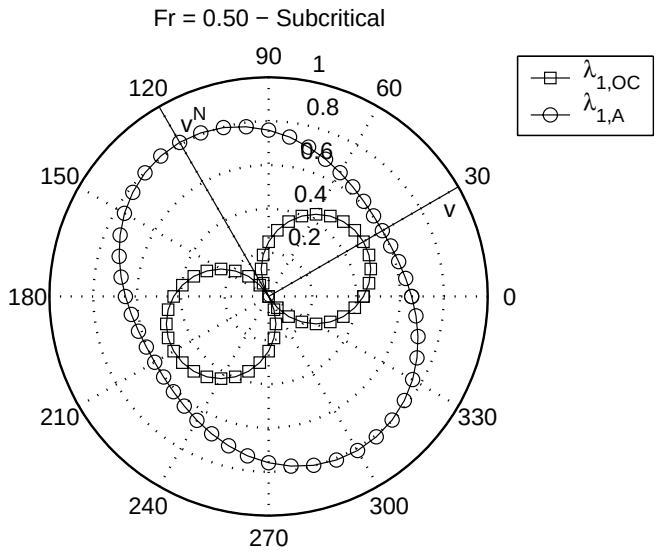

Figure 4.23: Subcritical Polar Correlation of λ_1^{OC} and λ_1^{A}

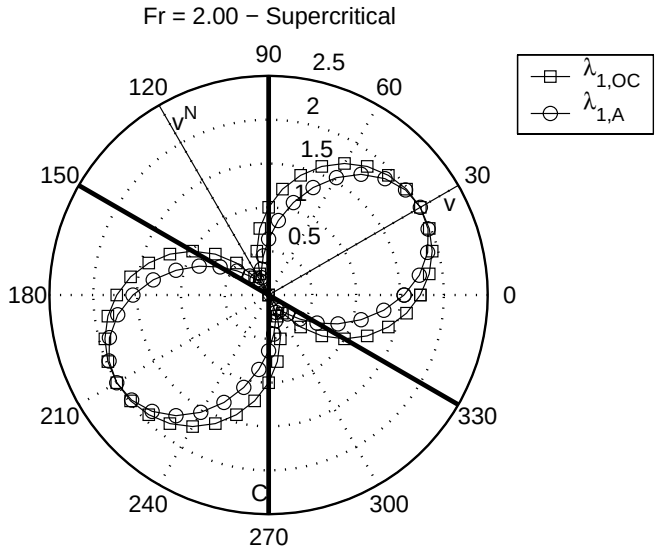

Figure 4.24: Supercritical Polar Correlation of λ_1^{OC} and λ_1^{A}

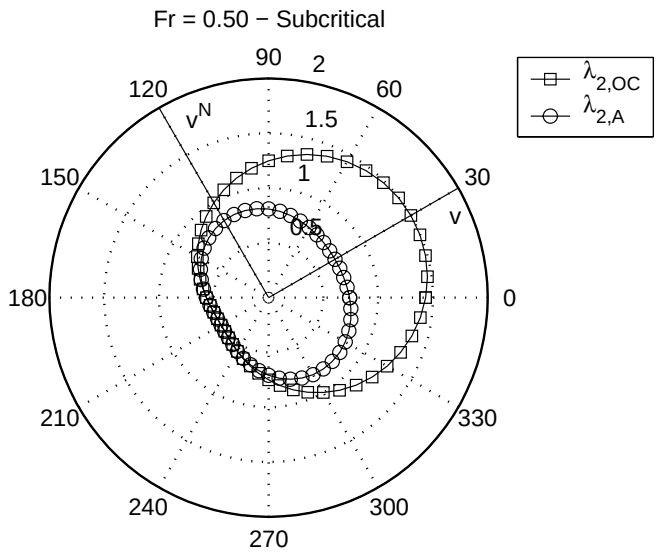

Figure 4.25: Subcritical Polar Correlation of λ_2^{OC} and λ_2^{A}

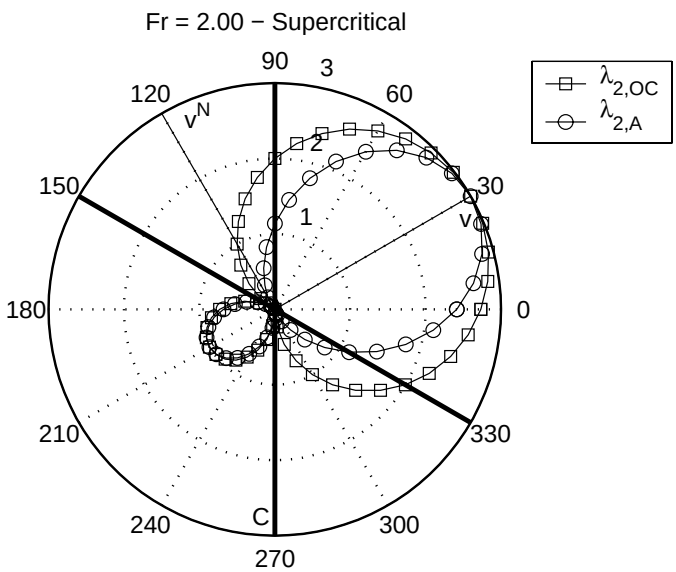

Figure 4.26: Supercritical Polar Correlation of λ_2^{OC} and λ_2^{A}

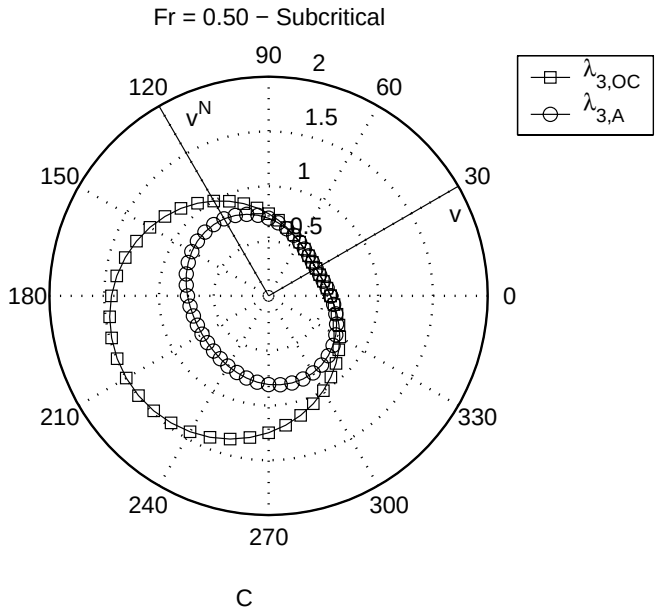

Figure 4.27: Subcritical Polar Correlation of λ_3^{OC} and λ_3^{A}

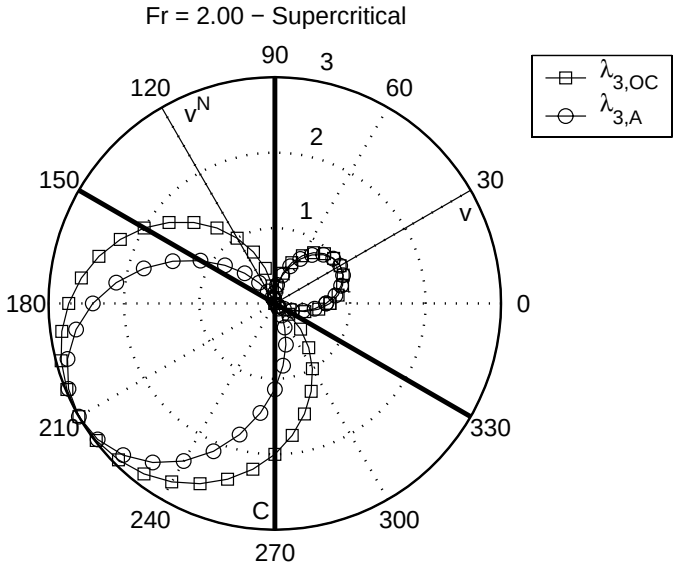

Figure 4.28: Supercritical Polar Correlation of λ_3^{OC} and λ_3^{A}

4.11 Spatial Discretization

The final step is to generate the semi-discrete spatial approximation to the characteristics-biased open channel flow conservation law system weak form. The standard procedure, following the one-dimensional development, is to

1. Define a conservation law system $L(\mathbf{q}) = 0$

2. Constrain the weak form test function arbitrariness

3. Implement the resultant weak statement formulation $\int_\Omega \Phi_\alpha L(\mathbf{q}) d\Omega = 0$

4. Define a continuum approximation to the state and group variables $\mathbf{q}(\mathbf{x}, t) \approx \mathbf{q}^h(\mathbf{x}, t) \equiv \Psi_\beta(\mathbf{x})\mathbf{Q}_\beta(t)$, hence the approximate weak statement $\int_{\hat{\Omega}} \Phi_\alpha L^h(\mathbf{q}) d\hat{\Omega} \approx 0$

5. Extremize the approximation error via the Galerkin definition $\Phi_\alpha = \Psi_\alpha$

6. Select the form of the approximation to be the inner product of a set of compact support Lagrangian interpolating polynomials of degree k and their associated expansion coefficients, hence $\mathbf{q}^N(\mathbf{x}, t) \equiv \mathbf{q}^h(\mathbf{x}, t) \equiv \{N_k(\mathbf{x})\}^T\{\mathbf{Q}(t)\}$ and $\Psi_\alpha(\mathbf{x}) \equiv \{N_k(\mathbf{x})\}$, hence form

$$\bigcup_{\Omega^h} \int_{\Omega^h} \{N_k(\mathbf{x})\} L(\mathbf{q}^h) d\Omega \equiv 0 \tag{4.208}$$

By the identified steps:

1. The conservation law system from (4.84)

$$L(\mathbf{q}) = \frac{\partial \mathbf{q}}{\partial t} + \frac{\partial f_j^c(\mathbf{q})}{\partial x_j} = 0 \tag{4.209}$$

leads to the modified conservation law system

$$L(\mathbf{q}) = \frac{\partial \mathbf{q}}{\partial t} + \frac{\partial f_j}{\partial x_j} - \frac{\partial}{\partial x_i}\left[\epsilon\psi\left(\sqrt{gh}(\alpha a_i a_j + \alpha^N a_i^N a_j^N)\frac{\partial \mathbf{q}}{\partial x_j} + a_i\delta\frac{\partial f_j^{cel}}{\partial x_j} + a_i\frac{\partial f_j^{conv}}{\partial x_j}\right)\right] = 0 \tag{4.210}$$

2,3. Forming the weak form for (4.210) with extremization leading to the set of test functions Φ_α

$$\begin{aligned}\int_\Omega \Phi_\alpha L(\mathbf{q}) d\Omega &= \int_\Omega \Phi_\alpha \left[\frac{\partial \mathbf{q}}{\partial t} + \frac{\partial f_j}{\partial x_j}\right. \\ &\quad \left. - \frac{\partial}{\partial x_i}\left[\epsilon\psi\left(\sqrt{gh}(\alpha a_i a_j + \alpha^N a_i^N a_j^N)\frac{\partial \mathbf{q}}{\partial x_j} + a_i\delta\frac{\partial f_j^{cel}}{\partial x_j} + a_i\frac{\partial f_j^{conv}}{\partial x_j}\right)\right]\right] d\Omega \\ &= 0 \end{aligned} \tag{4.211}$$

Distributing the test function Φ_α and expanding the integral isolates the second-order differential term

$$\begin{aligned}&\int_\Omega \Phi_\alpha \left[\frac{\partial \mathbf{q}}{\partial t} + \frac{\partial f_j}{\partial x_j}\right] d\Omega + \\ &\int_\Omega \Phi_\alpha \left[\frac{\partial}{\partial x_i}\left[\epsilon\psi\left(\sqrt{gh}(\alpha a_i a_j + \alpha^N a_i^N a_j^N)\frac{\partial \mathbf{q}}{\partial x_j} + a_i\delta\frac{\partial f_j^{cel}}{\partial x_j} + a_i\frac{\partial f_j^{conv}}{\partial x_j}\right)\right]\right] d\Omega = 0\end{aligned} \tag{4.212}$$

Integrating the second-order differential term by parts

$$\begin{aligned}&-\int_\Omega \frac{\Phi_\alpha}{\partial x_i}\left[\epsilon\psi\left(\sqrt{gh}(\alpha a_i a_j + \alpha^N a_i^N a_j^N)\frac{\partial \mathbf{q}}{\partial x_j} + a_i\delta\frac{\partial f_j^{cel}}{\partial x_j} + a_i\frac{\partial f_j^{conv}}{\partial x_j}\right)\right] d\Omega \\ &+\Phi_\alpha \frac{\partial}{\partial x_i}\left[\epsilon\psi\left(\sqrt{gh}(\alpha a_i a_j + \alpha^N a_i^N a_j^N)\frac{\partial \mathbf{q}}{\partial x_j} + a_i\delta\frac{\partial f_j^{cel}}{\partial x_j} + a_i\frac{\partial f_j^{conv}}{\partial x_j}\right)\right]\Bigg|_{\partial\Omega}\end{aligned} \tag{4.213}$$

As with the one-dimensional analysis, the characteristics bias should not influence the domain boundary conditions, hence $\Phi(\partial\Omega) = 0$. Having eliminated the boundary integral, the terminal continuum weak statement is

$$
\begin{aligned}
\int_\Omega \Phi_\alpha L(\mathbf{q}) d\Omega &= \int_\Omega \left[\Phi_\alpha \left(\frac{\partial \mathbf{q}}{\partial t} + \frac{\partial f_j}{\partial x_j} \right) \right. \\
&\quad \left. + \epsilon\psi \frac{\partial \Phi_\alpha}{\partial x_i} \left(\sqrt{gh}(\alpha a_i a_j + \alpha^N a_i^N a_j^N) \frac{\partial \mathbf{q}}{\partial x_j} + a_i \delta \frac{\partial f_j^{cel}}{\partial x_j} + a_i \frac{\partial f_j^{conv}}{\partial x_j} \right) \right] d\Omega \\
&= 0 \qquad (4.214)
\end{aligned}
$$

4. Continuum approximations to the vector of state variables $\mathbf{q}$ and the flux vectors $f_j(\mathbf{q})$, $f_j^{cel}(\mathbf{q})$, and $f_j^{conv}(\mathbf{q})$ are formed via a linear combination of spatially dependent weight functions and temporally dependent expansion coefficients. For a generic scalar variable p

$$
p(\mathbf{x}, t) \approx p^N(\mathbf{x}, t) \equiv \sum_{\beta=1}^{N} \Psi_\beta(\mathbf{x}) P_\beta(t) \qquad (4.215)
$$

Approximating the state and group variables

$$
\begin{aligned}
\mathbf{q}(\mathbf{x}, t) \approx \mathbf{q}^N(\mathbf{x}, t) &\equiv \sum_{\beta=1}^{N} \Psi_\beta(\mathbf{x}) \mathbf{Q}_\beta(t) && (4.216) \\
f_j(\mathbf{x}, t) \approx f_j^N(\mathbf{x}, t) \approx f_j^N(\mathbf{q}^N(\mathbf{x}, t)) &\equiv \sum_{\beta=1}^{N} \Psi_\beta(\mathbf{x}) F_{j,\beta}(\mathbf{q}^N, t) && (4.217) \\
f_j^{cel}(\mathbf{x}, t) \approx f_j^{cel^N}(\mathbf{x}, t) \approx f_j^{cel^N}(\mathbf{q}^N(\mathbf{x}, t)) &\equiv \sum_{\beta=1}^{N} \Psi_\beta(\mathbf{x}) F_{j,\beta}^{cel}(\mathbf{q}^N, t) && (4.218) \\
f_j^{conv}(\mathbf{x}, t) \approx f_j^{conv^N}(\mathbf{x}, t) \approx f_j^{conv^N}(\mathbf{q}^N(\mathbf{x}, t)) &\equiv \sum_{\beta=1}^{N} \Psi_\beta(\mathbf{x}) F_{j,\beta}^{conv}(\mathbf{q}^N, t) && (4.219)
\end{aligned}
$$

where

$$
\mathbf{q} = \left\{ \begin{array}{c} h \\ m_1 \\ m_2 \end{array} \right\} \quad \text{and} \quad f_j = \left\{ \begin{array}{c} m_j \\ \frac{m_j}{h} m_1 + g \frac{h^2}{2} \delta_1^j \\ \frac{m_j}{h} m_2 + g \frac{h^2}{2} \delta_2^j \end{array} \right\} \qquad (4.220)
$$

$$f_j^{cel} = \left\{ \begin{array}{c} 0 \\ g\frac{h^2}{2}\delta_1^j \\ g\frac{h^2}{2}\delta_2^j \end{array} \right\} \quad \text{and} \quad f_j^{conv} = \left\{ \begin{array}{c} m_j \\ \frac{m_j}{h}m_1 \\ \frac{m_j}{h}m_2 \end{array} \right\} \tag{4.221}$$

While the continuum approximation (4.215) can accomodate the upstream parameters, for computational efficiency this dissertation employs piecewise constant, locally averaged values for ϵ, ψ, $\mathbf{a}$, $\mathbf{a}^N$, α, α^N and δ. The final issue is the handling of $\sqrt{gh}$ in the dissipation term. The square root of gh will be approximated via (4.215) as a grouped variable

$$\sqrt{gh(\mathbf{x},t)} \approx \sqrt{(gh)^N(\mathbf{x},t)} \quad \equiv \quad \sum_{\beta=1}^{N} \Psi_\beta(\mathbf{x}) SQRGH_\beta(\mathbf{q}^N, t) \tag{4.222}$$

Generating the continuum approximation to the continum statement (4.214)

$$\begin{aligned} \int_\Omega \Phi_\alpha L^N(\mathbf{q}) d\Omega \quad &= \quad \int_\Omega \left[\Phi_\alpha \left(\Psi_\beta \frac{d\mathbf{Q}_\beta}{dt} + \frac{\partial \Psi_\beta}{\partial x_j} F_{j,\beta} \right) \right. \\ &\quad + \epsilon\psi \frac{\partial \Phi_\alpha}{\partial x_i} \left(\sqrt{g}\ \Psi_\beta SQRGH_\beta \left(\alpha a_i a_j + \alpha^N a_i^N a_j^N \right) \frac{\partial \Psi_\beta}{\partial x_j} \mathbf{Q}_\beta \right. \\ &\quad \left. \left. + a_i \delta \frac{\partial \Psi_\beta}{\partial x_j} F_{j,\beta}^{cel} + a_i \frac{\partial \Psi_\beta}{\partial x_j} F_{j,\beta}^{conv} \right) \right] d\Omega \\ &\approx \quad 0 \end{aligned} \tag{4.223}$$

5. Forming the Galerkin weak statement of (4.223), by defining $\Phi_\alpha = \Psi_\alpha$, to extremize the approximation error

$$
\begin{aligned}
\int_\Omega \Psi_\alpha L^N(\mathbf{q}) d\Omega &= \int_\Omega \Psi_\alpha \Psi_\beta \, d\Omega \, \frac{d\mathbf{Q}_\beta}{dt} \\
&+ \int_\Omega \Psi_\alpha \frac{\partial \Psi_\beta}{\partial x_j} \, d\Omega \, F_{j,\beta} \\
&+ \epsilon\psi \left(\alpha a_i a_j + \alpha^N a_i^N a_j^N\right) SQRGH_\beta \int_\Omega \Psi_\beta \frac{\partial \Psi_\alpha}{\partial x_i} \frac{\partial \Psi_\beta}{\partial x_j} \, d\Omega \, \mathbf{Q}_\beta \\
&+ \epsilon\psi a_i \delta \int_\Omega \frac{\partial \Psi_\alpha}{\partial x_i} \frac{\partial \Psi_\beta}{\partial x_j} \, d\Omega \, F_{j,\beta}^{cel} \\
&+ \epsilon\psi a_i \int_\Omega \frac{\partial \Psi_\alpha}{\partial x_i} \frac{\partial \Psi_\beta}{\partial x_j} \, d\Omega \, F_{j,\beta}^{conv} \\
&\approx 0
\end{aligned}
\tag{4.224}
$$

Performing the integrals, the essential form of (4.224) is

$$
[\mathbf{M}] \frac{d\{\mathbf{Q}\}}{dt} + \{\mathbf{RES}\} = \{\mathbf{0}\} \tag{4.225}
$$

where $[\mathbf{M}]$ is the matrix of coefficients pre-multiplying the time derivative and $\{\mathbf{RES}\}$ is the remainder of the continuum weak statement (4.224).

5. For this research, the bi-linear quadratic finite element will used as the interpolating function $\{N_k(\mathbf{x})\}$.

4.12 Temporal Discretization and Newton Construction

As discussed in the on-dimensional developments, a Θ implicit time step procedure combined with the Newton iteration algorithm will be employed to solve the spatially discretized problem statement. Hence

$$
[\mathbf{M}]\{\Delta\mathbf{Q}\} + \Delta t \{\mathbf{RES}\}_{n+\theta} = \{\mathbf{F}\} \tag{4.226}
$$

$$\left([\mathbf{M}] + \frac{\partial\{\mathbf{RES}\}}{\partial\{\mathbf{Q}\}}\right)\{\delta\mathbf{Q}\}^{p+1} = -\{\mathbf{F}\}^{p} \tag{4.227}$$

$$\{\Delta\mathbf{Q}\} = \sum_{1}^{p+1}\{\delta\mathbf{Q}\}^{p} \quad , \quad \{\mathbf{Q}\}_{n+1} = \{\mathbf{Q}\}_{n} + \{\Delta\mathbf{Q}\} \tag{4.228}$$

Heed that for two and three dimensional problems, direct solves of (4.227) become exceedingly cumbersome. This research exploits the GMRES solver combined with a bandwidth jacobian preconditioner. Note that this is the first publication on the open channel equations to use this solution technique, hence there are no references.

For second-order temporal accuracy, this research will employ the trapezoid rule yielding $\Theta = 0.5$. Determination of $\partial\{\mathbf{RES}\}/\partial\{\mathbf{Q}\}$ from the Galerkin weak statement form of the characteristics-biased conservation law system (4.224) starts with

$$\{\mathbf{RES}\} = \left\{\begin{array}{c} \mathbf{RH} \\ \mathbf{RM1} \\ \mathbf{RM2} \end{array}\right\} \tag{4.229}$$

hence

$$\frac{\partial\{\mathbf{RES}\}}{\partial\{\mathbf{Q}\}} = \left[\begin{array}{ccc} \frac{\partial RH}{\partial H} & \frac{\partial RH}{\partial M1} & \frac{\partial RH}{\partial M2} \\ \frac{\partial RM1}{\partial H} & \frac{\partial RM1}{\partial M1} & \frac{\partial RM1}{\partial M2} \\ \frac{\partial RM2}{\partial H} & \frac{\partial RM2}{\partial M1} & \frac{\partial RM2}{\partial M2} \end{array}\right] = \left[\begin{array}{ccc} \mathbf{JHH} & \mathbf{JHM1} & \mathbf{JHM2} \\ \mathbf{JM1H} & \mathbf{JM1M1} & \mathbf{JM1M2} \\ \mathbf{JM2H} & \mathbf{JM2M1} & \mathbf{JM2M2} \end{array}\right] = [\mathbf{JAC}] \tag{4.230}$$

Expressing each component of $\{\mathbf{RES}\}$ courtesy (4.224) where the state variable and grouped flux approximations, (4.220) and (4.221), are expressed in the interior and rightmost bracketed terms

$$
\begin{aligned}
\mathbf{RH} \quad = \quad & \int_\Omega \Psi_\alpha \frac{\partial \Psi_\beta}{\partial x_j}\, d\Omega \;\; [m_j]_\beta \\
& + \epsilon\psi \left(\alpha a_i a_j + \alpha^N a_i^N a_j^N\right) \left[\sqrt{gh}\right]_\beta \int_\Omega \Psi_\beta \frac{\partial \Psi_\alpha}{\partial x_i} \frac{\partial \Psi_\beta}{\partial x_j}\, d\Omega \;\; [h]_\beta \\
& + \epsilon\psi a_i \delta \int_\Omega \frac{\partial \Psi_\alpha}{\partial x_i} \frac{\partial \Psi_\beta}{\partial x_j}\, d\Omega \;\; [0] \\
& + \epsilon\psi a_i \int_\Omega \frac{\partial \Psi_\alpha}{\partial x_i} \frac{\partial \Psi_\beta}{\partial x_j}\, d\Omega \;\; [m_j]_\beta
\end{aligned} \tag{4.231}
$$

$$
\begin{aligned}
\mathbf{RM1} \quad = \quad & \int_\Omega \Psi_\alpha \frac{\partial \Psi_\beta}{\partial x_j}\, d\Omega \;\; \left[\frac{m_j}{h} m_1 + \frac{g}{2} h^2 \delta_j^1\right]_\beta \\
& + \epsilon\psi \left(\alpha a_i a_j + \alpha^N a_i^N a_j^N\right) \left[\sqrt{gh}\right]_\beta \int_\Omega \Psi_\beta \frac{\partial \Psi_\alpha}{\partial x_i} \frac{\partial \Psi_\beta}{\partial x_j}\, d\Omega \;\; [m_1]_\beta \\
& + \epsilon\psi a_i \delta \int_\Omega \frac{\partial \Psi_\alpha}{\partial x_i} \frac{\partial \Psi_\beta}{\partial x_j}\, d\Omega \;\; \left[\frac{g}{2} h^2 \delta_j^1\right]_\beta \\
& + \epsilon\psi a_i \int_\Omega \frac{\partial \Psi_\alpha}{\partial x_i} \frac{\partial \Psi_\beta}{\partial x_j}\, d\Omega \;\; \left[\frac{m_j}{h} m_1\right]_\beta
\end{aligned} \tag{4.232}
$$

$$
\begin{aligned}
\mathbf{RM2} \quad = \quad & \int_\Omega \Psi_\alpha \frac{\partial \Psi_\beta}{\partial x_j}\, d\Omega \;\; \left[\frac{m_j}{h} m_2 + \frac{g}{2} h^2 \delta_j^2\right]_\beta \\
& + \epsilon\psi \left(\alpha a_i a_j + \alpha^N a_i^N a_j^N\right) \left[\sqrt{gh}\right]_\beta \int_\Omega \Psi_\beta \frac{\partial \Psi_\alpha}{\partial x_i} \frac{\partial \Psi_\beta}{\partial x_j}\, d\Omega \;\; [m_2]_\beta \\
& + \epsilon\psi a_i \delta \int_\Omega \frac{\partial \Psi_\alpha}{\partial x_i} \frac{\partial \Psi_\beta}{\partial x_j}\, d\Omega \;\; \left[\frac{g}{2} h^2 \delta_j^2\right]_\beta \\
& + \epsilon\psi a_i \int_\Omega \frac{\partial \Psi_\alpha}{\partial x_i} \frac{\partial \Psi_\beta}{\partial x_j}\, d\Omega \;\; \left[\frac{m_j}{h} m_2\right]_\beta
\end{aligned} \tag{4.233}
$$

The jacobian is thus generated according to (4.230). Note that the terms within the bracketed state variable and flux group approximations are subject to differentiaion by the state variable approximation as the β index can be considered as distributed throughout the entire term. To prevent conflicts with indicial notation convention and to emphasize that the variable group is being approximated, the β is kept outside as the bracket subscript. Hence

$$
\begin{aligned}
\mathbf{JHH} \quad = \quad & \frac{\partial}{\partial h_\beta}\left(\int_\Omega \Psi_\alpha \frac{\partial \Psi_\beta}{\partial x_j}\, d\Omega \;\; [m_j]_\beta\right) \\
& + \frac{\partial}{\partial h_\beta}\left(\epsilon\psi\left(\alpha a_i a_j + \alpha^N a_i^N a_j^N\right)\left[\sqrt{gh}\right]_\beta \int_\Omega \Psi_\beta \frac{\partial \Psi_\alpha}{\partial x_i}\frac{\partial \Psi_\beta}{\partial x_j}\, d\Omega \;\; [h]_\beta\right) \\
& + \frac{\partial}{\partial h_\beta}\left(\epsilon\psi a_i \delta \int_\Omega \frac{\partial \Psi_\alpha}{\partial x_i}\frac{\partial \Psi_\beta}{\partial x_j}\, d\Omega \;\; [0]\right) \\
& + \frac{\partial}{\partial h_\beta}\left(\epsilon\psi a_i \int_\Omega \frac{\partial \Psi_\alpha}{\partial x_i}\frac{\partial \Psi_\beta}{\partial x_j}\, d\Omega \;\; [m_j]_\beta\right) \\
= \quad & 0 \\
& + \epsilon\psi\left(\alpha a_i a_j + \alpha^N a_i^N a_j^N\right)\left[\sqrt{gh}\right]_\beta \int_\Omega \Psi_\beta \frac{\partial \Psi_\alpha}{\partial x_i}\frac{\partial \Psi_\beta}{\partial x_j}\, d\Omega \;\; [1] \\
& + \epsilon\psi\left(\alpha a_i a_j + \alpha^N a_i^N a_j^N\right) h_\beta \int_\Omega \frac{\partial \Psi_\beta}{\partial x_j}\frac{\partial \Psi_\alpha}{\partial x_i}\Psi_\beta\, d\Omega \;\; \left[\frac{1}{2\sqrt{gh}}\right]_\beta \\
& + 0 \\
& + 0
\end{aligned}
\tag{4.234}
$$

$$
\begin{aligned}
\mathbf{JHM1} \quad = \quad & \frac{\partial}{\partial m_{1,\beta}}\left(\int_\Omega \Psi_\alpha \frac{\partial \Psi_\beta}{\partial x_j}\, d\Omega \;\; [m_j]_\beta\right) \\
& + \frac{\partial}{\partial m_{1,\beta}}\left(\epsilon\psi\left(\alpha a_i a_j + \alpha^N a_i^N a_j^N\right)\left[\sqrt{gh}\right]_\beta \int_\Omega \Psi_\beta \frac{\partial \Psi_\alpha}{\partial x_i}\frac{\partial \Psi_\beta}{\partial x_j}\, d\Omega \;\; [h]_\beta\right) \\
& + \frac{\partial}{\partial m_{1,\beta}}\left(\epsilon\psi a_i \delta \int_\Omega \frac{\partial \Psi_\alpha}{\partial x_i}\frac{\partial \Psi_\beta}{\partial x_j}\, d\Omega \;\; [0]\right) \\
& + \frac{\partial}{\partial m_{1,\beta}}\left(\epsilon\psi a_i \int_\Omega \frac{\partial \Psi_\alpha}{\partial x_i}\frac{\partial \Psi_\beta}{\partial x_j}\, d\Omega \;\; [m_j]_\beta\right) \\
= \quad & \int_\Omega \Psi_\alpha \frac{\partial \Psi_\beta}{\partial x_j}\, d\Omega \;\; \left[\delta_j^1\right] \\
& + 0 \\
& + 0 \\
& + \epsilon\psi a_i \int_\Omega \frac{\partial \Psi_\alpha}{\partial x_i}\frac{\partial \Psi_\beta}{\partial x_j}\, d\Omega \;\; \left[\delta_j^1\right]
\end{aligned}
\tag{4.235}
$$

$$
\begin{aligned}
\mathbf{JHM2} \quad = \quad & \frac{\partial}{\partial m_{2,\beta}} \left(\int_\Omega \Psi_\alpha \frac{\partial \Psi_\beta}{\partial x_j} \, d\Omega \; [m_j]_\beta \right) \\
& + \frac{\partial}{\partial m_{2,\beta}} \left(\epsilon\psi \left(\alpha a_i a_j + \alpha^N a_i^N a_j^N \right) \left[\sqrt{gh} \right]_\beta \int_\Omega \Psi_\beta \frac{\partial \Psi_\alpha}{\partial x_i} \frac{\partial \Psi_\beta}{\partial x_j} \, d\Omega \; [h]_\beta \right) \\
& + \frac{\partial}{\partial m_{2,\beta}} \left(\epsilon\psi a_i \delta \int_\Omega \frac{\partial \Psi_\alpha}{\partial x_i} \frac{\partial \Psi_\beta}{\partial x_j} \, d\Omega \; [0] \right) \\
& + \frac{\partial}{\partial m_{2,\beta}} \left(\epsilon\psi a_i \int_\Omega \frac{\partial \Psi_\alpha}{\partial x_i} \frac{\partial \Psi_\beta}{\partial x_j} \, d\Omega \; [m_j]_\beta \right) \\
= \quad & \int_\Omega \Psi_\alpha \frac{\partial \Psi_\beta}{\partial x_j} \, d\Omega \; \left[\delta_j^2 \right] \\
& + 0 \\
& + 0 \\
& + \epsilon\psi a_i \int_\Omega \frac{\partial \Psi_\alpha}{\partial x_i} \frac{\partial \Psi_\beta}{\partial x_j} \, d\Omega \; \left[\delta_j^2 \right]
\end{aligned} \tag{4.236}
$$

$$
\begin{aligned}
\mathbf{JM1H} \quad = \quad & \frac{\partial}{\partial h_\beta} \left(\int_\Omega \Psi_\alpha \frac{\partial \Psi_\beta}{\partial x_j} \, d\Omega \; \left[\frac{m_j}{h} m_1 + \frac{g}{2} h^2 \delta_j^1 \right]_\beta \right) \\
& + \frac{\partial}{\partial h_\beta} \left(\epsilon\psi \left(\alpha a_i a_j + \alpha^N a_i^N a_j^N \right) \left[\sqrt{gh} \right]_\beta \int_\Omega \Psi_\beta \frac{\partial \Psi_\alpha}{\partial x_i} \frac{\partial \Psi_\beta}{\partial x_j} \, d\Omega \; [m_1]_\beta \right) \\
& + \frac{\partial}{\partial h_\beta} \left(\epsilon\psi a_i \delta \int_\Omega \frac{\partial \Psi_\alpha}{\partial x_i} \frac{\partial \Psi_\beta}{\partial x_j} \, d\Omega \; \left[\frac{g}{2} h^2 \delta_j^1 \right]_\beta \right) \\
& + \frac{\partial}{\partial h_\beta} \left(\epsilon\psi a_i \int_\Omega \frac{\partial \Psi_\alpha}{\partial x_i} \frac{\partial \Psi_\beta}{\partial x_j} \, d\Omega \; \left[\frac{m}{h} m_1 \right]_\beta \right) \\
= \quad & \int_\Omega \Psi_\alpha \frac{\partial \Psi_\beta}{\partial x_j} \, d\Omega \; \left[-\frac{m_j}{h} \frac{m_1}{h} + gh\delta_j^1 \right]_\beta \\
& + \epsilon\psi \left(\alpha a_i a_j + \alpha^N a_i^N a_j^N \right) m_{1,\beta} \int_\Omega \frac{\partial \Psi_\beta}{\partial x_j} \frac{\partial \Psi_\alpha}{\partial x_i} \Psi_\beta \, d\Omega \; \left[\frac{1}{2\sqrt{gh}} \right]_\beta \\
& + \epsilon\psi a_i \delta \int_\Omega \frac{\partial \Psi_\alpha}{\partial x_i} \frac{\partial \Psi_\beta}{\partial x_j} \, d\Omega \; \left[gh\delta_j^1 \right]_\beta \\
& + \epsilon\psi a_i \int_\Omega \frac{\partial \Psi_\alpha}{\partial x_i} \frac{\partial \Psi_\beta}{\partial x_j} \, d\Omega \; \left[-\frac{m_j}{h} \frac{m_1}{h} \right]_\beta
\end{aligned} \tag{4.237}
$$

$$
\begin{aligned}
\mathbf{JM1M1} \quad = \quad & \frac{\partial}{\partial m_{1,\beta}} \left(\int_\Omega \Psi_\alpha \frac{\partial \Psi_\beta}{\partial x_j} \, d\Omega \, \left[\frac{m_j}{h} m_1 + \frac{g}{2} h^2 \delta_j^1 \right]_\beta \right) \\
& + \frac{\partial}{\partial m_{1,\beta}} \left(\epsilon\psi \left(\alpha a_i a_j + \alpha^N a_i^N a_j^N \right) \left[\sqrt{gh} \right]_\beta \int_\Omega \Psi_\beta \frac{\partial \Psi_\alpha}{\partial x_i} \frac{\partial \Psi_\beta}{\partial x_j} \, d\Omega \, \left[m_1 \right]_\beta \right) \\
& + \frac{\partial}{\partial m_{1,\beta}} \left(\epsilon\psi a_i \delta \int_\Omega \frac{\partial \Psi_\alpha}{\partial x_i} \frac{\partial \Psi_\beta}{\partial x_j} \, d\Omega \, \left[\frac{g}{2} h^2 \delta_j^1 \right]_\beta \right) \\
& + \frac{\partial}{\partial m_{1,\beta}} \left(\epsilon\psi a_i \int_\Omega \frac{\partial \Psi_\alpha}{\partial x_i} \frac{\partial \Psi_\beta}{\partial x_j} \, d\Omega \, \left[\frac{m_j}{h} m_1 \right]_\beta \right) \\
= \quad & \int_\Omega \Psi_\alpha \frac{\partial \Psi_\beta}{\partial x_j} \, d\Omega \, \left[\frac{m_j}{h} + \frac{m_1}{h} \delta_j^1 \right]_\beta \\
& + \epsilon\psi \left(\alpha a_i a_j + \alpha^N a_i^N a_j^N \right) \left[\sqrt{gh} \right]_\beta \int_\Omega \Psi_\beta \frac{\partial \Psi_\alpha}{\partial x_i} \frac{\partial \Psi_\beta}{\partial x_j} \, d\Omega \, [1] \\
& + 0 \\
& + \epsilon\psi a_i \int_\Omega \frac{\partial \Psi_\alpha}{\partial x_i} \frac{\partial \Psi_\beta}{\partial x_j} \, d\Omega \, \left[\frac{m_j}{h} + \frac{m_1}{h} \delta_j^1 \right]_\beta
\end{aligned} \tag{4.238}
$$

$$
\begin{aligned}
\mathbf{JM1M2} \quad = \quad & \frac{\partial}{\partial m_{2,\beta}} \left(\int_\Omega \Psi_\alpha \frac{\partial \Psi_\beta}{\partial x_j} \, d\Omega \, \left[\frac{m_j}{h} m_1 + \frac{g}{2} h^2 \delta_j^1 \right]_\beta \right) \\
& + \frac{\partial}{\partial m_{2,\beta}} \left(\epsilon\psi \left(\alpha a_i a_j + \alpha^N a_i^N a_j^N \right) \left[\sqrt{gh} \right]_\beta \int_\Omega \Psi_\beta \frac{\partial \Psi_\alpha}{\partial x_i} \frac{\partial \Psi_\beta}{\partial x_j} \, d\Omega \, \left[m_1 \right]_\beta \right) \\
& + \frac{\partial}{\partial m_{2,\beta}} \left(\epsilon\psi a_i \delta \int_\Omega \frac{\partial \Psi_\alpha}{\partial x_i} \frac{\partial \Psi_\beta}{\partial x_j} \, d\Omega \, \left[\frac{g}{2} h^2 \delta_j^1 \right]_\beta \right) \\
& + \frac{\partial}{\partial m_{2,\beta}} \left(\epsilon\psi a_i \int_\Omega \frac{\partial \Psi_\alpha}{\partial x_i} \frac{\partial \Psi_\beta}{\partial x_j} \, d\Omega \, \left[\frac{m_j}{h} m_1 \right]_\beta \right) \\
= \quad & \int_\Omega \Psi_\alpha \frac{\partial \Psi_\beta}{\partial x_j} \, d\Omega \, \left[\frac{m_1}{h} \delta_j^2 \right]_\beta \\
& + 0 \\
& + 0 \\
& + \epsilon\psi a_i \int_\Omega \frac{\partial \Psi_\alpha}{\partial x_i} \frac{\partial \Psi_\beta}{\partial x_j} \, d\Omega \, \left[\frac{m_1}{h} \delta_j^2 \right]_\beta
\end{aligned} \tag{4.239}
$$

$$
\begin{aligned}
\mathbf{JM2H} \quad = \quad & \frac{\partial}{\partial h_\beta}\left(\int_\Omega \Psi_\alpha \frac{\partial \Psi_\beta}{\partial x_j}\, d\Omega \ \left[\frac{m_j}{h} m_2 + \frac{g}{2} h^2 \delta_j^2\right]_\beta\right) \\
& + \frac{\partial}{\partial h_\beta}\left(\epsilon\psi\left(\alpha a_i a_j + \alpha^N a_i^N a_j^N\right) \left[\sqrt{gh}\right]_\beta \int_\Omega \Psi_\beta \frac{\partial \Psi_\alpha}{\partial x_i}\frac{\partial \Psi_\beta}{\partial x_j}\, d\Omega \ [m]_\beta\right) \\
& + \frac{\partial}{\partial h_\beta}\left(\epsilon\psi a_i \delta \int_\Omega \frac{\partial \Psi_\alpha}{\partial x_i}\frac{\partial \Psi_\beta}{\partial x_j}\, d\Omega \ \left(\frac{g}{2} h_\beta^2 \delta_j^2\right)\right) \\
& + \frac{\partial}{\partial h_\beta}\left(\epsilon\psi a_i \int_\Omega \frac{\partial \Psi_\alpha}{\partial x_i}\frac{\partial \Psi_\beta}{\partial x_j}\, d\Omega \ \left[\frac{m_j}{h} m_2\right]_\beta\right) \\
= \quad & \int_\Omega \Psi_\alpha \frac{\partial \Psi_\beta}{\partial x_j}\, d\Omega \ \left[-\frac{m_j}{h}\frac{m_2}{h} + gh\delta_j^2\right]_\beta \\
& + \epsilon\psi\left(\alpha a_i a_j + \alpha^N a_i^N a_j^N\right) m_{2,\beta} \int_\Omega \frac{\partial \Psi_\beta}{\partial x_j}\frac{\partial \Psi_\alpha}{\partial x_i}\Psi_\beta\, d\Omega \ \left[\frac{1}{2\sqrt{gh}}\right]_\beta \\
& + \epsilon\psi a_i \delta \int_\Omega \frac{\partial \Psi_\alpha}{\partial x_i}\frac{\partial \Psi_\beta}{\partial x_j}\, d\Omega \ \left[gh\delta_j^2\right]_\beta \\
& + \epsilon\psi a_i \int_\Omega \frac{\partial \Psi_\alpha}{\partial x_i}\frac{\partial \Psi_\beta}{\partial x_j}\, d\Omega \ \left[-\frac{m_j}{h}\frac{m_2}{h}\right]_\beta
\end{aligned} \tag{4.240}
$$

$$
\begin{aligned}
\mathbf{JM2M1} \quad = \quad & \frac{\partial}{\partial m_{1,\beta}}\left(\int_\Omega \Psi_\alpha \frac{\partial \Psi_\beta}{\partial x_j}\, d\Omega \ \left[\frac{m_j}{h} m_2 + \frac{g}{2} h^2 \delta_j^2\right]_\beta\right) \\
& + \frac{\partial}{\partial m_{1,\beta}}\left(\epsilon\psi\left(\alpha a_i a_j + \alpha^N a_i^N a_j^N\right) \left[\sqrt{gh}\right]_\beta \int_\Omega \Psi_\beta \frac{\partial \Psi_\alpha}{\partial x_i}\frac{\partial \Psi_\beta}{\partial x_j}\, d\Omega \ [m_2]_\beta\right) \\
& + \frac{\partial}{\partial m_{1,\beta}}\left(\epsilon\psi a_i \delta \int_\Omega \frac{\partial \Psi_\alpha}{\partial x_i}\frac{\partial \Psi_\beta}{\partial x_j}\, d\Omega \ \left[\frac{g}{2} h^2 \delta_j^2\right]_\beta\right) \\
& + \frac{\partial}{\partial m_{1,\beta}}\left(\epsilon\psi a_i \int_\Omega \frac{\partial \Psi_\alpha}{\partial x_i}\frac{\partial \Psi_\beta}{\partial x_j}\, d\Omega \ \left[\frac{m_j}{h} m_2\right)\right]_\beta \\
= \quad & \int_\Omega \Psi_\alpha \frac{\partial \Psi_\beta}{\partial x_j}\, d\Omega \ \left[\frac{m_2}{h}\delta_j^1\right]_\beta \\
& + 0 \\
& + 0 \\
& + \epsilon\psi a_i \int_\Omega \frac{\partial \Psi_\alpha}{\partial x_i}\frac{\partial \Psi_\beta}{\partial x_j}\, d\Omega \ \left[\frac{m_2}{h}\delta_j^1\right]_\beta
\end{aligned} \tag{4.241}
$$

$$
\begin{aligned}
\mathbf{JM2M2} \quad = \quad & \frac{\partial}{\partial m_{2,\beta}} \left(\int_\Omega \Psi_\alpha \frac{\partial \Psi_\beta}{\partial x_j} \, d\Omega \, \left[\frac{m_j}{h} m_2 + \frac{g}{2} h^2 \delta_j^2 \right]_\beta \right) \\
& + \frac{\partial}{\partial m_{2,\beta}} \left(\epsilon \psi \left(\alpha a_i a_j + \alpha^N a_i^N a_j^N \right) \left[\sqrt{gh} \right]_\beta \int_\Omega \Psi_\beta \frac{\partial \Psi_\alpha}{\partial x_i} \frac{\partial \Psi_\beta}{\partial x_j} \, d\Omega \, \left[m_2 \right]_\beta \right) \\
& + \frac{\partial}{\partial m_{2,\beta}} \left(\epsilon \psi a_i \delta \int_\Omega \frac{\partial \Psi_\alpha}{\partial x_i} \frac{\partial \Psi_\beta}{\partial x_j} \, d\Omega \, \left[\frac{g}{2} h^2 \delta_j^2 \right]_\beta \right) \\
& + \frac{\partial}{\partial m_{2,\beta}} \left(\epsilon \psi a_i \int_\Omega \frac{\partial \Psi_\alpha}{\partial x_i} \frac{\partial \Psi_\beta}{\partial x_j} \, d\Omega \, \left[\frac{m_j}{h} m_2 \right]_\beta \right) \\
= \quad & \int_\Omega \Psi_\alpha \frac{\partial \Psi_\beta}{\partial x_j} \, d\Omega \, \left[\frac{m_j}{h} + \frac{m_2}{h} \delta_j^2 \right]_\beta \\
& + \epsilon \psi \left(\alpha a_i a_j + \alpha^N a_i^N a_j^N \right) \left[\sqrt{gh} \right]_\beta \int_\Omega \Psi_\beta \frac{\partial \Psi_\alpha}{\partial x_i} \frac{\partial \Psi_\beta}{\partial x_j} \, d\Omega \, [1] \\
& + 0 \\
& + \epsilon \psi a_i \int_\Omega \frac{\partial \Psi_\alpha}{\partial x_i} \frac{\partial \Psi_\beta}{\partial x_j} \, d\Omega \, \left[\frac{m_j}{h} + \frac{m_2}{h} \delta_j^2 \right]_\beta
\end{aligned} \tag{4.242}
$$

Substantial non-linearity is evident within the jacobian via the grouped variables. As with the one-dimensional formulation, the contributions from the paramters a_i, a_i^N, α, α^N, δ, and ψ, while implicit functions of h and m_j, are not included for computational efficiency.

4.13 Determination of ψ

As in the one-dimensional development, the nodal solution slopes, hence solution and slope continuity, can be qualified by subtracting the element unit normal vectors at the common node:

$$|\hat{n}_R - \hat{n}_L| \approx 0 \qquad \text{solution and slope are continuous} \tag{4.243}$$

$$|\hat{n}_R - \hat{n}_L| \approx 1 \qquad \text{solution is continuous, slope is discontinuous} \tag{4.244}$$

$$|\hat{n}_R - \hat{n}_L| \to 2 \qquad \text{solution is discontinuous} \tag{4.245}$$

This qualitative behavior can be normalized in terms of a solution continuity gauge φ

$$\varphi = \frac{1}{2}|\hat{n}_R - \hat{n}_L| = \sqrt{\frac{1 - cos(\theta)}{2}} \tag{4.246}$$

where θ is the angle between $\hat{n}_R$ and $\hat{n}_L$.

At a normal hydraulic jump, $\theta = 90°$ and hence $\varphi = 1/\sqrt{2} \approx \psi_{max}$. As in the one-dimensional development, ψ can be mapped to φ with a spline:

$$\psi \quad = \quad \begin{cases} \psi_{min} & \varphi \leq \varphi_C \\ \psi_{max} + \frac{\psi_{max} - \psi_{min}}{(\varphi_D - \varphi_C)^3}[-(\varphi_D - 3\varphi_C)\varphi_D^2 & \\ \quad -6\varphi_D\varphi_C + 3(\varphi_D + \varphi_C)\varphi^2 - 2\varphi^3] & \varphi_C < \varphi < \varphi_D \\ \psi_{max} & \varphi \geq \varphi_D \end{cases} \tag{4.247}$$

where $\varphi_C = 0$, $\varphi_D = 1/\sqrt{2}$, $\psi_{max} \leq 2 - \psi_{min}$, and experimental results indicate $1/4 \leq \psi_{min} \leq 1/2$.

The final step is to solve φ from the unit normals of the element common nodes. For a function q in the $(\mathbf{x}, q)$ space, the unit normal to q is defined as

$$n = \frac{\left(\frac{\partial q}{\partial x_1}\hat{i} \;+\; \frac{\partial q}{\partial x_2}\hat{j} \;+\; \frac{\partial q}{\partial q}\hat{k}\right)}{\sqrt{\left(\frac{\partial q}{\partial x_1}\right)^2 + \left(\frac{\partial q}{\partial x_2}\right)^2 + \left(\frac{\partial q}{\partial q}\right)^2}} = \frac{\left(\frac{\partial q}{\partial x_1}\hat{i} \;+\; \frac{\partial q}{\partial x_2}\hat{j} \;+\; 1\hat{k}\right)}{\sqrt{\left(\frac{\partial q}{\partial x_1}\right)^2 + \left(\frac{\partial q}{\partial x_2}\right)^2 + 1}} \tag{4.248}$$

where $(\hat{i}, \hat{j}, \hat{k})$ are unit vectors in the (x_1, x_2, q) directions respectively.

For a four element cartesian discretization, a first-order finite difference approximation to $\partial q/\partial x_1$ and $\partial q/\partial x_2$ at the common node i, j on the four elements is

$$\frac{\partial q}{\partial x_1}_L = \frac{q_{i,j} - q_{i-1,j}}{\Delta x_{i-1/2,j}} \quad , \quad \frac{\partial q}{\partial x_1}_R = -\frac{q_{i+1,j} - q_{i,j}}{\Delta x_{i+1/2,j}} \tag{4.249}$$

$$\frac{\partial q}{\partial x_2}_B = \frac{q_{i,j} - q_{i,j-1}}{\Delta x_{i,j-1/2}} \quad , \quad \frac{\partial q}{\partial x_2}_T = -\frac{q_{i,j+1} - q_{i,j}}{\Delta x_{i,j+1/2}} \tag{4.250}$$

where $\Delta x_{\mp 1/2}$ is the length of the left/right and bottom/top elements respectively. For each element, a unit normal at node (i, j) can hence be calculated. To calculate φ, each unit normal will be subracted from the other three. The largest difference will then be substituted into the spline mapping to get ψ. For the two-dimensional research, the nodal kinetic energy will be employed as the measure of continuity.

4.14 Summary

The two-dimensional inviscid open channel equations have been parabolized for numerical solution via the determination of the characteristics-biased flux divergence. This dissipative mechanism was developed on the continuum level and the modified problem statement, coupled with the trapezoid time integration rule, remains second order accurate in both space in time. Physically significant propagation modes, bi-modal and mono-axial, were recognized along with the streamline and cross-flow wedge regions for supercritical flow. The behavior of the hyperbolic open channel eigenvalues were investigated within these wedges and throughout the entire flowfield for subcritical flow to insure the consistency of the dissipative flux jacobian eigenvalues through the form of streamline upstream eigenvalues and free parameters α, α^N, and δ. Finally, this minimally dissipative mechanism induces a variable level of dissipation based on local solution continuity.

Chapter 5

Discussion and Results, Two Dimensions

Having established the modified open channel equation system courtesy the characteristics biased flux divergence, the results must be compared against available validations to assess algorithm performance. Within the open channel flow analysis community, two standard dam break benchmarkss for the homogenous form of the equations are the partial dam break and the circular dam break. Additionally, a new benchmark is introduced, the square harbor, which is similar to the classic driven cavity benchmark.

5.1 Partial Dam Break

Partial dam breaks, where only part of the dam fails, lead to flow patterns far more complex than those witnessed when the entire dam fails. A complete dam failure for the two-dimensional open channel equations yields nothing more than the one-dimesional solution distributed uniformly across

the breadth of the channel. The partial dam break, however, induces a fully two-dimensional flow field and, based on the placement of the failure, may introduce strong asymetric flow.

This challenging benchmark was introduced by Fennema, *et al* [47] in 1990 to compare two second-order, explicit finite difference algorithms on a structured 40x40 uniform grid: MacCormack [48,49] and Gabutti [50]. While the results have set the basis for comparison, the limitations of the algorithms are evident in dispersive error modes which are subsequently damped through liberal application of prinipal axis artificial dissipation developed by Jameson [51]. As such, these results should be used to indicate solution trends rather than definitive behavior.

This problem was revisited in 1993 by Alcrudo, *et al* [52] and Glaister [53]. Alcrudo employed a Gudonov finite volume construction, on an identical structured grid, based on MUSCL variable extrapolation and min-mod slope limiters while Glaister introduces a finite differences scheme based on flux difference splitting of the linearized Riemann problem. While both results are crisper than those presented by Fennema, the results presented by Glaister, while monotone, are substantially more diffused than those presented by Alcrudo.

Ambrosi [54], in 1995, presented a TVD version of the Lax-Wendroff finite volume algorithm solved on the now de-facto structured grid. These second-order accurate results were the most diffused of those published to date.

A strutured grid of finite volume triangles to support Roe's scheme was introduced by Anastasiou, *et al* [55] in 1997. This second order implementation yielded results more diffused than those of Fennema and Alcrudo but better than those of Glaister and Ambrosi.

An unstructured finite volume triangle mesh broke from the standard in 1998 with Paillere [56]. His algorithm employed a characteristics based diagonalization of the governing equations and the flux jacobian eigenvalues to provide the upwinding directions. While the algorithm was only first order accurate, the dam break results were no more diffused than those presented by Ambrosi.

Unlike any of the other results, however, deep depressions are seen in h at the dam outlet coners.

5.1.1 Problem Statement

For this problem, the dam is assumed to fail instaneously. The computational domain consists of a 200 meter long and 200 meter wide channel. The dam is 10 meters thick and the non-symmetric breach is 75 meters wide. The "upper" remnant of the dam is 30 meters, the "lower" remnant is 95 meters wide, and both remnants remain 10 meters thick. Figure (5.1) details the geometry. A frictionless, horizontal bottom is assumed in conjunction with the homogenous form of the invisicd open channel equation system. A tailwater/reservior ratio h_t/h_r of 0.5 was employed for the initial height. The simulation was run for $0 \leq t \leq 7.2\ s$ seconds for comparison with published results.

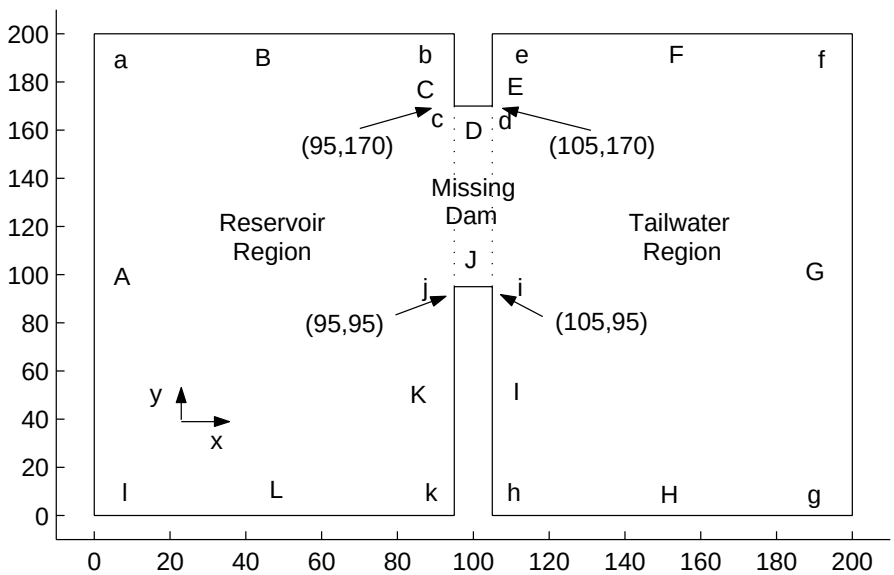

Figure 5.1: Partial Dam Break : Computational Domain

5.1.2 Boundary and Initial Conditions

In accordance with Figure (5.1), the applied boundary conditions are summarized in Table (5.1). While this problem is to model a channel which theoretically extends beyond the computational domain in the x direction, solid boundary conditions of $m_1 = 0$ are inconsistently applied to edges A and G. Computational experiments in which the solid boundary is replaced with a physically consistent Neumann condition for m_1 on edges A and G yields results quite unlike those presented in the literature. Thus, while not explicitly stated in the literature, all computational domain boundaries have been assumed solid.

Moreover, heed that no Dirichlet data is specified on h, hence the Jacobian is rank-deficient and direct solves of the equation system will fail. Becaues this problem has no closed form solution, analytical boundary values of h for the computational domain boundary can not be determined as they were with the one-dimensional dam break. Rather than assuming a Dirichlet value to set the level of h (be it $h = 5$ or $h = 10$ in "back corners" l and g respectively), the selected GMRES solver will readily accomodate this issue. This subtle issue, be it unrecognized or purposefully neglected, is not reported in the literature. Additionally, this may explain why the published simulations are terminated at $t = 7.2\ s$, well before the reservoir height at corner l drops below 10 meters or the tailwater height at corner g increases above 5 meters.

The application of the initial condition of zero momentum is readily applied. The imposed

Table 5.1: Partial Dam Break : Boundary Conditions

Edges / Corners	**Dirichlet**	**Neumann**
c,d,i,j		$\nabla h \cdot \mathbf{n} = \nabla m_1 \cdot \mathbf{n} = \nabla m_2 \cdot \mathbf{n} = 0$
A,C,E,G,I,K	$m_1 = 0$	$\nabla h \cdot \mathbf{n} = \nabla m_2 \cdot \mathbf{n} = 0$
B,D,F,H,J,L	$m_2 = 0$	$\nabla h \cdot \mathbf{n} = \nabla m_1 \cdot \mathbf{n} = 0$
a,b,e,f,g,h,k,l	$m_1 = m_2 = 0$	$\nabla h \cdot \mathbf{n} = 0$

height ratio is straightfoward for the reservoir and tailwater regions of the computational domain. The 10x75 m region within the "missing dam", however, warrants discussion. A natural idea is to divide the missing dam in half at the boundary $x = 100$ and have the reservoir side assume the reservior initial condition and the tailwater side assume the tailwater initial condition. As two elements comprise the missing dam width, the step discontinuity must be interpolated over one of these elements. For this reasearch, the discontinuity was interpolated over the reservoir side of the missing dam as summarized in Table (5.2).

For the grid refinement study, Section (5.1.3.3), this initial condition was duplicated exactly to prevent error caused by variation in the initial condition.

5.1.3 Results

Following the one-dimensional dam break results, the performance of the algorithm will be assessed in several key areas. The first will be the verification of the dissipation controller acting as a constant and a non-linear function of the solution kinetic energy. These results, in the form of carpet plots of the h distribution, are visually compared with published results to verify correct trends in the solution. Additionally, contours of the Froude number and the upstream parameters for the non-linear ψ test are given in Appendix (B). Convergence of the iterative quasi-Newton iteration algorithm is determined next followed by the impact of iteration on the solution norms.

Table 5.2: Partial Dam Break : Initial Conditions

Region	**h**	**m1, m2**
Reservoir	$10\,m$	$0\,m^2/s$
Tailwater	$5\,m$	$0\,m^2/s$
Missing Dam	$(-x+105)\,m$, $95 \leq x \leq 100$	$0\,m^2/s$
	$5\,m$, $100 \leq x \leq 105$	$0\,m^2/s$

Having verified an accurate implementation of the algorithm, the grid refinement study is performed to verify convergence in the solution error as a function of the H^0 norm and energy seminorm. All tests employed bi-linear quadrilateral elements to support the finite element theory.

5.1.3.1 Dissipation Controller Verification

The first test, as in the one-dimensional dam break, is the impact of the dissipation controller ψ, operating both linearly (constant) and non-linearly (solution dependent) on the solution. Operating as a constant, low levels of dissipation will not stabilize the solution while high levels of dissipation will diffuse the solution.

All tests were conducted on the "standard" uniform grid with the algorithm parameters held constant as given in Table (5.3). Rather than imposing a constant value of Courant number, defined as

$$C \equiv max\left(\frac{\left(u \pm \sqrt{gh}\right)\Delta t}{\Delta x}\right) \tag{5.1}$$

Table 5.3: 2D Dissipation Controller Verification : Constant Parameters

Parameter	**Value**	
Number of Elements (N)	$40x40$	
Δt	0.1	
Number of Iterations	3	
$2\mu_o$	0.2	
ϵ_{Fr}	0.2	
ψ_{min}	0.25	(non-linear ψ only)
ψ_{max}	1.00	

a constant Δt was chosen so the solutions could be readily compared at identical time stations. The value of the Courant number is $C < 0.3$ for every time station of all tests.

Five tests were conducted employing $\psi = 0.25,\ 0.50,\ 0.75,\ 1.0\ s$ and $\psi = \psi(ke)$ where $ke = 1/2\ u^2$ is the nodal kinetic energy. Note that the values of ψ_{min} and ψ_{max}, for the non-linear test, were not adjusted in any manner. A constant value of $\psi = 0$ is not reported as the solution was divergent. Results were extracted at representative times of $t = 1,\ 3,\ 5,\ 7.2\ s$ seconds with the last time selected for direct comparison with published solutions. Solution stabilty and accuracy was qualified through carpet plots of the h distribution. The distributions of the Froude number and the upstream parameters α, α^N, and δ as well as the distribution of ψ are given in Appendix (B) for visual indication that the controllers are operating correctly.

Because no closed form solution exists for this problem, analytical evaluation of solution error norms are to assess accuracy are not available. To provide a more mathematically substantial accuracy measure, the extremum values of h and the maximum values of $m_{1,2}$ and m will be reported as well as the Sobolev norms (H^0) and the energy semi-norms ($\|q\|_E$) of h and $m_{1,2}$. Following the one-dimensional results, the divergent H^1 norm was not evaluated.

The norms, extended from the one-dimensional formulation, are

$$\|q\|_{H^0} = H^0(q,q) = \left(\int_{R^n} q^2 d\tau\right)^{1/2} \tag{5.2}$$

$$\|h\|_E = E(h,h) = \int_{R^n} \frac{1}{2}\nabla h \cdot \left(\epsilon\psi\left(\alpha a_i a_j + \alpha^N a_i^N a_j^N\right)\sqrt{gh}\right)\nabla h\, d\tau \tag{5.3}$$

$$\|m_1\|_E = E(m_1,m_1) = \int_{R^n} \frac{1}{2}\nabla m_1 \cdot \left(\epsilon\psi\left(\alpha a_i a_j + \alpha^N a_i^N a_j^N\right)\sqrt{gh}\right)\nabla m_1\, d\tau \tag{5.4}$$

$$\|m_2\|_E = E(m_2,m_2) = \int_{R^n} \frac{1}{2}\nabla m_2 \cdot \left(\epsilon\psi\left(\alpha a_i a_j + \alpha^N a_i^N a_j^N\right)\sqrt{gh}\right)\nabla m_2\, d\tau \tag{5.5}$$

Quantifying the values of $h_{min,max}$, $m_{1,max}$, $m_{2,max}$, and m_{max} shows that, unsurprisingly, as the level of constant dissipation is increased, the value of h_{min} increased while all the maximum

values decreased at all time stations. The values of h_{min} vary in the third and second significant digit for time stations of $t = 1.0, 3.0\ s$ and $5.0, 7.2\ s$ respectively. At the final time station, the minimum value of h varies by nearly a meter or 25% of the value at $\psi = 0.25$. The values of h_{max} vary in the fifth significant digit for $\psi > 0.25$. Examining the momentum components, they vary in the second significant digit with the range at $t = 1.0\ s$ being nearly 7 m^2/s for m_1 and 3 m^2/s for m_2 or 28% and 38% of the $\psi = 0.25$ values respectively. At $t = 7.2\ s$, the range is 4.6 m^2/s and 7.6 m^2/s for m_1 and m_2 respectively, yielding 14% and 27% of the $\psi = 0.25$ values. Similar trends are evident in the m term with a range of 7 m^2/s and 5.5 m^2/s at the first and final time station. With respect to the norms, the H^0 norm decreases with increasing dissipation while the energy semi-norm increases as the diffusion coefficient, a function of ψ, increases. These results are not surprising per the definition of the norms. Clearly the level of the dissipation has a tremendous effect on these extremum values.

Studying the extremum values and norms of the non-linear dissipation controller show them to lie between the values predicted by constant values of $\psi = 0.25$ and $\psi = 0.5$. On these data alone it would seem that a constant value of ψ would be adequate for this problem. The carpet plots of h, however, show dispersion error in the $\psi = 0.25$ plot in the tailwater region both in the corners and along the dam remnant face. As the level of dissipation is increased, the solution clearly becomes overly diffused, particularly the variations fore and aft of the missing dam region. The non-linear controller, however, retains the resolution of the $\psi = 0.25$ solution without the dispersion.

Comparing these results with published solutions reveals that, even with $\psi = 1$, the h distribution is less diffused than that reported by Galister, Ambrosi, and Paillere. The non-linear ψ results compare well with the best results reported by Fennema and Alcrudo, the only results which predict the depression upstream of the missing dam and the plateau within the missing dam. Without values of the norms nor the state variable extrema, however, no further comparision can be made.

Examining the distributions of ψ, Fr, α, α^N, and δ in Appendix (B), the upstream parameters are all functioning as expected. Note that, as this flow is primarily sub-critical, δ is barely evident while α and α^N radiate outwards from the missing dam region. The dissipation controller ψ is seen to first operate at the discontinuity within the missing dam and then focuses on the depth spikes at the corners of the dam. While a sharp front propagates into the tailwater region, the grid is so coarse (5x5 meters) that the variation in height (approximately 2 meters), spread over approximately four elemenents, does not "trigger" the dissipation controller as being a discontinuity.

Table 5.4: 2D Dissipation Controller Verification : Extrema ($t = 1.0\ s$)

t = 1	**h results**		**m1 results**	**m2 results**	**m results**
ψ	h_{min}	h_{max}	$m_{1,max}$	$m_{2,max}$	m_{max}
0.25	4.921063	10.057351	25.180816	8.884978	25.215876
0.50	4.936148	10.026688	22.098657	7.361883	22.098844
0.75	4.950265	10.021253	19.899643	6.427534	19.903152
1.00	4.959443	10.025018	18.213552	5.807490	18.224143
$\psi(ke)$	4.909443	10.048784	22.417174	9.123905	22.483411

Table 5.5: 2D Dissipation Controller Verification : Extrema ($t = 3.0\ s$)

t = 3	**h results**		**m1 results**	**m2 results**	**m results**
ψ	h_{min}	h_{max}	$m_{1,max}$	$m_{2,max}$	m_{max}
0.25	4.930327	10.022548	29.542387	20.240602	30.405503
0.50	4.982130	10.014459	27.304083	16.972681	27.978304
0.75	4.994855	10.013247	25.753720	14.957584	26.267385
1.00	4.998408	10.010336	24.392853	13.421704	24.807574
$\psi(ke)$	4.954905	10.015874	28.517252	19.274707	29.529035

Table 5.6: 2D Dissipation Controller Verification : Extrema ($t = 5.0\ s$)

t = 5	**h results**		**m1 results**	**m2 results**	**m results**
ψ	h_{min}	h_{max}	$m_{1,max}$	$m_{2,max}$	m_{max}
0.25	4.421270	10.012626	31.835529	24.779477	33.663352
0.50	4.784378	10.009249	29.559813	21.721344	31.898450
0.75	4.996785	10.007972	27.799187	19.531580	29.030430
1.00	4.999382	10.006719	26.553275	17.743389	27.353570
$\psi(ke)$	4.656925	10.010458	31.441727	23.362980	33.171130

Table 5.7: 2D Dissipation Controller Verification : Extrema ($t = 7.2\ s$)

t = 7.2	**h results**		**m1 results**	**m2 results**	**m results**
ψ	h_{min}	h_{max}	$m_{1,max}$	$m_{2,max}$	m_{max}
0.25	4.000185	10.011970	33.596184	28.837794	35.162590
0.50	4.302820	10.007345	31.898450	25.467154	33.592395
0.75	4.704919	10.005537	30.304912	23.151197	31.519532
1.00	4.999802	10.003568	28.921942	21.213407	29.631201
$\psi(ke)$	4.278696	10.009204	33.881255	27.280684	36.354832

Table 5.8: 2D Dissipation Controller Verification : Norms ($t = 1.0\ s$)

t = 1.0	**h results**		**m1 results**		**m2 results**	
ψ	$\|h\|_{H^0}$	$\|h\|_E$	$\|m_1\|_{H^0}$	$\|m_1\|_E$	$\|m_2\|_{H^0}$	$\|m_2\|_E$
0.25	1.09477e+03	1.51281+02	4.82056e+02	1.00310e+04	4.85123e+01	8.11260e+02
0.50	1.09469e+03	2.37096+02	4.57900e+02	1.78781e+04	4.85123e+01	1.05730e+03
0.75	1.09460e+03	3.18213+02	4.37339e+02	2.18726e+04	4.47395e+01	1.23976e+03
1.00	1.09452e+03	4.02396+02	4.19838e+02	2.41891e+04	4.42651e+01	1.36723e+03
$\psi(ke)$	1.09472e+03	1.99257+02	4.69480e+02	1.34432e+04	4.74141e+01	1.00541e+03

Table 5.9: 2D Dissipation Controller Verification : Norms ($t = 3.0\ s$)

t = 3.0	**h results**		**m1 results**		**m2 results**	
ψ	$\|h\|_{H^0}$	$\|h\|_E$	$\|m_1\|_{H^0}$	$\|m_1\|_E$	$\|m_2\|_{H^0}$	$\|m_2\|_E$
0.25	1.09035e+03	1.08111e+02	9.09650e+02	1.02330e+04	2.78983e+02	4.10372e+03
0.50	1.09011e+03	1.63363e+02	8.78938e+02	1.65592e+04	2.55119e+02	6.06463e+03
0.75	1.08992e+03	2.07431e+02	8.52675e+02	2.16398e+04	2.37170e+02	7.11637e+03
1.00	1.08977e+03	2.49361e+02	8.29376e+02	2.60697e+04	2.23285e+02	7.70145e+03
$\psi(ke)$	1.09032e+03	1.11935e+02	9.02651e+02	1.12265e+04	2.72733e+02	4.29219e+03

Table 5.10: 2D Dissipation Controller Verification : Norms ($t = 5.0\ s$)

t = 5.0	**h results**		**m1 results**		**m2 results**	
ψ	$\|h\|_{H^0}$	$\|h\|_E$	$\|m_1\|_{H^0}$	$\|m_1\|_E$	$\|m_2\|_{H^0}$	$\|m_2\|_E$
0.25	1.08588e+03	1.07881e+02	1.21742e+03	1.06889e+04	5.06691e+02	5.56007e+03
0.50	1.08541e+03	1.52123e+02	1.17973e+03	1.69890e+04	4.75345e+02	8.83746e+03
0.75	1.08503e+03	1.85903e+02	1.14714e+03	2.24604e+04	4.47965e+02	1.13075e+04
1.00	1.08473e+03	2.17453e+02	1.11804e+03	2.74133e+04	4.23676e+02	1.31207e+04
$\psi(ke)$	1.08591e+03	1.12257e+02	1.21115e+03	1.25508e+04	5.00170e+02	5.82244e+03

Table 5.11: 2D Dissipation Controller Verification : Norms ($t = 7.2\ s$)

t = 7.2	**h results**		**m1 results**		**m2 results**	
ψ	$\|h\|_{H^0}$	$\|h\|_E$	$\|m_1\|_{H^0}$	$\|m_1\|_E$	$\|m_2\|_{H^0}$	$\|m_2\|_E$
0.25	1.08065e+03	1.10842e+02	1.50922e+03	1.13123e+04	6.90995e+02	6.98182e+03
0.50	1.08004e+03	1.55522e+02	1.46493e+03	1.79337e+04	6.59083e+02	1.10391e+04
0.75	1.07942e+03	1.85368e+02	1.42533e+03	2.36978e+04	6.28274e+02	1.43589e+04
1.00	1.07890e+03	2.10182e+02	1.38949e+03	2.91175e+04	5.98773e+02	1.70619e+04
$\psi(ke)$	1.08098e+03	1.20675e+02	1.50398e+03	1.41541e+04	6.86871e+02	7.32010e+03

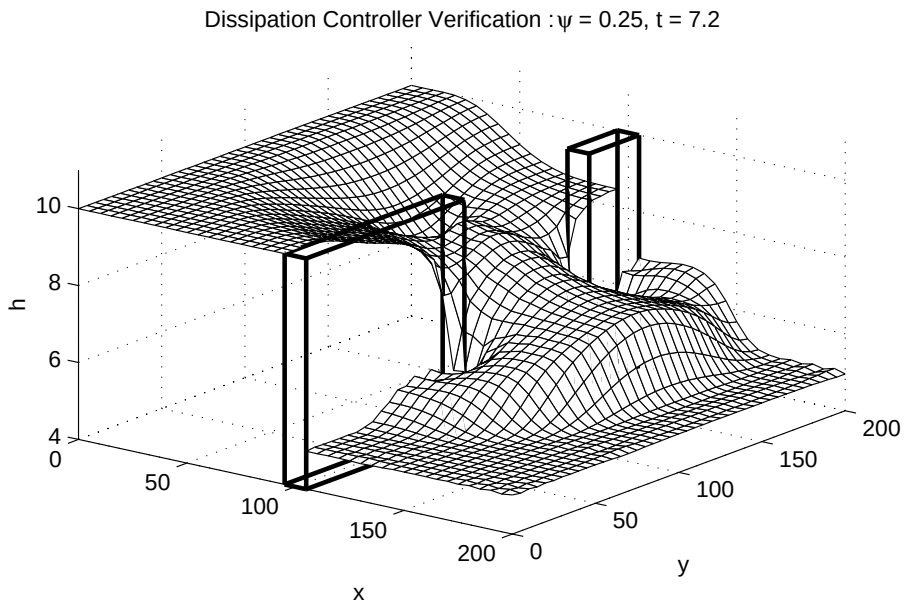

Figure 5.2: 2D Dissipation Controller Verification : $\psi = 0.25$

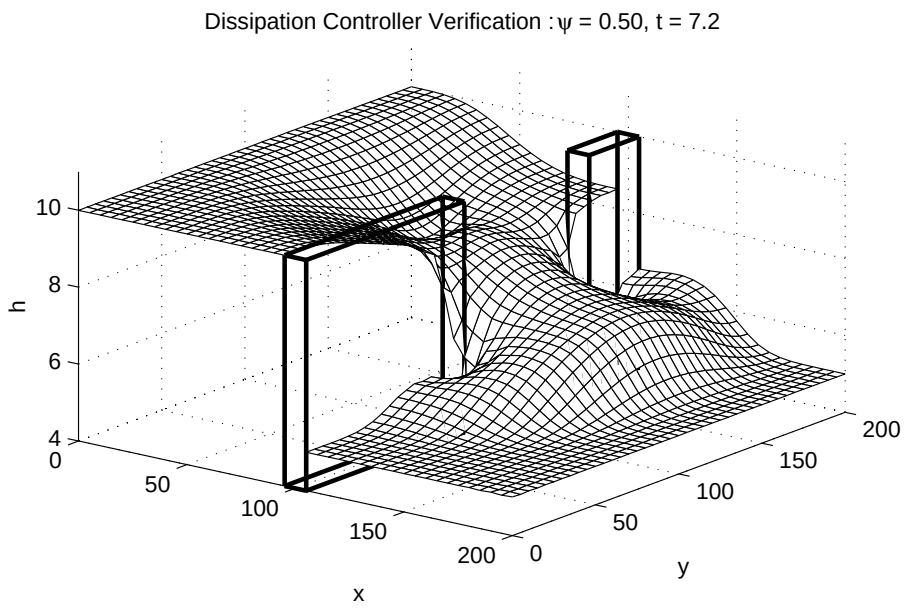

Figure 5.3: 2D Dissipation Controller Verification : $\psi = 0.50$

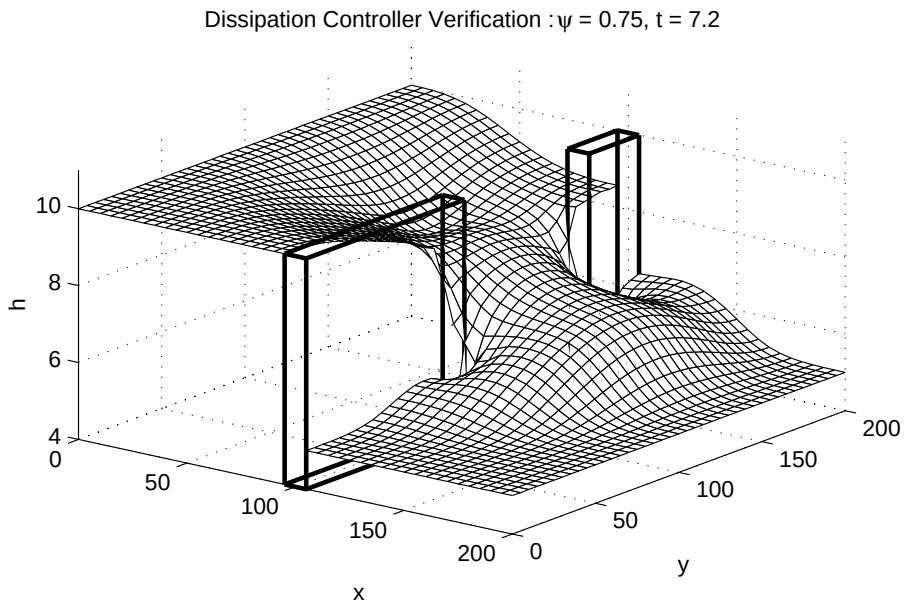

Figure 5.4: 2D Dissipation Controller Verification : $\psi = 0.75$

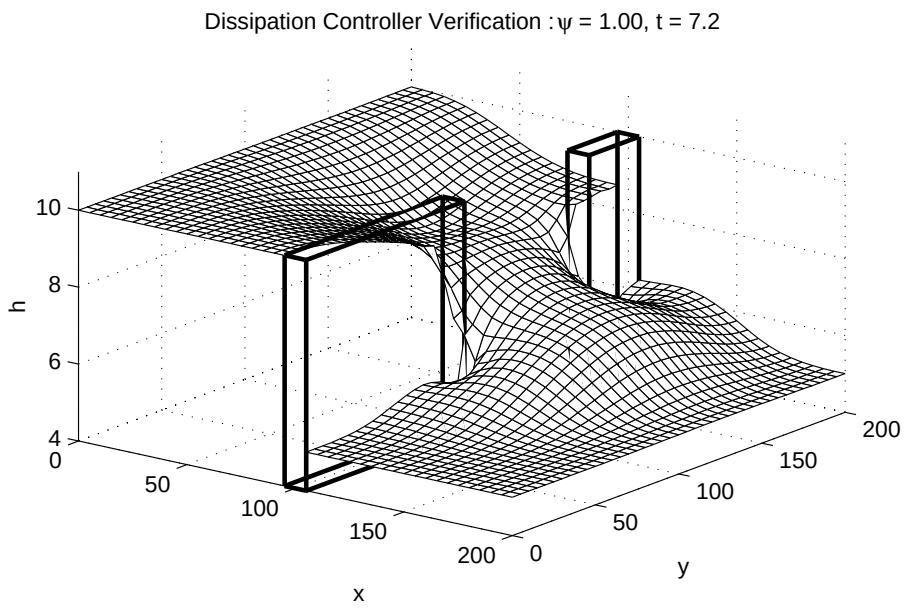

Figure 5.5: 2D Dissipation Controller Verification : $\psi = 1.00$

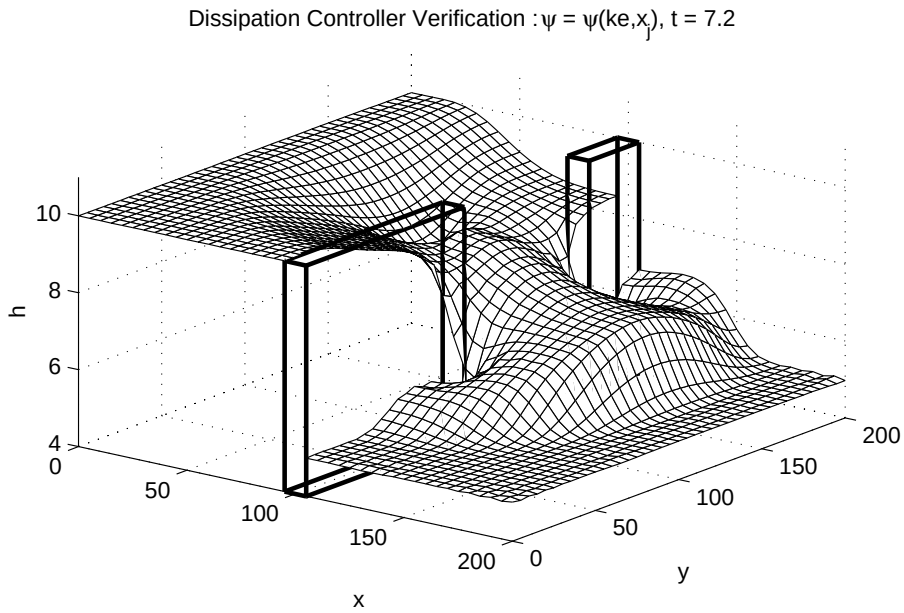

Figure 5.6: 2D Dissipation Controller Verification : $\psi = \psi(ke)$

5.1.3.2 Quasi-Newton Algorithm Convergence Study

The next test, as with the one-dimensional dam break, is to assess the convergence rate of the quasi-Newton iteration algorithm. As stated in section(3.3), a fully Newton formulation will converge quadratically. Quasi-Newton formulations will exhibit converge rates anywhere from nearly quadratic to divergent. Having explicitly formed a quasi-Newton algorithm in section (4.12), iterate convergence and solution impact must be assessed. For this set of tests, the convergence criteria of the GMRES solver was decreased from a relative value of $1e-6$ to $1e-10$ to insure that the solver converged at least as well as the quasi-Newton iteration algorithm.

For this test, eight iterate values of $max(\delta Q_h, \delta Q_{m1}, \delta Q_{m2},)$ for the non-linear $\psi = \psi(ke)$ were studied at time stations of $t = 1,\ 3,\ 5,\ 7.2\ s$ with the parameters held constant as given in Table (5.3) excluding the number of Jacobian iterates.

Solution convergence rates, obtained as best fit lines to all time stations, are summarized in Table (5.12) and the iterate solution increments are presented in Tables (5.13)-(5.14). The convergence in $max(\delta Q)$, Figures (5.7) - (5.9), is near linear for all state variables and all time steps, unlike the one-dimensional dam break, Figures (3.10) - (3.11) which were exactly linear after the initial three iterations. The nonlinearity of the dissipative flux divergence, mostly unincorporated into the quasi-Newton formulation, has a clear impact on the rate of iterate convergence.

The convergence in the norms with respect to number of iterations gives considerable insight into the convergence criteria for the state variables. At all time stations, presented in tables (5.15) - (5.18), the norms converge to six significant digits in anywhere from six to eight iterations. Correlating this data with the $max(\delta Q)$ shows that imposing a convergence criteria of $1e-6$ for the change in all three state variables will yield norms converged to six significant digits.

Having quantified quasi-Newton convergence, solution impact must be assessed in terms of the H^0 and $||q||_E$ norms as the discrete error norm is unavailable. Because the carpet plots are difficult to compare directly, four line plots of h at the final time station will be presented for the assessment: $y = 130\ m$, $x = 80\ m$, $x = 100\ m$, and $x = 120\ m$. Figures (5.10) - (5.11) show no discernible difference in h in going from two to three iterations. Point evaluations, such as these profiles, may therefore incorrectly suggest to a converged solution whereas the solution norms provide a more rigorous convergence criteria.

Table 5.12: 2D Quasi-Newton Convergence Verification : $max(\delta Q)$ Convergence Rates

	Convergence Rates		
Time	$max(\delta Q_h)$	$max(\delta Q_{m1})$	$max(\delta Q_{m2})$
1.0	0.9295	0.9267	0.9755
3.0	0.9663	0.9222	0.9293
5.0	0.8860	0.8860	0.8969
7.2	0.9199	0.9091	0.8978
All	0.9276	0.9181	0.9267

Table 5.13: 2D Quasi-Newton Convergence Verification : Iterates and $max(\delta Q)$ ($t = 1.0,\ 3.0\ s$)

	$t = 1.0$			$t = 3.0$		
Iterate	δQ_h^p	δQ_{m1}^p	δQ_{m2}^p	δQ_h^p	δQ_{m1}^p	δQ_{m2}^p
1	2.0529e-01	1.9805e+00	1.0763e+00	1.6304e-01	1.5583e+00	6.7050e-01
2	7.3071e-03	5.0647e-02	2.5895e-02	3.0774e-03	1.4357e-02	4.8426e-03
3	1.5924e-04	1.8539e-03	1.0654e-03	9.4134e-05	4.7496e-04	2.0034e-04
4	6.9147e-06	1.4617e-04	5.3996e-05	4.1365e-06	2.0806e-05	6.7460e-06
5	2.7704e-07	1.1965e-05	2.4974e-06	1.7542e-07	8.8460e-07	2.4375e-07
6	2.3700e-08	1.0192e-06	1.1715e-07	7.3733e-09	3.7381e-08	1.0213e-08
7	2.0600e-09	8.7612e-08	5.5230e-09	3.1177e-10	1.9084e-09	5.1094e-10
8	1.7896e-10	7.5739e-09	2.4838e-10	1.3147e-11	1.3767e-10	2.5464e-11

Table 5.14: 2D Quasi-Newton Convergence Verification : Iterates and $max(\delta Q)$ $(t = 5.0,\ 7.2\ s)$

	$t = 5.0$			$t = 7.2$		
Iterate	δQ_h^p	δQ_{m1}^p	δQ_{m2}^p	δQ_h^p	δQ_{m1}^p	δQ_{m2}^p
1	1.5010e-01	1.3407e+00	4.6390e-01	1.3374e-01	1.2361e+00	4.6144e-01
2	1.2827e-03	6.7507e-03	3.1312e-03	2.6531e-03	1.3159e-02	4.5441e-03
3	2.3094e-05	4.5157e-04	7.9836e-05	3.3964e-05	2.3146e-04	1.0297e-04
4	1.4699e-06	3.2935e-05	5.2581e-06	1.8012e-06	9.9709e-06	4.8075e-06
5	1.0751e-07	2.4068e-06	3.2945e-07	1.1040e-07	5.7716e-07	3.1372e-07
6	7.8411e-09	1.7552e-07	2.0459e-08	6.9264e-09	3.3335e-08	2.2536e-08
7	5.7081e-10	1.2776e-08	1.2753e-09	4.4171e-10	1.9212e-09	1.6047e-09
8	4.1484e-11	9.2847e-10	8.0079e-11	2.8640e-11	1.2484e-10	1.1352e-10

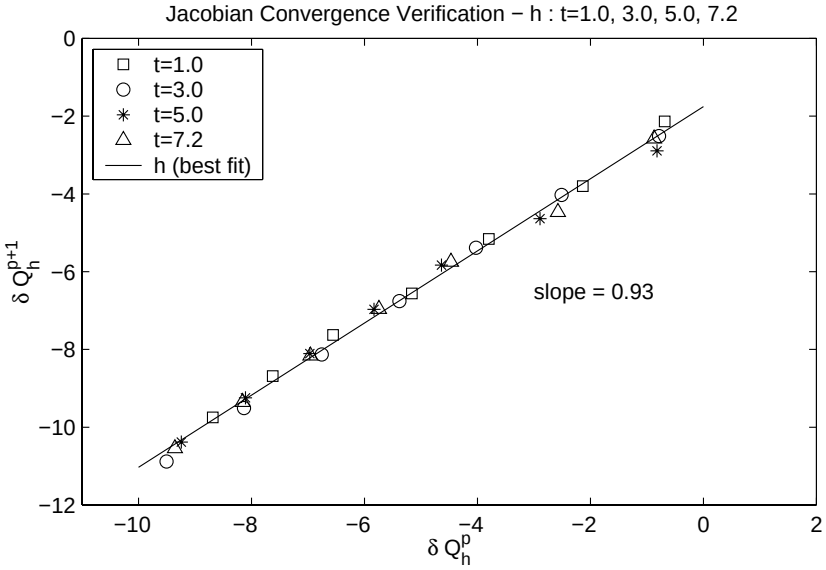

Figure 5.7: 2D Quasi-Newton Convergence Verification : $max(\delta Q_h)$ $(t = 1.0,\ 3.0,\ 5.0,\ 7.2\ s)$

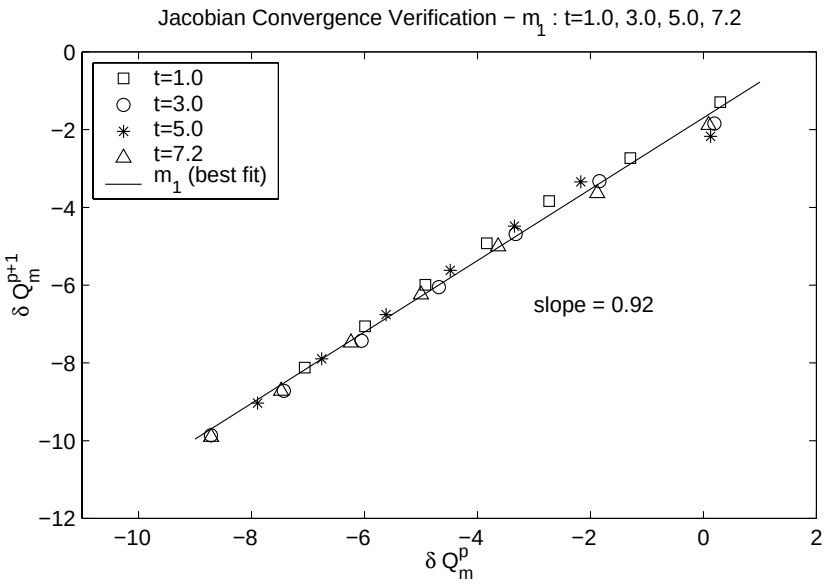

Figure 5.8: 2D Quasi-Newton Convergence Verification : $max(\delta Q_{m1})$ $(t = 1.0,\ 3.0,\ 5.0,\ 7.2\ s)$

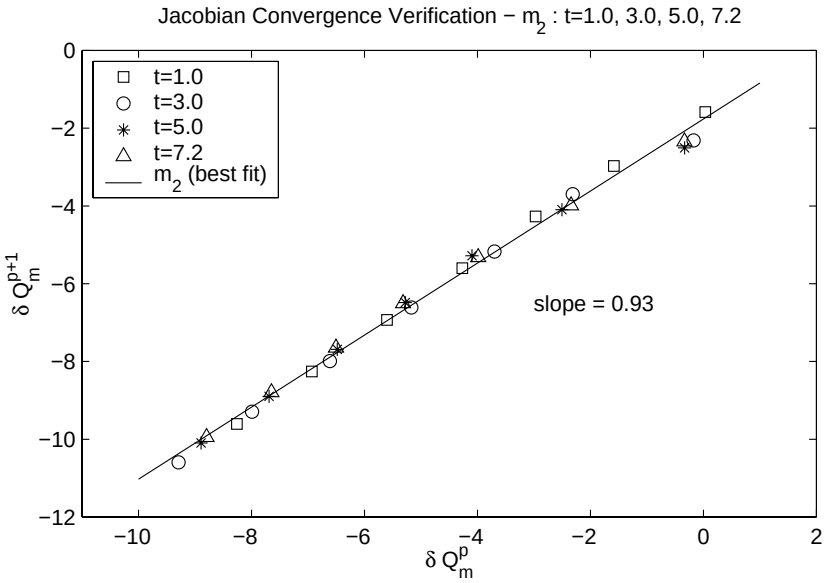

Figure 5.9: 2D Quasi-Newton Convergence Verification : $max(\delta Q_{m2})$ $(t = 1.0,\ 3.0,\ 5.0,\ 7.2\ s)$

Table 5.15: 2D Quasi-Newton Convergence Verification : Iterate Norms ($t = 1.0\ s$)

$t = 1.0$	h results		m1 results		m1 results	
	$\|h\|_{H^0}$	$\|h\|_E$	$\|m_1\|_{H^0}$	$\|m_1\|_E$	$\|m_2\|_{H^0}$	$\|m_2\|_E$
Iterations	$1e+03$	$1e+02$	$1e+02$	$1e+04$	$1e+01$	$1e+03$
2	1.0947203	1.9794248	4.6936763	1.3321741	4.7427519	1.0042047
3	1.0947206	1.9925021	4.6948572	1.3442227	4.7417022	1.0055796
4	1.0947206	1.9925528	4.6948039	1.3443044	4.7414134	1.0054141
5	1.0947206	1.9925748	4.6948026	1.3443231	4.7414112	1.0054160
6	1.0947206	1.9925743	4.6948025	1.3443236	4.7414103	1.0054156
7	1.0947206	1.9925745	4.6948024	1.3443237	4.7414103	1.0054156
8	1.0947206	1.9925745	4.6948024	1.3443237	4.7414103	1.0054156

Table 5.16: 2D Quasi-Newton Convergence Verification : Iterate Norms ($t = 3.0\ s$)

$t = 3.0$	h results		m1 results		m1 results	
	$\|h\|_{H^0}$	$\|h\|_E$	$\|m_1\|_{H^0}$	$\|m_1\|_E$	$\|m_2\|_{H^0}$	$\|m_2\|_E$
Iterations	$1e+03$	$1e+02$	$1e+02$	$1e+04$	$1e+02$	$1e+03$
2	1.0903272	1.1190619	9.0267127	1.1226857	2.7271177	4.2912631
3	1.0903270	1.1193489	9.0265223	1.1226476	2.7273457	4.2921783
4	1.0903270	1.1193552	9.0265179	1.1226542	2.7273343	4.2921946
5	1.0903270	1.1193556	9.0265172	1.1226536	2.7273345	4.2921947
6	1.0903270	1.1193556	9.0265171	1.1226536	2.7273344	4.2921946
7	1.0903270	1.1193556	9.0265171	1.1226536	2.7273344	4.2921946
8	1.0903270	1.1193556	9.0265171	1.1226536	2.7273344	4.2921946

Table 5.17: 2D Quasi-Newton Convergence Verification : Iterate Norms ($t = 5.0\ s$)

$t = 5.0$	h results		m1 results		m1 results	
	$\|h\|_{H^0}$	$\|h\|_E$	$\|m_1\|_{H^0}$	$\|m_1\|_E$	$\|m_2\|_{H^0}$	$\|m_2\|_E$
Iterations	$1e+03$	$1e+02$	$1e+03$	$1e+04$	$1e+02$	$1e+03$
2	1.0859141	1.1225411	1.2111603	1.2549760	5.0015796	5.8223155
3	1.0859141	1.1225673	1.2111552	1.2550802	5.0017043	5.8224237
4	1.0859141	1.1225714	1.2111547	1.2550830	5.0017000	5.8224410
5	1.0859141	1.1225720	1.2111547	1.2550836	5.0017000	5.8224412
6	1.0859141	1.1225720	1.2111547	1.2550836	5.0016999	5.8224412
7	1.0859141	1.1225720	1.2111547	1.2550836	5.0016999	5.8224412
8	1.0859141	1.1225720	1.2111547	1.2550836	5.0016999	5.8224412

Table 5.18: 2D Quasi-Newton Convergence Verification : Iterate Norms ($t = 7.2\ s$)

$t = 7.2$	h results		m1 results		m1 results	
	$\|h\|_{H^0}$	$\|h\|_E$	$\|m_1\|_{H^0}$	$\|m_1\|_E$	$\|m_2\|_{H^0}$	$\|m_2\|_E$
Iterations	$1e+03$	$1e+02$	$1e+03$	$1e+04$	$1e+02$	$1e+03$
2	1.0809873	1.2069451	1.5039920	1.4153482	6.8687194	7.3201709
3	1.0809873	1.2067591	1.5039897	1.4154233	6.8687160	7.3201079
4	1.0809872	1.2067549	1.5039892	1.4154133	6.8687154	7.3201059
5	1.0809872	1.2067555	1.5039892	1.4154139	6.8687152	7.3201062
6	1.0809872	1.2067555	1.5039892	1.4154139	6.8687152	7.3201062
7	1.0809872	1.2067555	1.5039892	1.4154139	6.8687152	7.3201062
8	1.0809872	1.2067555	1.5039892	1.4154139	6.8687152	7.3201062

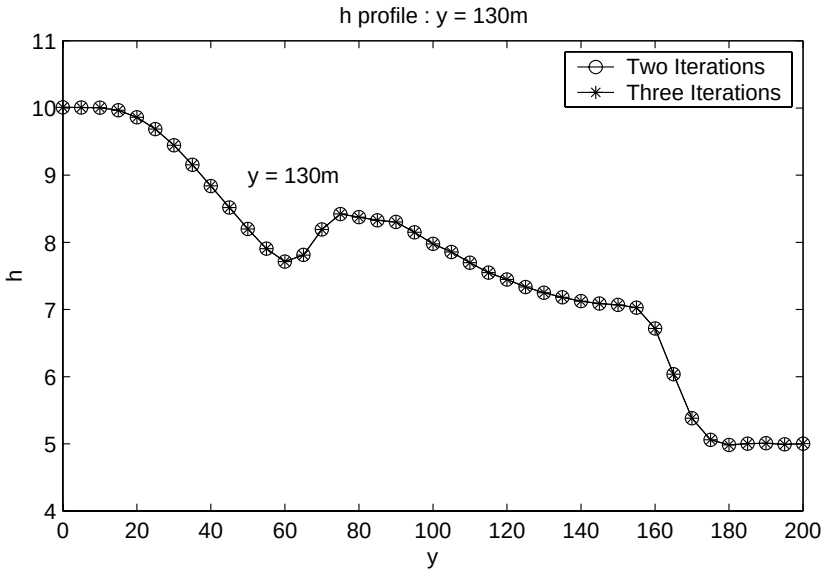

Figure 5.10: 2D Quasi-Newton Convergence Verification : h profile ($t = 7.2\ s, y = 130\ m$)

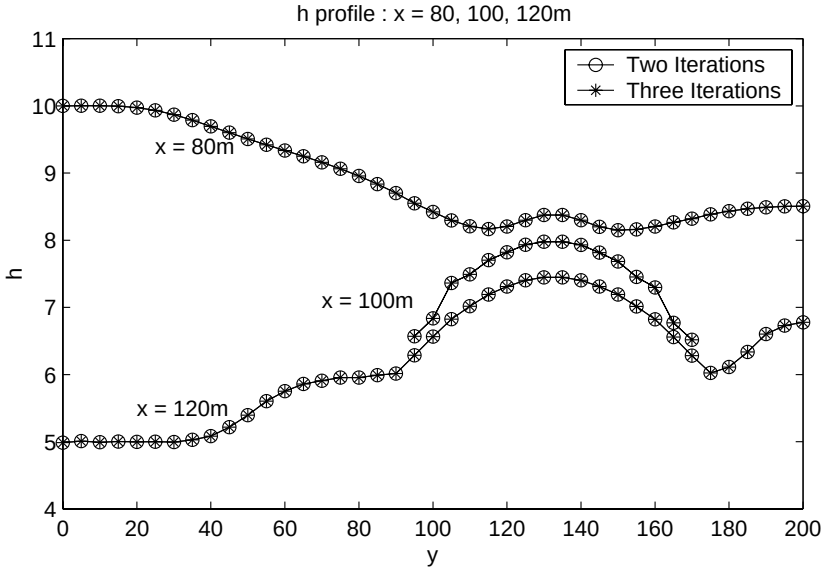

Figure 5.11: 2D Quasi-Newton Convergence Verification : h profile ($t = 7.2\ s, x = 80, 100, 120\ m$)

5.1.3.3 Grid Refinement Study

The final test is to verify solution convergence under temporal and spatial refinement. As discussed in Section (3.4), the norms will converge at a rate of $2k$, where $k = 1$ for the linear basis, assuming the temporal truncation error is adequately small. The testing procedure will follow that of the one-dimensional dam break:

1. An initial spatial discretization is selected and the transient solution is solved repeatedly with uniform temporal refinements. Upon solution convergence at all time stations, the temporal truncation error has been rendered negligible.

2. The spatial discretization is uniformly refined and (1) is repeated.

3. (2) is repeated until the temporally converged solutions exhibit convergence in spatial discretization.

Grid discretizations of 20, 40, 80, and 160 elements were considered with an initial time step of $\Delta t = 0.1\ s$. As the mesh was refined, the time step was refined accordingly as given in Table (5.19) gives the test, discretization, and corresponding Δt for each test. All other solution parameters are held constant as given in Table (5.3). Temporal convergence was assessed at time stations of $t = 1,\ 3,\ 5,\ 7.2\ s$.

Tables (C.1) - (C.4) present the energy norm temporal convergence data for each spatial discretization respectively. Each table contains the four time stations at which the energy norms were extracted and the respective five temporal refinement tests. Tables (C.5) - (C.8) follows an identical format for the H^0 norm.

For each discretization and related time station, the fifth temporal discretization, Table (5.19), was selected as the discretization which sufficiently minimizes the temporal truncation error in (3.12). Thus, the error convergence rate becomes effectively a function of the grid refinement. Tables (C.9)

Table 5.19: 2D Grid Refinement Verification : Δt Summary

	Δt for Each Grid			
Test	20	40	80	160
1	0.100000	0.050000	0.0250000	0.01250000
2	0.050000	0.025000	0.0125000	0.00625000
3	0.025000	0.012500	0.0062500	0.00312500
4	0.012500	0.006250	0.0031250	0.00156250
5	0.006250	0.003125	0.0015625	0.00078125

- (C.12) list the temporally converged energy norms and convergence rates for each mesh at each time station. The H^0 norms are given in Tables (C.13) - (C.16).

The final error convergence rates measured in each norm are compiled in Tables (5.20) - (5.21). Studying the convergence rates based on the energy norm indicates that, for h, the convergence rate improved as the time station increased. With the exception of the $80x80$ grid at $t = 1.0\ s$, the convergence rate in h is greater than two and thus indicative of an order of accuracy greated the second order for a formally second order algorithm. The convergence rate in m_1 also indicates a higher order method for the $160x160$ grid for time stations greater than $t = 1.0\ s$ while remaining nominally second order for the $80x80$ grid. For m_2 at $t = 1.0\ s$, the convergence rate is polluted by the coarse grid error associated with the initial $20x20$ grid and can be considered erroneous. The convergence rate at the remaining time stations approaches quadratic as the time station increases. Heed that all convergence rates improved in going from the $80x80$ to the $160x160$ grid, with the exception of m_2 at $t = 1.0\ s$, indicating that the initial $20x20$ grid is barely capable of supporting a quality solution. Additionally, the convergence rate increases with increasing time stations for h and m_2 while it peaks at $t = 3.0\ s$ for m_2. Unlike the one-dimensional dam break, no round-off error is evident.

Table 5.20: 2D Grid Refinement Verification : Error Convergence Rate in Energy Norm

	Mesh	$t = 1.0$	$t = 3.0$	$t = 5.0$	$t = 7.2$
$e^h(\|\|h\|\|_E)$	80	0.5800	2.1362	2.2177	3.4464
	160	2.0772	2.3074	2.9954	3.5677
$e^h(\|\|m_1\|\|_E)$	80	1.3971	2.0980	1.9586	1.8381
	160	1.7387	2.3069	2.2234	2.0536
$e^h(\|\|m_2\|\|_E)$	80	-3.3929	0.7860	1.3733	1.6106
	160	-2.4109	1.1418	1.8308	1.9789

Table 5.21: 2D Grid Refinement Verification : Error Convergence Rate in H^0 Norm

	Mesh	$t = 1.0$	$t = 3.0$	$t = 5.0$	$t = 7.2$
$e^h(\|\|h\|\|_{H^0})$	80	6.4594	4.9860	4.1417	3.1088
	160	1.7807	1.9159	1.9827	1.9999
$e^h(\|\|m_1\|\|_{H^0})$	80	-1.2455	-2.1715	-4.1680	-0.9341
	160	1.4673	1.7056	1.9146	1.9999
$e^h(\|\|m_2\|\|_{H^0})$	80	0.2216	0.9730	1.2402	1.0977
	160	1.3802	1.6249	1.8776	1.9576

The error convergence measured in the H^0 norm exceeds quadratic for h in the $80x80$ discretization and the algorithm ranges from *sixth* to *third* order accurate in this variable on the coarse grids. The convergence rate decreases to quadratic for the $160x160$ grid. For m_1, however, the coarse grid can not support a quality solution, hence the estimated convergence rates are invalid for the $80x80$ grid. Refining the grid to $160x160$ yields convergence rates which approach quadratic. Likewise, for m_2, the coarse convergence rate is nominally linear while nearly quadratic for the fine grid. From the poor convergence of $m_{1,2}$ on the coarse grid and the decreasing convergence rate of h with increasing time, the high convergence rates in h should be considered fortuitous rather than indicative of a higher order algorithm. As with the energy norm, the fine grid convergence rates increase with increasing time station and no round-off error is evident.

Having assessed the solution error convergence rate under uniform grid refinement and verified solution convergence, a new benchmark solution is available from the $160x160$ grid at $t = 7.2\ s$. The Courant number, obtained with a constant $\Delta t = 0.0125$, is less than 0.3 for all time stations. Heed that this solution is visually identical to those generated with smaller Courant numbers and is therefore presented as representative of all the $160x160$ solutions. This fine grid solution, Figures (5.12) - (5.13), reveals flow features unobtainable from the coarser grid solutions, notable the plateau which develops within the missing dam section and along the back edge of the tailwater region. Note that the advancing hydraulic jump is crisply resolved over approximately five elements with no visible over- or undershoot. Additionally, no spurious oscillations are evident along the solution boundaries.

5.1.4 Discussion

The performance of the characteristics biased open channel flow equation system was investigated with respect to the dissipation controller ψ, quasi-Newton iteration convergence rates, and solution error convergence under uniform grid refinement. The non-linear dissipation controller, with solution continuity gauged by the nodal kinetic energy, was found to yield better results than constant values of ψ. Comparing the carpet plots of the h distribution with published solutions reveals that, even with $\psi = 1$, the h distribution is lessed diffused than that reported by Galister, Ambrosi, and Paillere. The non-linear ψ results compare well with the best results reported by Fennema and Alcrudo, the only results which predict the depression upstream of the missing dam and the plateau within the missing dam. Solution extrema and norms for the standard benchmark case were presented and stand alone as no other reports of these values are available.

The quasi-Newton iteration algorithm was found to converge linearly. While profiles of the h distribution at representative domain slices are indistinguishable to the eye, the convergence in the norms with increasing iterations revealed a convergence criteria of $1e-6$ on all $max(\delta Q)$ yielded

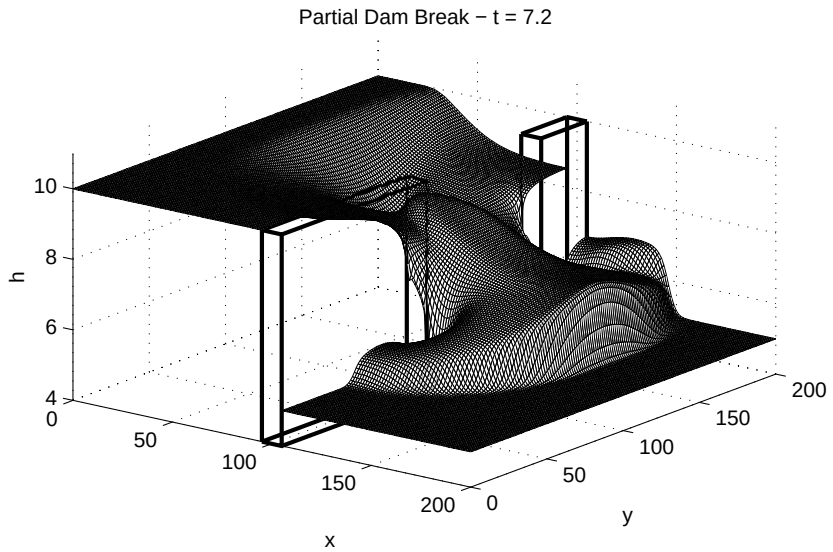

Figure 5.12: Partial Dam Benchmark : h Carpet ($t = 7.2\ s$)

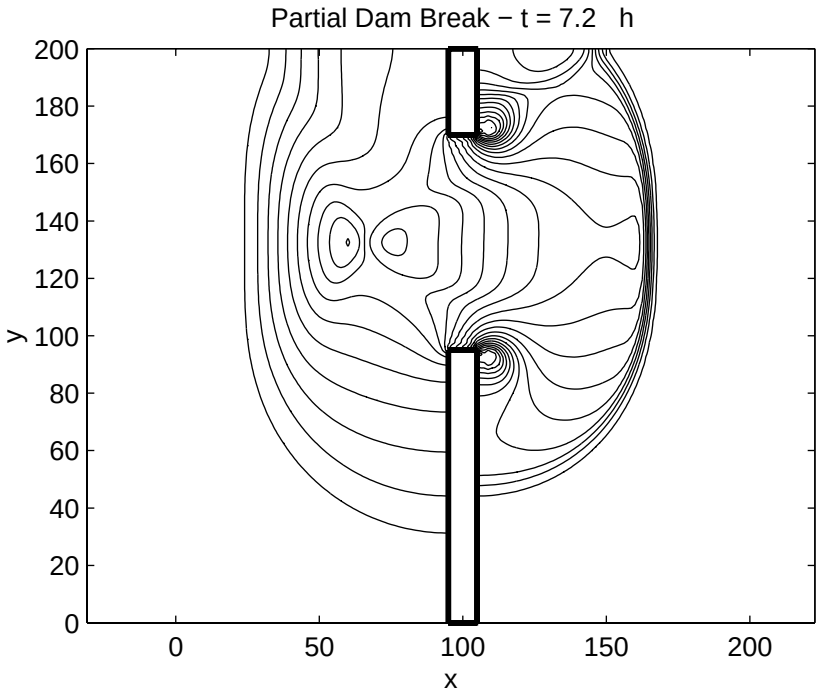

Figure 5.13: Partial Dam Benchmark : h Contour ($t = 7.2\ s$)

norms converged to six significant digits.

Under uniform grid refinement, the convergence in solution error based on the energy norm and the H^0 norm indicated an algorithm which varied from nominally second order accurate to as high as third order accurate. The error convergence rate based on energy norms was primarily slightly better than quadratic while the convergence rate based on the H^0 norms exhibited improper convergence on the coarse grids of $20x20$ - $80x80$ while improving to quadratic on the fine grid of $160x160$.

From the grid refinement study, a new benchmark for the partial dam break was introduced via carpet and contour plots of h from the $160x160$ grid. These plots revealed flow features previously unobservable on the published $40x40$ grids, notabley the crisp plateaus within the missing dam section and along the upper edge of the tailwater region.

5.2 Circular Dam Break

Having verified the characteristics-biased flux divergence theory for the inviscid open channel equation system on the challenging partial dam break problem, the next benchmark is the circular dam break. Introduced in 1993 by Alcrudo *et al* [52] in the same paper presenting the partial dam break results for the high-resolution Godunov alogorithm, this problem features a circular am in the center of a square computational domain featuring a uniform 50x50 grid. At time zero, the dam is removed and the solution propagates radially outward. Interestingly, Alcrudo's results indicate four small "islands" of height centered at the axial lines of 45, 135, 225, and 315 degrees and a "squaring" of the solution along the privileged flow directions (i.e. the global (x, y) coordinate axes). Employing a body-fitted computational grid eliminated both the islands and the squaring while greatly improving the resolution of the h distribution.

Anastasiou, *et al* [55] also treat this problem in their 1997 paper. While not exhibiting the islands nor the squaring witnessed by Alcrudo, their solution is hardly radially symmetric behind

the advancing wave front. Body fitted grids were not presented.

Tseng [57] presented a detailed comparison of four high-resolution, non-oscillatory algoritms (a first-order Roe, second-order TVD and ENO, and a third-order ENO) in 1999 for a body fitted grid of finite volume quadrilaterals. These results compare will with the body fitted grid results of Alcrudo. A composite scheme, presented the same year by Liska, *et al* [58], switched from a second order Lax-Wendroff finite difference scheme to a first-order Lax-Friedrichs scheme in regions of solution discontinuity. Their results, presented on the cartesian grid, appear nearly identical to the body-fitted results of Alcrudo and Tseng.

5.2.1 Problem Statement

For this problem, as with the partial dam break, the dam is assumed to fail instantaneously. The cartesian computational domain is a 50m by 50m tailwater region. Centered at (25,25) is a circular reservoir with a radius of 11m. Figure (5.14) details the geometry. A frictionless, horizontal bottom is assumed. A tailwater/reservoir ratio of 0.1 was employed to obtain the initial height distribution. For comparison with the publications, the simulation was run for $0 \leq t \leq 0.69$ seconds.

Casual inspection of this problem indicates it to be nearly trivial in comarison to the partial dam break - simple geometry with, upon transformation to polar-coordinates, a one-dimensional variation along the axial direction. Intuition, reinforced by published numerical results, suggests a series of concentric circles propogating outward from the dam. A careful investigation of the interpolated initial condition, presented in this research, indicates otherwise.

5.2.2 Boundary and Initial Conditions

In accordance with Figure (5.14), the applied boundary conditions, defined by Alcrudo *et al* [52], are summarized in Table (5.22). The initial condition is $m_1 = m_2 = 0m^2/s$ throughout the domain

while $h = 1m$ in the tailwater region and $h = 10m$ in the reservoir region. To apply the initial condition for h, all nodes satisfying

$$y = \pm\sqrt{11^2 - (x - 25)^2} + 25 \tag{5.6}$$

were assigned $h = 10$, all other nodes were assigned $h = 1$. Clearly some interpolation of the initial condition must occur around the reservoir wall. Plotting the interpolated initial condition, Figure (5.15), reveals a distribution unlike a perfect circle.

The interpolated initial condition does exhibit symmetry, albeit not radial symmetry. The islands witnessed by Alcrudo arise directly from the straight lines inclined at $\pm 45^{\cdot}$ from the x axis. Moreover, the "squaring" of the solution is a direct conseqence of the vertical and horizontal initial condition on the x and y axes respectively. Heed that the original problem statement lacks a dissipative mechanism to diffuse the initial condition, hence correct solutions should closely mirror the initial condition. Only excessive artificial dissipation will yield concentric circles outside the dam perimeter and a circular advancing wave front.

5.2.3 Results

The characteristics biased flux divergence algorithm was employed on a uniform cartesian 50x50 grid with bi-linear quadrilateral finite elements. The non-linear dissipation controller used the nodal kinetic energy to gauge solution continuity. The algorithm parameters are summarized in Table

Table 5.22: Circular Dam Break : Boundary Conditions

Edges /Corners	**Dirichlet**	**Neumann**
a,b,c,d	$h = 1,\ m_1 = m_2 = 0$	
A,C	$h = 1,\ m_1 = 0$	$\nabla m_2 \cdot \mathbf{n} = 0$
B,D	$h = 1,\ m_2 = 0$	$\nabla m_1 \cdot \mathbf{n} = 0$

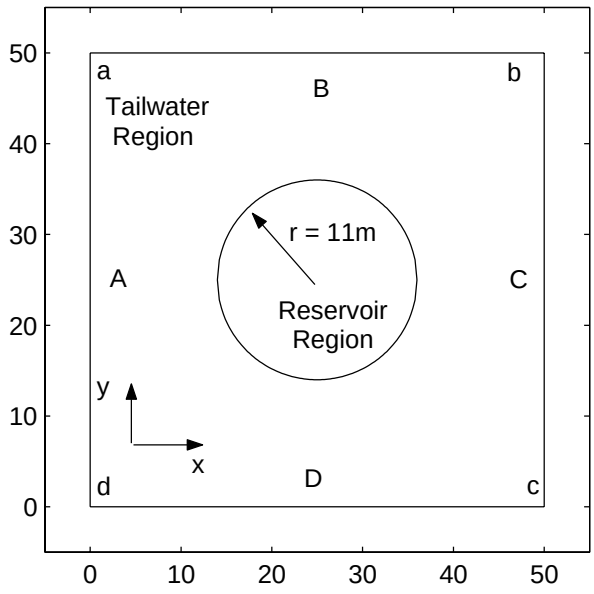

Figure 5.14: Circular Dam Break : Computational Domain

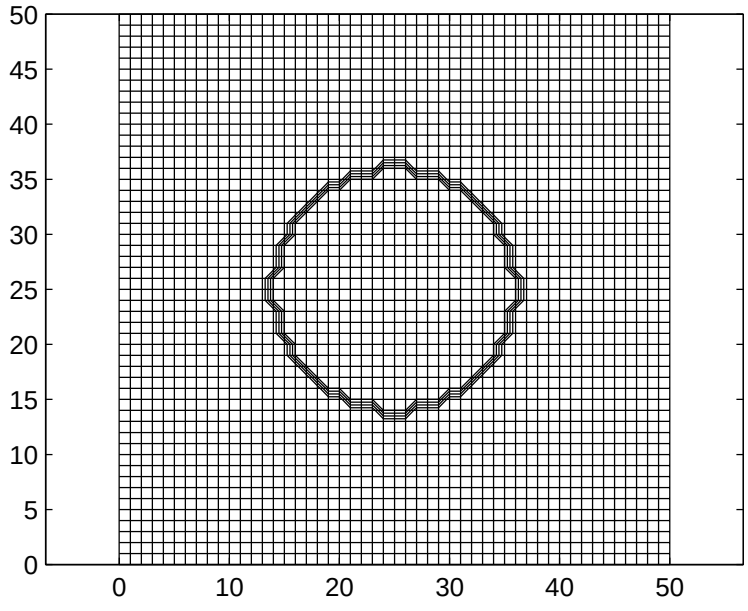

Figure 5.15: Circular Dam Break : Interpolated Initial Condition

(5.23). Contour and carpet plots of the h distribution are presented at a time station of $t = 0.69\ s$ for comparison with published solutions. As with the partial dam break, extremum values of h and maximum values of m_1, m_2 as well as the H^0 norm and energy semi-norm are presented at time stations of $t = 0.1,\ 0.3,\ 0.5,\ 0.69\ s$ to provide data for future comparisons.

Examining the extremum values in h, Table (5.24), indicates a 2% - 0.1% overshoot and an 18% - 9% undershoot at time stations $t = 0.1\ s$ and $1 = 0.69\ s$ respectively. This dispersion error, however, is not indicative of a poorly performing algorithm. Rather, the interpolated initial condition is so extreme that the coarse grid is simply unable to support a monotone solution without excessive artificial dissipation. As such, a monotone solution will be inaccurate. Examining the carpet plot of h at $t = 0.69\ s$, Figure (), shows a fair balance between accuracy and stability. Plotting the contours of h with the same levels used by Alcrudo show not only his "islands" but also "penninsulas" along the global x and y axes, caused by the observed squaring of the initial condition along these lines. Note that the initial condition is evident interior to the islands while the contours within the initial dam region are perfectly concentric circles. The perimeter of the advancing fron is slightly squared along the global coordinate axes but all other indications of the initial condition are gone. Recalling the dissipative flux divergence to be a function of the length scale and the solution gradient and

Table 5.23: Circular Dam Break : Constant Parameters

Parameter	**Value**
Number of Elements (N)	$50x50$
Δt	0.01
Convergence Criteria	1e-7
$2\mu_o$	0.2
ϵ_{Fr}	0.2
ψ_{min}	0.25
ψ_{max}	1.00

recognizing the grid to be too coarse to support and accurate monotone solution based on the extreme initial condition, the excessive dissipation induced by the characteristics-bias flux divergence is both consistent and appropriate. Heed that this solution is the truest reflection of the initial condition published to date.

While the initial condition is not radially symmetric, there is inherent circular symmetry albeit rough. The maximum values of m_1 and m_2 should therefore be identical as well as their associated norms. Tables (5.24) and (5.25) indicate this to be true. While the tabulated values are reported to only eight and six significant digits, the values were identical to round-off error. Unsurprisingly, the norms of h decrease as the solution evolves while the norms of m_1 and m_2 increase.

In an effort to encourage more monotone solutions, experiments were performed in which the minimum value of ψ was increased from 0.25 to values of 0.5, 0.75, and 1.00. Even with the algorithm fully upwinded, small undershoot dispersion error on the order of 1% to 0.1% for time stations $t = 0.1\ s$ and $t = 0.69\ s$ was evident. No overshoot was evident while the solution was damped enough to yield the symmetric circles and islands akin to Alcrudo's results. No amount of parameter manipulation could recover the solution presented by Liska.

Table 5.24: Circular Dam Break : Extrema

	h results		**m1 results**	**m2 results**	**m results**
Time	h_{min}	h_{max}	$m_{1,max}$	$m_{2,max}$	m_{max}
0.10	0.819991	10.203806	20.405777	20.405777	21.498241
0.30	0.886637	10.055146	27.079261	27.079261	28.524171
0.50	0.897027	10.043838	26.465846	26.465846	27.465778
0.69	0.913906	10.010247	25.762526	25.762526	26.090165

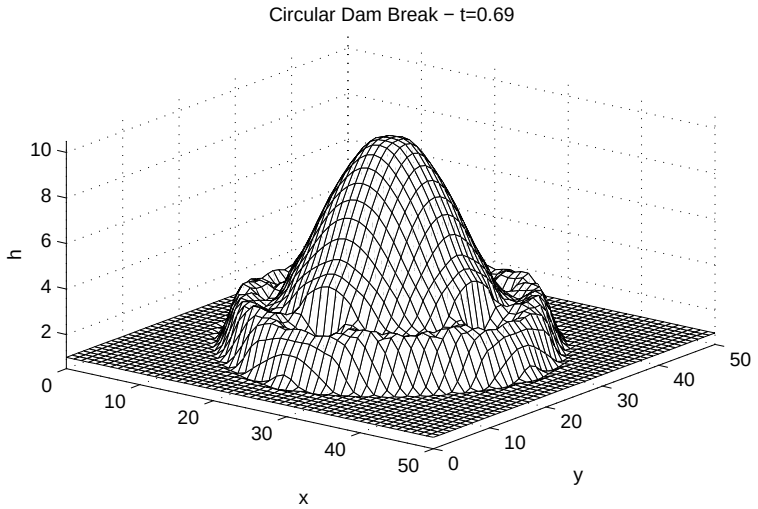

Figure 5.16: Circular Dam Break : h Carpet Plot ($t = 0.69\ s$)

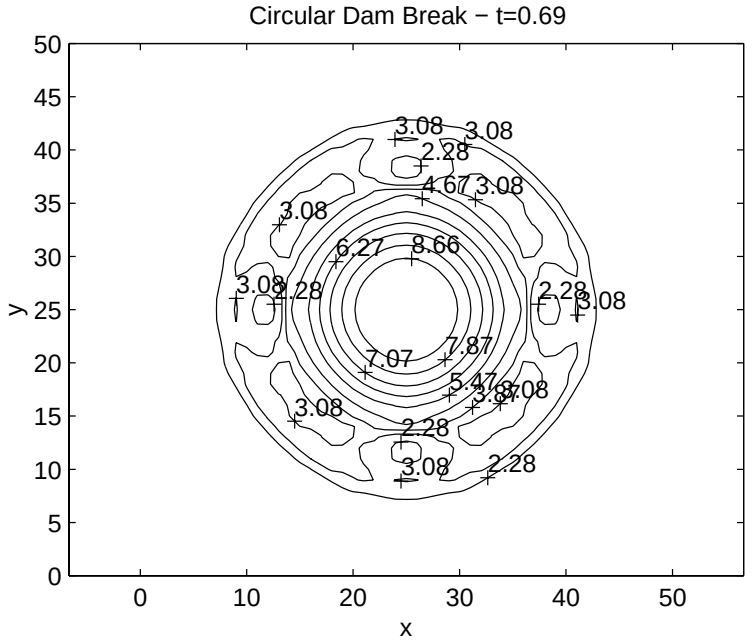

Figure 5.17: Circular Dam Break : h Contour Plot ($t = 0.69\ s$)

Table 5.25: Circular Dam Break : Norms

	h results		**m1 results**		**m2 results**	
Time	$\|h\|_{H^0}$	$\|h\|_E$	$\|m_1\|_{H^0}$	$\|m_1\|_E$	$\|m_2\|_{H^0}$	$\|m_2\|_E$
0.10	4.97223e+02	9.84188e+03	9.84188e+03	1.36932e+02	1.08892e+02	1.08892e+02
0.30	1.64880e+02	5.38393e+03	5.38393e+03	1.28904e+02	2.18531e+02	2.18531e+02
0.50	1.02133e+02	3.50160e+03	3.50160e+03	1.20573e+02	2.82778e+02	2.82778e+02
0.69	7.20643e+01	2.81389e+03	2.81389e+03	1.12838e+02	3.22634e+02	3.22634e+02

5.2.4 Discussion

The circular dam break, solved on a cartesian grid, is a very difficult problem due to the interpolated initial condition. This research has shown that not only is the grid inadequate to support a solution which is both monotone and accurate, the published solutions are highly suspect as they lack solution character fundamental to the initial condition. Alcrudo's results are the closest to these new results while those by Liska correlate so perfectly with the body-fitted results of Tseng and Alcrudo that they should be considered suspect.

5.3 River Harbor

The final benchmark, the river harbor, is a new problem intended to introduce the open channel community to the subtleties of the driven cavity of incompressible Navier-Stokes. The driven cavity is a standard benchmark and has been used to test many algorithms [59]. The computational domain is a unit square with solid boundaries. At time zero, the upper "lid" is impulsively accelerated to a constant velocity. For viscous flow simulations, the lid velocity is selected to yield appropriate Reynolds numbers. The boundary condition singularities at the upper corners yield serious computational difficulties for increasing Reynolds numbers. The vorticity-streamfunction formulation,

in particular, exhibits sharp spikes in omega which lead to dispersive error modes througout the computational domain.

5.3.1 Problem Statement

Unlike the partial and circular dam break benchmarks, no dam is involved in this problem. The computational domain is a small 5x5 meter harbor with a frictionless, horizontal bottom. Figure (5.18) details the geometry. The left, right, and bottom boundaries are assumed solid while the upper boundary borders a river. The water height is initially a uniform 1 meters and the harbor is quiesent. At time zero, the river interface is instantaneously accelerated to a momentum of $1m^2/s$. To maintain the character of the driven cavity problem, the river interface is assumed solid. The simulation is run to steady state.

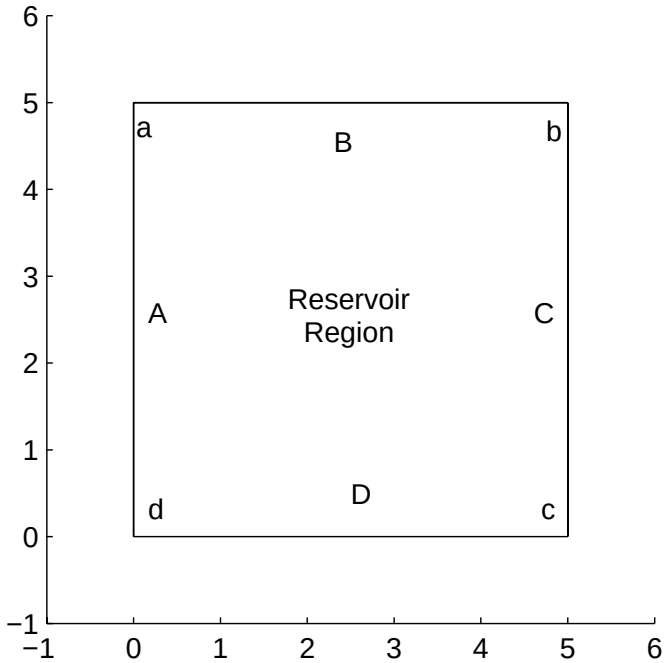

Figure 5.18: River Harbor : Computational Domain

5.3.2 Boundary and Initial Conditions

In accordance with Figure (5.18), the applied boundary conditions are summarized in Table (5.26). The initial condition is $h = 1$ meters and $m_{1,2} = 0$ throughout the computational domain.

5.3.3 Results

The characteristics biased flux divergence algorithm was employed on a uniform cartesian 50x50 grid with bi-linear quadrilateral finite elements. The non-linear dissipation controller used the nodal kinetic energy to gauge solution continuity. Contour and carpet plots of the h distribution as well as a contour plot of the momentum m and quiver plots of the momentum vectors are presented at the steady state. Extremum values of h and maximum values of m_1, m_2 as well as the H^0 norm and energy semi-norm are presented at the steady state to provide data for future comparisons.

Steady state conditions were obtained by running the model for 200 seconds and examining the change in the solution H^0 and energy norms. Four plots of the convergence in the norms are presented: the first two, Figures (5.19) - (5.20), highlight the initial convergence of the norms by employing a y-axis scale of $-0.01 - 0.05$, the second two, Figures (5.21) - (5.22), highlight the final convergence of the norms by refining the y-axis scale to $-1e-5$ to $5e-5$. The norms and extrema at the final time step, $t = 200\,s$, are given in Tables (5.28) and (5.29) respectively. Table (5.28) also

Table 5.26: River Harbor : Boundary Conditions

Edges / Corners	**Dirichlet**	**Neumann**
B	$m_1 = 1,\ m_2 = 0$	$\nabla h \cdot \mathbf{n} = 0$
a,b	$m_1 = 1,\ m_2 = 0$	$\nabla h \cdot \mathbf{n} = 0$
A,C	$m_1 = 0$	$\nabla h \cdot \mathbf{n} = \nabla m_2 \cdot \mathbf{n} = 0$
D	$m_2 = 0$	$\nabla h \cdot \mathbf{n} = \nabla m_1 \cdot \mathbf{n} = 0$
c,d	$m_1 = m_2 = 0$	$\nabla h \cdot \mathbf{n} = 0$

Table 5.27: River Harbor : Constant Parameters

Parameter	**Value**
Number of Elements (N)	$50x50$
Δt	0.1
Convergence Criteria	1e-7
$2\mu_o$	0.2
ϵ_{Fr}	0.2
ψ_{min}	0.25
ψ_{max}	1.00

gives the change in the norms in going to the last step and the change is seen to occur in anywhere from the seventh to eleventh significant digit, indicating a well converged solution.

The convergence plots show the norms to oscillate at solution steps prior to 200, i.e. 20 seconds. After the solution has stabilized from the discontinuous initial condition, the convergence is seen to be monotone from steps 600 (60 seconds) to the end of the simulation. Note that the norm for m_1 shows the most oscillation as that is the direction in which the initial condition was applied. Moreover, the energy norm in m_1 converges from the bottom since the m_1 distribution is smoothened over time yielding an energy decrease. Even though though the reservoir height h is intrinsically connected to m_1, its oscillations dampen out well before those exhibited by m_1.

Table 5.28: River Harbor : Steady-State Norms

	h results		**m1 results**		**m2 results**	
	$\|h\|_{H^0}$	$\|h\|_E$	$\|m_1\|_{H^0}$	$\|m_1\|_E$	$\|m_2\|_{H^0}$	$\|m_2\|_E$
Norm	3.53566e+00	4.69778e-04	1.11560e+00	2.21411e-01	1.03842e+00	5.26871e-02
Δ Norm	5.98250e-11	2.20666e-11	1.23879e-07	-5.08697e-09	1.32042e-07	-5.08697e-09

Table 5.29: River Harbor : Steady State Extrema

h results		**m1 result**	**m2 result**	**m result**
h_{min}	h_{max}	$m_{1,max}$	$m_{2,max}$	m_{max}
9.65612e-01	1.13403e+00	1	4.92072e-01	1

Examining the carpet and contour plots of h, Figures (5.23) and (5.24) show two spikes in the upper corners of the harbor. These spikes, analogous to the spikes observed in the vorticity-streamfunction driven cavity, arise from the boundary condition singularity at corners a and b. The characterisitics-bias algorithm yields an h distribution which is nearly monotone on the uniform grid. Refining the mesh along the river interface would undoubtedly encourage a more monotone distribution.

The contour plot of m is somewhat symmetric but biased towards the right side. Additionally, contours are seen to radiate from the two lower corners due to the Dirichlet conditions of $m_1 = m_2 = 0$ imposed on nodes c and d. These boundary conditions do not permit the solution to propagate smoothly around the harbor perimeter, rather it must stagnate in these two corners. Likewise, strong momentum gradients are evident in the upper right corner b, again due to the imposed Dirichlet boundary conditions. The central stagnation point is near the center of the harbor but slightly biased towards the upper right corner. The quiver plot reveals the direction of rotation to be clockwise with the greatest momentum along the river interface. The momentum directions are aligned with their associated edges and turn smoothly around the corners. No regions of recirculation are evident for this problem.

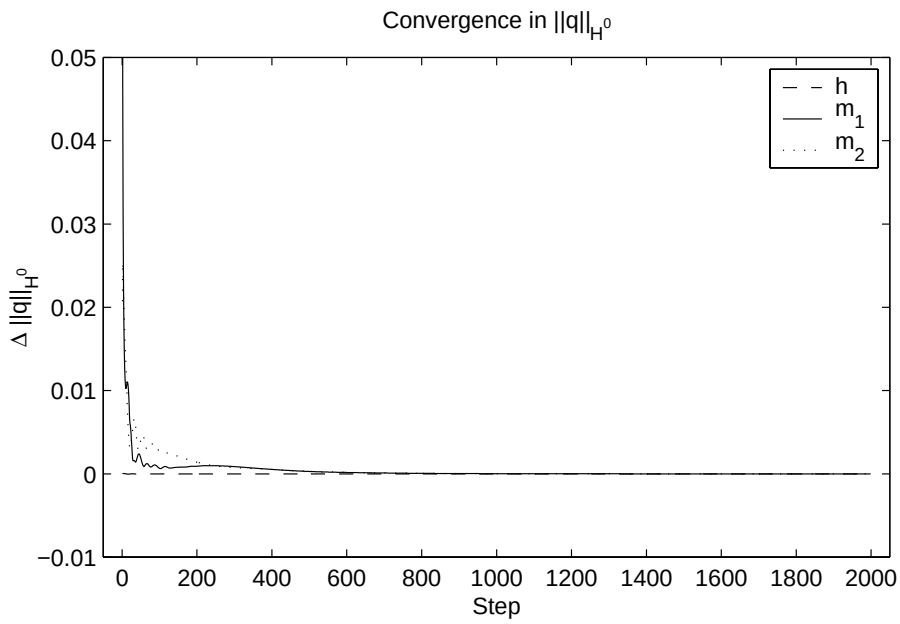

Figure 5.19: River Harbor : Initial Convergence in $||q||_{H^0}$

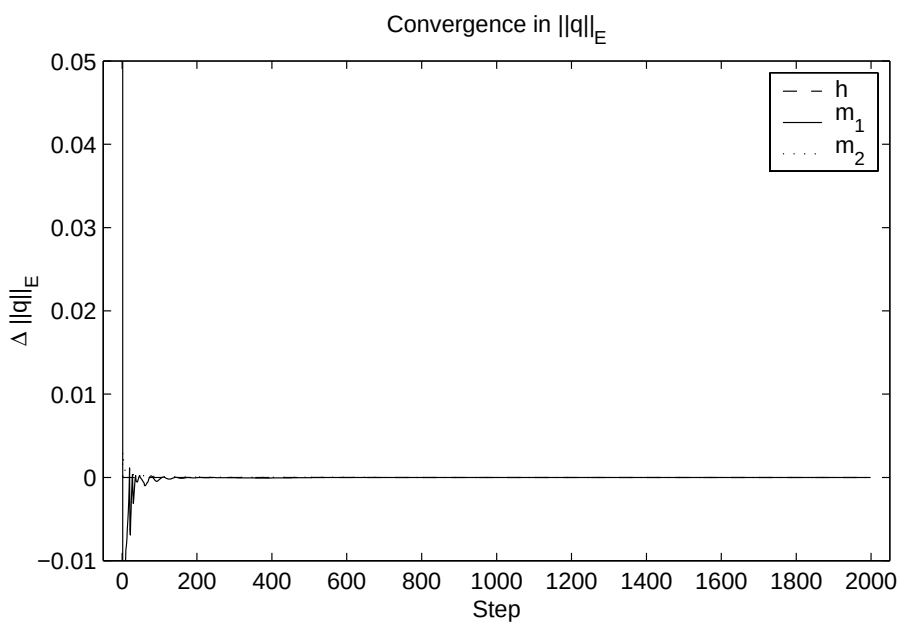

Figure 5.20: River Harbor : Initial Convergence in $||q||_E$

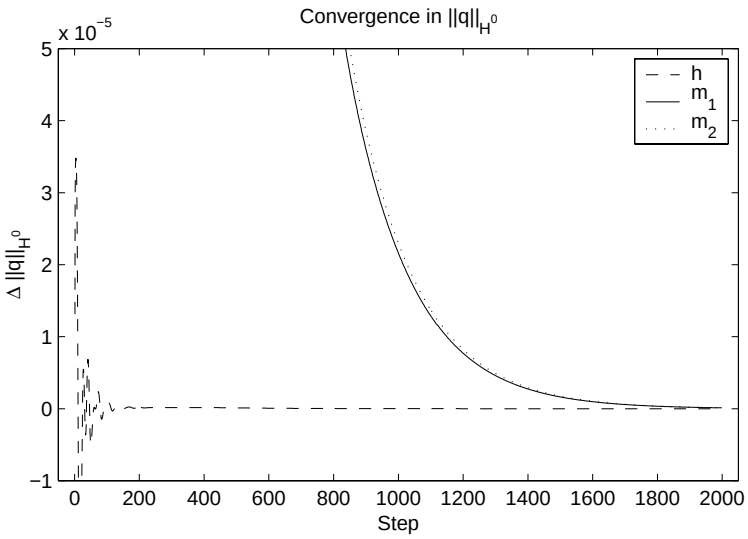

Figure 5.21: River Harbor : Final Convergence in $||q||_{H^0}$

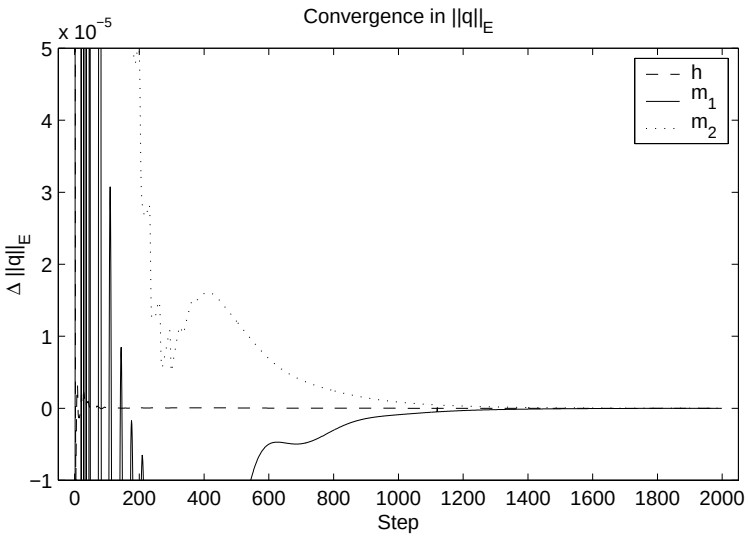

Figure 5.22: River Harbor : Final Convergence in $||q||_E$

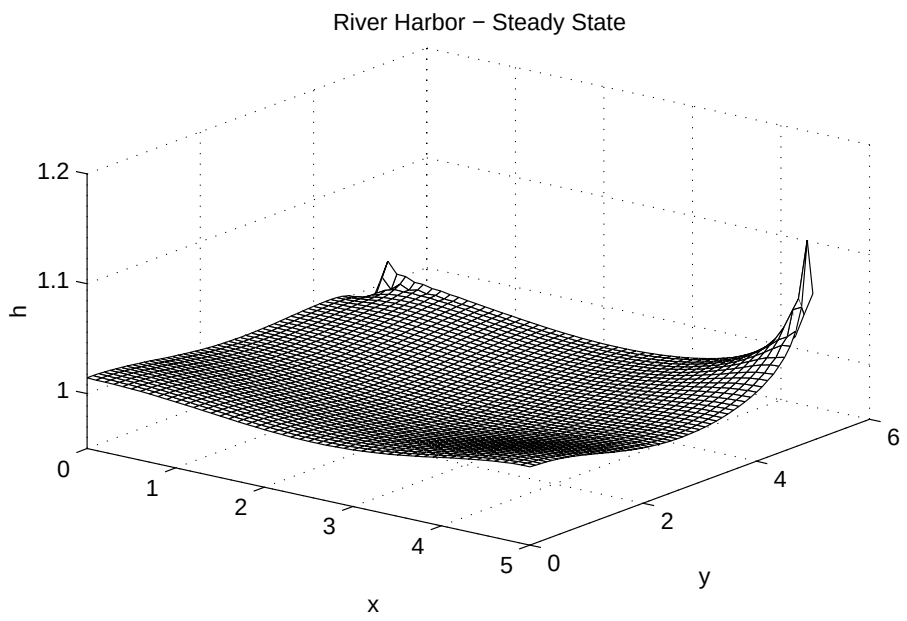

Figure 5.23: River Harbor : Carpet Plot of h

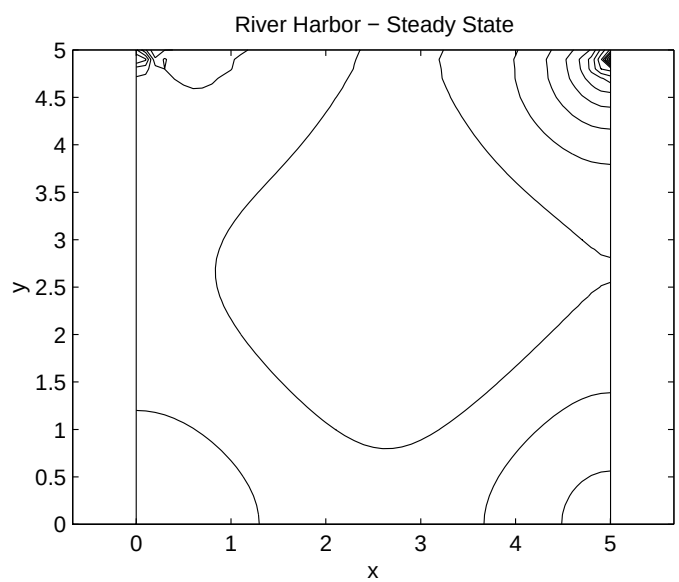

Figure 5.24: River Harbor : Contour Plot of h

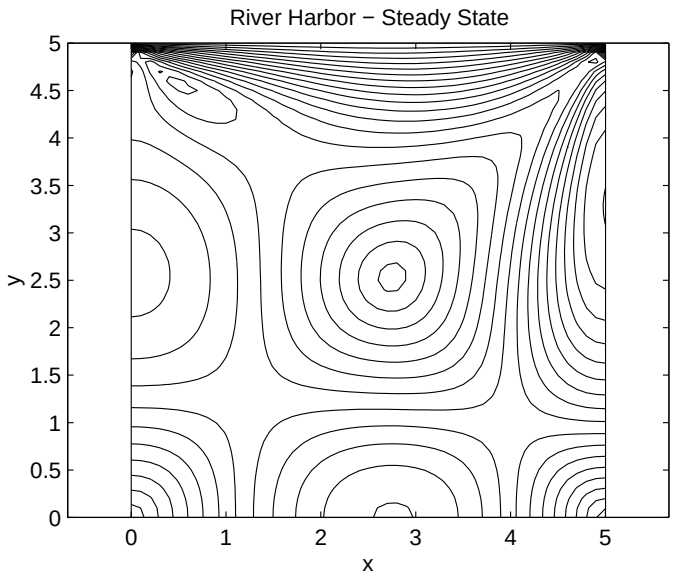

Figure 5.25: River Harbor : Contour Plot of m

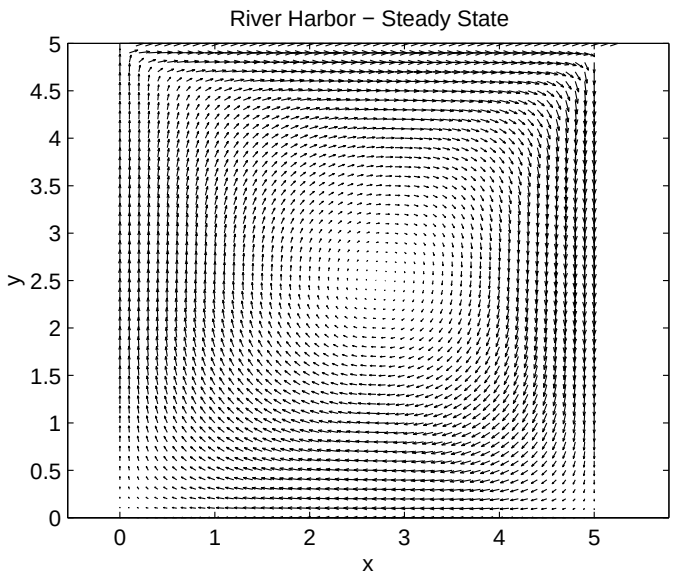

Figure 5.26: River Harbor : Quiver Plot of $m_{1,2}$

5.3.4 Discussion

As with the circular dam break, a seemingly simple problem is unexpectedly difficult. The singularities in the boundary conditions at the four corners induce spikes in the h solution at the river interface while completely stagnating the low in the lower corners. Some minor dispersion was evident in the h distribution at the upper right corner; non-uniform grid refinement would readily eliminate this issue. This new problem is a substantially challenging benchmark for the open-channel equations.

Chapter 6

Conclusions and Recommendations

This research has successfully applied the characteristics-biased flux jacobian decomposition [37]-[38] to the open channel conservation law system. A minimally dissipative algorithm has been achieved which, from a theoretical perspective, is highly accurate as the magnitude of the dissipation mechanism is proportional to the characteristic speeds of the solution of the hyperbolic conservation law system. Moreover, the dissipative mechanism is non-linearly controlled by local solution gradient, thereby effecting dissipation on in regions of steep solution and solution slope gradient. Finally, the construction of the dissipative mechanism is, by design, in complete harmony with the assessed flow field properties of mono-axial and bi-modal solution propagation for all directions and all Froude numbers.

In one dimension, this theoretical umbrella is found to encompass both the flux difference and flux vector splitting algorithms while reflecting significant physical content. As mulit-dimensional applications of flux splitting algorithms is heuristic and debatable, no conclusion can be drawn other than the characteristic-bias form suffers no ambiguity upon extension to higher dimensionality.

Computational experiments in one dimension indicate an algorithm which is accurate and stable.

No overshoot was evident in the dam break model while only moderate undershoot was witnessed. Solution error convergence under grid refinement, measured in the H^0 norm was exactly quadratic and thus indicative of a second order accurate dissipative method. Error convergence measured in the energy norm, however reflected a higher order accurate method that ranged between nearly second and fourth order accurate. Clearly the careful implementation of the characteristics, and hence underlying problem physics, yields a more accurate algorithm.

The two dimensional theoretical development introduced the new dependency lines for the open channel equation system, lines along which the momentum equations become linearly dependent for critical flow. The celerity and convection analyses also introduced linear dependency issues, all of which were rectified through the truly multidimensional character of the characteristics-bias flux jacobian decomposition. Analyzing the characteristics of the inviscid open channel equations via polar plots revealed new insight into propagation modes an the recognition of mono-axial and bi-modal fields. The conjugate lines and associated streamline and crossflow wedge regions, new to this problem class, were carefully exploited to yield a dissipative operator which is physically consistent with the original problem statement. Additionally, the upstream parameters insure smooth transitions in the composite jacobian approximation in accordance to physical requirements.

Two-dimensional computational experiments and benchmarks revealed an algorithm that performs as well if not better than available in the current literature. The partial dam break results were accurate and monotone while the fine grid solutions presented flow features as yet unreported. A critical assessment of the circular dam break on a cartesian grid unearthed a surprisingly challenging initial condition and the conclusion that the grid is inadequate to support a solution which is both monotone and true to the initial condition. The reported results are the most accurate to date and give pause to several published solutions. The harbor problem, analagous to the driven cavity, has introduced a new validation model to the open channel community for algorithm testing.

Finally, all results reported mathematically viable results in the form of solution extremums and norms as an additional measure of comparison to hopefully replace the "eyeball" norm employed in the current literature.

Heed that the base level of dissipation, $\psi = 0.25$, was not varied for any test, neither were the spline forms of the imposed upstream eigenvalues and associated parameters. As a results, the algorithm solved four challenging problems without the need for "turning knobs," a considerable downfall of many dissipative algorithms.

This research has opened the door for additional research in the application of this theory to the open channel equations. Suggestions for further research include

- A verification of the assumption that the state variable derivatives with respect to η_1 remain bounded for $Fr = \infty$, hence solidifying the linear dependence issue recognized for the convection limit of the open channel equations.

- An investigation of the variable used to gauge solution continuity. Unreported experimentation indicates that, based on the domain and initial condition, some variables yield better solutions than others. With the goal of removing knobs from the algorithm, a general-purpose variable needs to be identified and implemented.

- The manner in which element average values are calculated warrants further investigation. Unreported experimentation indicates that, for example, calculating the element average Froude number as the element average $|u|$ divided by the element averaged $\sqrt{gh}$ introduces noticably more dissipation than element averaging the nodal values of Fr. As such, algorithms can be stabilized (or overly diffused) by the manner in which data is averaged.

- The implementation of the grouped variable formulation should be assessed for accuracy, particularly in the momentum equations. More accurate results may be achieved by interpolating

the convection term u (for one dimension) and $u_{1,2}$ for two dimensions via hypermatrix construction. Moreover, this interpolation would admit additional terms into the energy norm calculation.

- The inviscid form of the open channel equations is an appropriate starting point for application of this theory. Additional utility would be gained through the addition of source terms in the form of bed slopes and friction factors, admitting additional benchmarks and the opportunity for validations with experimental data.

BIBLIOGRAPHY

Bibliography

1. Henderson, F.M. *Open Channel Flow*, The Macmillan Company, New York, 1966.

2. Miller, W.A. *Numerical Solution of the Equations for Unsteady Open-Channel Flow*, Georgia Institute of Technology, 1971.

3. Gladwell, I. and Wait, R. *A Survey of Numerical Methods for Partial Differential Equations*, Clarendon Press, Oxford, 1979

4. Lapidus, L. *Numerical Solution of Partial Differential Equations in Science and Engineering*, Wiley, New York, 1982.

5. Botha, J.F. *Fundamental Concepts in the Numerical Solution of Differential Equations*, John Wiley & Sons, New York, 1983.

6. Hirsch, C.H. *Numerical Computation of Internal and External Flows. Vol.2 Computational Methods of Inviscid and Viscous Flows*, Wiley, Chichester, 1990.

7. Coirer W., and van Leer, B., *Numerical Flux Formulas for the Euler and Navier-Stokes Equations: II. Progress in Flux Vector Splitting*, AIAA-91-1566, 1991.

8. Roe, P.L., *Approximate Riemann Solvers, Parameter Vectors, and Difference Schemes*, Journal of Computational Physics 43, 357-372, 1981.

9. Hughes, T.J.R., *Recent Progess in the Development and Understanding of SUPG Methods with Special Reference to the Compressible Euler and Navier-Stokes Equations*, International Journal for Numerical Methods in Fluids 7, 11, 1987.

10. Hicks, F.E. and Steffler, P.M., *Characteristic Dissipative Galerkin Scheme for Open-Channel Flow*, Journal of Hydraulics Engineering 118, 337-352, 1992.

11. Baker, A.J. and Kim, J.W., *A Taylor Weak Statement Algorithm for Hyperbolic Conservation Laws*, International Journal for Numerical Methods in Fluids 7, 489-520, 1987.

12. Hines, A.M. *A CFD Laboratory Expert System for Free Surface Hydromechanic Flow Analysis*, PhD Dissertation, University of Tennessee, Knoxville, 1988.

13. Brufau, P. and Garcia-Navarro P., *Two-Dimensional Dam Break Flow Simulation*, International Journal for Numerical Methods in Fluids 33, 35-58, 2000.

14. Baker, A.J. *Finite Element Computational Fluid Mechanics*, Taylor & Francis, 1983.

15. Bautista, E., Clemmens, A.J. and Strelkoff, T., *Comparison of Numerical Procedures for Gate Stroking*, Journal of Irrigation and Drainage Engineering 123, 129-136, 1997.

16. Yulistiyanto, B., and Zech, Y. *Free-Surface Flow Around Cylinder: Shallow-Water Modeling with Diffusion-Dispersion*, Journal of Hydraulic Engineering 124, 419-429, 1998.

17. Wang, J.S., Ni, H.G., and He, Y.S., *Finite Difference TVD Scheme for Computation of Dam-Break Problems*, Journal of Hydraulic Engineering 126, 153-262, 2000.

18. Molls, T., and Zhao, G., *Depth-Averaged Simulation of Supercritical Flow in Channel with Wavey Sidewall*, Journal of Hydraulic Engineering 126, 437-445, 2000.

19. Parrish, J.B., and Khalsa, R.D., *Calibration of Open Channel Flow Computer Simulations*, Conference Proceedings; Managing Water: Copaing with Scarcity and Abundance, 338-342, 1997.

20. Altai, W., Zhang, J., and Chu, V.H., *Shallow Turbulent Flow Simulation Using Two Length-Scale Model*, Journal of Engineering Mechanics 125, 780-788, 1999.

21. Lyn, D.A., Chiu, K., and Blatchley, E.R. *Numerical Modeling of a Flow and Disinfection in UV Disinfection Channels*, Journal of Environmental Engineering 125, 17-26, 1999.

22. Sofialidis, D. and Prinos, P., *Numerical Study of Momentum Exchange in Compound Open Channel Flow*, Journal of Hydraulic Engineering 125, 152-165, 1999.

23. Mihlbachler, T., Water Resource Engineer, Ogden International, Personal Communication.

24. Katopodes, N.D., *A Dissipative Galerkin Scheme for Open Channel Flow*, Journal of Hydraulic Engineering 110, 450-466, 1984.

25. King, I.P., *Finite Elements Models for Unsteady Flow Routing Through Irregular Channels*, Finite Elements in Water Resources, 4.165-4.181, Pentch Press, London, 1976.

26. Cooley, R.L., and Moin, S.A., *Finite Element Solution of Saint-Venant Equations*, Journal of the Hydraulics Division 102, 759-775, 1976.

27. Keuning, D.H., *Application of Finite Element Method to Open Channel Flow*, Journal of the Hydraulics Division 102, 459-468, 1976.

28. Meissner, U., *An Explicit-Implicit Water-Level Model for tidal Computations of Rivers*, Computer Methods in Applied Mechanics and Engineering 13, 221-232, 1978.

29. Katopodes, N.D., and Strelkoff, T., *Two-dimensional Shallow Wave-Water Models*, Journal of the Engineering Mechanics Division 105, 317-334, 1979.

30. Katopodes, N.D., *Finite Element Model for Open-Channel Flow Near Critical Conditions*, Finite Elements in Water Resources III, 5.37-5.46, University of Mississippi Press, 1980.

31. Gray, W.G., *Do Finite Element Models Simulate Surface Flow?*, Finite Elements in Water Resources III, 1.122-1.136, University of Mississippi Press, 1980.

32. Katopodes, N.D., *Finite Element Computation of Inertia-Dominated Free-Surface Flow*, Finite Element Flow Analysis, 479-486, North Holland Publishing Co., 1982.

33. Cappelaere, B. *Accurate Diffusive Wave Routing*, Journal of Hydraulic Engineering 123, 174-181, 1997.

34. Iannelli, G.S. *A Globally Well-Posed Accurate and Efficient Finite Element CFD Algorithm for Compressible Aerodynamics*, PhD Dissertation, University of Tennessee, Knoxville, 1992.

35. Iannelli, G.S., and Baker, A.J., *An Intrinsically N-Dimensional Generalized Flux Vector Splitting Implicit Finite Element Euler Algorithm*, AIAA 91-1566, 1991.

36. Iannelli, G.S., *A CFD Euler Solver from a Physical Acoustics-Convection Flux Divergence Decomposition*, US Army Technical Report, ARO DAAH04-96-1-0095, 1997

37. Iannelli, J. *A CFD Euler Solver from a Physical Acoustics-Convection Flux Jacobian Decomposition*, International Journal for Numerical Methods in Fluids 31, 821-860, 1999.

38. Iannelli, J. *Physical Multidimensional Upwinding from an Acoustics-Convection Euler Jacobian Decomposition*, International Journal for Numerical Methods in Fluids, submitted 2000.

39. Baker, A.J., and Pepper, *D.W. Finite Elements 123*, McGraw-Hill, 1991.

40. Fletcher, C.A.J. *Computational Galerkin Methods*, Springer-Verlag, New York, 1984.

41. Oden, J.T. and Reddy, J.N. *Introduction to the Mathematicl Theory of Finite Elements*, Wiley, New Yori, 1976.

42. Delis, A.I., and Skeels, *C.P. TVD Schemes for Open Channel Flow*, International Journal for Numerical Methods in Fluids 26, 791-809, 1998.

43. Iannelli, J. *Personal Communication*, University of Tennessee, Knoxville, July 03, 2000.

44. Levy, D.W., Powell, K.G., and van Leer, B. *Use of a Rotated Riemann Solver for the Two-Dimensional Euler Equations*, Journal of Computational Physics 106, 201-214, 1993.

45. Davis, S.F, *A Rotationally-Biased Upwind Difference Scheme for the Euler Equations*, Journal of Computational Physics 56, 65-92, 1984.

46. Zucrow, M.J. and Hoffman, J.D. *Gas Dynamics*, John Wiley & Sons, Inc., New York, 1976.

47. Fennema, R.J., and Chaudhry, M.H. *Explicit Methods for 2-D Transient Free-Surface Flows*, Journal of Hydraulic Engineering 116, 1013-1034, 1990.

48. Fennema, R.J., and Chaudhry, M.H. *Second-Order Numerical Schemes for Unsteady Free-Surface Flows with Shocks*, Water Resources 22, 1923-1930, 1986.

49. Fennema, R.J., and Chaudhry, M.H. *Simulation of One-Dimensional Dam-Break Flows*, Journal of Hydraulic Resources 24, 41-51, 1987.

50. Gabutti, B. *On Two Upwind Finite-Difference Schemes for Hyperbolic Equations in Non-Conservative Form*, Computational Fluids 11, 207-230, 1983.

51. Jameson, A., Schmidt, and Turkel, E. *Numerical Solutions of the Euler Equations by the Finite Volume Methods Using Runge-Kutta Time-Stepping Schemes*, Proceedings of the AIAA 14th Fluid and Plasma Dynamics Conference, American Institute of Aeronautics and Astronautics, 1181-1259, 1981

52. Alcrudo, F., and Garcia-Navarro P. *A High-Resolution Godunov-Type Scheme in Finite Volumes for the 2D Shallow-Water Equations*, International Journal for Numerical Methods in Fluids 16, 489-505, 1993.

53. Glaister, P. *Flux Difference Splitting for Open Channel Flows*, International Journal for Numerical Methods in Fluids 16, 629-654, 1993.

54. Ambrosi, D. *Approximation of Shallow Water Equations by Roe's Riemann Solver*, International Journal for Numerical Methods in Fluids 20, 157-168, 1995.

55. Anasatasiou, K., and Chan, *C.T. Solution of the 2D Shallow Water Equations Using the Finite Volume Method on Unstructured Triangular Meshes*, International Journal for Numerical Methods in Fluids 24, 1225-1245, 1997

56. Paillere, D., Degrez, G., and Deconinck, H. *Multidimensional Upwind Schemes for the Shallow Water Equation*, International Journal for Numerical Methods in Fluids 26, 987-1000, 1998.

57. Tseng, M. *Explicit Finite Volume Non-Oscillatory Schemes for 2D Transient Free-Surface Flows*, International Journal for Numerical Methods in Fluids 30, 831-843, 1999.

58. Liska, R., and Wendroff, B., *Two-Dimensional Shallow Water Equations by Composite Schemes*, International Journal for Numerical Methods in Fluids 30, 461-479, 1999.

59. Kolesnikov, A. *Efficient Implementation of High Order Methods in Computational Fluid Dynamics*, PhD Dissertation, University of Tennessee, Knoxville, 2000.

APPENDICES

Appendix A

Grid Refinement Data, 1D Dam Break

Table A.1: 1D Grid Refinement Verification : Solution Energy Norm (25 Elements)

	h results		**m results**	
0.1	$\|h\|_E$	$\Delta\|h\|_E$	$\|m\|_E$	$\Delta\|m\|_E$
1	9.669062354965844e-03		2.641081216784008e-03	
2	9.534533826979007e-03	-1.345285279868366e-04	2.634192486394505e-03	-6.888730389502818e-06
3	9.485713463637552e-03	-4.882036334145565e-05	2.631632465684306e-03	-2.560020710199156e-06
4	9.478982968064277e-03	-6.730495573275055e-06	2.631255165669056e-03	-3.773000152498124e-07
5	9.478610593663474e-03	-3.723744008022473e-07	2.631235649855006e-03	-1.951581404986691e-08
6	9.478555294649853e-03	-5.529901362169576e-08	2.631233271480835e-03	-2.378374171219111e-09
0.2	$\|h\|_E$	$\Delta\|h\|_E$	$\|m\|_E$	$\Delta\|m\|_E$
1	4.005409472941128e-03		1.918328814920807e-03	
2	3.990752876742462e-03	-1.465659619866600e-05	1.922890544392257e-03	4.561729471449973e-06
3	3.984665746974508e-03	-6.087129767953434e-06	1.924397138017260e-03	1.506593625002963e-06
4	3.984045829025902e-03	-6.199179486063300e-07	1.924799786397720e-03	4.026483804600405e-07
5	3.984125821449901e-03	7.999242399893414e-08	1.924909347614150e-03	1.095612164299722e-07
6	3.984153618987767e-03	2.779753786614353e-08	1.924938091807316e-03	2.874419316608277e-08
0.5	$\|h\|_E$	$\Delta\|h\|_E$	$\|m\|_E$	$\Delta\|m\|_E$
1	1.949465062903835e-03		1.048840702312543e-03	
2	1.945779672787171e-03	-3.685390116664033e-06	1.045945788507972e-03	-2.894913804571105e-06
3	1.944104869288382e-03	-1.674803498788891e-06	1.044882630517091e-03	-1.063157990880944e-06
4	1.943975772584784e-03	-1.290967035980084e-07	1.044748199324135e-03	-1.344311929560651e-07
5	1.944016242076291e-03	4.046949150706552e-08	1.044747853499355e-03	-3.458247800538355e-10
6	1.944028548195147e-03	1.230611885593043e-08	1.044748793836181e-03	9.403368259833927e-10
0.8	$\|h\|_E$	$\Delta\|h\|_E$	$\|m\|_E$	$\Delta\|m\|_E$
1	1.454403886410061e-03		8.070415676773926e-04	
2	1.453961819370145e-03	-4.420670399159568e-07	8.090898867654278e-04	2.048319088035228e-06
3	1.453540736305724e-03	-4.210830644210250e-07	8.096384561773006e-04	5.485694118727508e-07
4	1.453568153856994e-03	2.741755126991867e-08	8.097445576608208e-04	1.061014835201978e-07
5	1.453609006195167e-03	4.085233817311025e-08	8.097649155939595e-04	2.035793313873852e-08
6	1.453620124712176e-03	1.111851700898864e-08	8.097696971671614e-04	4.781573201837266e-09

Table A.2: 1D Grid Refinement Verification : Solution Energy Norm (50 Elements)

	h results		**m results**	
0.1	$\|h\|_E$	$\Delta\|h\|_E$	$\|m\|_E$	$\Delta\|m\|_E$
1	3.861823979624518e-03		1.851347288377591e-03	
2	3.867037769209649e-03	5.213789585130791e-06	1.871670955516509e-03	2.032366713891794e-05
3	3.868683235267329e-03	1.645466057680067e-06	1.880257199962555e-03	8.586244446045967e-06
4	3.868586521941262e-03	-9.671332606682806e-08	1.883139823392763e-03	2.882623430208123e-06
5	3.868694974386058e-03	1.084524447960040e-07	1.883672486023417e-03	5.326626306538258e-07
6	3.868764354944524e-03	6.938055846592711e-08	1.883759677891412e-03	8.719186799519343e-08
0.2	$\|h\|_E$	$\Delta\|h\|_E$	$\|m\|_E$	$\Delta\|m\|_E$
1	2.170347741499057e-03		1.095657708065799e-03	
2	2.159980690525843e-03	-1.036705097321421e-05	1.092061476856014e-03	-3.596231209785066e-06
3	2.154970808512452e-03	-5.009882013390973e-06	1.090452802052125e-03	-1.608674803888930e-06
4	2.152943717619991e-03	-2.027090892461024e-06	1.089820210195042e-03	-6.325918570830678e-07
5	2.152685607760762e-03	-2.581098592288611e-07	1.089732800070059e-03	-8.741012498298013e-08
6	2.152686752805153e-03	1.145044390901684e-09	1.089729905547961e-03	-2.894522097918531e-09
0.5	$\|h\|_E$	$\Delta\|h\|_E$	$\|m\|_E$	$\Delta\|m\|_E$
1	1.356752167130199e-03		7.669760196120192e-04	
2	1.356503434400119e-03	-2.487327300799546e-07	7.640733972668270e-04	-2.902622345192247e-06
3	1.355873647363439e-03	-6.297870366800060e-07	7.627845809545400e-04	-1.288816312286977e-06
4	1.355516076146690e-03	-3.575712167489063e-07	7.622712602727878e-04	-5.133206817521489e-07
5	1.355499811914047e-03	-1.626423264296240e-08	7.622090074484400e-04	-6.225282434782920e-08
6	1.355514462776497e-03	1.465086244987687e-08	7.622104121747306e-04	1.404726290583219e-09
0.8	$\|h\|_E$	$\Delta\|h\|_E$	$\|m\|_E$	$\Delta\|m\|_E$
1	1.154268111795001e-03		7.579496554698972e-04	
2	1.158408127572854e-03	4.140015777853116e-06	7.578446678858218e-04	-1.049875840754017e-07
3	1.159303940751705e-03	8.958131788509675e-07	7.573828173970745e-04	-4.618504887472395e-07
4	1.159489818103632e-03	1.858773519269885e-07	7.571212616987588e-04	-2.615556983156945e-07
5	1.159557787677644e-03	6.796957401186861e-08	7.571077090685848e-04	-1.355263017403189e-08
6	1.159579934302370e-03	2.214662472616209e-08	7.571175911429600e-04	9.882074375163266e-09

Table A.3: 1D Grid Refinement Verification : Solution Energy Norm (100 Elements)

	h results		**m results**	
0.1	$\|h\|_E$	$\Delta\|h\|_E$	$\|m\|_E$	$\Delta\|m\|_E$
1	2.120107792306588e-03		1.062793255728839e-03	
2	2.109964398599142e-03	-1.014339370744577e-05	1.059054259359359e-03	-3.738996369479853e-06
3	2.103779445397595e-03	-6.184953201546998e-06	1.057193971138143e-03	-1.860288221216004e-06
4	2.100944937228981e-03	-2.834508168614129e-06	1.056342207676250e-03	-8.517634618931610e-07
5	2.099813564564370e-03	-1.131372664611111e-06	1.056008599227115e-03	-3.336084491349731e-07
6	2.099664463818819e-03	-1.491007455508599e-07	1.055963439786348e-03	-4.515944076696234e-08
0.2	$\|h\|_E$	$\Delta\|h\|_E$	$\|m\|_E$	$\Delta\|m\|_E$
1	1.368026623455716e-03		7.534893944549408e-04	
2	1.366871205110155e-03	-1.155418345560964e-06	7.551892119693330e-04	1.699817514392199e-06
3	1.365398759723721e-03	-1.472445386433872e-06	7.555561591761780e-04	3.669472068449850e-07
4	1.364660957829634e-03	-7.378018940871599e-07	7.556677673157596e-04	1.116081395815659e-07
5	1.364358974513846e-03	-3.019833157880299e-07	7.557080434265776e-04	4.027611081799942e-08
6	1.364322388940655e-03	-3.658557319098123e-08	7.557146521928177e-04	6.608766240094772e-09
0.5	$\|h\|_E$	$\Delta\|h\|_E$	$\|m\|_E$	$\Delta\|m\|_E$
1	1.025242838617461e-03		6.087708841962188e-04	
2	1.026844644077013e-03	1.601805459551867e-06	6.064566996693447e-04	-2.314184526874038e-06
3	1.026709015477947e-03	-1.356285990658773e-07	6.050031665757259e-04	-1.453533093618837e-06
4	1.026486030563500e-03	-2.229849144471177e-07	6.043245388376878e-04	-6.786277380380328e-07
5	1.026363083546189e-03	-1.229470173108940e-07	6.040491381628042e-04	-2.754006748836727e-07
6	1.026355568770218e-03	-7.514775970983781e-09	6.040151074070661e-04	-3.403075573811878e-08
0.8	$\|h\|_E$	$\Delta\|h\|_E$	$\|m\|_E$	$\Delta\|m\|_E$
1	7.665950672123594e-04		4.751433493132909e-04	
2	7.691606137632164e-04	2.565546550857035e-06	4.790279500578087e-04	3.884600744517830e-06
3	7.696835339868030e-04	5.229202235865465e-07	4.802888433761122e-04	1.260893318303497e-06
4	7.697929388735582e-04	1.094048867551810e-07	4.807488560650082e-04	4.600126888959738e-07
5	7.698158542920833e-04	2.291541852518335e-08	4.809164866391689e-04	1.676305741607313e-07
6	7.698241664276181e-04	8.312135534776013e-09	4.809412219088852e-04	2.473526971625856e-08

Table A.4: 1D Grid Refinement Verification : Solution Energy Norm (200 Elements)

	h results		**m results**	
0.1	$\|h\|_E$	$\Delta\|h\|_E$	$\|m\|_E$	$\Delta\|m\|_E$
1	1.331977141820669e-03		7.376219740218146e-04	
2	1.330964724489040e-03	-1.012417331628995e-06	7.387702608081727e-04	1.148286786358086e-06
3	1.328958455317776e-03	-2.006269171263980e-06	7.384815793458610e-04	-2.886814623116914e-07
4	1.327713065491990e-03	-1.245389825785996e-06	7.383136260627855e-04	-1.679532830755519e-07
5	1.327150390041929e-03	-5.626754500610755e-07	7.382297355523925e-04	-8.389051039297060e-08
6	1.326927952605021e-03	-2.224374369079029e-07	7.381976336551430e-04	-3.210189724949745e-08
0.2	$\|h\|_E$	$\Delta\|h\|_E$	$\|m\|_E$	$\Delta\|m\|_E$
1	1.116605647829543e-03		7.017746882263794e-04	
2	1.120975864590784e-03	4.370216761240969e-06	7.004468308080698e-04	-1.327857418309607e-06
3	1.121186517895092e-03	2.106533043080578e-07	6.988019611977172e-04	-1.644869610352559e-06
4	1.121024973482842e-03	-1.615444122499143e-07	6.977886287896585e-04	-1.013332408058665e-06
5	1.120895658513463e-03	-1.293149693791084e-07	6.973184128210838e-04	-4.702159685747572e-07
6	1.120833227763520e-03	-6.243074994298492e-08	6.971292686973610e-04	-1.891441237227703e-07
0.5	$\|h\|_E$	$\Delta\|h\|_E$	$\|m\|_E$	$\Delta\|m\|_E$
1	8.599553207108537e-04		5.769305468148300e-04	
2	8.645894068466268e-04	4.634086135773098e-06	5.756023249309319e-04	-1.328221883898067e-06
3	8.650760917289820e-04	4.866848823552100e-07	5.740190415719413e-04	-1.583283358990665e-06
4	8.650920189439725e-04	1.592721499046185e-08	5.730832307967704e-04	-9.358107751708273e-07
5	8.650425049716707e-04	-4.951397230179740e-08	5.726462298684871e-04	-4.370009282833251e-07
6	8.650111340886161e-04	-3.137088305457409e-08	5.724701450097320e-04	-1.760848587550662e-07
0.8	$\|h\|_E$	$\Delta\|h\|_E$	$\|m\|_E$	$\Delta\|m\|_E$
1	7.916914495704038e-04		5.498371059320546e-04	
2	7.969750785668596e-04	5.283628996455856e-06	5.485925326863446e-04	-1.244573245710087e-06
3	7.977322242048830e-04	7.571456380233354e-07	5.471359954523215e-04	-1.456537234023050e-06
4	7.978478380282387e-04	1.156138233557183e-07	5.462037151590271e-04	-9.322802932943634e-07
5	7.978349946651056e-04	-1.284336313309934e-08	5.457698187462559e-04	-4.338964127712560e-07
6	7.978179685312885e-04	-1.702613381705798e-08	5.455949559392753e-04	-1.748628069806217e-07

Table A.5: 1D Grid Refinement Verification : Solution Energy Norm (400 Elements)

	h results		**m results**	
0.1	$\|h\|_E$	$\Delta\|h\|_E$	$\|m\|_E$	$\Delta\|m\|_E$
1	1.107172553227080e-03		6.854639750696289e-04	
2	1.110750994016972e-03	3.578440789891958e-06	6.853005209904045e-04	-1.634540792243809e-07
3	1.110806071027749e-03	5.507701077698580e-08	6.837660640782318e-04	-1.534456912172678e-06
4	1.110659037758658e-03	-1.470332690910788e-07	6.828673434821952e-04	-8.987205960365530e-07
5	1.110488848237242e-03	-1.701895214159966e-07	6.823393669211396e-04	-5.279765610556033e-07
6	1.110400727558006e-03	-8.812067923600307e-08	6.821004240404576e-04	-2.389428806820124e-07
0.2	$\|h\|_E$	$\Delta\|h\|_E$	$\|m\|_E$	$\Delta\|m\|_E$
1	7.068614565199564e-04		4.435857052159049e-04	
2	7.016537037664389e-04	-5.207752753517525e-06	4.418749360996289e-04	-1.710769116276020e-06
3	7.021512407012636e-04	4.975369348247461e-07	4.423449929237358e-04	4.700568241069168e-07
4	7.016596247066824e-04	-4.916159945812229e-07	4.422318507209485e-04	-1.131422027872962e-07
5	7.013075284986632e-04	-3.520962080192118e-07	4.421334399912947e-04	-9.841072965381800e-08
6	7.011489377878281e-04	-1.585907108350585e-07	4.420901453999815e-04	-4.329459131317565e-08
0.5	$\|h\|_E$	$\Delta\|h\|_E$	$\|m\|_E$	$\Delta\|m\|_E$
1	5.814770415788096e-04		3.808239634310004e-04	
2	5.768217655166406e-04	-4.655276062169003e-06	3.779176191229309e-04	-2.906344308069525e-06
3	5.740765981741228e-04	-2.745167342517734e-06	3.765153027948258e-04	-1.402316328105106e-06
4	5.735845396763502e-04	-4.920584977726470e-07	3.763562175873155e-04	-1.590852075102739e-07
5	5.732130785882153e-04	-3.714610881348909e-07	3.762421310476750e-04	-1.140865396405313e-07
6	5.730464608729526e-04	-1.666177152627414e-07	3.761935129911653e-04	-4.861805650966831e-08
0.8	$\|h\|_E$	$\Delta\|h\|_E$	$\|m\|_E$	$\Delta\|m\|_E$
1	5.549994233599805e-04		3.617817232085285e-04	
2	5.566685350481080e-04	1.669111688127538e-06	3.639790519777737e-04	2.197328769245233e-06
3	5.556066021218512e-04	-1.061932926256764e-06	3.629064287601053e-04	-1.072623217668409e-06
4	5.547520182768192e-04	-8.545838450320017e-07	3.626026732081683e-04	-3.037555519369876e-07
5	5.543448359649186e-04	-4.071823119006137e-07	3.624770325069107e-04	-1.256407012576355e-07
6	5.541604657498314e-04	-1.843702150871804e-07	3.624219398461277e-04	-5.509266078296228e-08

Table A.6: 1D Grid Refinement Verification : Solution H^0 Norm (25 Elements)

	h results		**m results**	
0.1	$\|h\|_{H^0}$	$\Delta\|h\|_{H^0}$	$\|m\|_{H^0}$	$\Delta\|m\|_{H^0}$
1	9.893262933240478e-01		9.182361133670272e-02	
2	9.892298200202173e-01	-9.647330383044661e-05	9.174591352656498e-02	-7.769781013773625e-05
3	9.891940448052939e-01	-3.577521492337254e-05	9.171363157904353e-02	-3.228194752145919e-05
4	9.891893067804347e-01	-4.738024859229917e-06	9.170966426888832e-02	-3.967310155200687e-06
5	9.891891085098622e-01	-1.982705725156464e-07	9.170971198054299e-02	4.771165466876948e-08
6	9.891890848868453e-01	-2.362301687597324e-08	9.170975127565671e-02	3.929511371847383e-08
0.2	$\|h\|_{H^0}$	$\Delta\|h\|_{H^0}$	$\|m\|_{H^0}$	$\Delta\|m\|_{H^0}$
1	9.735027238084365e-01		1.453330984176338e-01	
2	9.734247552308766e-01	-7.796857755992814e-05	1.451962550129267e-01	-1.368434047070988e-04
3	9.733958013740965e-01	-2.895385678003404e-05	1.451432480158669e-01	-5.300699705981793e-05
4	9.733919615007893e-01	-3.839873307209807e-06	1.451361650540683e-01	-7.082961798604570e-06
5	9.733918154801674e-01	-1.460206219272564e-07	1.451359744524469e-01	-1.906016214026085e-07
6	9.733918017209280e-01	-1.375923941449031e-08	1.451359740231038e-01	-4.293430888591132e-10
0.5	$\|h\|_{H^0}$	$\Delta\|h\|_{H^0}$	$\|m\|_{H^0}$	$\Delta\|m\|_{H^0}$
1	9.246816672586745e-01		2.466640112855948e-01	
2	9.246131334682538e-01	-6.853379042071062e-05	2.465972797912239e-01	-6.673149437089188e-05
3	9.245880771604434e-01	-2.505630781035606e-05	2.465725320611912e-01	-2.474773003269259e-05
4	9.245845909160511e-01	-3.486244392392202e-06	2.465688996272982e-01	-3.632433893008269e-06
5	9.245843944882864e-01	-1.964277646093748e-07	2.465686602239927e-01	-2.394033054853306e-07
6	9.245843637370432e-01	-3.075124321849643e-08	2.465686200867906e-01	-4.013720211748506e-08
0.8	$\|h\|_{H^0}$	$\Delta\|h\|_{H^0}$	$\|m\|_{H^0}$	$\Delta\|m\|_{H^0}$
1	8.734773341559646e-01		3.175030443187643e-01	
2	8.734057366990692e-01	-7.159745689544472e-05	3.174632842774241e-01	-3.976004134020883e-05
3	8.733805437453527e-01	-2.519295371650188e-05	3.174478563134046e-01	-1.542796401948765e-05
4	8.733767397702882e-01	-3.803975064498033e-06	3.174456129894287e-01	-2.243323975914535e-06
5	8.733763885519706e-01	-3.512183175402583e-07	3.174454895398048e-01	-1.234496239121974e-07
6	8.733763167126188e-01	-7.183935180066214e-08	3.174454716068721e-01	-1.793293269436447e-08

Table A.7: 1D Grid Refinement Verification : Solution H^0 Norm (50 Elements)

	h results		**m results**	
0.1	$\|h\|_{H^0}$	$\Delta\|h\|_{H^0}$	$\|m\|_{H^0}$	$\Delta\|m\|_{H^0}$
1	1.001601860983777e+00		1.031911063858952e-01	
2	1.001551267958094e+00	-5.059302568288793e-05	1.030433696137642e-01	-1.477367721309936e-04
3	1.001529685262235e+00	-2.158269585894601e-05	1.029771014919342e-01	-6.626812182999875e-05
4	1.001521433307799e+00	-8.251954435989362e-06	1.029513298029701e-01	-2.577168896410187e-05
5	1.001520329957666e+00	-1.103350133035974e-06	1.029478461460492e-01	-3.483656920905132e-06
6	1.001520298305905e+00	-3.165176098995914e-08	1.029477494333375e-01	-9.671271170019757e-08
0.2	$\|h\|_{H^0}$	$\Delta\|h\|_{H^0}$	$\|m\|_{H^0}$	$\Delta\|m\|_{H^0}$
1	9.860565666144501e-01		1.543698666608982e-01	
2	9.860105217249826e-01	-4.604488946746699e-05	1.542795805335259e-01	-9.028612737230213e-05
3	9.859916242748830e-01	-1.889745009964194e-05	1.542428944785793e-01	-3.668605494658306e-05
4	9.859845313124788e-01	-7.092962404198211e-06	1.542292271945560e-01	-1.366728402329986e-05
5	9.859835645025713e-01	-9.668099074655601e-07	1.542273508161965e-01	-1.876378359494391e-06
6	9.859835265126329e-01	-3.798993841730436e-08	1.542272749395911e-01	-7.587660541541474e-08
0.5	$\|h\|_{H^0}$	$\Delta\|h\|_{H^0}$	$\|m\|_{H^0}$	$\Delta\|m\|_{H^0}$
1	9.381282704036442e-01		2.526375871038967e-01	
2	9.380871847702921e-01	-4.108563335214477e-05	2.526008435892422e-01	-3.674351465454695e-05
3	9.380703887417207e-01	-1.679602857140861e-05	2.525857299678915e-01	-1.511362135064864e-05
4	9.380640841769883e-01	-6.304564732384499e-06	2.525800477497153e-01	-5.682218176206177e-06
5	9.380632118644159e-01	-8.723125723975045e-07	2.525792246789261e-01	-8.230707892464828e-07
6	9.380631729761506e-01	-3.888826527465028e-08	2.525791773457860e-01	-4.733314007410172e-08
0.8	$\|h\|_{H^0}$	$\Delta\|h\|_{H^0}$	$\|m\|_{H^0}$	$\Delta\|m\|_{H^0}$
1	8.876685420687759e-01		3.222980131758895e-01	
2	8.876260301885900e-01	-4.251188018589147e-05	3.222708681513329e-01	-2.714502455664070e-05
3	8.876086920475327e-01	-1.733814105731035e-05	3.222596986159897e-01	-1.116953534319176e-05
4	8.876021970950436e-01	-6.494952489055628e-06	3.222554991210415e-01	-4.199494948176064e-06
5	8.876012941156852e-01	-9.029793583970047e-07	3.222548868330049e-01	-6.122880366055128e-07
6	8.876012521592773e-01	-4.195640790349842e-08	3.222548506246715e-01	-3.620833338713325e-08

Table A.8: 1D Grid Refinement Verification : Solution H^0 Norm (100 Elements)

	h results		**m results**	
0.1	$\|h\|_{H^0}$	$\Delta\|h\|_{H^0}$	$\|m\|_{H^0}$	$\Delta\|m\|_{H^0}$
1	9.979095590897655e-01		1.094311770222628e-01	
2	9.978861542530184e-01	-2.340483674712068e-05	1.093613400440786e-01	-6.983697818419010e-05
3	9.978747161393411e-01	-1.143811367732006e-05	1.093303888656223e-01	-3.095117845630657e-05
4	9.978699373840901e-01	-4.778755250955946e-06	1.093179739531319e-01	-1.241491249039106e-05
5	9.978681137631035e-01	-1.823620986662888e-06	1.093133167079920e-01	-4.657245139899624e-06
6	9.978678647276652e-01	-2.490354382711502e-07	1.093126797904174e-01	-6.369175746118172e-07
0.2	$\|h\|_{H^0}$	$\Delta\|h\|_{H^0}$	$\|m\|_{H^0}$	$\Delta\|m\|_{H^0}$
1	9.823837028805158e-01		1.590572860181561e-01	
2	9.823631096192246e-01	-2.059326129122407e-05	1.590245850832270e-01	-3.270093492910298e-05
3	9.823530278429369e-01	-1.008177628769591e-05	1.590093468216862e-01	-1.523826154081753e-05
4	9.823487731866057e-01	-4.254656331137419e-06	1.590029741325943e-01	-6.372689091899142e-06
5	9.823471446528164e-01	-1.628533789377329e-06	1.590005475972781e-01	-2.426535316180090e-06
6	9.823469211887375e-01	-2.234640789078313e-07	1.590002101406701e-01	-3.374566080183161e-07
0.5	$\|h\|_{H^0}$	$\Delta\|h\|_{H^0}$	$\|m\|_{H^0}$	$\Delta\|m\|_{H^0}$
1	9.343450466775334e-01		2.556786125259790e-01	
2	9.343246503178544e-01	-2.039635967898690e-05	2.556608029205711e-01	-1.780960540792575e-05
3	9.343144747788111e-01	-1.017553904325563e-05	2.556519611571595e-01	-8.841763411593373e-06
4	9.343101585243792e-01	-4.316254431979694e-06	2.556481855850985e-01	-3.775572060993326e-06
5	9.343085017123532e-01	-1.656812025907506e-06	2.556467332067321e-01	-1.452378366406659e-06
6	9.343082734317877e-01	-2.282805655617892e-07	2.556465281545025e-01	-2.050522295848900e-07
0.8	$\|h\|_{H^0}$	$\Delta\|h\|_{H^0}$	$\|m\|_{H^0}$	$\Delta\|m\|_{H^0}$
1	8.837219014655781e-01		3.247817472325381e-01	
2	8.837011998168721e-01	-2.070164870593416e-05	3.247687908063267e-01	-1.295642621140791e-05
3	8.836905147423971e-01	-1.068507447499201e-05	3.247619209170874e-01	-6.869889239313753e-06
4	8.836859467643176e-01	-4.567978079572654e-06	3.247589556838284e-01	-2.965233258989119e-06
5	8.836841904340965e-01	-1.756330221036606e-06	3.247578094332297e-01	-1.146250598715870e-06
6	8.836839487852640e-01	-2.416488324996635e-07	3.247576485685640e-01	-1.608646656992008e-07

Table A.9: 1D Grid Refinement Verification : Solution H^0 Norm (200 Elements)

	h results		**m results**	
0.1	$\|h\|_{H^0}$	$\Delta\|h\|_{H^0}$	$\|m\|_{H^0}$	$\Delta\|m\|_{H^0}$
1	9.960654830260441e-01		1.126115564909221e-01	
2	9.960565352289700e-01	-8.947797074165820e-06	1.125894286528869e-01	-2.212783803519358e-05
3	9.960517902849354e-01	-4.744944034573706e-06	1.125790138867672e-01	-1.041476611969572e-05
4	9.960493006623308e-01	-2.489622604628927e-06	1.125736585460766e-01	-5.355340690613164e-06
5	9.960482233991292e-01	-1.077263201532119e-06	1.125713445199751e-01	-2.314026101499222e-06
6	9.960478049759105e-01	-4.184232187398607e-07	1.125704468723904e-01	-8.976475846939058e-07
0.2	$\|h\|_{H^0}$	$\Delta\|h\|_{H^0}$	$\|m\|_{H^0}$	$\Delta\|m\|_{H^0}$
1	9.805363959160109e-01		1.613532726171978e-01	
2	9.805277673357922e-01	-8.628580218772441e-06	1.613402730727140e-01	-1.299954448380491e-05
3	9.805230912490621e-01	-4.676086730048823e-06	1.613334189372648e-01	-6.854135449207988e-06
4	9.805206589628567e-01	-2.432286205444889e-06	1.613298729480562e-01	-3.545989208597611e-06
5	9.805196060551258e-01	-1.052907730891839e-06	1.613283386105981e-01	-1.534337458114488e-06
6	9.805191964179595e-01	-4.096371662987153e-07	1.613277410637967e-01	-5.975468014007834e-07
0.5	$\|h\|_{H^0}$	$\Delta\|h\|_{H^0}$	$\|m\|_{H^0}$	$\Delta\|m\|_{H^0}$
1	9.324352034697380e-01		2.572093286833746e-01	
2	9.324262347598453e-01	-8.968709892642757e-06	2.572011535000395e-01	-8.175183335068503e-06
3	9.324213330423414e-01	-4.901717503891234e-06	2.571968536786583e-01	-4.299821381226199e-06
4	9.324187906590888e-01	-2.542383252590596e-06	2.571946080519376e-01	-2.245626720687177e-06
5	9.324176852465395e-01	-1.105412549384788e-06	2.571936305469599e-01	-9.775049777394074e-07
6	9.324172556832572e-01	-4.295632822781670e-07	2.571932505266539e-01	-3.800203059456386e-07
0.8	$\|h\|_{H^0}$	$\Delta\|h\|_{H^0}$	$\|m\|_{H^0}$	$\Delta\|m\|_{H^0}$
1	8.817414326901425e-01		3.260619937472315e-01	
2	8.817319030282812e-01	-9.529661861296113e-06	3.260556817556236e-01	-6.311991607887979e-06
3	8.817267351908581e-01	-5.167837423103450e-06	3.260521697717537e-01	-3.511983869886048e-06
4	8.817240342187335e-01	-2.700972124625167e-06	3.260503727060216e-01	-1.797065732112024e-06
5	8.817228659038850e-01	-1.168314848420948e-06	3.260495955213386e-01	-7.771846829984774e-07
6	8.817224116781176e-01	-4.542257674433614e-07	3.260492932636501e-01	-3.022576884892381e-07

Table A.10: 1D Grid Refinement Verification : Solution H^0 Norm (400 Elements)

	h results		**m results**	
0.1	$\|h\|_{H^0}$	$\Delta\|h\|_{H^0}$	$\|m\|_{H^0}$	$\Delta\|m\|_{H^0}$
1	9.951376975260517e-01		1.141386220685416e-01	
2	9.951341724043381e-01	-3.525121713643387e-06	1.141316307745259e-01	-6.991294015698535e-06
3	9.951323262249293e-01	-1.846179408793169e-06	1.141279217883488e-01	-3.708986177103357e-06
4	9.951311835919359e-01	-1.142632993444970e-06	1.141254694976502e-01	-2.452290698590209e-06
5	9.951305862040752e-01	-5.973878606235772e-07	1.141242187244211e-01	-1.250773229100055e-06
6	9.951303230968646e-01	-2.631072106851207e-07	1.141236674376123e-01	-5.512868088003442e-07
0.2	$\|h\|_{H^1}$	$\Delta\|h\|_{H^1}$	$\|m\|_{H^1}$	$\Delta\|m\|_{H^1}$
1	9.796025684982461e-01		1.624738071307197e-01	
2	9.795994846630339e-01	-3.083835212192021e-06	1.624713759986872e-01	-2.431132032520988e-06
3	9.795975425226915e-01	-1.942140342436893e-06	1.624684578200615e-01	-2.918178625688217e-06
4	9.795963898616541e-01	-1.152661037395752e-06	1.624667278429136e-01	-1.729977147896244e-06
5	9.795957699507402e-01	-6.199109139348735e-07	1.624658090862713e-01	-9.187566422930171e-07
6	9.795954983004341e-01	-2.716503060273823e-07	1.624654091293210e-01	-3.999569503088107e-07
0.5	$\|h\|_{H^1}$	$\Delta\|h\|_{H^1}$	$\|m\|_{H^1}$	$\Delta\|m\|_{H^1}$
1	9.314806954329599e-01		2.579915358224739e-01	
2	9.314773203748312e-01	-3.375058128640696e-06	2.579889488467747e-01	-2.586975699214733e-06
3	9.314751999066462e-01	-2.120468185040636e-06	2.579869272215454e-01	-2.021625229275958e-06
4	9.314740055785464e-01	-1.194328099751729e-06	2.579858253721647e-01	-1.101849380735764e-06
5	9.314733552761246e-01	-6.503024218007525e-07	2.579852404505220e-01	-5.849216426767612e-07
6	9.314730693356931e-01	-2.859404315547209e-07	2.579849841929334e-01	-2.562575885933782e-07
0.8	$\|h\|_{H^1}$	$\Delta\|h\|_{H^1}$	$\|m\|_{H^1}$	$\Delta\|m\|_{H^1}$
1	8.807495413693204e-01		3.267157905676762e-01	
2	8.807453218892007e-01	-4.219480119638241e-06	3.267130415563760e-01	-2.749011300207105e-06
3	8.807431470740795e-01	-2.174815121214202e-06	3.267114546073884e-01	-1.586948987608583e-06
4	8.807418161295083e-01	-1.330944571220627e-06	3.267105435862087e-01	-9.110211796614642e-07
5	8.807411287093082e-01	-6.874202000961560e-07	3.267100803750841e-01	-4.632111246238857e-07
6	8.807408264805577e-01	-3.022287504705901e-07	3.267098777142660e-01	-2.026608180716316e-07

Table A.11: 1D Grid Refinement Verification : Solution H^1 Norm (25 Elements)

	h results		**m results**	
0.1	$\|h\|_{H^1}$	$\Delta\|h\|_{H^1}$	$\|m\|_{H^1}$	$\Delta\|m\|_{H^1}$
1	1.830376302551840e+00		8.222346365689027e-01	
2	1.820096069704834e+00	-1.028023284700597e-02	8.194665170290322e-01	-2.768119539870550e-03
3	1.816331655924051e+00	-3.764413780783071e-03	8.184118378979330e-01	-1.054679131099134e-03
4	1.815814977552386e+00	-5.166783716650247e-04	8.182611653249487e-01	-1.506725729842895e-04
5	1.815788625797489e+00	-2.635175489706931e-05	8.182516774852483e-01	-9.487839700450529e-06
6	1.815784988089996e+00	-3.637707492787357e-06	8.182500274787153e-01	-1.650006532960546e-06
0.2	$\|h\|_{H^1}$	$\Delta\|h\|_{H^1}$	$\|m\|_{H^1}$	$\Delta\|m\|_{H^1}$
1	1.518821951206387e+00		8.218766989339278e-01	
2	1.514360881027330e+00	-4.461070179057058e-03	8.187072043824783e-01	-3.169494551449437e-03
3	1.512746186988900e+00	-1.614694038429842e-03	8.175467829498601e-01	-1.160421432618297e-03
4	1.512532500847474e+00	-2.136861414261393e-04	8.173864002938313e-01	-1.603826560288013e-04
5	1.512525297243222e+00	-7.203604251992957e-06	8.173785975283976e-01	-7.802765433662096e-06
6	1.512524867440097e+00	-4.298031248683998e-07	8.173776254784024e-01	-9.720499951626493e-07
0.5	$\|h\|_{H^1}$	$\Delta\|h\|_{H^1}$	$\|m\|_{H^1}$	$\Delta\|m\|_{H^1}$
1	1.296018412910507e+00		7.674227136024216e-01	
2	1.294532141073849e+00	-1.486271836657949e-03	7.661223094982912e-01	-1.300404104130459e-03
3	1.293995920203130e+00	-5.362208707191396e-04	7.657136193402458e-01	-4.086901580453439e-04
4	1.293921600519805e+00	-7.431968332483052e-05	7.656400380487878e-01	-7.358129145806913e-05
5	1.293917500795676e+00	-4.099724129069671e-06	7.656286395635717e-01	-1.139848521602982e-05
6	1.293916857547365e+00	-6.432483110607734e-07	7.656259863038575e-01	-2.653259714269218e-06
0.8	$\|h\|_{H^1}$	$\Delta\|h\|_{H^1}$	$\|m\|_{H^1}$	$\Delta\|m\|_{H^1}$
1	1.197615493363614e+00		7.604810663168847e-01	
2	1.197257981690776e+00	-3.575116728380401e-04	7.603200374266788e-01	-1.610288902059720e-04
3	1.197076790120044e+00	-1.811915707319312e-04	7.602386595962363e-01	-8.137783044248614e-05
4	1.197059353046340e+00	-1.743707370405190e-05	7.602297612095278e-01	-8.898386708477979e-06
5	1.197061736820406e+00	2.383774065917166e-06	7.602304433272157e-01	6.821176878890611e-07
6	1.197062481701936e+00	7.448815300126199e-07	7.602306721233926e-01	2.287961768931979e-07

Table A.12: 1D Grid Refinement Verification : Solution H^1 Norm (50 Elements)

	h results		**m results**	
0.1	$\|h\|_{H^1}$	$\Delta\|h\|_{H^1}$	$\|m\|_{H^1}$	$\Delta\|m\|_{H^1}$
1	1.945924996691714e+00		1.169828636367098e+00	
2	1.935520410226579e+00	-1.040458646513498e-02	1.162983094616853e+00	-6.845541750245099e-03
3	1.931294554230465e+00	-4.225855996114136e-03	1.160141245858843e+00	-2.841848758009968e-03
4	1.929725166489429e+00	-1.569387741035877e-03	1.159069253552309e+00	-1.071992306533875e-03
5	1.929515868692894e+00	-2.092977965351128e-04	1.158923457303817e+00	-1.457962484920916e-04
6	1.929509925423437e+00	-5.943269457020506e-06	1.158918509297173e+00	-4.948006643967773e-06
0.2	$\|h\|_{H^1}$	$\Delta\|h\|_{H^1}$	$\|m\|_{H^1}$	$\Delta\|m\|_{H^1}$
1	1.689706287689728e+00		1.089668480819686e+00	
2	1.685459980365559e+00	-4.246307324168974e-03	1.086676614873872e+00	-2.991865945813910e-03
3	1.683658641584746e+00	-1.801338780812900e-03	1.085455489546220e+00	-1.221125327651951e-03
4	1.682977518701881e+00	-6.811228828651483e-04	1.085009040646526e+00	-4.464488996940297e-04
5	1.682884701492849e+00	-9.281720903198121e-05	1.084944728069978e+00	-6.431257654804234e-05
6	1.682881188927613e+00	-3.512565236007958e-06	1.084940645601189e+00	-4.082468789023963e-06
0.5	$\|h\|_{H^1}$	$\Delta\|h\|_{H^1}$	$\|m\|_{H^1}$	$\Delta\|m\|_{H^1}$
1	1.476687541499752e+00		1.029118629137122e+00	
2	1.475561376783162e+00	-1.126164716590106e-03	1.027650808899067e+00	-1.467820238054918e-03
3	1.475108627910173e+00	-4.527488729888507e-04	1.027235114059956e+00	-4.156948391109694e-04
4	1.474943298687400e+00	-1.653292227730141e-04	1.027118862501926e+00	-1.162515580299672e-04
5	1.474919226856978e+00	-2.407183042207883e-05	1.027093444366169e+00	-2.541813575707152e-05
6	1.474917539570503e+00	-1.687286474982841e-06	1.027088002758678e+00	-5.441607491052380e-06
0.8	$\|h\|_{H^1}$	$\Delta\|h\|_{H^1}$	$\|m\|_{H^1}$	$\Delta\|m\|_{H^1}$
1	1.381337248920697e+00		1.015188105097186e+00	
2	1.380995780940304e+00	-3.414679803930287e-04	1.014281915271560e+00	-9.061898256259582e-04
3	1.380877497893873e+00	-1.182830464310225e-04	1.014114038513529e+00	-1.678767580310936e-04
4	1.380839134436495e+00	-3.836345737795455e-05	1.014088564480395e+00	-2.547403313402086e-05
5	1.380833079190307e+00	-6.055246188019225e-06	1.014077619236283e+00	-1.094524411193731e-05
6	1.380832402621629e+00	-6.765686779708346e-07	1.014073689452328e+00	-3.929783955136656e-06

Table A.13: 1D Grid Refinement Verification : Solution H^1 Norm (100 Elements)

	h results		**m results**	
0.1	$\|h\|_{H^1}$	$\Delta\|h\|_{H^1}$	$\|m\|_{H^1}$	$\Delta\|m\|_{H^1}$
1	2.207320551799839e+00		1.566437021998365e+00	
2	2.201193052205626e+00	-6.127499594212882e-03	1.562053914808834e+00	-4.383107189531055e-03
3	2.197554652000630e+00	-3.638400204995840e-03	1.559764203201863e+00	-2.289711606970890e-03
4	2.196026325711071e+00	-1.528326289559345e-03	1.558845834987551e+00	-9.183682143121263e-04
5	2.195439722202825e+00	-5.866035082457977e-04	1.558500143781007e+00	-3.456912065438189e-04
6	2.195359572153596e+00	-8.015004922912183e-05	1.558451911676159e+00	-4.823210484805607e-05
0.2	$\|h\|_{H^1}$	$\Delta\|h\|_{H^1}$	$\|m\|_{H^1}$	$\Delta\|m\|_{H^1}$
1	1.955280007478174e+00		1.464119209310317e+00	
2	1.953040892096303e+00	-2.239115381871049e-03	1.462717066903205e+00	-1.402142407112006e-03
3	1.951935429394384e+00	-1.105462701918913e-03	1.462158556082196e+00	-5.585108210091061e-04
4	1.951470696925981e+00	-4.647324684030618e-04	1.461950960933412e+00	-2.075951487838790e-04
5	1.951291322652400e+00	-1.793742735809456e-04	1.461876343887427e+00	-7.461704598510366e-05
6	1.951266868620756e+00	-2.445403164408333e-05	1.461865670215290e+00	-1.067367213702930e-05
0.5	$\|h\|_{H^1}$	$\Delta\|h\|_{H^1}$	$\|m\|_{H^1}$	$\Delta\|m\|_{H^1}$
1	1.766298210994281e+00		1.428997034986796e+00	
2	1.765892790776185e+00	-4.054202180960864e-04	1.427271774625132e+00	-1.725260361663983e-03
3	1.765462635545578e+00	-4.301552306069656e-04	1.426810042971945e+00	-4.617316531869697e-04
4	1.765310290218301e+00	-1.523453272769260e-04	1.426696534155383e+00	-1.135088165620246e-04
5	1.765255133779567e+00	-5.515643873410525e-05	1.426669862686043e+00	-2.667146933998943e-05
6	1.765246343103115e+00	-8.790676452097301e-06	1.426662338701750e+00	-7.523984292934216e-06
0.8	$\|h\|_{H^1}$	$\Delta\|h\|_{H^1}$	$\|m\|_{H^1}$	$\Delta\|m\|_{H^1}$
1	1.665037971556815e+00		1.398037910309299e+00	
2	1.666238678074100e+00	1.200706517284988e-03	1.398025457684368e+00	-1.245262493099197e-05
3	1.666281786207864e+00	4.310813376395828e-05	1.397864560790729e+00	-1.608968936390731e-04
4	1.666259335099482e+00	-2.245110838194897e-05	1.397795267964505e+00	-6.929282622403221e-05
5	1.666249736411432e+00	-9.598688050171944e-06	1.397771332679218e+00	-2.393528528688016e-05
6	1.666248531021447e+00	-1.205389984937355e-06	1.397767388929191e+00	-3.943750026991211e-06

Table A.14: 1D Grid Refinement Verification : Solution H^1 Norm (200 Elements)

	h results		**m results**	
0.1	$\|h\|_{H^1}$	$\Delta\|h\|_{H^1}$	$\|m\|_{H^1}$	$\Delta\|m\|_{H^1}$
1	2.623547427613691e+00		2.112592037825107e+00	
2	2.620850549284223e+00	-2.696878329468078e-03	2.110346876383860e+00	-2.245161441246868e-03
3	2.619336521976562e+00	-1.514027307660815e-03	2.109684076049681e+00	-6.628003341790922e-04
4	2.618449195637916e+00	-8.873263386459662e-04	2.109350102068297e+00	-3.339739813839060e-04
5	2.618088419829139e+00	-3.607758087769142e-04	2.109228537134645e+00	-1.215649336518965e-04
6	2.617951699663267e+00	-1.367201658721839e-04	2.109185380533335e+00	-4.315660130993493e-05
0.2	$\|h\|_{H^1}$	$\Delta\|h\|_{H^1}$	$\|m\|_{H^1}$	$\Delta\|m\|_{H^1}$
1	2.419892909454006e+00		2.056673484231235e+00	
2	2.418452718650780e+00	-1.440190803225772e-03	2.054804258635016e+00	-1.869225596219160e-03
3	2.417632582238835e+00	-8.201364119448940e-04	2.054358242724456e+00	-4.460159105597050e-04
4	2.417340860900473e+00	-2.917213383621942e-04	2.054264563308999e+00	-9.367941545734837e-05
5	2.417228989051864e+00	-1.118718486088355e-04	2.054257420101901e+00	-7.143207097826121e-06
6	2.417189089656939e+00	-3.989939492532457e-05	2.054261166894011e+00	3.746792109904362e-06
0.5	$\|h\|_{H^1}$	$\Delta\|h\|_{H^1}$	$\|m\|_{H^1}$	$\Delta\|m\|_{H^1}$
1	2.239528180758012e+00		2.006938647542619e+00	
2	2.239645671999281e+00	1.174912412689189e-04	2.005042124284432e+00	-1.896523258186900e-03
3	2.238986352075977e+00	-6.593199233040359e-04	2.004551211835408e+00	-4.909124490239947e-04
4	2.238912447507281e+00	-7.390456869593720e-05	2.004497571485610e+00	-5.364034979793431e-05
5	2.238885194168707e+00	-2.725333857389600e-05	2.004503244255606e+00	5.672769995967997e-06
6	2.238879274226483e+00	-5.919942223986396e-06	2.004512281193279e+00	9.036937672846079e-06
0.8	$\|h\|_{H^1}$	$\Delta\|h\|_{H^1}$	$\|m\|_{H^1}$	$\Delta\|m\|_{H^1}$
1	2.174273409318550e+00		1.998733499507420e+00	
2	2.172604541875995e+00	-1.668867442555122e-03	1.996949158253540e+00	-1.784341253880051e-03
3	2.172540781933505e+00	-6.375994248974948e-05	1.996618879729983e+00	-3.302785235568262e-04
4	2.172456698381005e+00	-8.408355250022481e-05	1.996559427808786e+00	-5.945192119716225e-05
5	2.172447879644242e+00	-8.818736763060997e-06	1.996569088921310e+00	9.661112523984272e-06
6	2.172447630590215e+00	-2.490540267352515e-07	1.996579558928030e+00	1.047000672005360e-05

Table A.15: 1D Grid Refinement Verification : Solution H^1 Norm (400 Elements)

	h results		**m results**	
0.1	$\|h\|_{H^1}$	$\Delta\|h\|_{H^1}$	$\|m\|_{H^1}$	$\Delta\|m\|_{H^1}$
1	3.308917433693108e+00		2.946990164536061e+00	
2	3.312935847209436e+00	4.018413516327701e-03	2.945310934219260e+00	-1.679230316801394e-03
3	3.311439119730134e+00	-1.496727479302074e-03	2.944452706342011e+00	-8.582278772486518e-04
4	3.310783092251566e+00	-6.560274785676334e-04	2.944248530549650e+00	-2.041757923612053e-04
5	3.310565062964522e+00	-2.180292870441747e-04	2.944228765082983e+00	-1.976546666693224e-05
6	3.310478476427661e+00	-8.658653686088869e-05	2.944232499565253e+00	3.734482270090211e-06
0.2	$\|h\|_{H^1}$	$\Delta\|h\|_{H^1}$	$\|m\|_{H^1}$	$\Delta\|m\|_{H^1}$
1	3.084964274393239e+00		2.854692143234419e+00	
2	3.088834959107570e+00	3.870684714331052e-03	2.855442552622664e+00	7.504093882451102e-04
3	3.088538731218597e+00	-2.962278889730996e-04	2.855161423342409e+00	-2.811292802551435e-04
4	3.088583376475669e+00	4.464525707215117e-05	2.855002867612809e+00	-1.585557295999962e-04
5	3.088542382335487e+00	-4.099414018199354e-05	2.854937246472046e+00	-6.562114076302805e-05
6	3.088538125851293e+00	-4.256484193998489e-06	2.854922125395492e+00	-1.512107655399220e-05
0.5	$\|h\|_{H^1}$	$\Delta\|h\|_{H^1}$	$\|m\|_{H^1}$	$\Delta\|m\|_{H^1}$
1	2.930591931546653e+00		2.814570847210030e+00	
2	2.938388708082416e+00	7.796776535763161e-03	2.814411805636918e+00	-1.590415731120842e-04
3	2.939349411781339e+00	9.607036989227602e-04	2.814076234700904e+00	-3.355709360137737e-04
4	2.939517828153406e+00	1.684163720669929e-04	2.813926467652510e+00	-1.497670483940894e-04
5	2.939525898335876e+00	8.070182470287790e-06	2.813860214821909e+00	-6.625283060079923e-05
6	2.939532678875297e+00	6.780539421047393e-06	2.813839984881496e+00	-2.022994041306347e-05
0.8	$\|h\|_{H^1}$	$\Delta\|h\|_{H^1}$	$\|m\|_{H^1}$	$\Delta\|m\|_{H^1}$
1	2.887694637695821e+00		2.811346385314067e+00	
2	2.884387602877656e+00	-3.307034818164745e-03	2.808914975095652e+00	-2.431410218415309e-03
3	2.885802279182611e+00	1.414676304954732e-03	2.809088863995543e+00	1.738888998912280e-04
4	2.885477496541892e+00	-3.247826407188903e-04	2.808756321170777e+00	-3.325428247662465e-04
5	2.885461041947254e+00	-1.645459463794907e-05	2.808670796603904e+00	-8.552456687294097e-05
6	2.885462150483978e+00	1.108536724192533e-06	2.808642505229749e+00	-2.829137415494287e-05

Table A.16: 1D Grid Refinement Verification : Solution Energy Norm ($t = 0.1\ s$)

t=0.1

Elements	$\|h\|_E$	$\|\Delta h\|_E$	**Slope**
25	9.478555294649853e-03		
50	3.868764354944524e-03	-5.609790939705329e-03	
100	2.099664463818819e-03	-1.769099891125705e-03	1.6649
200	1.326927952605021e-03	-7.727365112137981e-04	1.1950
400	1.110400727558006e-03	-2.165272250470151e-04	1.8354
	$\|m\|_E$	$\|\Delta m\|_E$	**Slope**
25	2.631233271480835e-03		
50	1.883759677891412e-03	-7.474735935894229e-04	
100	1.055963439786348e-03	-8.277962381050641e-04	-0.1473
200	7.381976336551430e-04	-3.177658061312050e-04	1.3813
400	6.821004240404576e-04	-5.609720961468538e-05	2.5020

Table A.17: 1D Grid Refinement Verification : Solution Energy Norm ($t = 0.2\ s$)

t=0.2

Elements	$\|h\|_E$	$\|\Delta h\|_E$	**Slope**
25	3.984153618987767e-03		
50	2.152686752805153e-03	-1.831466866182614e-03	
100	1.364322388940655e-03	-7.883643638644979e-04	1.2161
200	1.120833227763520e-03	-2.434891611771350e-04	1.6950
400	7.011489377878281e-04	-4.196842899756918e-04	-0.7855
	$\|m\|_E$	$\|\Delta m\|_E$	**Slope**
25	1.924938091807316e-03		
50	1.089729905547961e-03	-8.352081862593550e-04	
100	7.557146521928177e-04	-3.340152533551434e-04	1.3222
200	6.971292686973610e-04	-5.858538349545663e-05	2.5113
400	4.420901453999815e-04	-2.550391232973795e-04	-2.1221

Table A.18: 1D Grid Refinement Verification : Solution Energy Norm ($t = 0.5\ s$)

t=0.5

Elements	$\|h\|_E$	$\|\Delta h\|_E$	**Slope**
25	1.944028548195147e-03		
50	1.355514462776497e-03	-5.885140854186501e-04	
100	1.026355568770218e-03	-3.291588940062789e-04	0.8383
200	8.650111340886161e-04	-1.613444346816019e-04	1.0286
400	5.730464608729526e-04	-2.919646732156636e-04	-0.8557
	$\|m\|_E$	$\|\Delta m\|_E$	**Slope**
25	1.044748793836181e-03		
50	7.622104121747306e-04	-2.825383816614503e-04	
100	6.040151074070661e-04	-1.581953047676645e-04	0.8367
200	5.724701450097320e-04	-3.154496239733402e-05	2.3262
400	3.761935129911653e-04	-1.962766320185667e-04	-2.6374

Table A.19: 1D Grid Refinement Verification : Solution Energy Norm ($t = 0.8\ s$)

t=0.8

Elements	$\|h\|_E$	$\|\Delta h\|_E$	**Slope**
25	1.453620124712176e-03		
50	1.159579934302370e-03	-2.940401904098059e-04	
100	7.698241664276181e-04	-3.897557678747519e-04	-0.4066
200	7.978179685312885e-04	2.799380210367040e-05	3.7994
400	5.541604657498314e-04	-2.436575027814571e-04	-3.1217
	$\|m\|_E$	$\|\Delta m\|_E$	**Slope**
25	8.097696971671614e-04		
50	7.571175911429600e-04	-5.265210602420139e-05	
100	4.809412219088852e-04	-2.761763692340748e-04	-2.3910
200	5.455949559392753e-04	6.465373403039009e-05	2.0948
400	3.624219398461277e-04	-1.831730160931476e-04	-1.5024

Table A.20: 1D Grid Refinement Verification : Solution H^0 Norm ($t = 0.1\ s$)

t=0.1

Elements	$\|h\|_{H^0}$	$\|\Delta h\|_{H^0}$	**Slope**
25	9.891890848868453e-01		
50	1.001520298305905e+00	1.233121341905974e-02	
100	9.978678647276652e-01	-3.652433578239855e-03	3.4982
200	9.960478049759105e-01	-1.820059751754699e-03	2.0176
400	9.951303230968646e-01	-9.174818790459449e-04	1.9804
	$\|m\|_{H^0}$	$\|\Delta m\|_{H^0}$	**Slope**
25	9.170975127565671e-02		
50	1.029477494333375e-01	1.123799815768078e-02	
100	1.093126797904174e-01	6.364930357079898e-03	1.3905
200	1.125704468723904e-01	3.257767081973006e-03	1.8046
400	1.141236674376123e-01	1.553220565221905e-03	2.0753

Table A.21: 1D Grid Refinement Verification : Solution H^0 Norm ($t = 0.2\ s$)

t=0.2

Elements	$\|h\|_{H^0}$	$\|\Delta h\|_{H^0}$	**Slope**
25	9.733918017209280e-01		
50	9.859835265126329e-01	1.259172479170489e-02	
100	9.823469211887375e-01	-3.636605323895425e-03	3.5705
200	9.805191964179595e-01	-1.827724770777972e-03	1.9931
400	9.795954983004341e-01	-9.236981175253511e-04	1.9732
	$\|m\|_{H^0}$	$\|\Delta m\|_{H^0}$	**Slope**
25	1.451359740231038e-01		
50	1.542272749395911e-01	9.091300916487299e-03	
100	1.590002101406701e-01	4.772935201078993e-03	1.7286
200	1.613277410637967e-01	2.327530923126597e-03	2.0075
400	1.624654091293210e-01	1.137668065524317e-03	2.0344

Table A.22: 1D Grid Refinement Verification : Solution H^0 Norm ($t = 0.5\ s$)

t=0.5

Elements	$\|h\|_{H^0}$	$\|\Delta h\|_{H^0}$	**Slope**
25	9.245843637370432e-01		
50	9.380631729761506e-01	1.347880923910738e-02	
100	9.343082734317877e-01	-3.754899544362922e-03	3.6727
200	9.324172556832572e-01	-1.891017748530510e-03	1.9879
400	8.807408264805577e-01	-5.167642920269944e-02	-9.4605
	$\|m\|_{H^0}$	$\|\Delta m\|_{H^0}$	**Slope**
25	2.465686200867906e-01		
50	2.525791773457860e-01	6.010557258995408e-03	
100	2.556465281545025e-01	3.067350808716507e-03	1.8890
200	2.571932505266539e-01	1.546722372151421e-03	1.9495
400	3.267098777142660e-01	6.951662718761209e-02	-10.1355

Table A.23: 1D Grid Refinement Verification : Solution H^0 Norm ($t = 0.8\ s$)

t=0.8

Elements	$\|h\|_{H^0}$	$\|\Delta h\|_{H^0}$	**Slope**
25	8.733763167126188e-01		
50	8.876012521592773e-01	1.422493544665848e-02	
100	8.836839487852640e-01	-3.917303374013303e-03	3.7041
200	8.817224116781176e-01	-1.961537107146416e-03	2.0053
400	8.807408264805577e-01	-9.815851975598644e-04	2.0024
	$\|m\|_{H^0}$	$\|\Delta m\|_{H^0}$	**Slope**
25	3.174454716068721e-01		
50	3.222548506246715e-01	4.809379017799431e-03	
100	3.247576485685640e-01	2.502797943892465e-03	1.8518
200	3.260492932636501e-01	1.291644695086136e-03	1.8918
400	3.267098777142660e-01	6.605844506158975e-04	1.9261

Table A.24: 1D Grid Refinement Verification : Solution H^1 Norm ($t = 0.1\ s$)

t=0.1

Elements	$\|h\|_{H^1}$	$\|\Delta h\|_{H^1}$	**Slope**
25	1.815784988089996e+00		
50	1.929509925423437e+00	1.137249373334408e-01	
100	2.195359572153596e+00	2.658496467301590e-01	-2.7287
200	2.617951699663267e+00	4.225921275096711e-01	-1.7827
400	3.310478476427661e+00	6.925267767643941e-01	-2.0264
	$\|m\|_{H^1}$	$\|\Delta m\|_{H^1}$	**Slope**
25	8.182500274787153e-01		
50	1.158918509297173e+00	3.406684818184577e-01	
100	1.558451911676159e+00	3.995334023789860e-01	-1.3774
200	2.109185380533335e+00	5.507334688571761e-01	-1.7914
400	2.944232499565253e+00	8.350471190319180e-01	-2.1258

Table A.25: 1D Grid Refinement Verification : Solution H^1 Norm ($t = 0.2\ s$)

t=0.2

Elements	$\|h\|_{H^1}$	$\|\Delta h\|_{H^1}$	**Slope**
25	1.512524867440097e+00		
50	1.682881188927613e+00	1.703563214875159e-01	
100	1.951266868620756e+00	2.683856796931430e-01	-1.6827
200	2.417189089656939e+00	4.659222210361829e-01	-2.1226
400	3.088538125851293e+00	6.713490361943544e-01	-1.7216
	$\|m\|_{H^1}$	$\|\Delta m\|_{H^1}$	**Slope**
25	8.173776254784024e-01		
50	1.084940645601189e+00	2.675630201227865e-01	
100	1.461865670215290e+00	3.769250246141009e-01	-1.8307
200	2.054261166894011e+00	5.923954966787210e-01	-2.2352
400	2.854922125395492e+00	8.006609585014810e-01	-1.8323

Table A.26: 1D Grid Refinement Verification : Solution H^1 Norm ($t = 0.5\ s$)

t=0.5

Elements	$\|h\|_{H^1}$	$\|\Delta h\|_{H^1}$	**Slope**
25	1.293916857547365e+00		
50	1.474917539570503e+00	1.810006820231380e-01	
100	1.765246343103115e+00	2.903288035326119e-01	-1.8170
200	2.238879274226483e+00	4.736329311233682e-01	-2.0230
400	2.939532678875297e+00	7.006534046488140e-01	-1.8719
	$\|m\|_{H^1}$	$\|\Delta m\|_{H^1}$	**Slope**
25	7.656259863038575e-01		
50	1.027088002758678e+00	2.614620164548205e-01	
100	1.426662338701750e+00	3.995743359430721e-01	-2.1294
200	2.004512281193279e+00	5.778499424915289e-01	-2.0319
400	2.813839984881496e+00	8.093277036882172e-01	-1.9517

Table A.27: 1D Grid Refinement Verification : Solution H^1 Norm ($t = 0.8\ s$)

t=0.8

Elements	$\|h\|_{H^1}$	$\|\Delta h\|_{H^1}$	**Slope**
25	1.197062481701936e+00		
50	1.380832402621629e+00	1.837699209196930e-01	
100	1.666248531021447e+00	2.854161283998180e-01	-1.7528
200	2.172447630590215e+00	5.061990995687682e-01	-2.3197
400	2.885462150483978e+00	7.130145198937630e-01	-1.7843
	$\|m\|_{H^1}$	$\|\Delta m\|_{H^1}$	**Slope**
25	7.602306721233926e-01		
50	1.014073689452328e+00	2.538430173289353e-01	
100	1.397767388929191e+00	3.836936994768632e-01	-2.0778
200	1.996579558928030e+00	5.988121699988389e-01	-2.2703
400	2.808642505229749e+00	8.120629463017190e-01	-1.8819

Appendix B

Additional Plots, 2D Dam Break

B.1 Time = 1.0 s

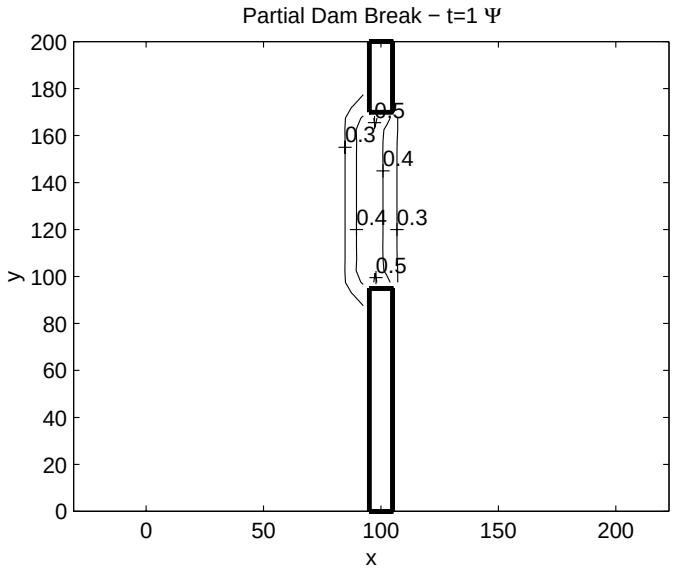

Figure B.1: Partial Dam Break : Contour Plot of ψ ($t = 1.0\ s$)

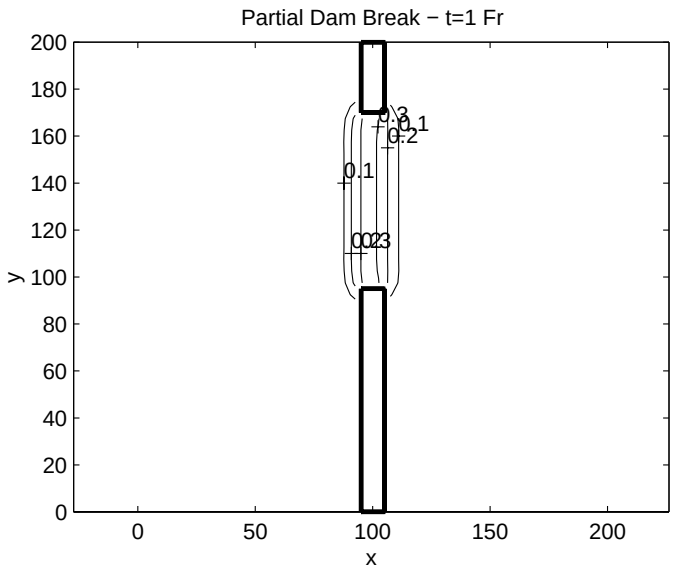

Figure B.2: Partial Dam Break : Contour Plot of Fr $(t = 1.0\ s)$

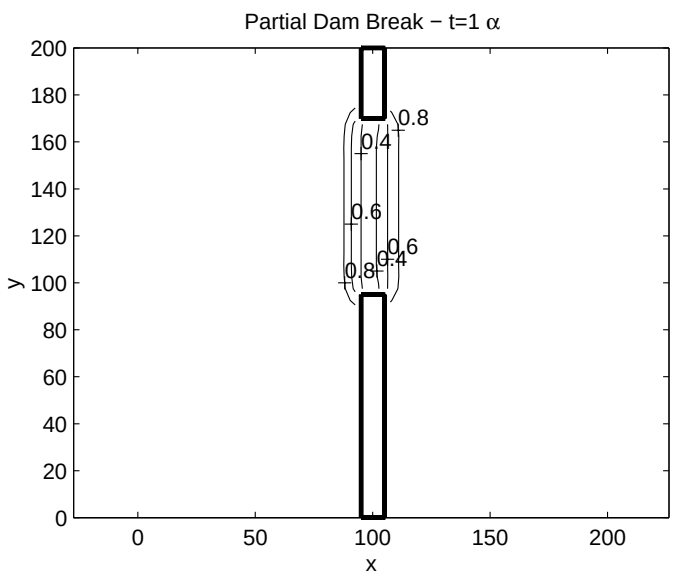

Figure B.3: Partial Dam Break : Contour Plot of α $(t = 1.0\ s)$

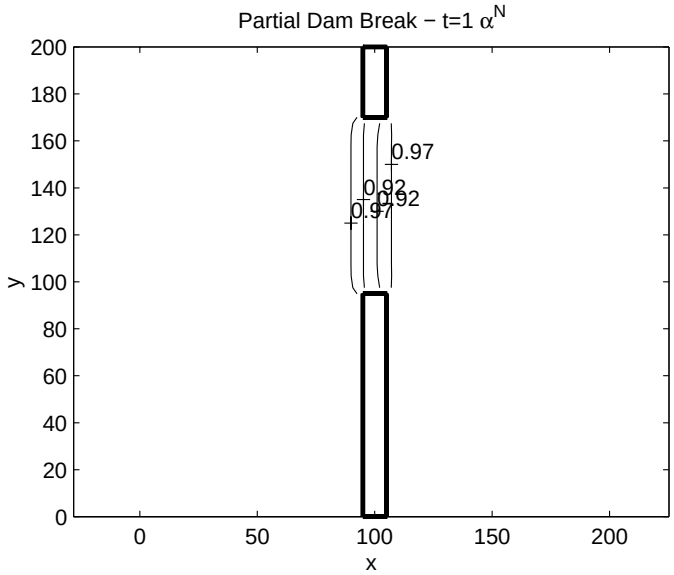

Figure B.4: Partial Dam Break : Contour Plot of α^N $(t = 1.0\ s)$

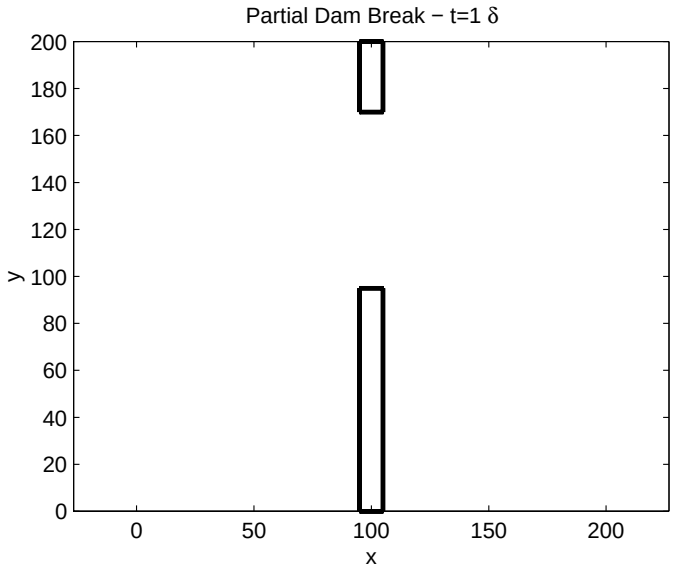

Figure B.5: Partial Dam Break : Contour Plot of δ $(t = 1.0\ s)$

B.2 Time = 3.0 s

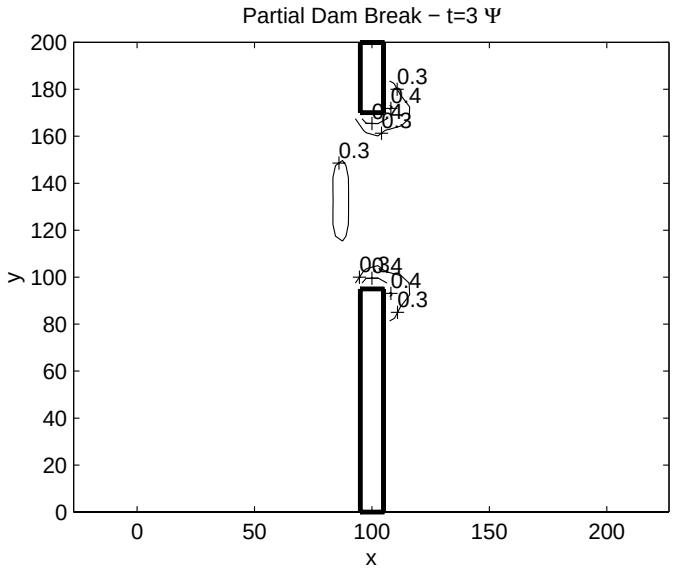

Figure B.6: Partial Dam Break : Contour Plot of ψ ($t = 3.0\ s$)

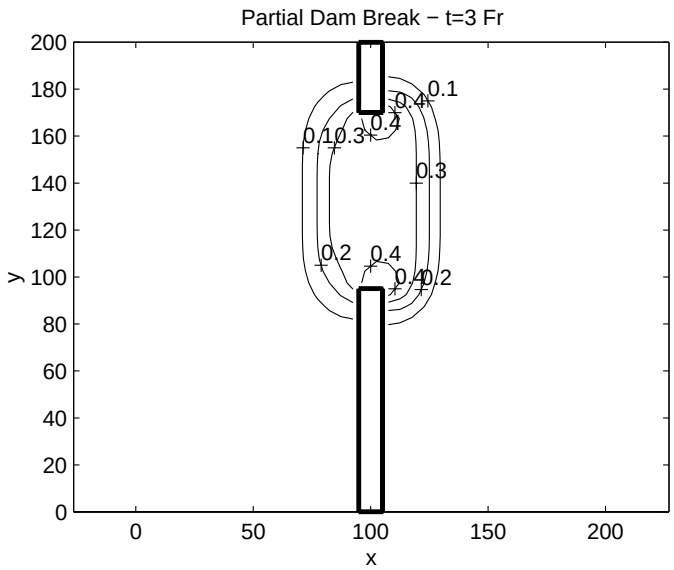

Figure B.7: Partial Dam Break : Contour Plot of Fr $(t = 3.0\ s)$

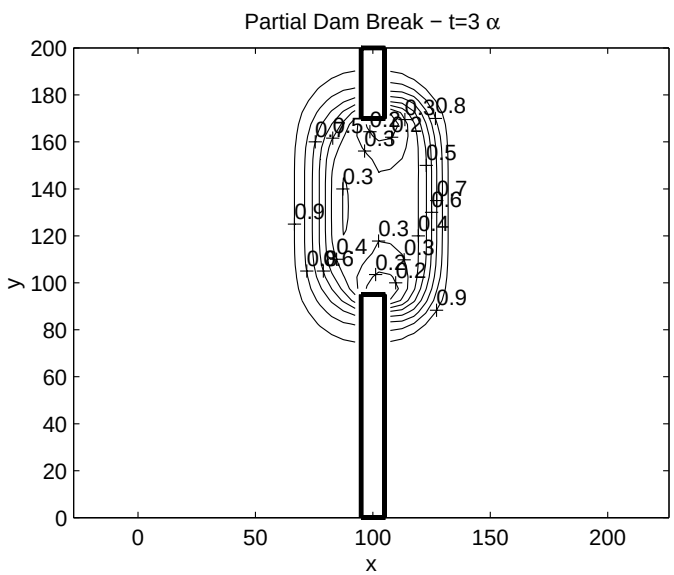

Figure B.8: Partial Dam Break : Contour Plot of α $(t = 3.0\ s)$

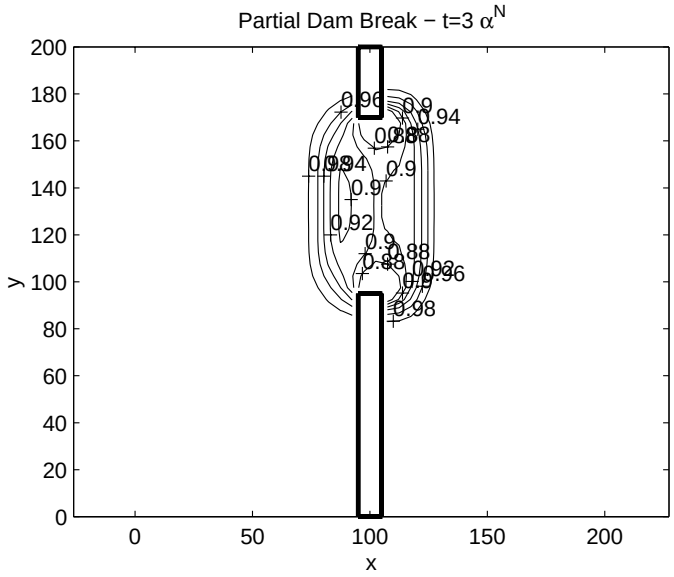

Figure B.9: Partial Dam Break : Contour Plot of α^N $(t = 3.0\ s)$

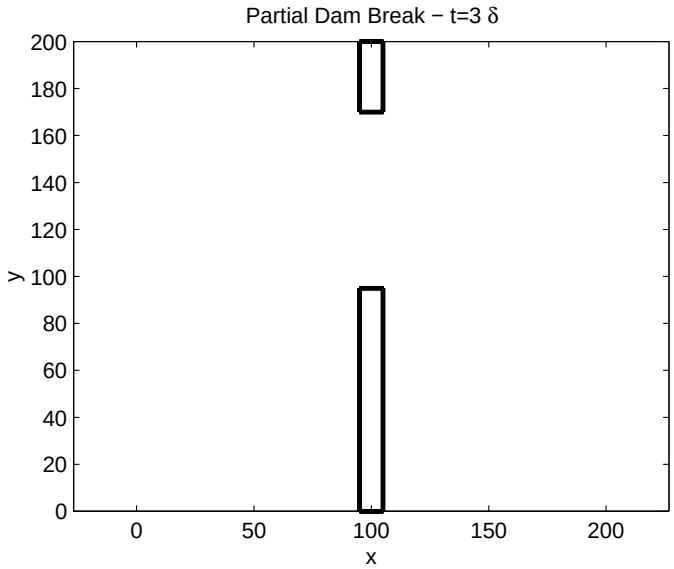

Figure B.10: Partial Dam Break : Contour Plot of δ $(t = 3.0\ s)$

B.3 Time = 5.0 s

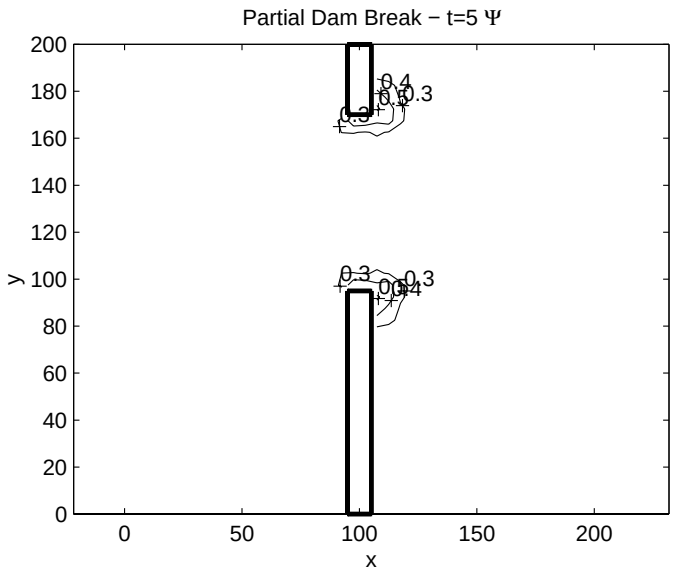

Figure B.11: Partial Dam Break : Contour Plot of ψ ($t = 5.0\ s$)

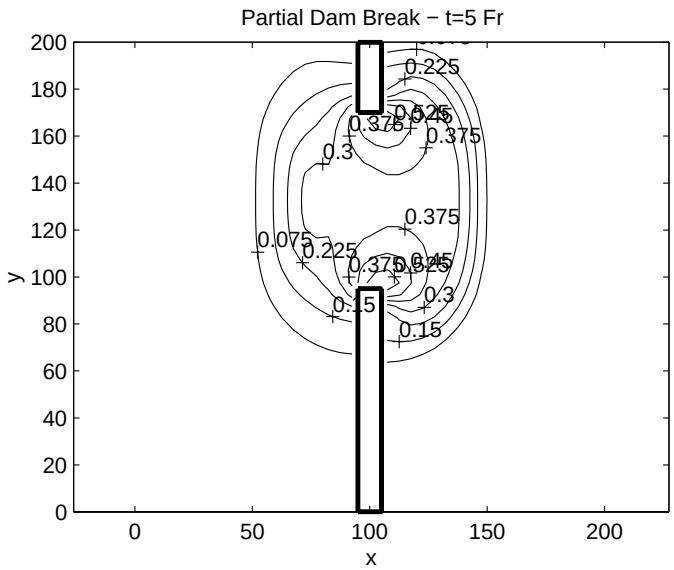

Figure B.12: Partial Dam Break : Contour Plot of Fr $(t = 5.0\ s)$

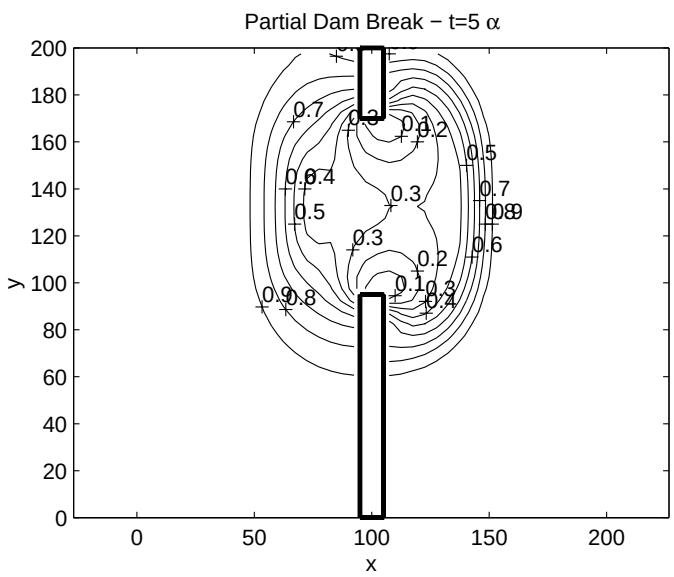

Figure B.13: Partial Dam Break : Contour Plot of α $(t = 5.0\ s)$

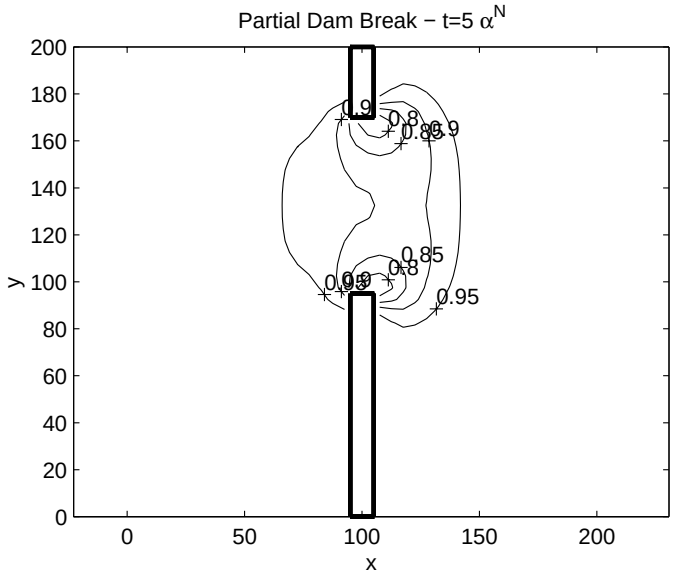

Figure B.14: Partial Dam Break : Contour Plot of α^N $(t = 5.0\ s)$

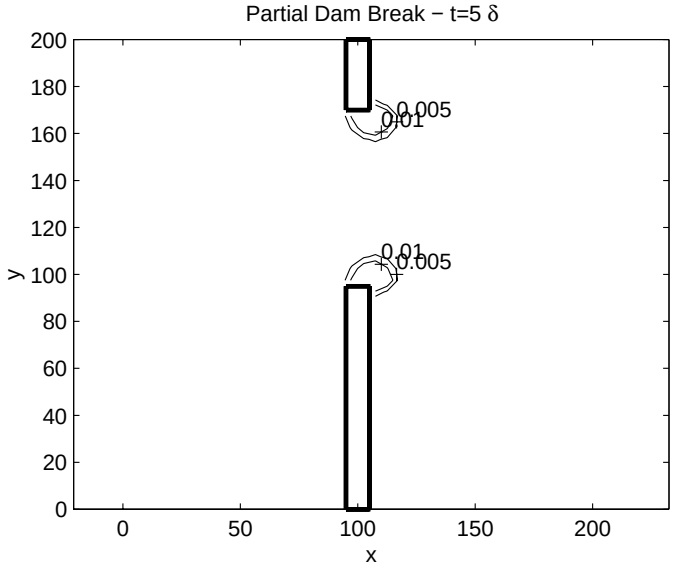

Figure B.15: Partial Dam Break : Contour Plot of δ $(t = 5.0\ s)$

B.4 Time = 7.2 s

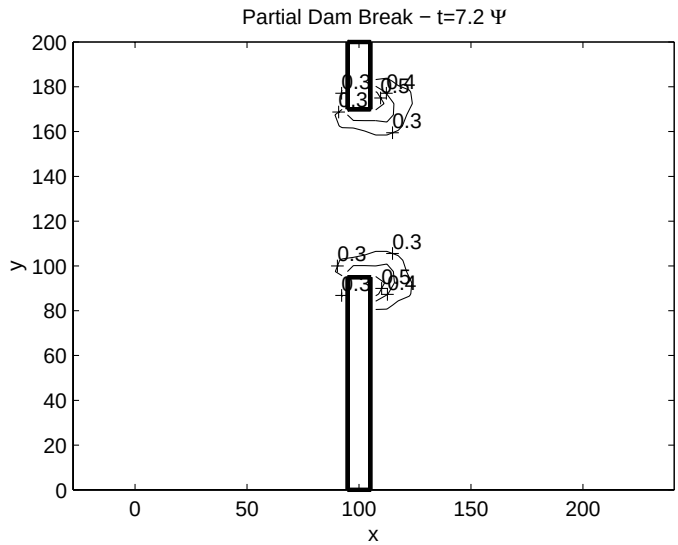

Figure B.16: Partial Dam Break : Contour Plot of ψ ($t = 7.2\ s$)

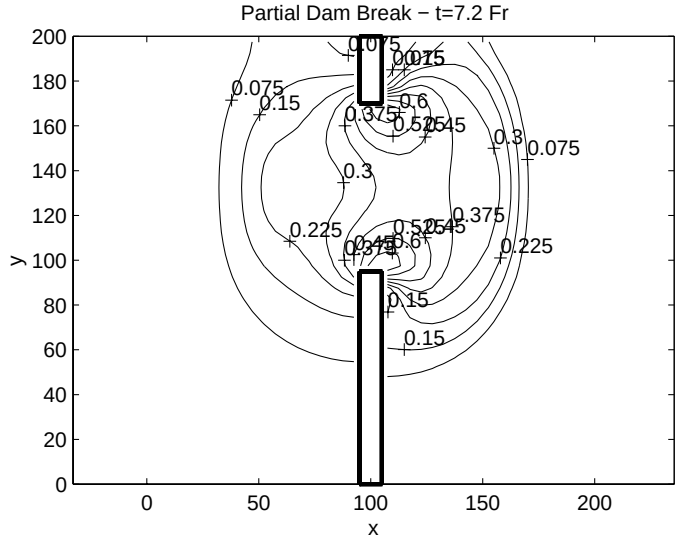

Figure B.17: Partial Dam Break : Contour Plot of Fr ($t = 7.2\ s$)

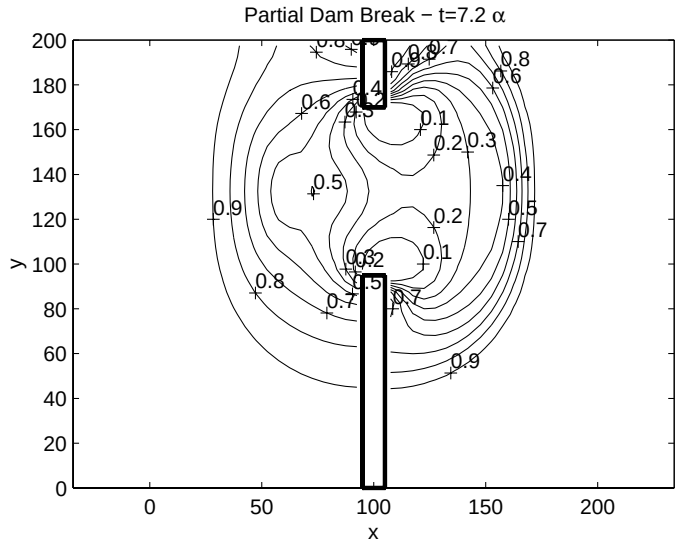

Figure B.18: Partial Dam Break : Contour Plot of α ($t = 7.2\ s$)

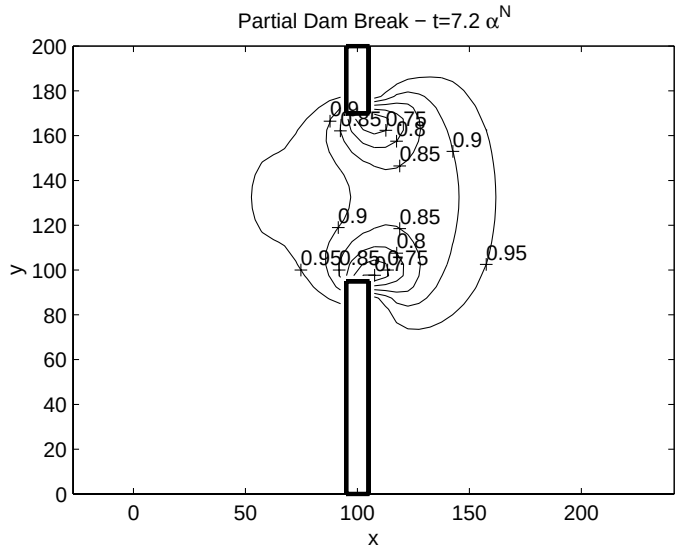

Figure B.19: Partial Dam Break : Contour Plot of α^N $(t = 7.2\ s)$

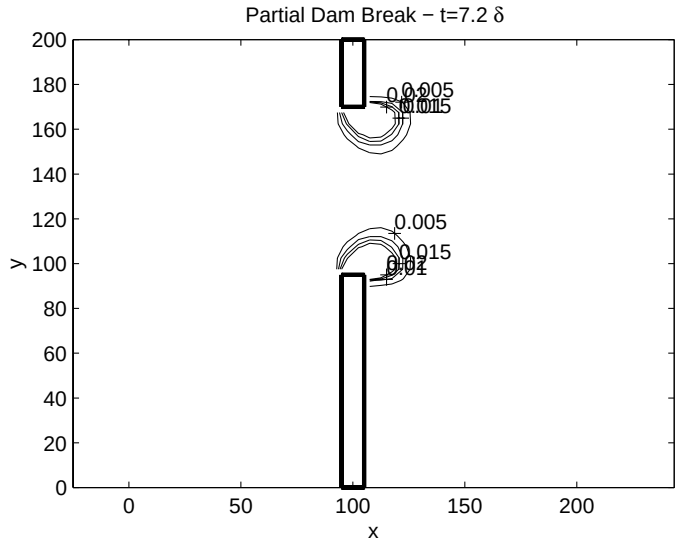

Figure B.20: Partial Dam Break : Contour Plot of δ $(t = 7.2\ s)$

Appendix C

Grid Refinement Data,

2D Partial Dam Break

Table C.1: 2D Grid Refinement Verification : Solution Energy Norm (20 Elements)

	h results		**m1 results**		**m2 results**	
1.0	$\|h\|_E$	$\Delta\|h\|_E$	$\|m_1\|_E$	$\Delta\|m_1\|_E$	$\|m_2\|_E$	$\Delta\|m_2\|_E$
1	3.39748e+02		2.63978e+04		5.06569e+02	
2	3.37747e+02	-2.00114e+00	2.63274e+04	-7.03442e+01	5.28947e+02	2.23782e+01
3	3.36940e+02	-8.06956e-01	2.63046e+04	-2.27972e+01	5.39660e+02	1.07128e+01
4	3.38760e+02	1.82073e+00	2.62980e+04	-6.66470e+00	5.44868e+02	5.20809e+00
5	3.37579e+02	-1.18185e+00	2.62962e+04	-1.79231e+00	5.47404e+02	2.53569e+00
3.0	$\|h\|_E$	$\Delta\|h\|_E$	$\|m_1\|_E$	$\Delta\|m_1\|_E$	$\|m_2\|_E$	$\Delta\|m_2\|_E$
1	2.25795e+02		2.35450e+04		6.79220e+03	
2	2.42412e+02	1.66175e+01	2.35525e+04	7.46492e+00	6.80957e+03	1.73672e+01
3	2.38463e+02	-3.94903e+00	2.35604e+04	7.92931e+00	6.81735e+03	7.78033e+00
4	2.39042e+02	5.78911e-01	2.35654e+04	5.02996e+00	6.82163e+03	4.28098e+00
5	2.55767e+02	1.67247e+01	2.35666e+04	1.20472e+00	6.82307e+03	1.44441e+00
5.0	$\|h\|_E$	$\Delta\|h\|_E$	$\|m_1\|_E$	$\Delta\|m_1\|_E$	$\|m_2\|_E$	$\Delta\|m_2\|_E$
1	2.80614e+02		2.48138e+04		1.06836e+04	
2	2.89380e+02	8.76626e+00	2.48545e+04	4.06294e+01	1.06990e+04	1.54365e+01
3	3.02202e+02	1.28212e+01	2.48654e+04	1.09802e+01	1.07048e+04	5.77132e+00
4	3.10250e+02	8.04838e+00	2.48704e+04	4.93296e+00	1.07089e+04	4.13758e+00
5	2.51146e+02	-5.91041e+01	2.48219e+04	-4.84905e+01	1.06892e+04	-1.97524e+01
7.2	$\|h\|_E$	$\Delta\|h\|_E$	$\|m_1\|_E$	$\Delta\|m_1\|_E$	$\|m_2\|_E$	$\Delta\|m_2\|_E$
1	3.69164e+02		2.75081e+04		1.48021e+04	
2	4.08774e+02	3.96096e+01	2.76133e+04	1.05241e+02	1.47673e+04	-3.47360e+01
3	3.38079e+02	-7.06951e+01	2.74834e+04	-1.29869e+02	1.47439e+04	-2.34010e+01
4	3.34540e+02	-3.53820e+00	2.74896e+04	6.14918e+00	1.47478e+04	3.91430e+00
5	4.70814e+02	1.36273e+02	2.77860e+04	2.96406e+02	1.48868e+04	1.38932e+02

Table C.2: 2D Grid Refinement Verification : Solution Energy Norm (40 Elements)

	h results		**m1 results**		**m2 results**	
1.0	$\|\|h\|\|_E$	$\Delta\|\|h\|\|_E$	$\|\|m_1\|\|_E$	$\Delta\|\|m_1\|\|_E$	$\|\|m_2\|\|_E$	$\Delta\|\|m_2\|\|_E$
1	1.98090e+02		1.33971e+04		1.01299e+03	
2	1.97594e+02	-4.95240e-01	1.33631e+04	-3.39956e+01	1.01406e+03	1.06804e+00
3	1.97418e+02	-1.76353e-01	1.33495e+04	-1.36534e+01	1.01439e+03	3.25366e-01
4	1.97380e+02	-3.84789e-02	1.33481e+04	-1.39975e+00	1.01443e+03	4.49775e-02
5	1.97374e+02	-5.61739e-03	1.33477e+04	-3.70423e-01	1.01445e+03	1.43296e-02
3.0	$\|\|h\|\|_E$	$\Delta\|\|h\|\|_E$	$\|\|m_1\|\|_E$	$\Delta\|\|m_1\|\|_E$	$\|\|m_2\|\|_E$	$\Delta\|\|m_2\|\|_E$
1	1.12597e+02		1.14157e+04		4.31836e+03	
2	1.12582e+02	-1.44699e-02	1.14145e+04	-1.13978e+00	4.31717e+03	-1.19597e+00
3	1.12578e+02	-4.79391e-03	1.14143e+04	-2.08837e-01	4.31688e+03	-2.88895e-01
4	1.12578e+02	5.19966e-04	1.14142e+04	-1.20538e-01	4.31686e+03	-1.83706e-02
5	1.12578e+02	-1.66592e-04	1.14142e+04	-1.28457e-02	4.31684e+03	-1.75506e-02
5.0	$\|\|h\|\|_E$	$\Delta\|\|h\|\|_E$	$\|\|m_1\|\|_E$	$\Delta\|\|m_1\|\|_E$	$\|\|m_2\|\|_E$	$\Delta\|\|m_2\|\|_E$
1	1.13138e+02		1.28356e+04		5.87492e+03	
2	1.13119e+02	-1.87707e-02	1.28342e+04	-1.36776e+00	5.87457e+03	-3.52039e-01
3	1.13114e+02	-4.80369e-03	1.28339e+04	-3.29739e-01	5.87451e+03	-5.92749e-02
4	1.13112e+02	-1.87539e-03	1.28337e+04	-1.50957e-01	5.87451e+03	-1.44483e-04
5	1.13112e+02	-2.38868e-04	1.28337e+04	-1.52786e-02	5.87451e+03	-7.38250e-03
7.2	$\|\|h\|\|_E$	$\Delta\|\|h\|\|_E$	$\|\|m_1\|\|_E$	$\Delta\|\|m_1\|\|_E$	$\|\|m_2\|\|_E$	$\Delta\|\|m_2\|\|_E$
1	1.21328e+02		1.44626e+04		7.35109e+03	
2	1.21321e+02	-7.04944e-03	1.44614e+04	-1.18528e+00	7.35070e+03	-3.83864e-01
3	1.21319e+02	-1.30139e-03	1.44612e+04	-2.11677e-01	7.35062e+03	-8.16648e-02
4	1.21320e+02	1.34400e-04	1.44611e+04	-5.26101e-02	7.35061e+03	-7.80989e-03
5	1.21319e+02	-1.16244e-04	1.44611e+04	-2.00381e-02	7.35061e+03	-7.03370e-03

Table C.3: 2D Grid Refinement Verification : Solution Energy Norm (80 Elements)

	h results		**m1 results**		**m2 results**	
1.0	$\|h\|_E$	$\Delta\|h\|_E$	$\|m_1\|_E$	$\Delta\|m_1\|_E$	$\|m_2\|_E$	$\Delta\|m_2\|_E$
1	1.03701e+02		8.43663e+03		9.69931e+02	
2	1.03621e+02	-8.03037e-02	8.43301e+03	-3.61902e+00	9.69973e+02	4.20777e-02
3	1.03598e+02	-2.26751e-02	8.43190e+03	-1.11164e+00	9.69987e+02	1.37023e-02
4	1.03590e+02	-7.85862e-03	8.43148e+03	-4.17481e-01	9.69988e+02	1.62476e-03
5	1.03588e+02	-1.96652e-03	8.43137e+03	-1.05448e-01	9.69989e+02	6.13920e-04
3.0	$\|h\|_E$	$\Delta\|h\|_E$	$\|m_1\|_E$	$\Delta\|m_1\|_E$	$\|m_2\|_E$	$\Delta\|m_2\|_E$
1	8.00246e+01		8.57716e+03		2.86354e+03	
2	8.00111e+01	-1.34687e-02	8.57609e+03	-1.07438e+00	2.86340e+03	-1.42127e-01
3	8.00078e+01	-3.37703e-03	8.57583e+03	-2.56301e-01	2.86337e+03	-2.89784e-02
4	8.00070e+01	-8.00417e-04	8.57577e+03	-6.02967e-02	2.86336e+03	-8.15038e-03
5	8.00068e+01	-2.04955e-04	8.57576e+03	-1.49756e-02	2.86336e+03	-1.82450e-03
5.0	$\|h\|_E$	$\Delta\|h\|_E$	$\|m_1\|_E$	$\Delta\|m_1\|_E$	$\|m_2\|_E$	$\Delta\|m_2\|_E$
1	8.34282e+01		9.74934e+03		4.01609e+03	
2	8.34362e+01	7.93126e-03	9.74942e+03	8.34275e-02	4.01607e+03	-1.74890e-02
3	8.34387e+01	2.50835e-03	9.74949e+03	7.24437e-02	4.01607e+03	-2.45406e-03
4	8.34393e+01	5.99575e-04	9.74951e+03	1.82527e-02	4.01607e+03	-9.61465e-04
5	8.34394e+01	1.65801e-04	9.74951e+03	5.52092e-03	4.01607e+03	-1.89218e-04
7.2	$\|h\|_E$	$\Delta\|h\|_E$	$\|m_1\|_E$	$\Delta\|m_1\|_E$	$\|m_2\|_E$	$\Delta\|m_2\|_E$
1	8.92544e+01		1.07343e+04		4.88288e+03	
2	8.92585e+01	4.12607e-03	1.07343e+04	-5.14450e-03	4.88283e+03	-5.18734e-02
3	8.92598e+01	1.25361e-03	1.07343e+04	2.53596e-02	4.88282e+03	-1.31050e-02
4	8.92601e+01	2.81819e-04	1.07343e+04	5.59042e-03	4.88282e+03	-3.23802e-03
5	8.92602e+01	7.96221e-05	1.07343e+04	2.10563e-03	4.88281e+03	-7.39145e-04

Table C.4: 2D Grid Refinement Verification : Solution Energy Norm (160 Elements)

	h results		**m1 results**		**m2 results**	
1.0	$\|h\|_E$	$\Delta\|h\|_E$	$\|m_1\|_E$	$\Delta\|m_1\|_E$	$\|m_2\|_E$	$\Delta\|m_2\|_E$
1	6.43635e+01		5.45298e+03		7.35333e+02	
2	7.42245e+01	9.86101e+00	6.32606e+03	8.73079e+02	7.34289e+02	-1.04410e+00
3	7.88150e+01	4.59047e+00	6.73249e+03	4.06433e+02	7.33803e+02	-4.86047e-01
4	8.10252e+01	2.21022e+00	6.92818e+03	1.95690e+02	7.33569e+02	-2.34022e-01
5	8.13653e+01	3.40035e-01	6.95829e+03	3.01061e+01	7.33533e+02	-3.60035e-02
3.0	$\|h\|_E$	$\Delta\|h\|_E$	$\|m_1\|_E$	$\Delta\|m_1\|_E$	$\|m_2\|_E$	$\Delta\|m_2\|_E$
1	6.04286e+01		6.50142e+03		1.94069e+03	
2	6.79676e+01	7.53896e+00	7.37183e+03	8.70417e+02	2.09381e+03	1.53121e+02
3	7.14771e+01	3.50952e+00	7.77703e+03	4.05194e+02	2.16509e+03	7.12804e+01
4	7.31669e+01	1.68976e+00	7.97212e+03	1.95093e+02	2.19941e+03	3.43202e+01
5	7.34268e+01	2.59964e-01	8.00214e+03	3.00143e+01	2.20469e+03	5.28003e+00
5.0	$\|h\|_E$	$\Delta\|h\|_E$	$\|m_1\|_E$	$\Delta\|m_1\|_E$	$\|m_2\|_E$	$\Delta\|m_2\|_E$
1	6.37168e+01		7.38119e+03		2.63966e+03	
2	7.29979e+01	9.28108e+00	8.37179e+03	9.90593e+02	3.13498e+03	4.95320e+02
3	7.73184e+01	4.32050e+00	8.83292e+03	4.61138e+02	3.36556e+03	2.30580e+02
4	7.93986e+01	2.08024e+00	9.05495e+03	2.22029e+02	3.47658e+03	1.11020e+02
5	7.97186e+01	3.20037e-01	9.08911e+03	3.41583e+01	3.49366e+03	1.70800e+01
7.2	$\|h\|_E$	$\Delta\|h\|_E$	$\|m_1\|_E$	$\Delta\|m_1\|_E$	$\|m_2\|_E$	$\Delta\|m_2\|_E$
1	6.55546e+01		7.23696e+03		3.46578e+03	
2	7.77357e+01	1.21810e+01	8.74480e+03	1.50784e+03	3.92456e+03	4.58781e+02
3	8.34061e+01	5.67049e+00	9.44673e+03	7.01927e+02	4.13813e+03	2.13570e+02
4	8.61364e+01	2.73023e+00	9.78470e+03	3.37964e+02	4.24096e+03	1.02830e+02
5	8.65564e+01	4.20036e-01	9.83669e+03	5.19945e+01	4.25678e+03	1.58200e+01

Table C.5: 2D Grid Refinement Verification : Solution H^0 Norm (20 Elements)

	h results		**m1 results**		**m2 results**	
1.0	$\|h\|_{H^0}$	$\Delta\|h\|_{H^0}$	$\|m_1\|_{H^0}$	$\Delta\|m_1\|_{H^0}$	$\|m_2\|_{H^0}$	$\Delta\|m_2\|_{H^0}$
1	1.11405e+03		4.60937e+02		3.81901e+01	
2	1.11408e+03	2.92766e-02	4.60972e+02	3.55571e-02	3.91105e+01	9.20381e-01
3	1.11409e+03	1.42090e-02	4.60999e+02	2.64979e-02	3.95840e+01	4.73523e-01
4	1.11410e+03	7.52073e-03	4.61018e+02	1.93637e-02	3.98234e+01	2.39384e-01
5	1.11410e+03	3.72845e-03	4.61029e+02	1.10171e-02	3.99428e+01	1.19378e-01
3.0	$\|h\|_{H^0}$	$\Delta\|h\|_{H^0}$	$\|m_1\|_{H^0}$	$\Delta\|m_1\|_{H^0}$	$\|m_2\|_{H^0}$	$\Delta\|m_2\|_{H^0}$
1	1.10860e+03		9.04800e+02		2.39872e+02	
2	1.10864e+03	4.35541e-02	9.04831e+02	3.07748e-02	2.40727e+02	8.54355e-01
3	1.10865e+03	1.53322e-02	9.04850e+02	1.91333e-02	2.41159e+02	4.32018e-01
4	1.10866e+03	6.61510e-03	9.04861e+02	1.05739e-02	2.41381e+02	2.22424e-01
5	1.10867e+03	6.98563e-03	9.04864e+02	2.98879e-03	2.41474e+02	9.27221e-02
5.0	$\|h\|_{H^0}$	$\Delta\|h\|_{H^0}$	$\|m_1\|_{H^0}$	$\Delta\|m_1\|_{H^0}$	$\|m_2\|_{H^0}$	$\Delta\|m_2\|_{H^0}$
1	1.10220e+03		1.21044e+03		4.46226e+02	
2	1.10221e+03	5.62672e-03	1.21054e+03	1.03068e-01	4.46727e+02	5.00981e-01
3	1.10221e+03	4.10625e-03	1.21059e+03	4.44073e-02	4.47063e+02	3.35770e-01
4	1.10222e+03	6.35722e-04	1.21061e+03	2.19103e-02	4.47241e+02	1.78762e-01
5	1.10228e+03	6.46644e-02	1.21054e+03	-7.30113e-02	4.47596e+02	3.54250e-01
7.2	$\|h\|_{H^0}$	$\Delta\|h\|_{H^0}$	$\|m_1\|_{H^0}$	$\Delta\|m_1\|_{H^0}$	$\|m_2\|_{H^0}$	$\Delta\|m_2\|_{H^0}$
1	1.09415e+03		1.49318e+03		6.21841e+02	
2	1.09409e+03	-5.76509e-02	1.49361e+03	4.22313e-01	6.21404e+02	-4.37076e-01
3	1.09420e+03	1.05896e-01	1.49354e+03	-6.18509e-02	6.21149e+02	-2.55292e-01
4	1.09420e+03	1.82608e-03	1.49359e+03	5.01240e-02	6.21156e+02	7.43419e-01
5	1.09406e+03	-1.37429e-01	1.49357e+03	-2.58563e-02	6.23366e+02	2.20939e+00

Table C.6: 2D Grid Refinement Verification : Solution H^0 Norm (40 Elements)

	h results		**m1 results**		**m2 results**	
1.0	$\|h\|_{H^0}$	$\Delta\|h\|_{H^0}$	$\|m_1\|_{H^0}$	$\Delta\|m_1\|_{H^0}$	$\|m_2\|_{H^0}$	$\Delta\|m_2\|_{H^0}$
1	1.09471e+03		4.69353e+02		4.74713e+01	
2	1.09471e+03	-1.43448e-04	4.69360e+02	7.10045e-03	4.75133e+01	4.19459e-02
3	1.09471e+03	-4.38933e-06	4.69364e+02	3.45792e-03	4.75266e+01	1.33617e-02
4	1.09471e+03	-4.14557e-05	4.69364e+02	-2.91640e-05	4.75295e+01	2.89801e-03
5	1.09471e+03	-1.71464e-06	4.69364e+02	1.19753e-04	4.75302e+01	6.35340e-04
3.0	$\|h\|_{H^0}$	$\Delta\|h\|_{H^0}$	$\|m_1\|_{H^0}$	$\Delta\|m_1\|_{H^0}$	$\|m_2\|_{H^0}$	$\Delta\|m_2\|_{H^0}$
1	1.09030e+03		9.01812e+02		2.72082e+02	
2	1.09030e+03	-8.88766e-05	9.01808e+02	-4.26902e-03	2.72089e+02	6.91432e-03
3	1.09030e+03	5.98959e-06	9.01810e+02	2.02764e-03	2.72091e+02	2.79585e-03
4	1.09030e+03	-1.06616e-05	9.01809e+02	-7.44735e-04	2.72094e+02	2.21777e-03
5	1.09030e+03	-2.26923e-06	9.01809e+02	-1.63850e-04	2.72094e+02	4.75595e-05
5.0	$\|h\|_{H^0}$	$\Delta\|h\|_{H^0}$	$\|m_1\|_{H^0}$	$\Delta\|m_1\|_{H^0}$	$\|m_2\|_{H^0}$	$\Delta\|m_2\|_{H^0}$
1	1.08586e+03		1.20980e+03		4.99231e+02	
2	1.08586e+03	-2.92871e-04	1.20979e+03	-8.78139e-03	4.99229e+02	-2.62715e-03
3	1.08586e+03	-4.24369e-05	1.20979e+03	-2.49752e-04	4.99229e+02	7.87688e-04
4	1.08586e+03	-5.81810e-06	1.20979e+03	-2.12161e-04	4.99231e+02	1.23898e-03
5	1.08586e+03	-6.08811e-06	1.20979e+03	-2.13827e-04	4.99230e+02	-1.68406e-04
7.2	$\|h\|_{H^0}$	$\Delta\|h\|_{H^0}$	$\|m_1\|_{H^0}$	$\Delta\|m_1\|_{H^0}$	$\|m_2\|_{H^0}$	$\Delta\|m_2\|_{H^0}$
1	1.08089e+03		1.50207e+03		6.86368e+02	
2	1.08089e+03	-2.66585e-04	1.50206e+03	-6.77652e-03	6.86357e+02	-1.04711e-02
3	1.08089e+03	-2.84414e-05	1.50206e+03	-3.24602e-04	6.86356e+02	-1.54986e-03
4	1.08089e+03	-1.46284e-07	1.50206e+03	1.60519e-04	6.86356e+02	-9.96802e-05
5	1.08089e+03	-5.95983e-06	1.50206e+03	-1.84710e-04	6.86355e+02	-2.52242e-04

Table C.7: 2D Grid Refinement Verification : Solution H^0 Norm (80 Elements)

	h results		**m1 results**		**m2 results**	
1.0	$\|h\|_{H^0}$	$\Delta\|h\|_{H^0}$	$\|m_1\|_{H^0}$	$\Delta\|m_1\|_{H^0}$	$\|m_2\|_{H^0}$	$\Delta\|m_2\|_{H^0}$
1	1.09493e+03		4.89119e+02		5.40171e+01	
2	1.09493e+03	9.11145e-06	4.89121e+02	2.40386e-03	5.40315e+01	1.44159e-02
3	1.09493e+03	9.10640e-06	4.89124e+02	2.62999e-03	5.40355e+01	4.04288e-03
4	1.09493e+03	5.30727e-06	4.89125e+02	8.55116e-04	5.40365e+01	9.98791e-04
5	1.09493e+03	1.10963e-06	4.89125e+02	2.38989e-04	5.40368e+01	2.53736e-04
3.0	$\|h\|_{H^0}$	$\Delta\|h\|_{H^0}$	$\|m_1\|_{H^0}$	$\Delta\|m_1\|_{H^0}$	$\|m_2\|_{H^0}$	$\Delta\|m_2\|_{H^0}$
1	1.09088e+03		9.15572e+02		2.87691e+02	
2	1.09088e+03	7.88072e-06	9.15571e+02	-1.72904e-03	2.87692e+02	1.19224e-03
3	1.09088e+03	6.25837e-06	9.15571e+02	2.05626e-04	2.87693e+02	4.86122e-04
4	1.09088e+03	9.78700e-08	9.15571e+02	1.15378e-04	2.87693e+02	1.39225e-05
5	1.09088e+03	2.43619e-08	9.15571e+02	4.31536e-05	2.87693e+02	9.92636e-06
5.0	$\|h\|_{H^0}$	$\Delta\|h\|_{H^0}$	$\|m_1\|_{H^0}$	$\Delta\|m_1\|_{H^0}$	$\|m_2\|_{H^0}$	$\Delta\|m_2\|_{H^0}$
1	1.08679e+03		1.22324e+03		5.21089e+02	
2	1.08679e+03	-3.09230e-05	1.22323e+03	-2.51719e-03	5.21088e+02	-7.88701e-04
3	1.08679e+03	-1.54148e-06	1.22323e+03	-2.68671e-04	5.21088e+02	-8.08046e-05
4	1.08679e+03	-3.18635e-06	1.22323e+03	-6.82291e-05	5.21088e+02	-8.55775e-05
5	1.08679e+03	-8.60555e-07	1.22323e+03	-9.02182e-06	5.21088e+02	-1.23776e-05
7.2	$\|h\|_{H^0}$	$\Delta\|h\|_{H^0}$	$\|m_1\|_{H^0}$	$\Delta\|m_1\|_{H^0}$	$\|m_2\|_{H^0}$	$\Delta\|m_2\|_{H^0}$
1	1.08241e+03		1.51828e+03		7.15792e+02	
2	1.08241e+03	-4.74657e-05	1.51828e+03	-2.36853e-03	7.15788e+02	-3.77371e-03
3	1.08241e+03	-2.31197e-06	1.51828e+03	-3.21012e-04	7.15787e+02	-8.69120e-04
4	1.08241e+03	-3.74256e-06	1.51828e+03	-9.69375e-05	7.15787e+02	-2.10035e-04
5	1.08241e+03	-9.88826e-07	1.51828e+03	-1.89914e-05	7.15787e+02	-5.01141e-05

Table C.8: 2D Grid Refinement Verification : Solution H^0 Norm (160 Elements)

	h results		**m1 results**		**m2 results**	
1.0	$\|\|h\|\|_{H^0}$	$\Delta\|\|h\|\|_{H^0}$	$\|\|m_1\|\|_{H^0}$	$\Delta\|\|m_1\|\|_{H^0}$	$\|\|m_2\|\|_{H^0}$	$\Delta\|\|m_2\|\|_{H^0}$
1	1.09570e+03		5.01722e+02		5.83563e+01	
2	1.09527e+03	-4.35918e-01	4.98343e+02	-3.37896e+00	5.72279e+01	-1.12841e+00
3	1.09510e+03	-1.61711e-01	4.97089e+02	-1.25348e+00	5.68093e+01	-4.18606e-01
4	1.09501e+03	-9.14021e-02	4.96381e+02	-7.08493e-01	5.65727e+01	-2.36603e-01
5	1.09500e+03	-1.40618e-02	4.96272e+02	-1.08999e-01	5.65363e+01	-3.64005e-02
3.0	$\|\|h\|\|_{H^0}$	$\Delta\|\|h\|\|_{H^0}$	$\|\|m_1\|\|_{H^0}$	$\Delta\|\|m_1\|\|_{H^0}$	$\|\|m_2\|\|_{H^0}$	$\Delta\|\|m_2\|\|_{H^0}$
1	1.09162e+03		9.26902e+02		3.02050e+02	
2	1.09126e+03	-3.60400e-01	9.22493e+02	-4.40945e+00	2.96284e+02	-5.76583e+00
3	1.09112e+03	-1.33696e-01	9.20857e+02	-1.63576e+00	2.94145e+02	-2.13893e+00
4	1.09105e+03	-7.55678e-02	9.19933e+02	-9.24562e-01	2.92936e+02	-1.20896e+00
5	1.09104e+03	-1.16258e-02	9.19790e+02	-1.42240e-01	2.92750e+02	-1.85994e-01
5.0	$\|\|h\|\|_{H^0}$	$\Delta\|\|h\|\|_{H^0}$	$\|\|m_1\|\|_{H^0}$	$\Delta\|\|m_1\|\|_{H^0}$	$\|\|m_2\|\|_{H^0}$	$\Delta\|\|m_2\|\|_{H^0}$
1	1.08796e+03		1.23806e+03		5.46236e+02	
2	1.08738e+03	-5.80650e-01	1.23108e+03	-6.98121e+00	5.34332e+02	-1.19042e+01
3	1.08716e+03	-2.15402e-01	1.22849e+03	-2.58980e+00	5.29916e+02	-4.41610e+00
4	1.08704e+03	-1.21749e-01	1.22703e+03	-1.46380e+00	5.27420e+02	-2.49606e+00
5	1.08702e+03	-1.87306e-02	1.22680e+03	-2.25200e-01	5.27036e+02	-3.84009e-01
7.2	$\|\|h\|\|_{H^0}$	$\Delta\|\|h\|\|_{H^0}$	$\|\|m_1\|\|_{H^0}$	$\Delta\|\|m_1\|\|_{H^0}$	$\|\|m_2\|\|_{H^0}$	$\Delta\|\|m_2\|\|_{H^0}$
1	1.08492e+03		1.53696e+03		7.47664e+02	
2	1.08360e+03	-1.31454e+00	1.52789e+03	-9.06895e+00	7.32598e+02	-1.50659e+01
3	1.08311e+03	-4.87652e-01	1.52453e+03	-3.36428e+00	7.27009e+02	-5.58898e+00
4	1.08284e+03	-2.75629e-01	1.52263e+03	-1.90155e+00	7.23850e+02	-3.15899e+00
5	1.08280e+03	-4.24045e-02	1.52234e+03	-2.92546e-01	7.23364e+02	-4.85999e-01

Table C.9: 2D Grid Refinement Verification : Solution Energy Norm ($t = 1.0\ s$)

t=1.0

Elements	$\|h\|_E$	$\|\Delta h\|_E$	**Slope**
20	3.37579e+02		
40	1.97374e+02	-1.40204e+02	
80	1.03588e+02	-9.37855e+01	5.8009e-01
160	8.13653e+01	-2.22235e+01	2.0772e+00
	$\|m_1\|_E$	$\|\Delta m_1\|_E$	**Slope**
20	2.62962e+04		
40	1.33477e+04	-1.29484e+04	
80	8.43137e+03	-4.91636e+03	1.3971e+00
160	6.95829e+03	-1.47308e+03	1.7387e+00
	$\|m_2\|_E$	$\|\Delta m_2\|_E$	**Slope**
20	5.47404e+02	0	0
40	1.01445e+03	4.67046e+02	0
80	9.69989e+02	-4.44609e+01	3.39295e+00 + 4.53236e+00i
160	7.33533e+02	-2.36455e+02	-2.41095e+00

Table C.10: 2D Grid Refinement Verification : Solution Energy Norm ($t = 3.0\ s$)

t=3.0

Elements	$\|h\|_E$	$\|\Delta h\|_E$	**Slope**
20	2.55767e+02		
40	1.12578e+02	-1.43189e+02	
80	8.00068e+01	-3.25715e+01	2.1362e+00
160	7.34268e+01	-6.57992e+00	2.3074e+00
	$\|m_1\|_E$	$\|\Delta m_1\|_E$	**Slope**
20	2.35666e+04		
40	1.14142e+04	-1.21524e+04	
80	8.57576e+03	-2.83845e+03	2.0980e+00
160	8.00214e+03	-5.73623e+02	2.3069e+00
	$\|m_2\|_E$	$\|\Delta m_2\|_E$	**Slope**
20	6.82307e+03		
40	4.31684e+03	-2.50623e+03	
80	2.86336e+03	-1.45347e+03	7.86010e-01
160	2.20469e+03	-6.58672e+02	1.14187e+00

Table C.11: 2D Grid Refinement Verification : Solution Energy Norm ($t = 5.0\ s$)

	t=5.0		
Elements	$\|h\|_E$	$\|\Delta h\|_E$	**Slope**
20	2.51146e+02		
40	1.13112e+02	-1.38033e+02	
80	8.34394e+01	-2.96732e+01	2.2177e+00
160	7.97186e+01	-3.72077e+00	2.9954e+00
	$\|m_1\|_E$	$\|\Delta m_1\|_E$	**Slope**
20	2.48219e+04		
40	1.28337e+04	-1.19881e+04	
80	9.74951e+03	-3.08422e+03	1.9586e+00
160	9.08911e+03	-6.60402e+02	2.2234e+00
	$\|m_2\|_E$	$\|\Delta m_2\|_E$	**Slope**
20	1.06892e+04		
40	5.87451e+03	-4.81472e+03	
80	4.01607e+03	-1.85843e+03	1.37336e+00
160	3.49366e+03	-5.22409e+02	1.83083e+00

Table C.12: 2D Grid Refinement Verification : Solution Energy Norm ($t = 7.2\ s$)

t=7.2

Elements	$\|h\|_E$	$\|\Delta h\|_E$	**Slope**
20	4.70814e+02		
40	1.21319e+02	-3.49494e+02	
80	8.92602e+01	-3.20597e+01	3.4464e+00
160	8.65564e+01	-2.70373e+00	3.5677e+00
	$\|m_1\|_E$	$\|\Delta m_1\|_E$	**Slope**
20	2.77860e+04		
40	1.44611e+04	-1.33248e+04	
80	1.07343e+04	-3.72674e+03	1.8381e+00
160	9.83669e+03	-8.97701e+02	2.0536e+00
	$\|m_2\|_E$	$\|\Delta m_2\|_E$	**Slope**
20	1.48868e+04		
40	7.35061e+03	-7.53621e+03	
80	4.88281e+03	-2.46779e+03	1.61062e+00
160	4.25678e+03	-6.26036e+02	1.97890e+00

Table C.13: 2D Grid Refinement Verification : Solution H^0 Norm ($t = 1.0\ s$)

t=1.0

Elements	$\|h\|_{H^0}$	$\|\Delta h\|_{H^0}$	**Slope**
20	1.11410e+03		
40	1.09471e+03	-1.93885e+01	
80	1.09493e+03	2.20316e-01	6.45948e+00
160	1.09500e+03	6.41208e-02	1.78071e+00
	$\|m_1\|_{H^0}$	$\|\Delta m_1\|_{H^0}$	**Slope**
20	4.61029e+02		
40	4.69364e+02	8.33445e+00	
80	4.89125e+02	1.97611e+01	-1.2455e+00
160	4.96272e+02	7.14676e+00	1.4673e+00
	$\|m_2\|_{H^0}$	$\|\Delta m_2\|_{H^0}$	**Slope**
20	3.99428e+01		
40	4.75302e+01	7.58741e+00	
80	5.40368e+01	6.50662e+00	2.2169e-01
160	5.65363e+01	2.49949e+00	1.3802e+00

Table C.14: 2D Grid Refinement Verification : Solution H^0 Norm ($t = 3.0\ s$)

t=3.0

Elements	$\|h\|_{H^0}$	$\|\Delta h\|_{H^0}$	**Slope**
20	1.10867e+03		
40	1.09030e+03	-1.83646e+01	
80	1.09088e+03	5.79480e-01	4.98602e+00
160	1.09104e+03	1.53556e-01	1.91599e+00
	$\|m_1\|_{H^0}$	$\|\Delta m_1\|_{H^0}$	**Slope**
20	9.04864e+02		
40	9.01809e+02	-3.05484e+00	
80	9.15571e+02	1.37622e+01	-2.1715e+00
160	9.19790e+02	4.21924e+00	1.7056e+00
	$\|m_2\|_{H^0}$	$\|\Delta m_2\|_{H^0}$	**Slope**
20	2.41474e+02		
40	2.72094e+02	3.06198e+01	
80	2.87693e+02	1.55991e+01	9.7300e-01
160	2.92750e+02	5.05742e+00	1.6249e+00

Table C.15: 2D Grid Refinement Verification : Solution H^0 Norm ($t = 5.0\ s$)

t=5.0

Elements	$\|h\|_{H^0}$	$\|\Delta h\|_{H^0}$	**Slope**
20	1.10228e+03		
40	1.08586e+03	-1.64209e+01	
80	1.08679e+03	9.30261e-01	4.14175e+00
160	1.08702e+03	2.35356e-01	1.98279e+00
	$\|m_1\|_{H^0}$	$\|\Delta m_1\|_{H^0}$	**Slope**
20	1.21054e+03		
40	1.20979e+03	-7.47921e-01	
80	1.22323e+03	1.34447e+01	-4.1680e+00
160	1.22680e+03	3.56612e+00	1.9146e+00
	$\|m_2\|_{H^0}$	$\|\Delta m_2\|_{H^0}$	**Slope**
20	4.47596e+02		
40	4.99230e+02	5.16347e+01	
80	5.21088e+02	2.18574e+01	1.2402e+00
160	5.27036e+02	5.94779e+00	1.8776e+00

Table C.16: 2D Grid Refinement Verification : Solution H^0 Norm ($t = 7.2\ s$)

t=7.2

Elements	$\|h\|_{H^0}$	$\|\Delta h\|_{H^0}$	**Slope**
20	1.09406e+03		
40	1.08089e+03	-1.31735e+01	
80	1.08241e+03	1.52703e+00	3.10883e+00
160	1.08280e+03	3.81765e-01	1.99997e+00
	$\|m_1\|_{H^0}$	$\|\Delta m_1\|_{H^0}$	**Slope**
20	1.49357e+03		
40	1.50206e+03	8.48965e+00	
80	1.51828e+03	1.62213e+01	-9.3411e-01
160	1.52234e+03	4.05558e+00	1.9999e+00
	$\|m_2\|_{H^0}$	$\|\Delta m_2\|_{H^0}$	**Slope**
20	6.23366e+02		
40	6.86355e+02	6.29896e+01	
80	7.15787e+02	2.94315e+01	1.0977e+00
160	7.23364e+02	7.57686e+00	1.9576e+00

VITA

Zachariah Chambers was born in Denver, Colorado on July 7, 1972. During his K-12 years he lived in Pennsylvania, California, and the former Yugoslavia, attending a total of eight different schools before graduating from Butler High School in Pennsylvania in 1990.

He then enrolled at Rose-Hulman Institute of Technology in Terre Haute, Indiana where he obtained his bachelor's degree in mechanical engineering in 1994. He stayed another two years to obtain his master's degree in mechanical engineering, focusing on computational fluid dynamics, in 1996. He and his wife then relocated to Knoxville, Tennessee where he began work on his PhD in engineering science and mechanics with a concentration in computational fluid dynamics.

In August of 2000, he completed his PhD and accepted an assistant professor of mechanical engineering position at his alma mater Rose-Hulman.